

University of New Hampshire

University of New Hampshire Scholars' Repository

Doctoral Dissertations

Student Scholarship

Spring 2021

DEVELOPMENT OF A SUNKEN OIL TRANSPORT TOOL USING MESOSCALE EXPERIMENTS

Melissa Denise Gloekler
University of New Hampshire, Durham

Follow this and additional works at: <https://scholars.unh.edu/dissertation>

Recommended Citation

Gloekler, Melissa Denise, "DEVELOPMENT OF A SUNKEN OIL TRANSPORT TOOL USING MESOSCALE EXPERIMENTS" (2021). *Doctoral Dissertations*. 2571.
<https://scholars.unh.edu/dissertation/2571>

This Dissertation is brought to you for free and open access by the Student Scholarship at University of New Hampshire Scholars' Repository. It has been accepted for inclusion in Doctoral Dissertations by an authorized administrator of University of New Hampshire Scholars' Repository. For more information, please contact nicole.hentz@unh.edu.

**DEVELOPMENT OF A SUNKEN OIL TRANSPORT TOOL
USING MESOSCALE EXPERIMENTS**

BY

MELISSA D. GLOEKLER

Bachelor of Science, Environmental Engineering, University of New Hampshire, 2016

DISSERTATION

Submitted to the University of New Hampshire
in Partial Fulfillment of
the Requirements for the Degree of

Doctor of Philosophy
In
Civil and Environmental Engineering
May 2021

ALL RIGHTS RESERVED

© 2021

Melissa D. Gloekler

This dissertation has been examined and approved in partial fulfillment of the requirements for the degree of Doctor of Philosophy in Civil and Environmental Engineering by:

Dissertation Director, Dr. Nancy E. Kinner
Professor of Civil and Environmental Engineering

Dr. Thomas P. Ballestero
Professor of Civil and Environmental Engineering

Dr. Eshan Dave
Associate Professor of Civil Engineering

Dr. Thomas Lippman
Professor of Oceanography

Dr. Philip Ramsey
Professor of Mathematics and Statistics

on 3 May 2021

Original approval signatures are on file with the University of New Hampshire Graduate School.

To my mom, Dr. Denise M. Gloekler, for being my number one fan, believing that one person can change the world, and for sharing her love of life, nature, and family.

Don't question why she needs to be so free. She'll tell you it's the only way to be.

-The Rolling Stones

ACKNOWLEDGEMENTS

This research was made possible by the support and funding of the University of New Hampshire (UNH) Coastal Response Research Center (CRRC) and the National Oceanic and Atmospheric Administration (NOAA). I would like to extend my appreciation to the responders, modelers, and restoration specialists at NOAA's Office of Response and Restoration (OR&R) for their willingness to help design and guide this research, specifically, Steve Lehmann, Scott Lundgren, John Tarpley, Jordon Stout, Ben Shorr, George Graettinger, Adam Davis, Carl Childs, Chris Barker, Doug Helton, Dan Hahn, Amy MacFadyen, and Lisa DiPinto.

Many thanks to Neil and Ora MacFarlane whose generous support led to the design & build of the MacFarlane Flume - I am grateful to you and your family for this once in a lifetime opportunity. This project could not have been accomplished without the substantial contributions, use of laboratories and instruments, equipment, and expertise provided by:

- Civil & Environmental Engineering Department: Dr. Tom Ballestero, Dr. Eshan Dave and research group, Dr. Paula Mouser, Dr. Robin Collins and Kellen Sawyer, Dr. James Malley, Maddy Wasiewski, Dr. Weiwei Mo, Dr. Raymond Cook, and Dr. Erin Bell.
- Thank you to the School of Marine Sciences and Ocean Engineering for travel support to conferences, as well as Dr. Tom Lippmann and Dr. Diane Foster.
- Chemical Engineering Department: Dr. Nan Yi
- UNH Technology Service Center: John Ahern, Kevan Carpenter, Darcy Fournier, Scott Campbell, and Noah Macadam.

To my advisor, Dr. Nancy E. Kinner, thank you for your guidance, in life and for the sake of science, and for shattering glass ceilings so that I, and the hundreds of female engineers you taught, can follow in your groundbreaking footsteps.

To the CRRC family, Kathy Mandsager, Jesse Ross, and Nancy Kinner, from our Caribbean adventures, flying around Denali, exploring the Colorado wilderness, dining at Brennan's in NOLA, watching sunsets in San Diego, and sailing through Robinhood Cove, I want to thank you all from the bottom of my heart for the countless memories and many laughs. Your daily support, words of encouragement, and ability to provide perspective carried me through this experience.

Thank you to those who contributed many hours designing, building, and troubleshooting the MacFarlane Flume: John Ahern, Matthew McGinnis, Kai Kleyensteuber, Nate LaTourette, Kellen Sawyer, Scott Campbell, Kevan Carpenter, Noah Macadam, Sam Wojichowski. As well as those who supported this dissertation research: Kate Haslett, Taler Bixler, Mina Aghababaei, Dan Macadam, Megan Verfaillie, Jessica Manning, Danielle Kalmbach, Nicola Elardo, Julie Settembrino, Emma Turgeon, Ryan Fournier, Olivia Luthringer, Joe DeGregorio, Josh Howard, and Sara Murcko.

Thank you to all of my friends for their continuous words of encouragement, reminding me of the bigger picture, and always being ready to adventure. Thank you to Matthew McGinnis for showing me patience in problem solving and for your unconditional support.

I wish to thank my family: my Mom for showing me how to work hard and that pressure is a privilege; my Dad for teaching me I am capable of anything and to ski down everything; my Brother for pushing me well beyond my comfort zone and getting me into nature; my Sister for feeding me throughout grad school and for keeping life spontaneous; my nieces for grounding me in reality yet inspiring creativity.

TABLE OF CONTENTS

ACKNOWLEDGEMENTS	v
TABLE OF CONTENTS	vii
LIST OF TABLES	x
LIST OF FIGURES	xii
LIST OF ACRONYMS	xiv
LIST OF SYMBOLS	xvi
ABSTRACT.....	xix
CHAPTER 1	1
1.1 Motivation and Background	1
1.2 Dissertation Organization	2
CHAPTER 2.....	5
2.1 Abstract.....	5
2.2 Introduction.....	6
2.3 Methods and Materials.....	11
2.3.1 Facility: MacFarlane Flume.....	11
2.3.2 Velocimetry Measurements	12
2.3.3 Hydraulic Analysis.....	14
2.3.4 Bottom Substrate.....	19
2.3.5 BSS Calculations	20
2.3.6 Sensitivity Analysis of BSS Methods	27
2.4 Results and Discussion	27
2.4.1 Hydraulic Analysis: Acrylic Boundary.....	28
2.4.2 Boundary Characteristics: All Substrate Materials.....	34
2.4.3 Comparison of Roughness Parameters	40
2.4.4 Evaluating BSS: All Substrate Materials.....	43
2.4.5 Research Limitations and Method Selection	58
2.4.6 Sensitivity Analysis of BSS Methods	61
2.5 Conclusion and Future Research	65
CHAPTER 3.....	68
3.1 Abstract.....	68
3.2 Introduction.....	69
3.3 Methods and Materials.....	74
3.3.1 Oil Preparation and Properties	74
3.3.2 Substrate Classification.....	76

3.3.3 Hydraulic Conditions	77
3.3.4 Oil CSS Experiments	85
3.4 Results	88
3.4.1 Viscosity Analysis	88
3.4.2 Oil CSS Experiments	91
3.5 Discussion	113
3.5.1 Oil CSS Experiments	113
3.5.2 Caveats to Research Findings	114
3.5.3 Factors Driving SOP Transport	115
3.5.4 Comparison to Literature	117
3.6 Conclusions and Future Research	119
CHAPTER 4	121
4.1 Abstract	121
4.2 Introduction	122
4.3 Methods: Tool Development	124
4.3.1 Stakeholder Engagement	124
4.3.2 SOTT Structure	128
4.4 Results and Discussion	148
4.4.1 Kalamazoo River Case Study	148
4.4.2 Application to Sunken Oil Spill	160
4.5 Conclusions and Future Research	161
CONCLUSIONS AND RECOMMENDATIONS	163
5.1 Conclusions	163
5.2 Significance	164
5.3 Recommendations for Future Research	165
LIST OF REFERENCES	167
APPENDICES	177
APPENDIX A: Chapter 2 Appendices	A.1-1
Appendix A.1: Hydraulic Analysis	A.1-1
Appendix A.2: Cross-Sectional Hydraulic Analysis	A.2-1
Appendix A.3: Boundary Layer Conditions	A.3-1
Appendix A.4: Particle Size Distribution	A.4-1
Appendix A.5: Estimating Manning's n	A.5-1
Appendix A.6: Percent Removal of Velocity Data	A.6-1
Appendix A.7: Eddy Diffusivity ($E(z)$) vs. Dimensionless Height ($Z+$)	A.7-1
Appendix A.8: Velocity Measurement Location	A.8-1

Appendix A.9: BSS Method for All Substrate Types.....	A.9-1
Appendix A.10: Sensitivity Analysis Plots.....	A.10-1
APPENDIX B: Chapter 3 Appendices.....	B.1-1
Appendix B.1: Fresh & Weathered Brookfield Viscosity	B.1-1
Appendix B.2: DHR and Brookfield Viscosity	B.2-1
Appendix B.3: Wells-Brookfield Viscosity Variability	B.3-1
Appendix B.4: Plots of Measured Responses	B.4-1
APPENDIX C: Chapter 4 Appendices.....	C.1-1
Appendix C.1: Catalogue of Sunken Oil Images.....	C.1-1
APPENDIX D: Protocols and Methods	D.1-1
Appendix D.1: MacFarlane Flume Protocol.....	D.1-1
Appendix D.2: Nortek Vectrino Profiler II Protocol	D.2-1
Appendix D.3: Creation and Installation of Substrates Protocol.....	D.3-1
Appendix D.4: Oil Open Pan Evaporative Protocol.....	D.4-1
Appendix D.5: Clay-Oil Mixtures and Testing Protocol.....	D.5-1
Appendix D.6: Density for Heavy Fuel Oil.....	D.6-1
Appendix D.7: Sunken Oil Critical Shear Stress Experimental Protocol.....	D.7-1

LIST OF TABLES

Table 2-1: Format of summary tables from the hydraulic analyses.....	14
Table 2-2: Sieve analysis showing the particle size distribution.	20
Table 2-3: <i>In-situ</i> hydraulic conditions for each VFD setting.	31
Table 2-4: Summary of derived and measured boundary parameters and characteristics used to calculate BSS.	39
Table 2-5: Comparison of CD values calculated from various methods derived within zLP	41
Table 2-6: Velocities for which BSS methods are valid in the MacFarlane Flume.	44
Table 2-7: Summary of BSS method scale and application. Note: the bold text indicates the methods used in subsequent CSS experiments.	60
Table 3-1: Sieve analysis showing the Particle Size Distribution (PSD) and Mean Texture Depth (MTD).	77
Table 3-2: Summary of experimental conditions.....	86
Table 3-3: Criteria of oil CSS threshold for $\nu_o > 6 \times 10^4$ cSt. [N.B., The $\nu_o > 6 \times 10^4$ cSt threshold is based on experimental data and future experiments should be conducted to resolve these ranges as the criteria may apply to a broader viscosity range].	94
Table 3-4: Criteria of oil CSS thresholds for $\nu_o < 2 \times 10^4$ cSt. [N.B., The $\nu_o < 2 \times 10^4$ cSt threshold is based on experimental data and future experiments should be conducted to resolve these ranges as the criteria may apply to a broader viscosity range].	99
Table 3-5: Summary of results for all of the oil CSS experimental trials.....	102
Table 3-6: Fitted equations for gravity spreading, rope formation, ripple formation, and SOP break-apart/resuspension CSS thresholds.	110
Table 4-1: Criteria describing the thresholds of oil movement applicable for $\nu_o > 6 \times 10^4$ cSt (typical of Alberta bitumen at $\sim 33^\circ\text{C}$). [N.B., The $\nu_o > 6 \times 10^4$ cSt threshold is based on experimental data and future experiments should be conducted to resolve these ranges as the criteria may apply to a broader viscosity range].	126
Table 4-2: Criteria describing the thresholds of oil movement applicable for $\nu_o < 2 \times 10^4$ cSt (typical of fresh No.6 HFO at $\sim 13^\circ\text{C}$). [N.B., The $\nu_o < 2 \times 10^4$ cSt threshold is based on experimental data and future experiments should be conducted to resolve these ranges as the criteria may apply to a broader viscosity range].	127
Table 4-3: Example of a scenario that does not follow all SOTT assumptions and warns the user the SOTT is not applicable.	131
Table 4-4: Example of a scenario that follows SOTT assumptions and can be used to predict sunken oil transport.	132
Table 4-5: An example of the environmental data input parameters used in the SOTT.	134
Table 4-6: Particle size range and associated CSS range used as input in the SOTT.....	135
Table 4-7: Oil properties or selection of a proxy oil as input parameters used in the SOTT.	143
Table 4-8: Empirically-derived equations of oil CSS from the flume-based experiments.	143
Table 4-9: Example of the TOC summary table.....	146
Table 4-10: Example of the sediment and oil transport summary table.	146
Table 4-11: SOTT input parameters used for the Kalamazoo River oil spill case study.....	151
Table 4-12: Summary table describing Kalamazoo River dimensions, water temperature, and oil condition for each SOTT scenario.	151
Table 4-13: SOTT results summarizing Uc for each scenario.	152

Table 4-14: SOT results summarizing the predicted oil τ_{OC} thresholds and the range of **Reoc** * for each scenario. 152

LIST OF FIGURES

Figure 2-1: A simplified velocity profile and subsequent boundary layer as it develops over a plate, illustrating the viscous sublayer adjacent to the boundary, the logarithmic layer and the velocity defect region.	7
Figure 2-2: Shields Diagram, referenced from Vanoni (2006), illustrating the relationship developed by Shields (1936) between dimensionless hydraulic (Re^*) and shear stress parameters (τ^*).	9
Figure 2-3: Longitudinal section of the MacFarlane Flume.	12
Figure 2-4: Vectrino Profiler II ADV measured instantaneous velocity used in BSS calculations.	13
Figure 2-5: Sampling locations of the longitudinal hydraulic analysis.	15
Figure 2-6: Flow chart outlining the step-by-step process of how BSS was calculated in this research.	21
Figure 2-7: Compilation of velocity measurements for acrylic, sand, fine pebble, and medium pebble; a line of best fit relates VFD Setting (Hz) with U (m/s) for $h = 30.5 \pm 1$ cm...	29
Figure 2-8: (a) Uniform conditions at VFD setting of 4 Hz. (b) Non-uniform conditions at VFD setting of 16 Hz.	32
Figure 2-9: (a) Steady state conditions for VFD setting of 4 Hz. (b) Unsteady flow regime at VFD setting of 16 Hz.	33
Figure 2-10: Three sampling ranges were compiled into one velocity profile based on the stream wise velocity (m/s) and the distance from the bottom (m) for (a) acrylic, (b) sand, (c) fine pebble, and (d) medium pebble.	36
Figure 2-11: Eight BSS estimates calculated for (a) acrylic, (b) sand), (c) fine pebble, and (d) medium pebble.	46
Figure 2-12: Comparison of BSS calculated using the TKE method over acrylic, sand, fine pebble, and medium pebble substrates, and quadratic relationships between average velocity and BSS established by Bagherimiyab and Lemmin (2013) and Pope et al. (2006).	51
Figure 2-13: Acrylic and sand BSS calculated using the Quadratic Friction Law compared with results from Thompson et al. (2006).	56
Figure 3-1: Plan view (top) and longitudinal section (bottom) of the MacFarlane Flume.	78
Figure 3-2: Wells-Brookfield viscosity measurements for FC and WC oil.	89
Figure 3-3: Formation of SOP based ρ_o and v_o for all oil conditions and experimental temperature range.	91
Figure 3-4: Area of oil and number of erosions for FC oil on fine pebble substrate at 10°C.	92
Figure 3-5: Area of oil and number of erosions for FC oil on fine pebble substrate at 25°C.	95
Figure 3-6: Rope formation (red box) at $U = 0.13$ m/s during Trial 4 (FC oil, 25°C, sand).	96
Figure 3-7: Ripple formation (red arrows) at $U = 0.27$ m/s during Trial 8 (WC oil, 24°C, sand)..	97
Figure 3-8: Type II erosion (red circle) at $U = 0.2$ m/s during Trial 17 (FC oil, 22°C, medium pebble).	98
Figure 3-9: Relation between velocity (m/s) and average BSS (Pa) on sand, fine pebble, and medium pebble substrates.	101
Figure 3-10: Gravity spreading, rope formation, ripple formation, and SOP break-apart/resuspension CSS thresholds and sediment CSS values on sand substrate.	107

Figure 3-11: Gravity spreading, rope formation, ripple formation, and SOP break-apart/resuspension CSS thresholds and sediment CSS values on fine pebble substrate.	108
Figure 3-12: Gravity spreading, rope formation, ripple formation, and SOP break-apart/resuspension CSS thresholds and sediment CSS values on medium pebble substrate.	109
Figure 3-13: Results from the oil CSS experiments presented in the form of a Shield's Curve.	111
Figure 4-1: Representative images of (a) type II erosions (red circle), (b) rope formation, and (c) ripple formation (red arrows) of oil on medium pebble, sand, and fine pebble substrates, respectively.	125
Figure 4-2: Overview of the SOTT structure showing the major processes by referencing the relevant equations, tables, and figures discussed in this chapter.	130
Figure 4-3: Example of the SOTT output displayed as a reference curve.	146
Figure 4-4: Comparison of scenario's valid oil CSS thresholds with respect to v_o	153
Figure 4-5: SOTT reference curve from Scenario 1.	157
Figure 4-6: SOTT reference curve from Scenario 2.	157
Figure 4-7: SOTT reference curve from Scenario 3.	158
Figure 4-8: SOTT reference curve from Scenario 4.	158

LIST OF ACRONYMS

%Corr	Percent correlation
3D	Three-dimensional
ADIOS	Automated Data Inquiry for Oil Spills
ADV	Acoustic Doppler velocimeter
API	American Petroleum Institute
ARD	Assessment and Restoration Division
aSOA	Artificial sand oil agglomerates
BSS	Bed shear stress
CLB	Cold Lake Bitumen
CRRC	Coastal Response Research Center
CSS	Critical shear stress
DHR	Discovery Hybrid Rheometer
DHR	Discovery Hybrid Rheometer
FC	Fresh oil and clay
FC	Fresh oil+clay
GNOME	General NOAA Operational Modeling Environment
HFO	Heavy fuel oil
ICCOPR	Interagency Coordinating Committee on Oil Pollution
IROS	Inland riverine oil spill
LP	Logarithmic profile
M/V	Motor/Vessel
MTD	Mean texture depth
NaN	Not a number
NOAA	National Oceanic and Atmospheric Administration

NRC	National Research Council
OPA	Oil-particle aggregates
OPA	Oil-particle aggregates
OR&R	Office of Response and Resotration
PSD	Particle size distribution
RMS	Root mean square
RSD	Relative standard deviation
SNR	Signal-to-noise ratio
SOA	Sand-oil agglomerates
SOM	Sunken oil mats
SOP	Sediment-oil patty
SOTT	Sunken oil transport tool
SP	Single point
SSC	Suspended sediment concentrations
T/B	Tank/Barge
TKE	Turbulent Kinetic Energy
UNH	University of New Hampshire
USCG	United States Coast Guard
USEPA	United States Environmental Protection Agency
USGS	United States Geological Survey
VFD	Variable frequency drive
WC	Weathered oil and clay
WC	Weathered oil+clay

LIST OF SYMBOLS

$\%Ev$	Percent mass loss
δ'	Laminar boundary layer thickness
\bar{u}_z	Average velocity at elevation, z
$\frac{z_o}{h}$	Relative roughness
$\bar{\tau}_w$	BSS arithmetic average
h_o	Oil thickness
C_D	Drag coefficient
C_T	Coefficient used to calculate μ_o
K_t	Coefficient used to calculate ρ_o
K_u	Fitted coefficient to calculate n
P_w	Wetted perimeter
R_h	Hydraulic radius
Re^*	Grain Reynolds number
Re_{oc}^*	Oil critical grain Reynold's number
Re_{sc}^*	Sediment critical grain Reynold's number
Re_w^*	<i>In-situ</i> grain Reynold's number
Re_x	Boundary Reynolds number
S_f	Slope of the energy grade line or friction slope
\bar{U}	Depth averaged velocity
U_c	Critical free-stream velocity
Z^+	Dimensionless elevation above the bed
d_{50}	Median grain size
d_p	Grain diameter for which $p\%$ of grains are finer (e.g., $d_{84} = 84\%$ finer)
$\frac{du}{dz}$	Velocity gradient
k_s	Nikuradse roughness length
$\bar{u}, \bar{v}, \bar{w}$	Average velocity in x, y, z -directions
u_{oc}^*	Oil critical friction (shear) velocity
u_{rms}	Velocity root mean square

u_{sc}^*	Sediment critical friction (shear) velocity
u_w^*	Friction velocity (shear velocity)
ν_o	Kinematic viscosity of oil
ν_w	Kinematic viscosity of water
y_c	Critical water level
z_{LP}	Logarithmic region of the velocity profile
z_o	Characteristic roughness length
γ_s	Specific weight of sediment
γ_w	Specific weight of water
η_o	Complex viscosity of oil
μ_o	Dynamic viscosity of oil
μ_w	Dynamic viscosity of water
$\rho_{o(F)}$	Density of fresh oil
$\rho_{o(FC)}$	Density of fresh oil+clay
$\rho_{o(W)}$	Density of weathered oil
$\rho_{o(WC)}$	Density of weathered oil+clay
ρ_o	Density of oil
ρ_s	Sediment density
ρ_w	Water density
τ^*	Dimensionless shear stress, Shields Parameter
τ_c	Critical shear stress
τ_{oc}	Oil critical shear stress
τ_{sc}	Sediment critical shear stress
τ_v	Bed shear stress in viscous sublayer
τ_w	Bed shear stress
C	TKE fitting parameter
h	Water depth
β	Fitted coefficient to calculate C_D
σ	Standard deviation

A	Cross-sectional area of flow
C	Chézy resistance coefficient
E	Specific energy
$E(z)$	Eddy diffusivity
Fr	Froude number
N	Number of data points
Re	Reynolds number
T	Temperature
U	Free-stream velocity
X	Distance from leading edge of the disturbance
b	Channel width
f	Darcy-Weisbach friction factor
g	Gravity
n	Manning's roughness parameter
t	Time spent weathering
u	Velocity in the x -direction
u', v', w'	Velocity fluctuations in x, y, z -directions
v	Velocity in the y -direction
w	Velocity in the z -direction
x	Longitudinal (stream wise) dimension
y	Transverse dimension
y	Water level
z	Vertical dimension
z	Elevation above the bed
α	Fitted coefficient to calculate C_D
δ	Turbulent boundary layer thickness
κ	Von Karman's constant
$\mu_{o(WC)}$	Dynamic viscosity of weathered oil+clay
$\mu_{o(FC)}$	Dynamic viscosity of fresh oil+clay

ABSTRACT

DEVELOPMENT OF A SUNKEN OIL TRANSPORT TOOL USING MESOSCALE EXPERIMENTS

Oil spilled into fresh or saline water can float, become submerged in the water column (i.e., submerged oil), or sink to the bottom (i.e., sunken oil). Once introduced to the environment, oil can negatively impact ecological and public health, and the economy. Non-floating oil spills pose unique challenges to responders including the complexity of trajectory modeling; the inability to detect, track and recover oil due to limited visibility; the lack of readily deployable response technology; and limited understanding of how bottom substrate dynamics influence its fate and behavior.

This dissertation research determined that the driving factors used to predict sunken oil transport are the oil's kinematic viscosity (ν_o) and the median sediment size (d_{50}). The stages of oil transport were characterized based on ν_o , and empirical relationships using ν_o and d_{50} were derived to predict the oil's critical shear stress (CSS). For $\nu_o < 2 \times 10^4$ cSt, thresholds of movement were defined as: (1) gravity dispersion, (2) rope formation, (3) ripple formation, and (4) break-apart/resuspension. For $\nu_o > 6 \times 10^4$ cSt, the stages include: (1) type II erosions, and (2) bedload transport.

Using the experimentally derived oil transport equations, a prototype sunken oil transport tool (SOTT) was developed to predict sunken oil transport in a current driven environment. In the event of a non-floating oil spill, responders can input the spilled oil's characteristics (i.e., density, viscosity) and *in-situ* environmental conditions (e.g., water velocity, temperature, sediment type) to evaluate if oil will transport along the bottom, resuspend into the water column, or be buried by sediments.

CHAPTER 1

INTRODUCTION

1.1 Motivation and Background

Once spilled into saline or fresh water, oil can negatively impact ecological and public health, and the economy. The fate and transport of the spilled oil depends upon the oil type; how and where it is spilled; *in-situ* environmental conditions; and the ability for responders to detect, monitor and remove it. The oil's density relative to the receiving water dictates if it will float (i.e., floating), be neutrally buoyant in the water column (i.e., submerged), or sink to the bottom (i.e., sunken), and viscosity quantifies the oil's resistance to flow. Over time, the density and viscosity of the oil can change due to temperature, weathering processes (e.g., evaporation, photo-oxidation), interactions with sediment, minerals or marine snow, and *in-situ* hydrodynamic conditions (e.g., waves, currents).

Challenges when responding to sunken oil include the complexity of trajectory modeling; the inability to detect, track and recover oil due to limited visibility; the lack of readily deployable response technology; and limited understanding of how bottom substrate dynamics influence its fate and behavior (ICCOPR, 2015; Michel & Hansen, 2017; NRC, 1999; Stout & Wang, 2016). The aim of this research is to address knowledge gaps through a series of laboratory and flume-based experiments with No. 6 Heavy Fuel Oil (HFO) to determine environmental conditions that could mobilize sunken oil.

The bed shear stress (BSS) quantifies the frictional force exerted by the fluid on the boundary (i.e., force per unit area) and is used to characterize thresholds of sediment transport as a function of *in-situ* hydrodynamics, skin-friction induced by bed roughness, form drag, and

momentum transfer caused by mobilized grains (Nelson et al., 1995; Shields, 1936; Soulsby, 1997). When sediment transport is initiated, the BSS has exceeded the sediment's critical shear stress (CSS), providing a quantitative indicator that can be used to estimate sediment transport rates (Shields, 1936). The concept of using CSS thresholds to predict sediment transport was applied to predicting sunken oil transport. The focus of this dissertation was to define the stages of sunken oil transport, quantify the oil's CSS at those thresholds, and develop a tool based on oil CSS experiments that responders can use to predict if *in-situ* environmental conditions are sufficient to mobilize sunken oil.

All flume-based experiments were conducted in the MacFarlane Flume, at the University of New Hampshire's (UNH) Coastal Response Research Center (CRRC). The MacFarlane Flume was designed to study the transport and remediation of non-floating oil. The preliminary design phase began in October 2016 and the first round of construction was completed in October 2017. In December 2017, the flume's test section cracked and revealed that the load-bearing beams were deflecting when it was full of water. After a year of testing and redesign, a central overhead structural support was installed in December 2018.

Prior to conducting oil CSS experiments, a hydraulic analysis on the MacFarlane flume was required to correlate *in-situ* velocity with motor settings, and characterize *in-situ* flow conditions, evaluate instrument limitations, and determine which BSS methods were valid over the working range of the motors.

1.2 Dissertation Organization

This dissertation is in the form of a methods paper (Chapter 2) and two journal publications (Chapters 3 and 4). Each chapter begins by introducing the problem and outlining the objectives. The Methods section describes the materials, processes, and protocols used to complete the

objectives of that chapter. The Results and Discussion section presents the experimental data, an interpretation of the results, and limitations to the research. Lastly, each chapter contains its own Conclusions and Recommended Future Research section to highlight the major findings, applications of research, and knowledge gaps that remain. Chapter 5 summarizes the major conclusions and recommended future research from Chapters 2, 3 and 4. Each chapter has its own appendix for supplementary information, but all protocols developed and used in this dissertation can be found in Appendix D: Protocols and Methods.

- Chapter 2 includes a hydraulic analysis of the MacFarlane Flume. The hydraulic analysis characterized *in-situ* flow conditions of the flume, boundary characteristics, and the operating limitations for instruments over the working range of the motors. Chapter 2 provided the foundation to support which BSS methods were valid for use in the flume. Many of the methods developed in Chapter 2 (e.g., post-processing velocity data, calculating BSS) were used in the subsequent CSS experiments. Additionally, results from the Chapter 2 sensitivity analysis were referenced and applied in Chapter 4 when discussing what field measurements responders should prioritize to improve BSS predictions.
- Chapter 3 describes the laboratory experiments that quantified the oil properties and sediment characteristics, and a series of flume-based experiments performed to determine the oil's CSS. This chapter discusses the process by which the oil's thresholds of movement were defined, how image and video data was post-processed, the driving factors used to predict oil movement, and the empirical relationships derived from experimental data to predict oil CSS as a function of sediment size and oil viscosity.

- Chapter 4 outlines the process of developing the sunken oil transport tool (SOTT). The results from the oil CSS experiments were discussed with spill responders from multiple agencies (e.g., U.S. Army Corps, USGS) that provided feedback as to how the data should be used and visualized in the SOTT. Chapter 4 includes a detailed description of the equations used to develop the Excel-based tool and the limitations and applications of the SOTT. A case study provides an example of how to use the tool, and interpret results, and validation for using the SOTT to predict sunken oil transport in a river.

CHAPTER 2

HYDRAULIC ANALYSIS OF A RECIRCULATING FLUME AND THE EFFECT OF BOUNDARY ROUGHNESS ON BED SHEAR STRESS

2.1 Abstract

A comprehensive hydraulic analysis of the Coastal Response Research Center's (CRRC) MacFarlane Flume was conducted to establish baseline flow conditions, identify instrument limitations, and determine the bed shear stress (BSS) methods valid under variable flow regimes. Near-bed velocity observations, using an acoustic Doppler velocimeter (ADV), were collected over four, static substrates (i.e., acrylic, sand, fine pebble, medium pebble) as velocity increased from 0.06 ± 0.01 m/s to 1.04 ± 0.05 m/s in 0.08 ± 0.02 m/s intervals. The velocity profile was analyzed, BSS was estimated using eight computational methods, and boundary parameters were calculated and compared with literature values. A sensitivity analysis was performed on select BSS methods to quantify the individual impact and establish relative importance of the input parameters on the estimates.

Major findings from the hydraulic analysis included: (1) empirical relationships to predict *in-situ* velocity based on motor settings; (2) the flow conditions that invalidated ADV measurements; (3) characterization of the flow regime at each velocity interval (i.e., laminar vs. turbulent, steady vs. unsteady); (4) identifying the Turbulent Kinetic Energy, Law of the Wall – Single Point, Quadratic Friction Law, Chézy/Momentum, and Manning/Momentum methods to be the most suitable BSS methods in the MacFarlane Flume; and (5) that local BSS estimates were equally sensitive to velocity and roughness variability, whereas the global methods tended to be more sensitive to roughness variability.

2.2 Introduction

Hydrodynamic forcing elements (e.g., tides, currents, waves) influence the dynamics of sediment transport by exerting friction on the bed of a water body. Bed shear stress (BSS) quantifies the frictional force exerted by the fluid on the boundary (i.e., force per unit area) and is used to characterize thresholds of sediment transport as a function of *in-situ* hydrodynamics, skin-friction induced by bed roughness, form drag, and momentum transfer caused by mobilized grains (Nelson et al., 1995; Shields, 1936; Soulsby, 1997).

The thresholds of sediment transport are classified as incipient motion, bedload transport, and entrainment or suspended load transport. Incipient motion occurs when individual grains begin to move, while the majority of sediment remains immobile. Bedload transport is identified by grains rolling, hopping and sliding along the bed, ultimately transporting material in the direction of the forcing element. Entrainment, recognized as the suspension of sediments into the water column, can occur through frictional exertion of the fluid and be exacerbated by turbulent diffusion (Soulsby, 1997). When sediment transport is initiated, the BSS has exceeded the sediment's critical shear stress (CSS), providing a quantitative indicator that can be used to estimate bedload and suspended sediment transport rates (Shields, 1936). *In-situ* measurements are necessary to quantify the relationship between the forcing and resistance elements (e.g., water velocity, particle size) when predicting sediment transport rates (Wilcock, 1996).

As flow moves over a flat plate or uniform bed, a boundary layer develops due to the no slip condition (Figure 2-1) (Elger et al., 2013; Yen, 2002). The boundary layer minimizes the momentum transferred from the flow field to the bed and depends on the flow velocity, sediment median grain size, and the viscosity of the water. A laminar sublayer forms adjacent to the boundary and is a function of the fluid's viscosity. The height of the sublayer increases further away from the leading edge of the plate or wall until small vortices, due to viscous drag, become

unstable causing the boundary layer to transition to a turbulent state. An artificially induced transition can occur, known as tripping the boundary layer, if there is a disturbance in the flow field or roughness elements (e.g., presence of a rock). A turbulent boundary layer is divided into three regions: the viscous sublayer, the logarithmic layer and the velocity defect region (Elger et al., 2013).

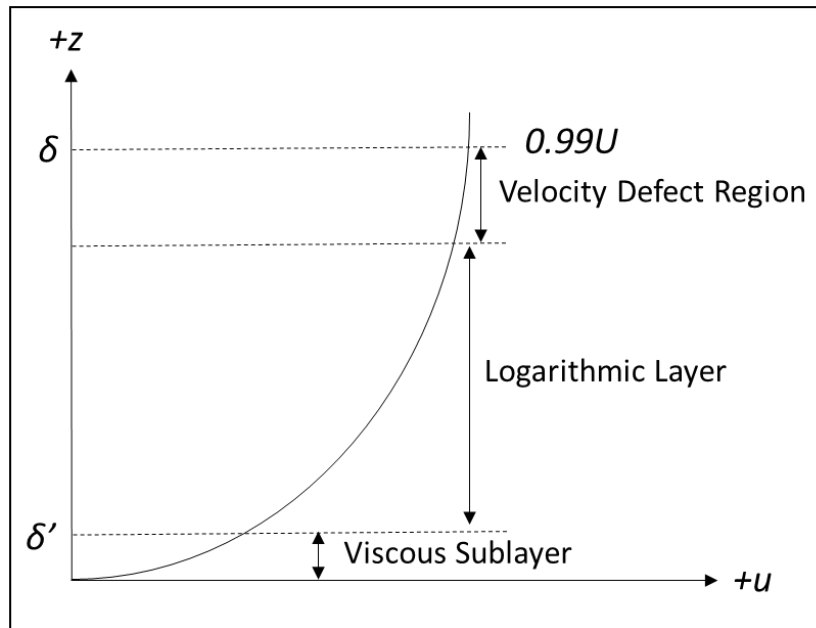


Figure 2-1: A simplified velocity profile and subsequent boundary layer as it develops over a plate, illustrating the viscous sublayer adjacent to the boundary, the logarithmic layer and the velocity defect region.

BSS, for a Newtonian fluid (e.g., water), is considered constant in the viscous sublayer and can be described by Newton’s Law of Viscosity (Eq. 2-1) (Elger et al., 2013; Soulsby, 1997; Yen, 2002).

$$\tau_v = \mu_w \frac{du}{dz} \quad \text{Eq. 2-1}$$

where: τ_v = BSS in the viscous sublayer (Pa), $\frac{du}{dz}$ = velocity gradient in the viscous sublayer (1/s), and μ_w = dynamic viscosity of the fluid (Pa*s). Newton’s Law of Viscosity is limited to laminar or smooth turbulent flow with minimal turbulent contributions near the boundary (i.e., when roughness elements do not protrude into the viscous sublayer) (Boudreau & Jorgensen, 2001;

Soulsby, 1997). Depending upon boundary roughness, fluid type, and average free-stream velocity, a small buffer layer may form between the viscous and turbulent layers. A logarithmic layer forms above the viscous layer or buffer layer, if present, and it transitions into the velocity defect region. The velocity defect region extends vertically into the water column until the velocity reaches 99% the free-stream velocity (U) of the bulk liquid (Elger et al., 2013; Yen, 2002). Free-stream velocity occurs some elevation above the bed where velocity is constant. Depending on where in the boundary layer the velocity is measured, the velocity profile can be expressed using a logarithmic function, a power law distribution or an exponential distribution (Yen, 2002). A velocity component is required to estimate BSS. Therefore, the method used to calculate BSS (e.g., Turbulent Kinetic Energy, Quadratic Friction Law) depends on how the velocity is calculated or measured, and if *in-situ* conditions fulfill method assumptions (e.g., steady state). Within the turbulent region of the boundary layer, for uniform, steady state conditions, BSS can be related to a surrogate value, friction velocity (Eq. 2-2) (Nelson et al., 1995).

$$u_w^* = \sqrt{\frac{\tau_w}{\rho_w}} \quad \text{Eq. 2-2}$$

where: u_w^* = friction velocity (m/s), τ_w = BSS (Pa), and ρ_w = water density (kg/m³). τ_w can also be expressed as a dimensionless value (τ^*) (Eq. 2-3) (Buscombe & Conley, 2012; Shields, 1936).

$$\tau^* = \frac{\tau_w}{g(\rho_s - \rho_w)d_{50}} \quad \text{Eq. 2-3}$$

where: τ^* = Shields Parameter (unitless), g = gravity (m/s²), ρ_s = sediment density (kg/m³), and d_{50} = median grain size (m). Dynamic similarity can be used to translate lab-based experiments to full-scale conditions with some measure of accuracy (Garcia, 2000; Shields, 1936; Soulsby, 1997; Vanoni, 2006). Based on laboratory experiments, Shields (1936) developed a diagram that can be used to estimate sediment transport by relating τ^* to the grain Reynolds number (Eq. 2-4).

$$Re^* = \frac{u_w^* d_{50}}{\nu_w} = \frac{u_w^* k_s}{\nu_w} \quad \text{Eq. 2-4}$$

where: Re^* = grain Reynolds number (unitless), k_s = Nikuradse roughness length (m), and ν_w = kinematic viscosity of water (m^2/s). Re^* is used to describe the environmental forcing conditions at the boundary. Flow is considered: hydraulically smooth for $Re^* < 5$, transitional if $5 < Re^* < 70$, and hydraulically rough for $Re^* > 70$. The black line in Figure 2-2, fitted from experimental data, illustrates the critical threshold of motion, “at which only a minor part (~1–10%) of the bed surface is moving (e.g., sliding, rolling, and colliding along the bed)” (van Rijn, 2007). The critical threshold (τ_c) is synonymous with CSS and is characteristic of the sediment’s properties. Sediment transport is initiated when $\tau_w \geq \tau_c$.

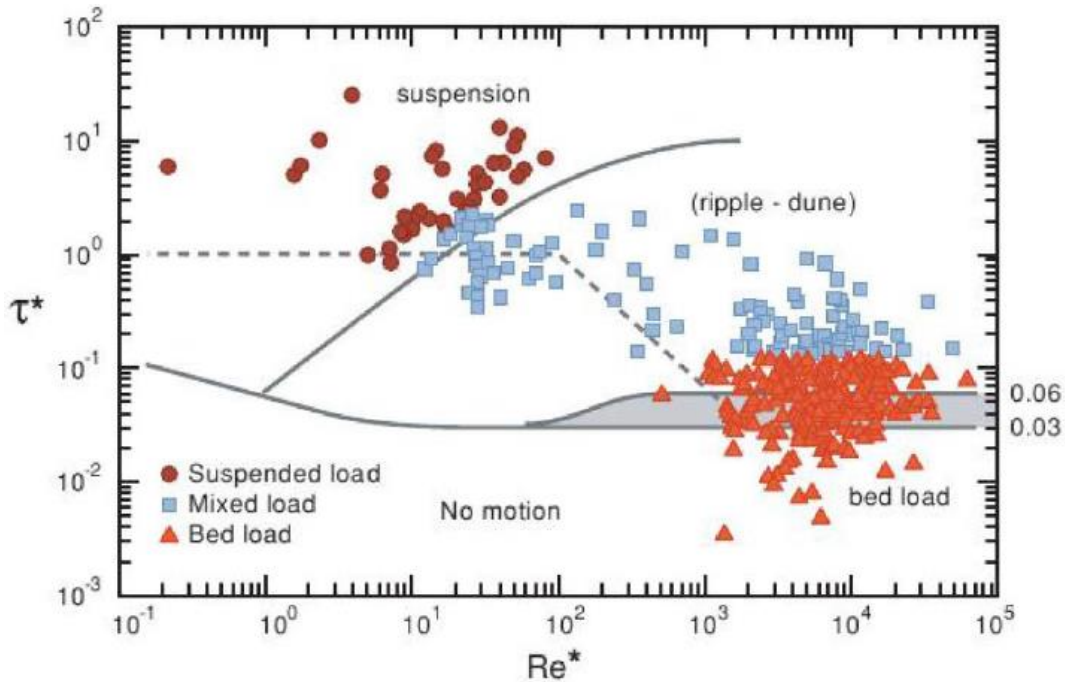


Figure 2-2: Shields Diagram, adjusted from Madsen and Grant (1976), illustrating the relationship developed by Shields (1936) between dimensionless hydraulic (Re^*) and shear stress parameters (τ^*).

Establishing thresholds of sediment movement and quantifying transport has applications across a variety of disciplines (e.g., riverine related scour, deposition and channel change (Biron et al.,

2004; Wilcock, 1996), nutrient diffusion into the water column (Wengrove et al., 2015), the transport of sunken oil (Cloutier et al., 2002; Simecek-Beatty, 2007)).

This chapter describes experiments conducted in CRRC's 2270-L recirculating flume. The flume was built as a result of a generous donation from Neil and Ora MacFarlane (Newport Beach, CA). Near-bed velocity observations (i.e., 0 to 9 cm from the bottom) were collected over four static substrates (i.e., acrylic, sand, fine pebble, medium pebble) as U increased from 0.06 ± 0.01 m/s to 1.04 ± 0.05 m/s in 0.08 ± 0.02 m/s intervals. A sieve analysis was performed to establish the particle size distribution for each substrate and determine common sediment descriptors (e.g., d_{50}). For each experimental setting, the velocity profile was analyzed, BSS was estimated using eight methods, and boundary parameters were calculated and compared with literature values.

Research Objectives:

1. Correlate *in-situ* water velocity with flume motor speeds.
2. Identify motor settings that exhibit unsteady, non-uniform, supercritical, or turbulent flow regimes.
3. Establish acoustic Doppler velocimeter (ADV) settings and limitations over the working range of the motors for acrylic, sand, fine pebble, and medium pebble substrates.
4. Characterize boundary parameters for an immobile acrylic (smooth), fine sand, fine pebble, and medium pebble substrates as a function of water velocity.
5. Calculate BSS based upon instantaneous velocity measurements and compare results for each experimental condition.
6. Perform a sensitivity analysis to quantify the impact of the hydraulic and boundary parameters on BSS estimates.

Eight methods were chosen to calculate BSS based upon their applicability to current driven flow regimes and sediment types, the diversity of input parameters, and the means to obtain input parameters (e.g., observational vs. derived). The methods were: (1) Newton's Law of Viscosity, (2) Law of the Wall – Logarithmic Profile, (3) Law of the Wall – Single Point, (4) the Quadratic Friction Law, (5) Indicator Function, (6) Turbulent Kinetic Energy, (7) the Momentum equation using the Chézy resistance coefficient, and (8) the Momentum equation using Manning's roughness coefficient. The findings provided an understanding of baseline conditions and were used to interpret results obtained in subsequent sunken oil CSS experiments using the recirculating flume (Chapter 3).

2.3 Methods and Materials

2.3.1 Facility: MacFarlane Flume

The MacFarlane Flume is a bottom-to-top recirculating system (Figure 2-3). The water is propelled by two 10 3/8 inch¹ propellers, housed in the lower tank, each driven by a 10 hp motor (ABB/Baldor Electric; Fort Smith, AR, USA). Each motor is controlled independently by an ABB variable frequency drive (VFD) from 0 to 20 Hz at 0.1 Hz intervals. Precise motor control ensures reproducible *in-situ* flow conditions based on the VFD setting. The lower tank, 1ft deep, 4 ft wide, 16 ft long, is enclosed on all four sides by acrylic panels. There are two openings in the bottom tank, an entrance and exit, allowing water to be funneled vertically into the upper channel and recirculated back down to the lower tank. The upper channel, 1 ft 10 inch deep, 1 ft wide, 13 ft long, consists of an open top, acrylic sidewalls, an acrylic bottom with zero slope. The acrylic

¹ The dimensions in Section 2.1 are the only ones given in English units because that is how the flume was designed and constructed.

sidewalls provide optimal viewing along the length of the upper channel, and the open top allows easy installations, adjustment, and removal of instruments before, during and after experiments.

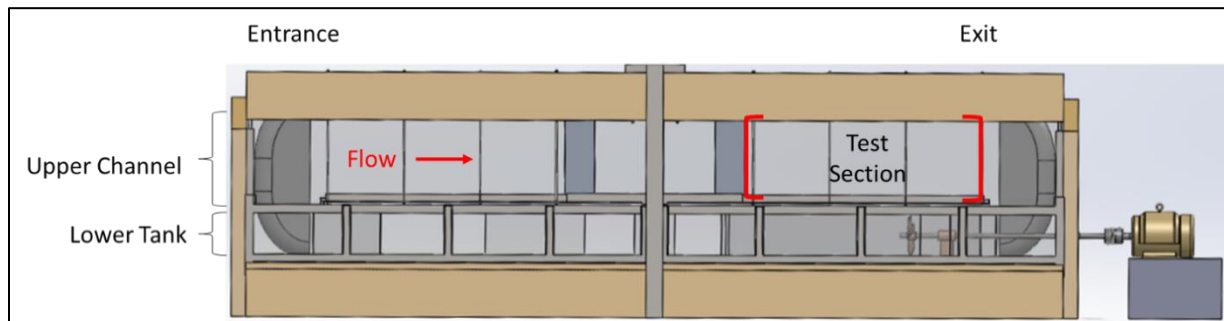


Figure 2-3: Longitudinal section of the MacFarlane Flume.

2.3.2 Velocimetry Measurements

The Vectrino Profiler II (Nortek Scientific; Vangroken, Norway), an ADV, measured the instantaneous longitudinal or stream wise (x), transverse (y), and vertical (z) velocity components (u , v , and w , respectively). [N.B., Average velocities are denoted using an overbar (e.g., \bar{u}) and fluctuations from the mean are denoted by an apostrophe (e.g., u')]. The Vectrino samples a 30 mm range at a spatial resolution of 1 mm; the sampling range begins 40 mm below the center beam to avoid flow-field interference (Figure 2-4) (Nortek AS, 2017). The sampling duration for each trial was a minimum of three minutes, to capture small scale turbulence events, using a sampling rate of 25 Hz resulting in approximately 4,625 data points per trial (Babaeyan-Koopaei et al., 2002; Pope et al., 2006; van Rijn, 2007).

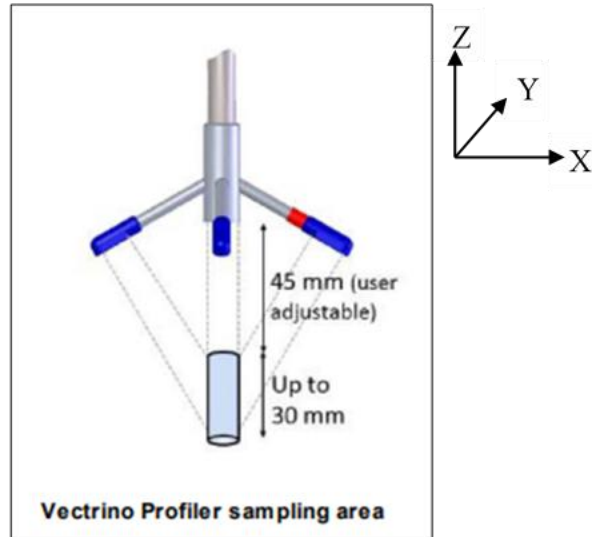


Figure 2-4: Vectrino Profiler II ADV measured instantaneous velocity used in BSS calculations.

Before each experiment, 20 grams of kaolinite clay were added to the water as a seeding material to improve the Vectrino’s Signal-to-Noise Ratio (SNR) and %Correlation (%Corr). A pulse is transmitted from the central transducer, reflected off the particles in the water rather than the water itself, and is detected by the four receivers (Nortek Scientific, 2012). The Vectrino’s “Ping Settings” (e.g., ping algorithm, velocity range) were adjusted for each trial based on water velocity and boundary conditions to minimize or eliminate weak spots and optimize the %Corr and SNR (Koca et al., 2017).

Data collected by the Vectrino was exported and evaluated using MatLab (MathWorks®; Natick, MA). All raw velocity datasets underwent a two-step filtering process. As recommended by the manufacturer, the first step evaluated data quality based on %Corr and SNR using a low pass filter. Data points were replaced with “Not a Number” (NaN) if the %Corr <70 or SNR <10; replacement rather than removal of data points was done to maintain the length of the time-series (Biron et al., 2004). A three pass, despiking filter was applied to each data set. With each pass, \bar{u} , \bar{v} , and \bar{w} , and the standard deviation, σ , were calculated for each sampling depth. Velocity data

within each vertical bin exhibited a normal (Gaussian). Therefore, outliers in each bin were detected and replaced with NaN if outside $\bar{u} \pm 3\sigma_u$, $\bar{v} \pm 3\sigma_v$, and $\bar{w} \pm 3\sigma_w$.

2.3.3 Hydraulic Analysis

2.3.3.1 Longitudinal: Acrylic Boundary

A longitudinal hydraulic analysis, over the acrylic boundary, identified the ideal test location within the upper channel and informed where within the test section the Vectrino was placed. Once determined, the Vectrino’s location stayed constant for the remainder of the flume experiments. Flow conditions (e.g., Froude (Fr) and Reynolds (Re) Numbers) for each VFD setting were calculated based on the measured velocity, water depth, and distance from the entrance. Results from the hydraulic analysis, were summarized in tables (Table 2-1) with non-uniform, unsteady, supercritical, and turbulent conditions highlighted in red.

Table 2-1: Format of summary tables from the hydraulic analyses.

VFD Setting (Hz)	$U \pm \sigma$ (m/s)	Re (Laminar < 750) (Turbulent >750)	Fr (Subcritical <1) (Critical =1) (Supercritical >1)	Uniform or Non-uniform	Steady or Unsteady
1 : : 17					

The sampling locations for the longitudinal analysis were: A) near the entrance, B), at the centerline, and C) within the test section (Figure 2-5).

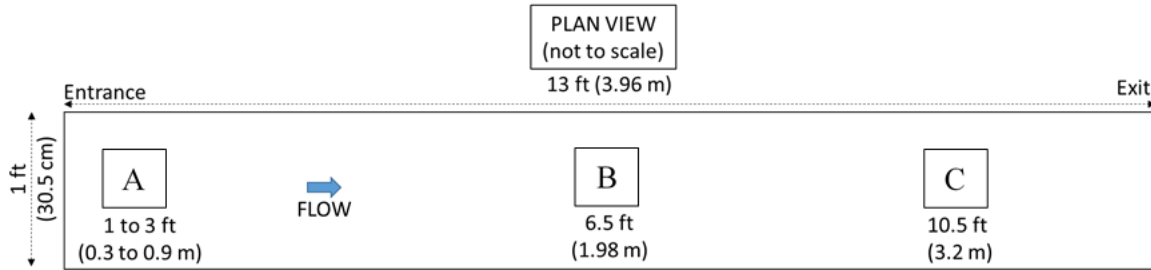


Figure 2-5: Sampling locations of the longitudinal hydraulic analysis.

A series of preliminary experiments established that a working water depth, h , of 30.5 ± 1 cm ensured the upper range of the VFD settings could be used while minimizing effects of the hydraulic jump in the test section. The hydraulic radius was 10.2 cm. It was determined using Eq. 2-5 based on $h = 30.5$ cm and was applied in calculations throughout this chapter.

$$R_h = \frac{A}{P_w} \quad \text{Eq. 2-5}$$

where: R_h = hydraulic radius (m), A = cross-sectional area of flow (m^2), and P_w = wetted perimeter (m). At each VFD setting and sampling location, the water level, distance along the length of the flume, and velocity were measured. The sampling location “A” moved further from the entrance as velocity increased to account for the lowest water level induced by the hydraulic jump. At sampling locations, A, B and C, for each VFD setting, 30-second time averaged velocity measurements were made using a flow probe held constant at 60% of the water depth (Global Water, FP211, USA). To compare flow probe measurements and determine U , instantaneous velocity was recorded by the Vectrino at sampling location C at 60% of the water depth. At sampling locations, A and B, the Vectrino’s instantaneous velocity measurements did not meet data quality metrics as specified by the manufacturer due to fluctuations in the water level and turbulence induced by the hydraulic jump. [N.B., The flow probe has a lower resolution than the Vectrino, when comparing the measured velocities; the flow probe velocity estimates were slightly larger (Appendix A.1: Hydraulic Analysis)].

Based on measured values, Re , a dimensionless parameter used to establish if the flow regime is laminar (i.e., viscous dominated) or turbulent (i.e., inertia dominated), was calculated for sampling location C (Eq. 2-6).

$$Re = \frac{UR_h}{\nu_w} \quad \text{Eq. 2-6}$$

where: U = free-stream velocity (m/s). For open channel flow conditions R_h is used as the characteristic length scale when calculating Re ; flow was considered turbulent for $Re > 750$ (Elger et al., 2013). Results from the longitudinal analysis were used to calculate Specific Energy, E , (Eq. 2-7) as a function of water velocity.

$$E = y + \frac{U^2}{2g} \quad \text{Eq. 2-7}$$

where: E = specific energy (m) and y = water level (m). A minimum E value indicates a minimum flow energy relative to the flow rate, specifying a critical flow depth, y_c (Eq. 2-8).

$$\frac{U^2}{2g} = \frac{1}{2}y_c \quad \text{Eq. 2-8}$$

The corresponding velocity at that depth is the critical velocity (Chaudhry, 2008). Fr is used to describe E in a dimensionless form by relating inertial and gravitational forces within the flow regime (Eq. 2-9).

$$Fr = \frac{U}{\sqrt{gh}} \quad \text{Eq. 2-9}$$

where flow is considered subcritical if $Fr < 1$, supercritical for $Fr > 1$, or critical when $Fr = 1$ (Chaudhry, 2008). Fr and Re are hydraulic descriptors useful when: (1) characterizing the flume's flow regime, and (2) scaling research findings from flume-based experiments to the natural environment.

When predicting sediment transport rates and estimating BSS, the flow regime is often assumed to be uniform and at steady state. It took between 10 and 15 seconds after changing the VFD setting for the test section to reach steady state. Steady state occurs when the velocity at a fixed point does not change with time (Le Roux, 2005; Vanoni, 2006). Confirmation that conditions within the test section were at steady state was accomplished by calculating and evaluating the root mean square (RMS) of u over a 20-second moving window (Eq. 2-10).

$$u_{rms} = \sqrt{\frac{1}{N} \sum_{i=1}^N u_i^2} \quad \text{Eq. 2-10}$$

where: u_{rms} = velocity root mean square (m/s), N = number of data points, and u_i = instantaneous water velocity (m/s). N was set as a moving window equal to 500 data points, including 250 velocity measurements before and after u_i . Steady state was confirmed as long as the u_{rms} was within the 95% confidence interval of \bar{u} for the duration of the trial run.

Flow conditions classified as uniform occur when the velocity vector is held constant through space, and are generally characterized by a constant flow depth (White, 2003). Using the velocity time series, flow was determined to be uniform as long as \bar{u} was significantly greater than \bar{v} and \bar{w} , and when \bar{v} and \bar{w} were approximately zero (Nikora & Goring, 2000).

2.3.3.2 Cross-Sectional: Acrylic Boundary

The velocity was measured 3.2 m from the entrance (discussed in Section 2.3.3.1 Longitudinal: Acrylic Boundary) at three locations within the cross-section to evaluate wall effects on U . Measurements were taken 6 cm, 15 cm, and 24 cm from the right sidewall across the channel. All velocity measurements were made using the Vectrino, set to a sampling range of 0 to 3 cm from the acrylic bottom. The velocity was held constant for three minutes while the Vectrino measured

velocity, and then the velocity was increased by 0.08 ± 0.02 m/s (i.e., 1 Hz) intervals until the upper range of the VFD setting was reached (i.e., 17 Hz).

Results from this section were used to determine if wall shear stress impacted BSS at the center of the channel. Based on the smooth boundary layer theory, the thickness of the boundary should range from 0.5 cm to 4 cm using Eq. 2-11 and Eq. 2-12, indicating that wall shear stress should not interfere with central BSS estimates (see Section 2.3.3.4 Boundary Layer Calculations). Comparison of near-wall and central BSS, using a Student's t-test, indicated that BSS estimates were not significantly different ($P\text{-value} > 0.05$) within the central 17 cm of the cross-section (Appendix A.2: Cross-Sectional Hydraulic Analysis). The practical implication of this finding applied to subsequent oil CSS experiments was that the diameter of the sunken oil blob should be less than 17 cm and injected into the center of the channel.

2.3.3.3 Vertical Analysis: Acrylic, Sand, Fine Pebble, Medium Pebble Boundaries

A vertical hydraulic analysis (e.g., 0 to 9 cm) was performed as a function of bottom roughness and water velocity. The Vectrino was placed 3.2 m from the entrance of the channel in the center of the cross-section. The sampling heights were divided into three segments based on the Vectrino's 3 cm sampling range, 0 to 3 cm, 3 to 6 cm, 6 to 9 cm, to develop a 9-cm velocity profile for each substrate. Data were collected for three minutes at each sampling height and velocity interval. Results from this analysis established the baseline boundary conditions and parameters of interest used to calculate BSS and evaluated the effect of bottom roughness on near-bed velocity profiles.

2.3.3.4 Boundary Layer Calculations

Re_x was calculated (Eq. 2-11) to understand the boundary layer's development over the length of the substrate.

$$Re_x = \frac{UX}{u_w} \quad \text{Eq. 2-11}$$

where: Re_x = boundary Reynolds number (unitless) and X = distance from the leading edge of the disturbance (m). For $Re_x < 5 \cdot 10^5$, the flow is considered laminar and the boundary layer thickness on a flat plate, δ' (m), was calculated using Eq. 2-12. When $Re_x > 5 \cdot 10^5$, the boundary layer thickness, δ (m), was calculated (Elger et al., 2013) using Eq. 2-13.

$$\delta' = \frac{5X}{Re_x^{1/2}} \quad \text{Eq. 2-12}$$

$$\delta = \frac{0.16X}{Re_x^{1/7}} \quad \text{Eq. 2-13}$$

δ was compared with the d_{84} for sand, fine pebble, and medium pebble substrates to determine if the particle size was sufficient to trip the boundary layer (i.e., if $d_{84} > 1/6 \cdot \delta$, boundary layer is tripped) (Elger et al., 2013) (Appendix A.3: Boundary Layer Conditions). Fine pebble and medium pebble substrates were large enough to trip the boundary layer at the start of the substrate, whereas the sand sediment size was not. Therefore, to ensure all boundary layers were turbulent, pebbles were glued to the leading edge of each sand substrate. Re^* was also used to determine the presence of a viscous sublayer for each substrate material and velocity setting (Eq. 2-4).

2.3.4 Bottom Substrate

Three replicate sieve analyses were conducted to determine the particle size distribution (PSD) for sand, fine pebble, and medium pebble substrates (Table 2-2) (ASTM, 2017b) and characterized based on the Wentworth Grade Scale (Appendix A.4: Particle Size Distribution) (Williams et al., 2006). Substrates used in experimental trials were adhered to 1.5 m long by 11.5 cm wide metal flashing with contact cement and centered within the test section.

Table 2-2: Sieve analysis showing the particle size distribution.

	Sediment Size (mm)		
	Sand	Fine Pebble	Medium Pebble
d_{10}	0.25	4.60	9.00
d_{25}	0.30	5.50	10.3
d_{50}	0.42	6.50	10.6
d_{84}	1.20	8.50	11.1
d_{90}	1.50	9.00	11.2

2.3.5 BSS Calculations

This section details the equations used to calculate BSS (τ_w), their limitations, and assumptions essential to the validity of each method. A general overview of BSS calculations is outlined in the flowchart shown in Figure 2-6. [N.B., The term BSS and τ_w were used when discussing shear stress for all methods, even for methods evaluating shear stress some elevation (z) above the boundary, where $0 \text{ cm} < z < 3 \text{ cm}$].

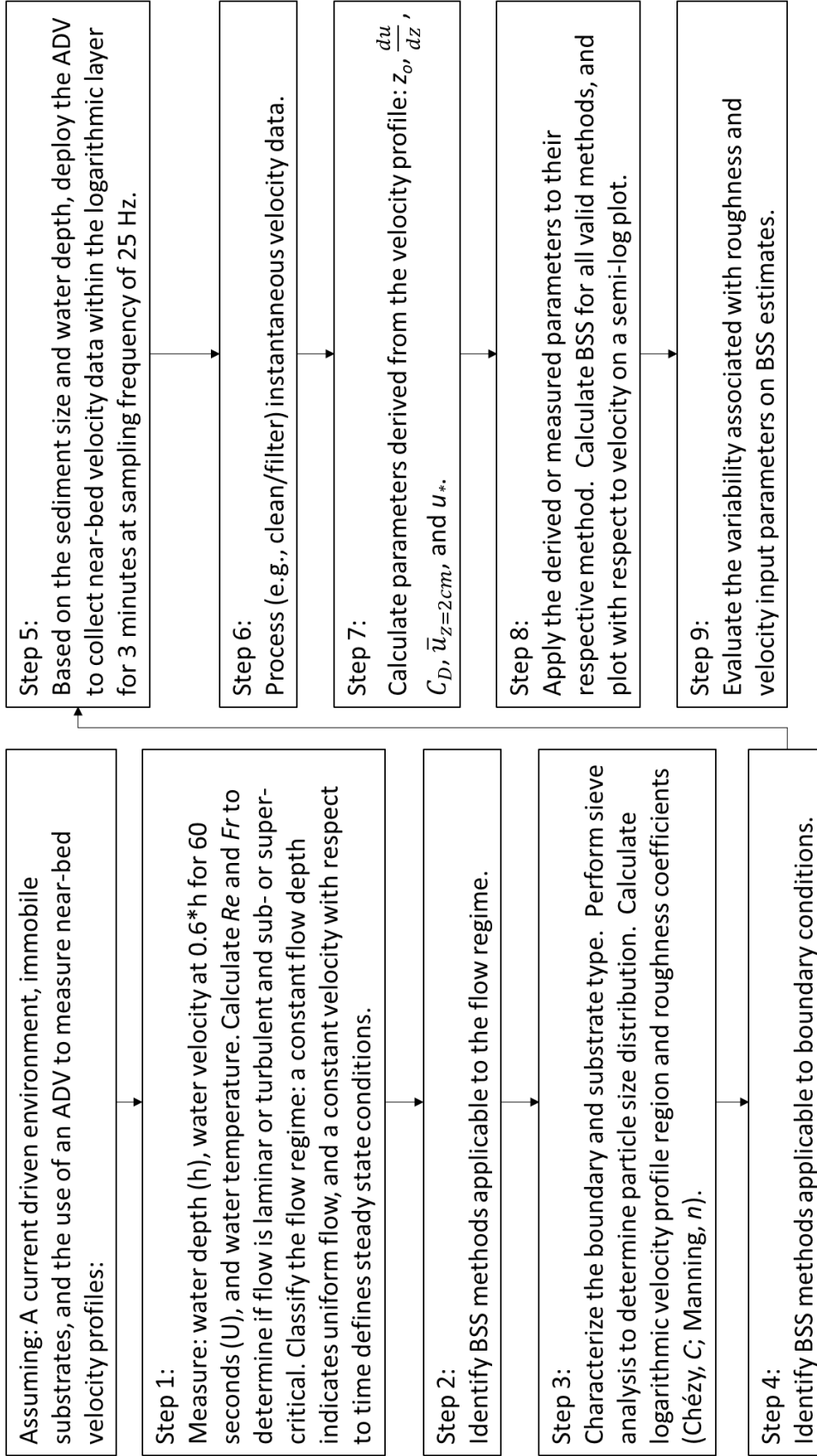


Figure 2-6: Flow chart outlining the step-by-step process of how BSS was calculated in this research.

2.3.5.1 Newton's Law of Viscosity

Assuming the presence of a viscous sublayer, Newton's Law of Viscosity (Eq. 2-1) was used to estimate τ_w ; see Section 2.2 for this method's assumptions and limitations.

2.3.5.2 Turbulent Kinetic Energy (TKE)

To calculate BSS, the TKE method uses 3D velocity fluctuations (i.e., u' , v' , w') (Eq. 2-14- Eq. 2-17).

$$u' = u - \bar{u} \quad \text{Eq. 2-14}$$

$$v' = v - \bar{v} \quad \text{Eq. 2-15}$$

$$w' = w - \bar{w} \quad \text{Eq. 2-16}$$

$$\tau_w = C \left[\frac{1}{2} \right] \rho_w (\overline{(u'^2)} + \overline{(v'^2)} + \overline{(w'^2)}) \quad \text{Eq. 2-17}$$

where: $C = 0.19$, and C is a fitting parameter valid for oceanic conditions and rough-bed open channel flow (Bagherimiyab & Lemmin, 2013; Biron et al., 2004; Pope et al., 2006; Soulsby, 1997; Stapleton & Huntley, 1995; Wren et al., 2017). τ_w is determined by multiplying the sum of the squares of the averaged velocity fluctuations by $C^{1/2} \rho_w$. The TKE method has been used to calculate τ_w in flume and field studies (e.g., riverine and estuarine) under simple and complex flow conditions (Biron et al., 2004; Kim et al., 2000; Nikora & Goring, 2000; Pope et al., 2006; Stapleton & Huntley, 1995). τ_w varies with height above the bed, experiencing a maximum at $0.1 * h$ and decreasing until it reaches the boundary; therefore, all τ_w estimates obtained from this method were calculated at $z \sim 3$ cm for $h = 30.5$ cm (Bagherimiyab & Lemmin, 2013; Biron et al., 2004).

TKE estimates of τ_w are limited by Doppler backscatter and the ADV sampling volume. Backscatter can be a result of increased Doppler noise from positive and negative buoyancy of

particles in the sampling volume, small-scale turbulence, acoustic beam divergence, and boundary interference (Kim et al., 2000; Pope et al., 2006).

2.3.5.3 Law of Wall – Logarithmic Profile (LP)

The Law of the Wall assumes a logarithmic velocity profile for steady, uniform flow in subcritical conditions and is commonly used in riverine and marine environments for fixed and weakly mobile sand and gravel beds (Le Roux, 2005; Pope et al., 2006; Soulsby, 1997; Wilcock, 1996). Following the assumption of a no slip condition for fully turbulent flow regimes, the natural log of the sampling depth is plotted against the velocity profile (Eq. 2-18) (Soulsby, 1997).

$$u(z) = \frac{u_w^*}{\kappa} \ln\left(\frac{z}{z_0}\right) \quad \text{Eq. 2-18}$$

where: von Karman's constant, $\kappa = 0.4$, z = elevation above the bed (m), and z_0 = characteristic roughness length (m). z_0 and u_w^* were derived from the velocity profile using linear regression (Nikora & Goring, 2000; Soulsby, 1997; Whiting & Dietrich, 1990) and τ_w was calculated by substituting u_w^* into Eq. 2-2.

2.3.5.4 Law of Wall – Single Point

The single point velocity method, the vertically-averaged form of Law of the Wall, assumes a logarithmic velocity profile and requires information describing the sediment size (e.g., d_{84}) (Eq. 2-19) (Whiting & Dietrich, 1990).

$$\tau_w = \frac{\rho(\bar{u}_z \kappa)^2}{\ln\left(\frac{10z}{d_{84}}\right)^2} \quad \text{Eq. 2-19}$$

where: \bar{u}_z = average velocity (m/s) at z and $\kappa = 0.4$. This method has been applied and proved successful in sand-bedded river bends (Dietrich & Smith, 1983) and gravel-bed channels (Whiting & Dietrich, 1990). d_{84} is representative of boundary features that dominate flow resistance because it accounts for the protrusion of larger grains into the flow field (Whiting & Dietrich,

1990). Depending on *in-situ* conditions, the single point average velocity must be based on a minimum sampling duration of 50-100 seconds, at measurements below a height of 2/10^{ths} the flow depth and 2 cm above an immobile bed of coarse sand or fine gravel substrate. If the bed is mobile, then sampling location should be just above the top of the bedload layer, or at the height of the largest grains rolling on the bed (Whiting & Dietrich, 1990; Wilcock, 1996).

2. 3.5.5 Indicator Function

A major limitation to the Law of the Wall – LP method is that z_o is derived from experimental data and precise measurement of z is necessary. An alternative graphical method that does not require estimation of z_o is known as the indicator function (Eq. 2-20).

$$u_w^* = \frac{du}{dz} z \kappa \quad \text{Eq. 2-20}$$

where: $\kappa = 0.4$. This method uses the derivative of the velocity profile with respect to z to calculate u_w^* . τ_w was calculated using \bar{u}_* , an average of the upper portion of the u_w^* profile after its peak and Eq. 2-2 (Örlü et al., 2010; Wengrove & Foster, 2014).

2. 3.5.6 Quadratic Friction Law

The Quadratic Friction Law applies to current driven environments with a steady, uniform, fully turbulent flow regime by quantifying the momentum dissipation due to bottom roughness (Eq. 2-21) (Pope et al., 2006; Soulsby, 1997; Wengrove et al., 2015).

$$\tau_w = \rho_w C_D \bar{U}^2 \quad \text{Eq. 2-21}$$

where: C_D = the drag coefficient (unitless) and \bar{U} = depth-averaged water velocity (m/s). Accurately estimating C_D is challenging due to spatial variability of natural flow regimes and the presence of bed forms (Biron et al., 2004). In many cases it is estimated using a constant value found in the literature. For this dissertation, empirical relationships derived from the velocity profile used a fitted power-law function to calculate C_D based upon z_o (Eq. 2-22) (Soulsby, 1997).

$$C_D = \alpha \left(\frac{z_o}{h} \right)^\beta \quad \text{Eq. 2-22}$$

where: z_o was derived from the Law of the Wall – LP method, and α and β are coefficients that change as a function of bottom substrate material, relative roughness, and bed mobility. Three methods can be used to fit the power-law function: Manning-Strickler, Dawson-Johns, and Soulsby. Soulsby's (1997) power-law coefficients apply to estimates of skin-friction for flat mobile and immobile beds of sand with steady flows in flumes. The Manning-Strickler (Strickler, 1923) applies to open channel and pipe flow, and Dawson-Johns (Dawson et al., 1983) pertains to shallow water flow over topography in coastal environments. The Dawson-Johns and Soulsby coefficients were derived based on experiments in oceanic environments, generally with a small relative roughness (i.e., $10^{-7} < \frac{z_o}{h} < 10^{-2}$), whereas Manning-Strickler applies to flow regimes with large relative roughness factors (i.e., $\frac{z_o}{h} > 10^{-4}$) characteristic of pipe and channel flow (Mehaute & Hanes, 2005). For all experimental conditions in this dissertation research, $\frac{z_o}{h} > 10^{-4}$ and experiments were conducted in an open channel, therefore, only the Manning-Strickler approach was used to calculate C_D , where $\alpha = 0.0474$ and $\beta = 1/3$.

2. 3.5.7 Chézy/Momentum

The Chézy/Momentum approach is the simplest method to calculate a global BSS, but it does not capture local, small-scale variation (Biron et al., 2004; Yen, 2002). The force balance approach uses the Chézy resistance coefficient (C) to calculate BSS for a section of river with similar hydrologic conditions (i.e., reach-averaged BSS) (Eq. 2-23).

$$C = \sqrt{8g * \left[1.2 + 2.03 \log \left(\frac{Rh}{d_{84}} \right) \right]^2} \quad \text{Eq. 2-23}$$

This method is generally applied to open channel flow (e.g., rivers, streams) under steady, uniform, and non-uniform hydraulic conditions. C was estimated using an empirical relationship, originally

developed to calculate the Darcy-Weisbach friction factor, f , by relating d_{84} and R_h (Elger et al., 2013; Leopold & Wolman, 1957; Limerinos, 1970). Eq. 2-23 was modified to directly calculate C , using $C = \sqrt{\frac{8g}{f}}$ (Chaudhry, 2008; Elger et al., 2013). For the purpose of this dissertation research, the slope of the energy grade line or friction slope, S_f , was used because it applies to uniform and non-uniform conditions (Eq. 2-24).

$$S_f = \frac{\left(\frac{U}{C}\right)^2}{R_h} \quad \text{Eq. 2-24}$$

U is the representative velocity component used in calculations, making it a global predictor of BSS (Babaeyan-Koopaei et al., 2002; Yen, 2002). τ_w was calculated by substituting Eq. 2-24 into Eq. 2-25.

$$\tau_w = \gamma_w R_h S_f \quad \text{Eq. 2-25}$$

where: γ_w = specific weight of water (N/m³).

2.3.5.8 Manning/Momentum

The Manning formula is commonly used to estimate stream flow, velocity, or friction slope in open channels (Yen, 2002). For this research, U was known and the Manning formula was used to calculate S_f for uniform, steady state conditions (Eq. 2-26) (Limerinos, 1970).

$$S_f = \left(\frac{U*n}{R_h^{2/3}}\right)^2 \quad \text{Eq. 2-26}$$

where: n = Manning's roughness parameter quantifies friction and form losses, and varies with water discharge and bed material size (U.S. Army Corp of Engineers, 1993). n has commonly been used to represent cross-sectional and reach resistance coefficients (Yen, 2002). Seven methods were used to estimate n based upon the PSD and of these, the median value was selected for use in BSS calculations (Appendix A.5: Estimating Manning's n). For the acrylic boundary,

$n=0.009$ was selected based on typical literature values for Lucite (Chaudhry, 2008). [N.B., Lucite is another term used to describe acrylic]. τ_w was then calculated using Eq. 2-25.

2.3.6 Sensitivity Analysis of BSS Methods

Based on results from the vertical hydraulic analysis, the methods that produced consistent estimates of BSS, regardless of flow condition or boundary type, were selected to undergo a sensitivity analysis. The purpose of the sensitivity analysis was to quantify the impact of input parameter variability on BSS estimates. Velocity and a roughness coefficient rely on *in-situ* conditions to estimate BSS. Therefore, the effects of experimental variability associated with those parameters on BSS estimates were evaluated.

The effect of velocity variability on BSS estimates was evaluated using the average velocity value and its associated standard deviation. For example, U was used to calculate BSS following the Chézy/Momentum method. Therefore, $U \pm \sigma$ represented the lower and upper velocity bounds in the sensitivity analysis. The variability associated with roughness parameters was determined by converting z_o , C_D , C , n , d_{50} , and d_{84} to like terms and using the minimum and maximum values as the lower and upper limits, respectively. Results from the sand substrate experiments were used for all velocity intervals as the reference conditions, varying only one input parameter at a time while holding all others constant.

2.4 Results and Discussion

Based on results from the longitudinal analysis and for $h = 30.5 \pm 1$ cm, all experiments used the Vectrino to collect velocimetry data 3.2 m from the entrance as velocity was increased in a stepwise manner from 0.06 m/s to 1.1 m/s in 0.07 m/s intervals (i.e., for VFD settings from 1 to 17 Hz in 1 Hz intervals). The location was selected so that turbulence induced by the hydraulic jump and backwash effects as the water recirculates to the lower tank were minimized. Water

temperature was kept constant ($25\pm 2^\circ\text{C}$) for all experiments, therefore, the physical properties used in these calculations assumed a water temperature of 25°C . This proved to be a valid assumption because regardless of the method, when BSS was analyzed using ρ_w or γ_w at 10°C rather than 25°C , BSS increased by 0.3%. A temperature of 10°C was used as the lower threshold because that is the minimum experimental temperature selected for the subsequent oil CSS experiments.

The results from the longitudinal, cross-sectional, horizontal, and vertical hydraulic analyses are presented in the following order: (1) correlation of VFD settings with *in-situ* velocity measurements, (2) characterization of the flow regime as a function of water velocity and substrate type, (3) identification of ADV limitations, (4) classification of boundary parameters and roughness coefficients, (5) BSS predictions using all valid methods, and (6) evaluation of BSS sensitivity on input parameter variability.

2.4.1 Hydraulic Analysis: Acrylic Boundary

2.4.1.1 VFD Correlation

Using data collected in the longitudinal hydraulic analysis, the VFD settings (x) were correlated with U (m/s) by averaging the upper 3 mm of the 0 to 9 cm profile for each substrate type (Figure 2-7).

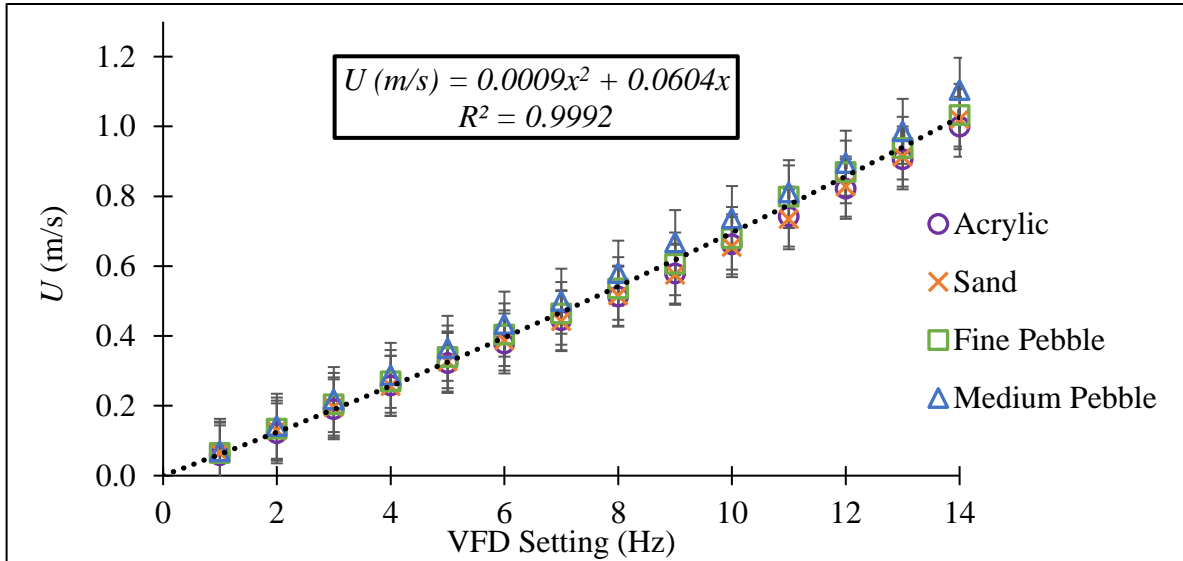


Figure 2-7: Compilation of velocity measurements for acrylic, sand, fine pebble, and medium pebble; a line of best fit relates VFD Setting (Hz) with U (m/s) for $h = 30.5 \pm 1$ cm.

U was calculated within the upper region of the measured profile because velocity was constant with respect to z . This fitted relationship only applied to VFD settings between 0 and 14 Hz and when $h = 30.5 \pm 1$ cm. The fitted line fell within $U \pm \sigma$ of the measured values regardless of substrate type. The relatively small variability in U was attributed to changes in water depth, sampling distance from the bed, sediment type, and measurement error due to bubble formation on the front prong of the Vectrino at high water velocities (i.e., for fine pebble and medium pebble at VFD settings ≥ 13 Hz).

The findings from this section quantified the relationship between the VFD settings and *in-situ* velocity for $h = 30.5 \pm 1$ cm. The correlation between VFD setting and velocity provided an estimate for U used in these calculations and subsequent chapters.

2.4.1.2 Characterizing the Flow Regime: Acrylic Boundary

The second objective of this research was to determine which VFD settings caused the test section's flow regime to be unsteady, non-uniform, turbulent, or supercritical for $R_h = 10.2$ cm

(Table 2-3). Further information about Fr , E , water level, and head loss due to the hydraulic jump as a function of velocity is given in Appendix A.1: Hydraulic Analysis. Uniform and steady state conditions were confirmed for VFD settings between 1 and 14 Hz, and non-uniform, unsteady flow occurred at VFD settings 15 to 17 Hz. Uniform (Figure 2-8a), non-uniform (Figure 2-8b), steady (Figure 2-9a) and unsteady (Figure 2-9b) conditions were compared for VFD settings of 4 Hz and 16 Hz. Calculation of Re indicated that flow was turbulent for all VFD settings. Flow within the test section was subcritical ($Fr < 1$) for VFD settings 1 to 7 Hz, transitioned to critical ($Fr = 1$) at 8 and 9 Hz, and was supercritical ($Fr > 1$) at VFD settings 10 to 17 Hz. [N.B., Small, non-breaking standing waves began forming just after the flume entrance at 5 Hz].

These results were used to determine which velocities and corresponding VFD settings violated method assumptions necessary to BSS approximations. VFD settings of 1 to 14 Hz correspond to U of 0.06 ± 0.01 m/s to 1.04 ± 0.05 m/s, and an increase in the VFD setting by 1 Hz results in an increase of U by 0.08 ± 0.02 m/s.

Table 2-3: *In-situ* hydraulic conditions for each VFD setting.

VFD Setting (Hz)	$U \pm \sigma$ (m/s)	Re (Laminar < 750) (Turbulent > 750)	Fr (Subcritical <1) (Critical =1) (Supercritical >1)	Uniform or Non-uniform	Steady or Unsteady
1	0.06 ± 0.01	5,022 (Turbulent)	0.10 (subcritical)	Uniform	Steady State
2	0.13 ± 0.01	10,215 (Turbulent)	0.23 (subcritical)	Uniform	Steady State
3	0.20 ± 0.01	15,699 (Turbulent)	0.35 (subcritical)	Uniform	Steady State
4	0.27 ± 0.01	20,827 (Turbulent)	0.47 (subcritical)	Uniform	Steady State
5	0.34 ± 0.02	26,319 (Turbulent)	0.59 (subcritical)	Uniform	Steady State
6	0.40 ± 0.02	31,156 (Turbulent)	0.70 (subcritical)	Uniform	Steady State
7	0.46 ± 0.03	35,999 (Turbulent)	0.80 (subcritical)	Uniform	Steady State
8	0.54 ± 0.03	41,661 (Turbulent)	0.94 (critical)*	Uniform	Steady State
9	0.61 ± 0.04	47,185 (Turbulent)	1.06 (critical)*	Uniform	Steady State
10	0.68 ± 0.04	53,110 (Turbulent)	1.18 (supercritical)	Uniform	Steady State
11	0.77 ± 0.04	59,962 (Turbulent)	1.33 (supercritical)	Uniform	Steady State
12	0.85 ± 0.04	66,341 (Turbulent)	1.47 (supercritical)	Uniform	Steady State
13	0.94 ± 0.04	72,751 (Turbulent)	1.63 (supercritical)	Uniform	Steady State
14	1.04 ± 0.05	80,767 (Turbulent)	1.80 (supercritical)	Uniform	Steady State
15	1.12 ± 0.06	86,985 (Turbulent)	1.94 (supercritical)	Non-uniform	Unsteady
16	1.15 ± 0.06	89,330 (Turbulent)	2.06 (supercritical)	Non-uniform	Unsteady
17	1.12 ± 0.06	86,793 (Turbulent)	2.05 (supercritical)	Non-uniform	Unsteady

*Due to the σ associated with U , the critical velocity overlaps at VFD settings of 8 and 9 Hz.

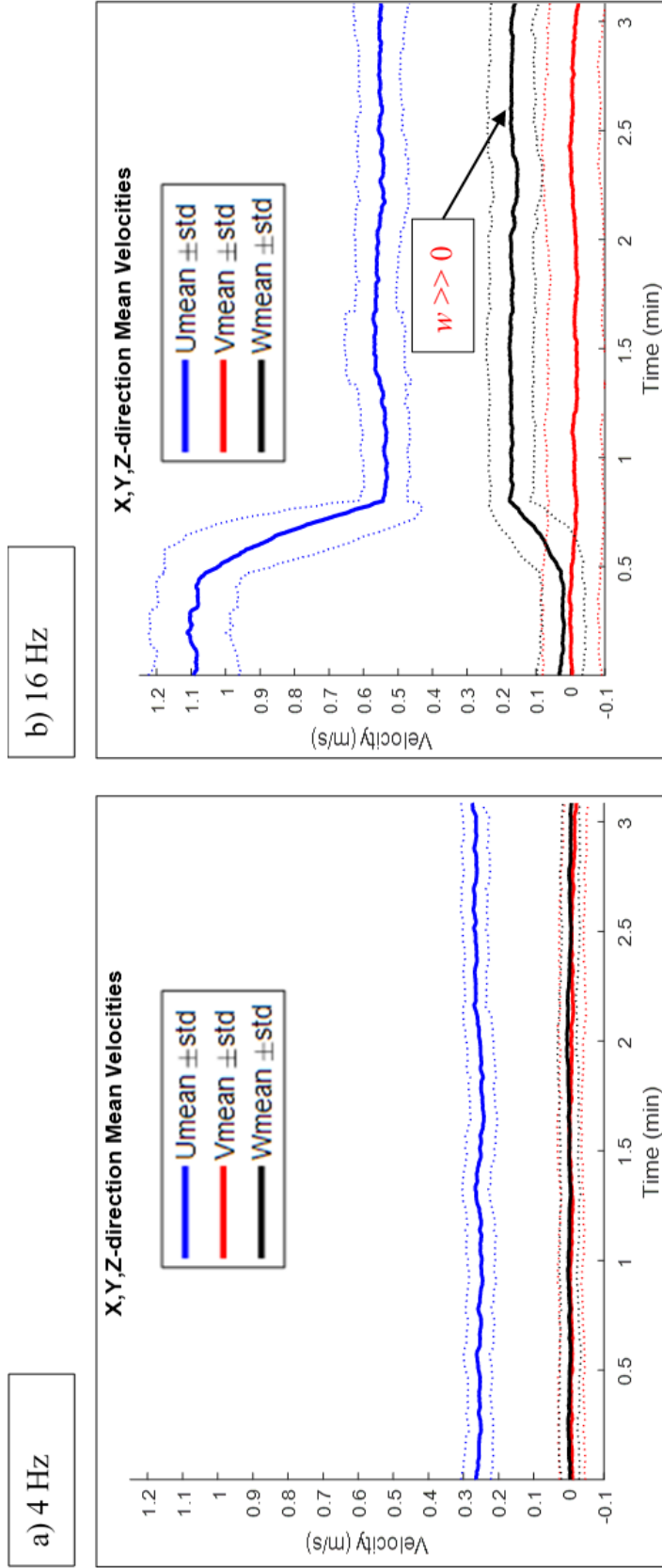


Figure 2-8: (a) Uniform conditions at VFD setting of 4 Hz. (b) Non-uniform conditions at VFD setting of 16 Hz.

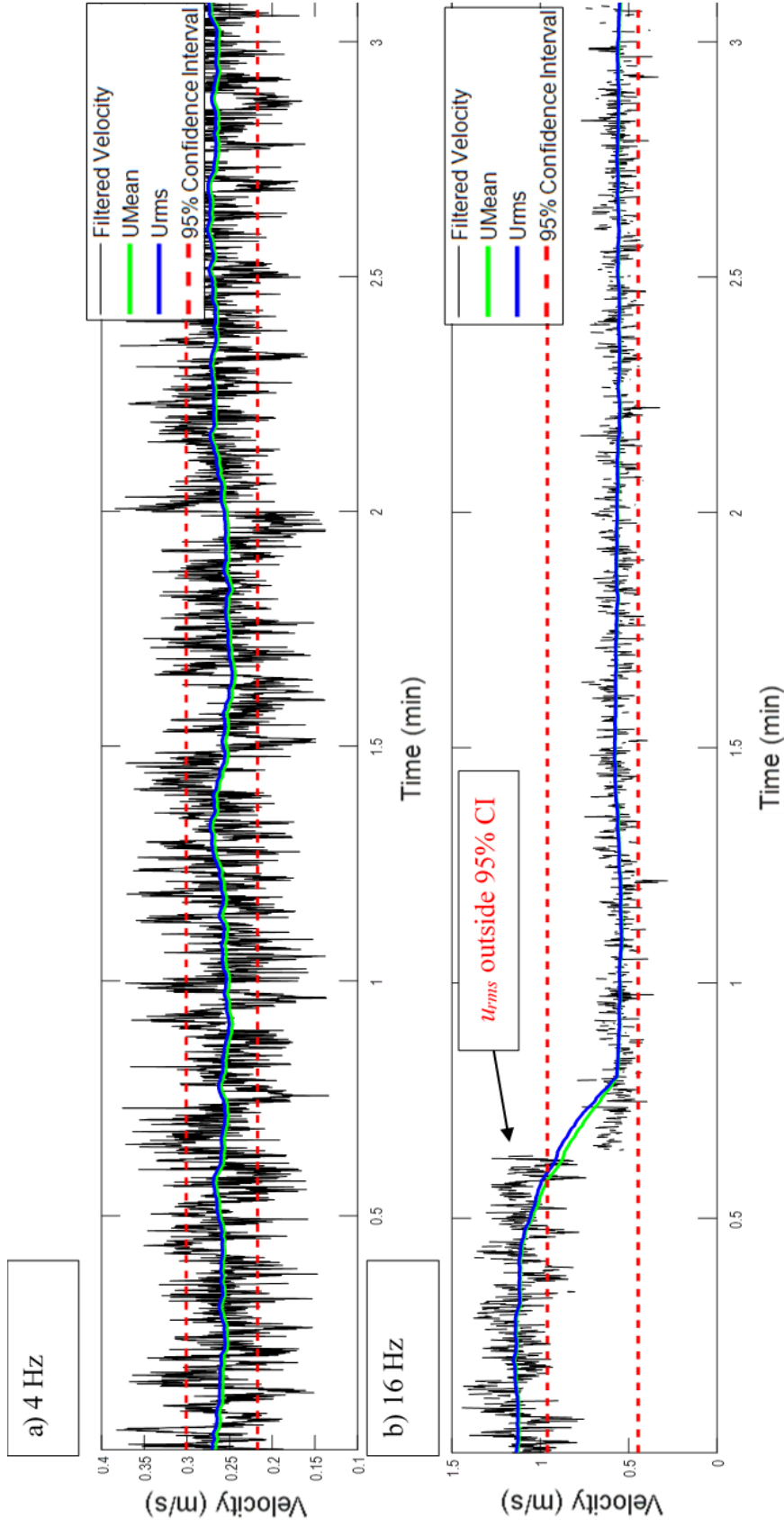


Figure 2-9: (a) Steady state conditions for VFD setting of 4 Hz. (b) Unsteady flow regime at VFD setting of 16 Hz.

2.4.1.3 Vectrino Limitations

Instantaneous velocity measurements were deemed reliable at VFD settings based upon the percent of data points removed and data quality metrics: 1 to 14 Hz for an acrylic and sand boundary, 1 to 13 Hz for the medium pebble substrate, and 1 to 12 Hz over fine pebble substrate. The percent removal of data points was calculated by relating the total number of raw data points and the number of data points eliminated during post-processing (Appendix A.6: Percent Removal of Velocity Data). Experimental trials with high removal rates (>18%) were repeated using different Vectrino settings to confirm that results were due to instrument error rather than user error. A threshold of 18% was selected based on experimental results because trials exceeding that removal rate tended to have gaps in the velocity time-series as a result of low SNR or low %Corr which led to erroneous velocity measurements. High removal rates were attributed to weak spots within the sampling volume as a result of irregular boundary conditions, the instrument shaking due to turbulence and motor vibrations, and bubble formation on the front prong for $z > 3$ cm.

Although the instantaneous velocity measurements for fine pebble and medium pebble substrates exhibited higher percent removal values at 13 Hz and 14 Hz, especially for profiles measured at $z > 3$ cm, subsequent CSS experiments were conducted for VFD settings up to 14 Hz to analyze oil movement for $U > 1$ m/s. **Based on these findings, the Vectrino recorded near-bed profiles ($z = 0$ to 3 cm), minimizing bubble formation at higher velocities, in subsequent studies of how oil movement was impacted as flow transitioned from sub- to super-critical conditions and for $U > 1$ m/s.**

2.4.2 Boundary Characteristics: All Substrate Materials

The velocity profile was analyzed and compiled for acrylic (Figure 2-10a), sand (Figure 2-10b), fine pebble (Figure 2-10c), and medium pebble (Figure 2-10d) substrates as a function of

water velocity. Three independent sampling locations (e.g., 0 to 3 cm, 3 to 6 cm, 6 to 9 cm) were compiled into a single velocity profile of $\bar{u}(z)$ for U of 0.06 to 1.04 m/s in 0.07 m/s intervals. Because the height of the Vectrino needed to be changed to measure these sections and due to an irregular boundary, the compilation of the three profiles resulted in slight discontinuity in the 0 to 9 cm velocity profile. [N.B., Boundary parameters are presented in terms of “mm”]. The red dotted lines for sand, fine pebble, and medium pebble represent the sediment d_{84} . Whereas, for the acrylic velocity profile the red dotted line is the boundary’s equivalent k_s . This was classified as “smooth” using the Moody Diagram’s Equivalent Sand Grain Roughness for plastic or glass pipe materials (Elger et al., 2013).

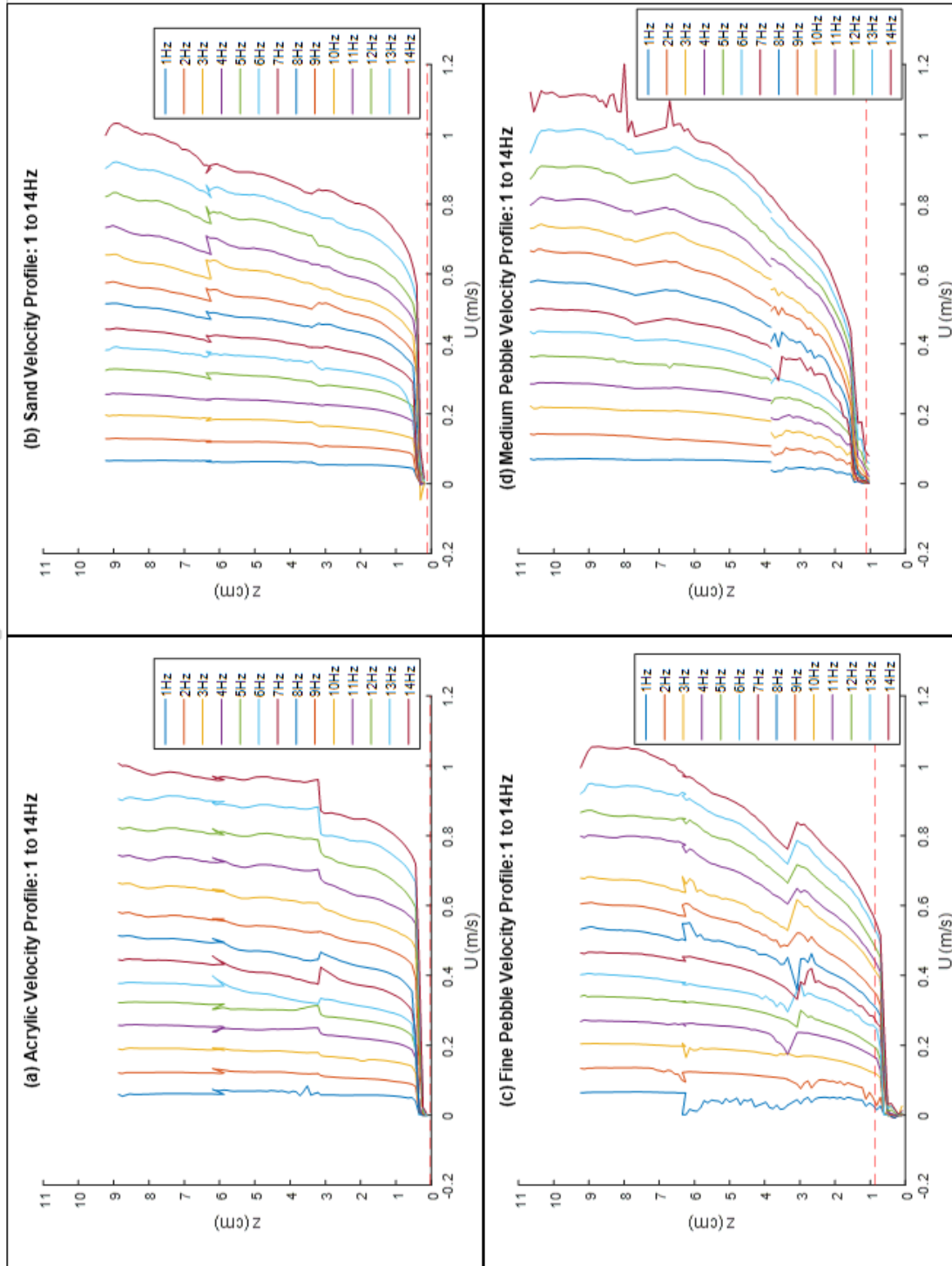


Figure 2-10: Three sampling ranges were compiled into one velocity profile based on the stream wise velocity (m/s) and the distance from the bottom (m) for (a) acrylic, (b) sand, (c) fine pebble, and (d) medium pebble.

The boundary parameters were calculated based on the velocity profiles and were used in BSS calculations. A small gap in the medium pebble profile ($z = 3.6$ to 3.7 cm) occurred because data points were not plotted due to a sampling weak spot causing erratic velocity measurements. Common boundary descriptors (e.g., k_s), relative roughness, and the theoretical logarithmic profile region for sand, fine pebble and medium pebble substrates (Soulsby, 1997; Whiting & Dietrich, 1990) were derived based on the PSD (Table 2-4).

The presence of a viscous sublayer was analyzed using Re^* , by rearranging Eq. 2-2 and using BSS calculated from the TKE method to solve for u_w^* . The TKE method was chosen as the reference because it: (1) is independent of elevation measurements, (2) is specific to local BSS estimates, and (3) aligns with literature values (Bagherimiyab & Lemmin, 2013; Pope et al., 2006; Thompson et al., 2006). A hydraulically-smooth boundary layer ($Re^* < 5$) was identified between 0.06 m/s to 1.04 m/s over the acrylic. A transitional boundary layer ($5 < Re^* < 70$) occurred over the velocity range of 0.06 m/s to 1.04 m/s over the sand. Hydraulically-rough flows ($Re^* > 70$) were observed over fine pebble and medium pebble beds between 0.06 m/s to 1.04 m/s.

The Law of the Wall – LP method assumes measurements are taken within the logarithmic region of the velocity profile, z_{LP} , which changes as a function of sediment size and water depth. The acrylic and sand estimates of z_o were analyzed within 0 to 3 cm from the bottom and had RSD values of 13% and 22% , respectively. The fine pebble and medium pebble estimates were derived from the 3 to 6 cm profiles and had higher levels of variability associated with z_o . Based on the RSD for fine pebble (52%) and medium pebble (50%), z_o variability suggested that this method was not as reliable for irregular boundaries because of its reliance on precise measurements of elevations above the bed and the associated velocity (Pope et al., 2006). Some variability is expected with z_o because boundary roughness varies spatially and z_o is not constant with velocity.

As shown by the data for acrylic, sand, and fine pebble, z_o increases with velocity until an inflection point, then decreases as velocity increases. This inflection suggests the velocity threshold where the effect of boundary roughness becomes less prominent due to an increasingly turbulent boundary. For acrylic and sand, z_o increased until it reached a peak at $U = 0.46$ m/s, and then consistently decreased until $U = 1.04$ m/s. Fine pebble z_o values followed a similar trend in that values increased until $U = 0.68$ m/s and then decreased until $U = 1.04$ m/s. Alternatively, medium pebble z_o values consistently increased until it reached a peak and plateaued for $U > 0.88$ m/s. This suggests that the velocities analyzed in this research were not fast enough for turbulence to minimize the effect of grain-induced drag for this sediment size. For each substrate type, the average z_o (\bar{z}_o) and the standard deviation (σ_{z_o}) were determined over the three-minute sampling duration (Table 2-4).

Table 2-4: Summary of derived and measured boundary parameters and characteristics used to calculate BSS.

Parameter (units)	Equation/Method	Acrylic	Sand	Fine Pebble	Medium Pebble
d_{50} (mm)	PSD	n/a	0.42	6.5	10.6
d_{84} (mm)	PSD	n/a	1.2	8.5	11.1
Relative Roughness	$\left(\frac{d_{84}}{h}\right)$ for $h = 305$ mm	$<5 \times 10^{-6}$	0.004	0.03	0.04
k_s (mm)	$k_s = 2.5d_{50}^c$	Smooth i.e., <0.0015	1.1	16.3	26.5
z_{LP} (mm)	$3 * d_{84} < z_{LP} < 0.2h$ Sample Range (mm)	0 to 61 0 to 30	3.6 to 61 0 to 30	25.5 to 61 30 to 60	33.3 to 61 30 to 60
$\bar{z}_o \pm \sigma_{z_o}$ (mm)	Law of Wall - LP (literature value)	0.8±0.1	0.9±0.2 (0.4) ^c	2.1±1.1	2.4±1.2 (3.0) ^c
Relative Roughness	$\left(\frac{z_o}{h}\right)$ for $h = 305$ mm	0.003	0.003	0.007	0.008
C_D (unitless) ^a	Quadratic Friction Law	0.0065±0.0004	0.0068±0.0005	0.0086±0.0002	0.0091±0.0002
C (m ^{1/2} /s) ^b	Chézy/Momentum	60.8	45.3	30.0	27.9
Manning, n (s/m ^{1/3}) ^b	Manning/Momentum (literature value)	0.009	0.015 (0.020) ^d	0.021 (0.024) ^d	0.022 (0.028) ^d

^a \bar{C}_D values were averaged over the entire velocity range with the associated sample standard deviation.

^b C and n did not change with respect to velocity because they were based on sediment size and hydraulic radius.

^c Soulsby, 1997

^d For a straight, uniform channel Aldridge & Garrett (1973) found: n for sand ($d_{50} = 0.4$ mm), n for fine gravel, and n over coarse gravel.

\bar{z}_o values determined in this research were on the same order of magnitude as those found in literature (Soulsby, 1997); the experimentally-derived values of \bar{z}_o over sand were larger by a factor of two, while those for medium pebble fell slightly below the literature value. The larger sand estimate may be attributed to z_o being derived from the 0 to 3 cm profile as opposed to using velocity profiles further from the bed or for over wider profile range. In general, z_o is often derived from profiles measured within 2 m from the bed, supporting the fact that a lower z_o value from literature is expected (Thompson et al., 2003). Additionally, when evaluated over a wider profile range (0 to 9 cm), z_o over the sand substrate decreased from 0.9 mm to 0.3 mm. As a result of the rapid rate of change in velocity near the bed, the fitted equation from the velocity profile tended to have a steeper slope and a larger y-intercept (z_o).

C_D was calculated from z_o . Hence, the region in which these values were obtained varies depending on z_{LP} , and changes with respect to velocity. Unlike C_D , an advantage to using the Manning formula and n is that when flow is fully turbulent over a rough rigid surface, n remains nearly constant and independent of flow depth, Reynolds number, or relative roughness (Yen, 2002).

2.4.3 Comparison of Roughness Parameters

To compare the different roughness parameters, C and n were expressed in terms of C_D using, $C_D = \frac{g}{C^2} = \frac{gn^2}{h^{1/3}}$ (Soulsby, 1997), and C_D based on sediment size by substituting $z_o = \frac{d_{50}}{12}$ and $z_o = 0.1 * d_{84}$ into Eq. 2-22 (Table 2-5).

Table 2-5: Comparison of C_D values calculated from various methods derived within z_{LP} .

Method & Parameter	Acrylic	Sand	Fine Pebble	Medium Pebble
C_D based on \bar{z}_o	0.0065	0.0068	0.0086	0.0091
C_D based on d_{50}	n/a	0.0031	0.0040	0.0042
C_D based on d_{84}	n/a	0.0035	0.0067	0.0073
C_D based on C	0.0026	0.0048	0.0109	0.0126
C_D based on n	0.0012	0.0031	0.0061	0.0069

For every sediment substrate, C_D based on d_{50} provided the lowest estimate, followed by C_D adjusted from n , and C_D calculated from d_{84} . For acrylic and sand, the next largest C_D was based on C and the largest derived from \bar{z}_o . Alternatively, for fine pebble and medium pebble, the second largest C_D was calculated from \bar{z}_o and the largest value estimated by C .

Four of the seven methods to calculate n rely on d_{50} as the representative grain size, one uses d_{84} , and two use d_{90} . n is then selected based on the median of those seven methods, therefore, as shown by these results, estimates should fall between those made using d_{50} and d_{84} . For sand and acrylic, C_D based on n and C are slightly lower than when derived from \bar{z}_o because \bar{z}_o estimates were taken close to the boundary (i.e., $z = 0$ to 3 cm). Fine pebble and medium pebble \bar{z}_o values were derived at a higher elevation from the bed (i.e., $z = 3$ to 6 cm), where the effect of a rapidly increasing velocity profile was minimized resulting in a smaller \bar{z}_o . Additionally, the increase in C_D based on C from sand to fine pebble occurred because d_{84} is the only variable in the equation, and d_{84} for fine pebble is ~ 7 x larger than for sand (e.g., 8.5 mm/1.2 mm = 7.08).

$C_D = 0.004$ at $z = 15$ cm is a commonly cited C_D value (i.e., Sternberg's smooth bed constant, $C_D = 0.003$ adjusted from $z = 10$ cm) (Sternberg, 1973), however, values may vary depending upon velocity and depth of measurement and therefore a range is expected (Thompson

et al., 2004). For example, Soulsby (1997) showed a spread in C_D of 0.004 to 0.01 for $\frac{z_0}{h} = 10^{-3}$, and Thompson et al. (2003) found that C_D varied between 0.0005 to 0.006 at $z = 15$ cm for a smooth boundary. In the CRRC flume experiments, the adjusted C_D values were less than 0.01, with the exception of fine pebble and medium pebble C_D based on C . To relate findings from this research to literature values, C_D was adjusting to $z = 15$ cm following Eq.18 and $C_{D_z} = \left(\frac{u_w^*}{u(z)}\right)^2$, where u_w^* was calculated from the Quadratic Friction Law.

After adjusting C_D to $z = 15$ cm, the average C_D over acrylic decreased from 0.007 to 0.006. Adjusted C_D values were then evaluated with respect to velocity, and the results showed that as U increased from 0.06 m/s to 1.04 m/s, C_D decreased from 0.006 to 0.005, respectively. Using the Quadratic Friction Law over an acrylic boundary, Thompson et al. (2004) found a decrease and plateauing of $C_D = 0.005$ as velocity increased, a similar value to those found in this research. A range of C_D values is expected and can be attributed to the different methods of approach, the elevation above the boundary where drag is calculated, the relative roughness, and the representative sediment grain size used in calculations.

Excluding the acrylic boundary, the median roughness parameter for all other substrate types was estimated using $z_0 = 0.1 * d_{84}$ and Eq. 2-22. In the field, where no direct boundary information or measurements can be collected, this method of obtaining C_D is recommended for open channel flow under similar hydraulic conditions. [N.B., The effect of roughness parameter on BSS estimates will be analyzed further in 2.4.6 Sensitivity Analysis of BSS Methods].

This research corroborated the literature that C_D varies at different depths, velocities, relative roughness, and bottom roughness. Hence, C_D must be derived from the measured velocity profiles ($z = 0$ to 3 cm) for each experimental condition in the CRRC flume to represent *in-situ* near-bed conditions. The range of C_D values was applied as the lower and

upper bounds for the roughness parameters when conducting the sensitivity analysis on the Quadratic Friction Law, the Chézy/Momentum, and the Manning/Momentum methods.

2.4.4 Evaluating BSS: All Substrate Materials

2.4.4.1 Method Applicability

BSS was calculated based on eight methods: (1) Newton's Law of Viscosity, (2) TKE, (3) Law of the Wall – LP, (4) Law of the Wall – Single Point, (5) Indicator Function, (6) Quadratic Friction Law, (7) Chézy/Momentum, and (8) Manning/Momentum. These methods were chosen based on their commonality among field and laboratory experiments, applicability to fluvial and marine current-driven environments, the diversity of velocity measurements, and variability in calculating roughness coefficients. All methods used to calculate BSS require a velocity measurement, but the type and location of the measurement depends upon the method's assumptions. Five of the eight methods assume a uniform, steady flow regime making all methods valid in the MacFarlane Flume for U between 0.06 and 1.04 m/s (i.e., VFD settings of 1 and 14 Hz). A summary of the velocities for which each BSS method is valid for use in the MacFarlane Flume is shown in Table 2-6.

Table 2-6: Velocities for which BSS methods are valid in the MacFarlane Flume.

Method Name	Acrylic (m/s)	Sand (m/s)	Fine Pebble (m/s)	Medium Pebble (m/s)
Newton’s Law of Viscosity	0 to 0.77	0 to 0.61	0 to 0.27	N/A
TKE	0 to 1.04	0 to 1.04	0 to 1.04	0 to 1.04
Law of Wall – LP	0 to 0.61	0 to 0.61	0 to 0.61	0 to 0.61
Law of Wall – Single Point	0 to 1.04	0 to 1.04	0 to 1.04	0 to 1.04
Indicator Function	0 to 1.04	0 to 1.04	0 to 1.04	0 to 1.04
Quadratic Friction Law	0 to 1.04	0 to 1.04	0 to 1.04	0 to 1.04
Chézy/Momentum	0 to 1.04	0 to 1.04	0 to 1.04	0 to 1.04
Manning/Momentum	0 to 1.04	0 to 1.04	0 to 1.04	0 to 1.04

The TKE, Indicator Function, Quadratic Friction Law, Chézy/Momentum, and Manning/Momentum were applicable for all hydraulic and boundary conditions exhibited during these experimental trials. The Law of the Wall – LP method was limited to subcritical hydraulic conditions (Wilcock, 1996) and, therefore, becomes invalid for $U > 0.61$ m/s in this flume for $h = 30.5$ cm. In addition, velocity measurements for the LP and Single Point methods require that the velocity used in BSS calculations is within z_{LP} . For this to hold true, fine pebble and medium pebble velocity measurements were obtained using sampling profiles within the range of 3 to 6 cm. [N.B., z_{LP} for the other substrates was 0 to 3 cm].

Validity of the Newton’s Law of Viscosity depends on the presence of a viscous sublayer. A smooth hydraulic boundary layer is a strong indication that a viscous sublayer is present. The presence of a sublayer was confirmed using eddy diffusivity, $E(z)$, (Eq. 2-27) and plotting it against the dimensionless height, Z^+ , (Eq. 2-28) (Boudreau & Jorgensen, 2001). A viscous sublayer was identified for: acrylic ($U < 0.77$ m/s), sand ($U < 0.61$ m/s), fine pebble ($U < 0.27$ m/s), and medium pebble (N/A for U) (Appendix A.7: Eddy Diffusivity ($E(z)$) vs. Dimensionless Height (Z^+)).

$$E(z) = \kappa u_w^* z \quad \text{Eq. 2-27}$$

$$Z^+ = \frac{z u_w^*}{\nu_w} \quad \text{Eq. 2-28}$$

Some methods are applicable for each boundary material, but are invalid at high velocities (e.g., Law of the Wall – LP). Alternatively, a method may not be valid over a rough boundary and may be restricted by sediment size (e.g., Newton’s Law of Viscosity). These exceptions are noted in the subsequent discussions.

2.4.4.2 BSS Estimates Evaluated by Substrate

A compilation of BSS estimates over acrylic (Figure 2-11a), sand (Figure 2-11b), fine pebble (Figure 2-11c), and medium pebble (Figure 2-11d) substrates are illustrated as a function of water velocity. The location of the velocity measurement used to calculate BSS changes are documented in Appendix A.8: Velocity Measurement Location. Figures for each method as a function of substrate type can be found in Appendix A.9: BSS Method for All Substrate Types.

Acrylic

Over the acrylic boundary, Newton’s Law of Viscosity is valid for $U < 0.77$ m/s and Law of the Wall – LP is valid for $U < 0.68$ m/s. Newton’s Law of Viscosity produces the largest BSS estimate for values where $U \leq 0.20$ m/s. For $0.27 \text{ m/s} \leq U \leq 0.61$ m/s, the Law of the Wall – LP BSS estimates were larger than all other methods. For $U > 0.61$ m/s, the Quadratic Friction Law produced the largest BSS estimates. The minimum estimate alternated between the Indicator Function and the Manning/Momentum methods for $U \leq 1.04$ m/s. The TKE and Quadratic Friction Law were similar and followed closely along the arithmetic mean until $U = 0.54$ m/s, after this threshold the average increased at a faster rate than TKE and at a slower rate than the Quadratic Friction Law. The arithmetic average of all BSS estimates ($\overline{\tau_w}$) at $U = 1.04$ m/s, excluding the invalid methods, was 2.31 ± 1.34 Pa.

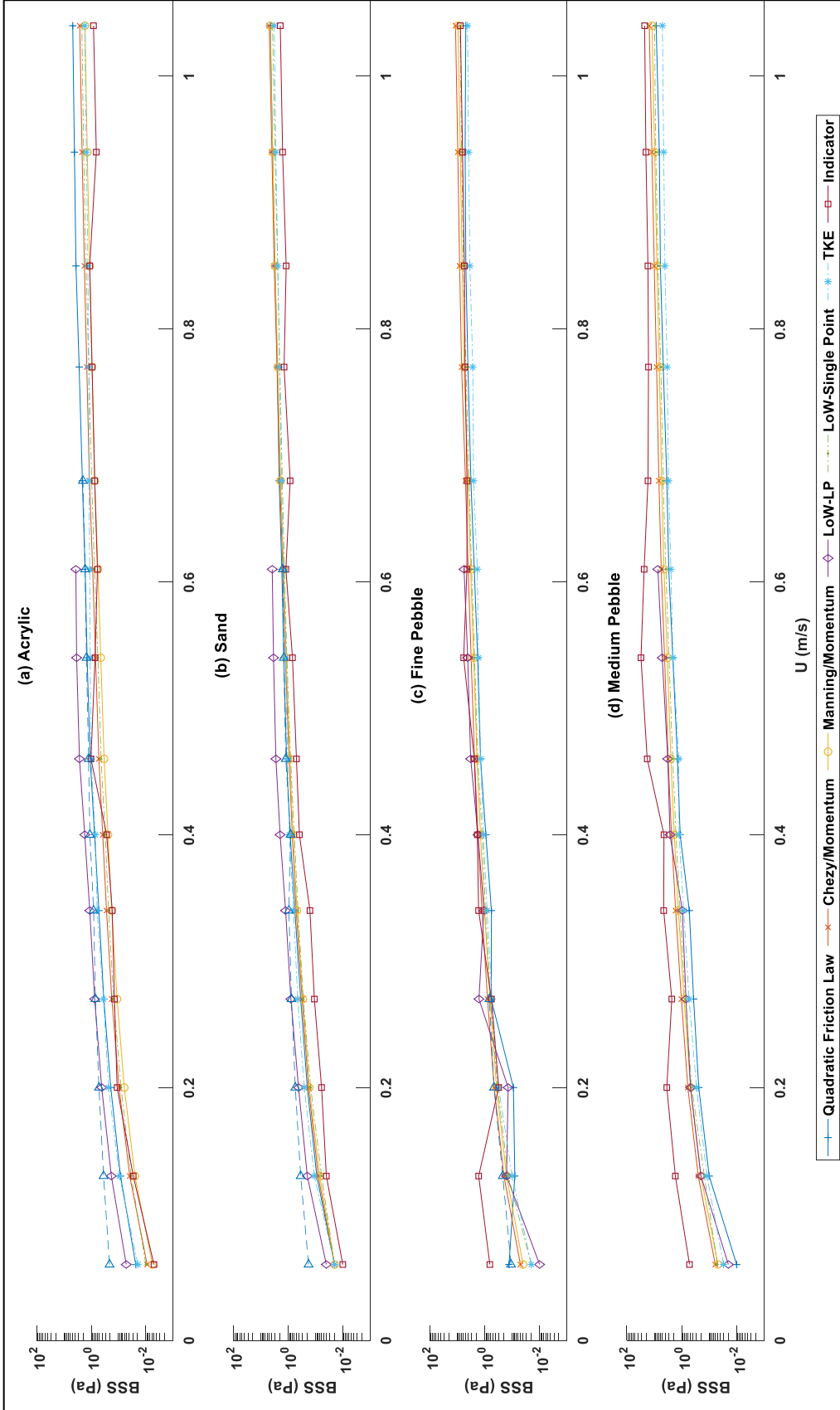


Figure 2-11: Eight BSS estimates calculated for (a) acrylic, (b) sand, (c) fine pebble, and (d) medium pebble.

Sand

For the sand substrate, the Law of the Wall – LP and Newton’s Law of Viscosity are valid for $U < 0.68$ m/s. Similar to the acrylic boundary, BSS estimates over the sand substrate were the largest for Newton’s Law of Viscosity method until $U > 0.20$ m/s. From $0.27 \text{ m/s} \leq U \leq 0.61 \text{ m/s}$, the maximum BSS estimate was calculated using the Law of the Wall – LP method. For $0.77 \text{ m/s} \leq U \leq 1.04 \text{ m/s}$, the highest value was calculated using the Chézy/Momentum formula, with the Quadratic Friction Law and Manning/Momentum producing similar estimates to the Chézy/Momentum. The Indicator Function method produced the lowest BSS estimates for all velocities. At $U = 1.04$ m/s, the Indicator Function produced a BSS estimate of 0.83 Pa, while the Chézy/Momentum estimate was 4.97 Pa. Omitting the invalid methods, $\bar{\tau}_w \pm \sigma$ at $U = 1.04$ m/s was 3.86 ± 1.13 Pa. Assuming $\rho_s = 2650 \text{ kg/m}^3$ for sand and from Eq. 2-3, $\tau^* = 0.57 \pm 0.17$. With the exception of the Law of the Wall – LP, the Indicator Function, and Newton’s Law of Viscosity, all other BSS estimates fell within the $\bar{\tau}_w \pm \sigma$.

Fine Pebble

Over the fine pebble boundary, Newton’s Law of Viscosity and the Law of the Wall – LP were invalid for $U < 0.34$ m/s and $U < 0.68$ m/s, respectively. Contrary to the acrylic and sand BSS estimates, for fine pebble, the Indicator Function estimates were highest for five of the 14 experimental trials (e.g., 0.06 m/s, 0.13 m/s, 0.34 m/s, 0.40 m/s, 0.54 m/s) and showed high variability at 0.06 and 0.13 m/s, peaked at 0.54 m/s, and then tracked closely with the arithmetic mean for $U > 0.61$ m/s. The Law of the Wall – LP method followed a pattern similar to that of acrylic and sand, producing some of the largest BSS estimates for $U \leq 0.61$ m/s. The Chézy/Momentum estimates were largest for $U \geq 0.68$ m/s. At $U = 1.04$ m/s, $\bar{\tau}_w \pm \sigma$ was 7.62 ± 2.75

Pa for all valid methods. Assuming $\rho_s = 2650 \text{ kg/m}^3$ for fine pebble and from Eq. 2-3, $\tau^* = 0.07 \pm 0.03$.

Medium Pebble

Over the medium pebble substrate, Newton's Law of Viscosity was invalid at all velocities. The Law of the Wall – LP was invalid for $U < 0.68 \text{ m/s}$. BSS estimates made by the Indicator Function were largest for all water velocities, and when included in averages it increased the RSD from 35% to 95%. In the fine pebble and medium pebble experiments, the Indicator Function based BSS estimates peaked prior to the flow becoming critical and then decreased until values followed with the trend established prior to the critical transition. BSS estimates obtained using the Quadratic Friction Law were lowest $0.06 \text{ m/s} \leq U \leq 0.40 \text{ m/s}$. For $U > 0.40 \text{ m/s}$, the lowest BSS estimate was made using the TKE method. Similar to acrylic, sand, and fine pebble, BSS estimates using the Law of the Wall – LP were higher compared to other methods. BSS values based on the Manning/Momentum method were at either the median value or were close to the median for the entire velocity range. At $U = 1.04 \text{ m/s}$, $\bar{\tau}_w \pm \sigma$, for all valid methods was $12.21 \pm 6.08 \text{ Pa}$. When the Indicator Function was excluded, $\bar{\tau}_w \pm \sigma$ decreased to $10.16 \pm 3.84 \text{ Pa}$. Assuming $\rho_s = 2650 \text{ kg/m}^3$ for medium pebble and from Eq. 2-3, $\tau^* = 0.06 \pm 0.02$. Due to the 60% increase in RSD when including this method, the Indicator Function was excluded in any averages for the medium pebble substrate and should not be used for estimating BSS in this flume when flow transitions from sub- to super-critical.

In the event where direct boundary measurements cannot be made, the roughness parameters and the drag coefficient determined in this research can be applied to similar *in-situ* flow conditions in the field. Overall, for each substrate type, the BSS estimates increased in magnitude with respect to U , while the RSD decreased. A wider spread in BSS estimates was

associated with rougher substrates, at $U = 1.04$ m/s, σ increased from 1.34, 1.13, 2.75, and 3.84 for acrylic, sand, fine pebble, and medium pebble, respectively. Wren et al. (2011) noted a 2 to 3 Pa spread in BSS between three methods for a discharge of 50 L/s ($U \sim 0.68$ m/s) and 65 L/s ($U \sim 0.81$ m/s). Additionally, the high variability associated with BSS estimates for medium pebble was corroborated by Buffington & Montgomery (1997), concluding “there is no definitive τ_{c50}^* for rough, turbulent flow characteristics of gravel bedded rivers, but rather there is a range of values that differs between investigative methodologies”. This makes it challenging to determine an accurate CSS estimate, especially for rough boundaries, and underscores the importance of using multiple methods to calculate BSS in the laboratory, so the range of global and local BSS field estimates can be readily compared.

For example, if heavy oil spilled into a gravel-bedded river and sank to the bottom, then responders would want to know for what *in-situ* BSS the oil could mobilize. If CRRC conducted oil CSS experiments in the MacFarlane Flume and determined that the oil resuspended at $U=1.04$ m/s on the medium pebble substrate, then the corresponding $\overline{\tau_w} \pm \sigma$ would be 10.16 ± 3.84 Pa. Using a global method, the oil CSS would be upwards of ~ 13 Pa, whereas the local method may predict oil CSS to be ~ 7 Pa. Depending on the method used, oil spill modelers can use the lower and upper oil CSS values to compare with the predicted *in-situ* BSS in relative terms to predict oil mobility.

Additionally, there was no consistent relationship to relate local and global estimates because results varied with respect to method, velocity, and boundary roughness. It is important to note that the disparity between local and global estimates were more prominent for rougher boundaries (i.e., fine pebble, medium pebble) than for the smoother substrates (i.e., acrylic, sand). When comparing TKE with Chézy/Momentum estimates on acrylic, TKE BSS estimates were

larger than Chézy/Momentum for $U < 0.77$ m/s. On sand, TKE BSS estimates were larger than Chézy/Momentum when $U < 0.54$ m/s. Whereas, over the fine pebble substrate Chézy/Momentum BSS was larger for all velocities and increased between 47% and 173% from TKE BSS estimates. Over the medium pebble substrate, Chézy/Momentum BSS was larger for all velocities and increased between 91% to 202% from TKE BSS estimates.

2.4.4.5 BSS Estimates Evaluated by Method

Newton's Law of Viscosity

Newton's Law of Viscosity is valid over acrylic, sand, and fine pebble substrates up to U of 0.77 m/s, 0.61 m/s and 0.27 m/s, respectively. With respect to substrate type, this method was the only one that estimated BSS to be largest over the acrylic boundary for four of the 14 velocity increments, followed by sand, fine pebble and medium pebble. Larger BSS estimates are anticipated over a smooth boundary in the viscous sublayer because the rate of change in velocity profile in this small region is larger than in the absence of roughness elements. The medium pebble substrate did not have a viscous sublayer, but a linear trend in the near-bed velocity profile ($z < 7$ mm) was identified as a roughness layer. This method requires confirmation of the presence of a viscous sublayer using specialized equipment to measure near-bed velocity profiles. **In the event of an oil spill, it is unlikely responders will be able to confirm the presence of a viscous sublayer, therefore, this method is not recommended for use in the subsequent flume experiments.**

TKE

The TKE method requires an instrument capable of obtaining instantaneous 3D velocimetry data. This method can be leveraged to produce a BSS profile or a single point estimate. This method is valid for all velocities and substrate types. For $0.20 \text{ m/s} < U \leq 1.04 \text{ m/s}$,

BSS over the acrylic was consistently lower compared to the other boundary types. When evaluating the TKE method, for $U \leq 0.46$ m/s, this method produced fairly similar BSS estimates regardless of boundary roughness. When $0.54 \text{ m/s} \leq U \leq 1.04 \text{ m/s}$, BSS estimates diverged from one another, showing that the rougher boundaries produced more turbulence and higher BSS approximations. The acrylic estimates of BSS plateaued whereas the rougher substrates continued to increase BSS with U , this is likely an artifact of the smoothness of the acrylic material limiting the excess turbulence even at $U \sim 1.04$ m/s.

BSS estimates based on TKE method were compared with a fitted equation ($\tau_w = 1.7885 * u^2$), derived from experimental data over a smooth boundary by Pope et al. (2006) and a fitted equation ($\tau_w = 4.59 * u^2$) for rough bed flows over gravel ($d_{50} = 1.5$ cm) substrate developed by Bagherimiyab and Lemmin (2013) (Figure 2-12).

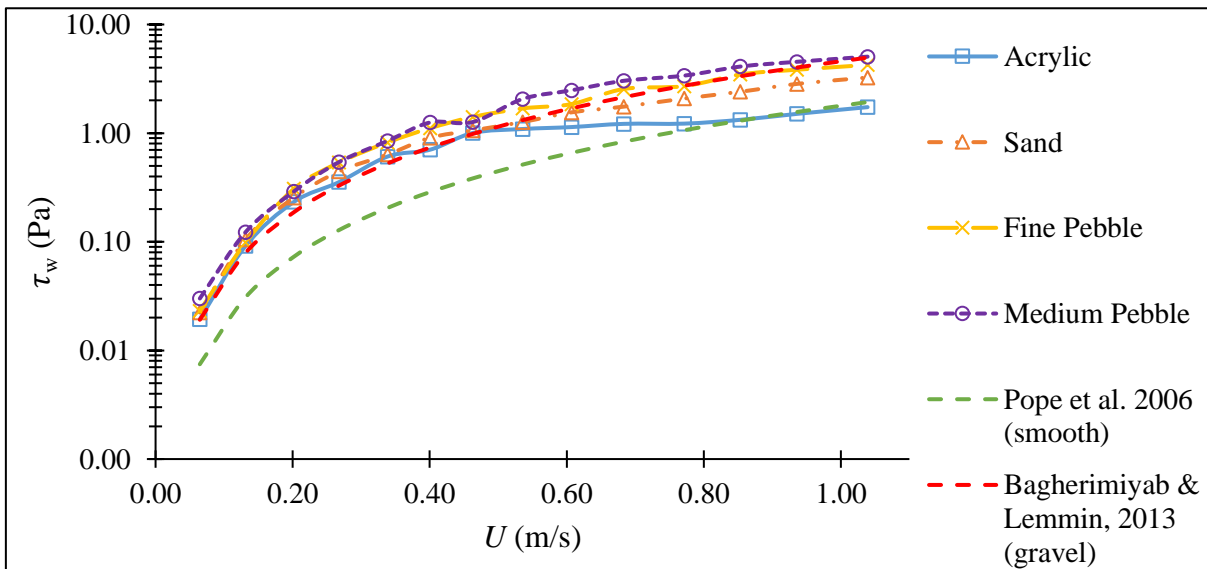


Figure 2-12: Comparison of BSS calculated using the TKE method over acrylic, sand, fine pebble, and medium pebble substrates, and quadratic relationships between average velocity and BSS established by Bagherimiyab and Lemmin (2013) and Pope et al. (2006).

The sampling volume for Pope et al. (2006) was centered at $z = 5$ cm ($\sim 14\%$ flow depth), whereas estimates presented from this research using the TKE method were obtained at 10% of

the flow depth. As previously discussed, a higher z may produce lower BSS estimates because a maximum value occurs at 10% of the flow depth and decreases with increasing z . Estimates by Pope et al. (2006) are lower than predictions from this research for $U < 0.77$ m/s, but converge for $U > 0.77$ m/s. The fitted equation for the smooth boundary produced lower BSS estimates compared to the field and flume data used to calculate it, indicating that a quadratic relationship does not accurately represent BSS estimates at low velocities.

Bagherimiyab and Lemmin (2013) measured the velocity profile throughout the entire water depth ($h = 19$ to 20 cm) and fitted a quadratic formula to the average BSS calculated using five methods (e.g., logarithmic velocity profile, TKE, Reynolds stress, wall similarity, spectral method). Based on the sediment size, BSS estimates would likely fall between the sand and fine pebble substrates. The fitted equation produced BSS estimates lower than those estimated over an acrylic bed for $U < 0.40$ m/s, for 0.40 m/s $< U < 0.85$ m/s estimates were between sand and fine pebble. When $U > 0.85$ m/s, BSS increased at a faster rate and converged with estimates predicted over the medium pebble substrate at $U = 1.04$ m/s. Both of the fitted quadratic relationships, using the average water velocity as a predictor for BSS, underestimated BSS at low velocities and predicted an exponential increase in BSS for $U > 1$ m/s.

Results calculated from the TKE method indicated that the BSS's rate of change slowed as velocity increased and may plateau. This trend was clear for the acrylic BSS estimates, calculated using the TKE method for U of 0.68 to 1.04 m/s, BSS increased from 1.22 to 1.74 Pa. For that same interval, using the Quadratic Friction Law, BSS estimates increased from 2.1 to 4.8 Pa. These findings indicated that a quadratic relationship may not be a good predictor for *in-situ*, local BSS estimates. **This method was used in subsequent CSS experiments with this flume because**

it produced consistent BSS estimates that captured localized turbulence and can be applied to any flow or boundary condition.

Law of the Wall – LP

The Law of the Wall – LP method was invalid in the MacFarlane Flume for $U < 0.68$ m/s because conditions within the test section become supercritical and no longer satisfied method assumptions. When $U \leq 0.54$ m/s, BSS estimates were similar regardless of boundary type (i.e., BSS ranged ± 0.60 Pa), and for $U \geq 0.61$ m/s, estimates increased at a faster rate with respect to boundary roughness causing deviations in BSS estimates. For $U < 0.77$ m/s, this method consistently estimated BSS over medium pebble to be largest, followed by fine pebble, acrylic, and sand. When $U > 0.77$ m/s, acrylic estimates exceeded sand BSS; this trend was not expected but has been noted by Biron et al. (2004) when comparing sand and acrylic boundaries in a flume study.

Results from this research showed a divergence in BSS estimates that coincided with the transition from sub- to super-critical conditions, supporting the claim that this method is only valid for sub-critical conditions and simple flow regimes (Pope et al., 2006). A higher standard deviation was associated with z_o for fine pebble and medium pebble substrates than for acrylic or sand. Biron et al. (2004) found the Law of the Wall – LP to be sensitive to bottom roughness because BSS estimates rely on precise near-bed velocity and elevation measurements. High variability associated with z_o for fine pebble and medium pebble may lead to inflated estimates of BSS. At higher water velocities, the Vectrino started to vibrate and bubbles formed on the front prong. This issue was exacerbated for non-uniform beds because the variability in grain size led to erroneous elevation measurements.

As documented in previous studies, the Law of the Wall – LP tends to over predict BSS compared with other methods (Bagherimiyab & Lemmin, 2013; Biron et al., 2004; Pope et al., 2006; Wilcock, 1996). For acrylic and sand, BSS estimates based on the Law of the Wall – LP were larger when compared with other all other methods. Over fine pebble, the Indicator Function sometimes produced higher estimates, and medium pebble the Law of the Wall – LP predicted high BSS estimates, only second to the Indicator Function (Bagherimiyab & Lemmin, 2013; Biron et al., 2004; Kim et al., 2000). After evaluating the roughness coefficients calculated from this method, z_o and C_D calculated from z_o , these parameters were consistent with literature values. This suggested that the high BSS estimates were a result of inflated u_w^* values. u_w^* is a function of the slope of the fitted regression line and near-bed velocity profiles used in the derivation were skewed by the rapidly increasing velocity close to the boundary.

The Law of the Wall – LP method was used in the oil CSS experiments to calculate C_D for the Quadratic Friction Law, but because of the high BSS estimates and limited application based on flow conditions it was not used to calculate BSS.

Law of the Wall – Single Point

The Law of the Wall – Single Point leverages *in-situ* measurable characteristics rather than values derived from the velocity profile (e.g., d_{84}) and therefore was applicable for all experimental conditions. BSS estimates calculated using this method increased with velocity and bottom roughness (e.g., BSS over medium pebble was largest, followed by fine pebble, sand, and acrylic). For all substrate types and velocity intervals, BSS estimates using Law of the Wall – Single Point produced values that fell within $\bar{\tau}_w \pm \sigma$. This suggests that d_{84} should be used as a representative grain size for all sediment types used in the oil CSS experiments. The Law of the Wall – Single Point provides a local estimate of BSS because it uses near-bed velocity data

($\bar{u}_{z=2cm}$), but does not require instruments capable of high spatial and temporal resolution necessary to measure a velocity profile. **Therefore, in the event where resources are limited and only single-point flow meters are available, this method could be used to provide a reliable BSS prediction. This method was used in subsequent CSS experiments and in the sunken oil transport tool (See Chapter 4).**

Indicator Function

The Indicator Function was theoretically applicable for all flow regimes and boundary types conducted in this research. Interestingly, BSS estimates reached a local peak for acrylic, fine pebble, and medium pebble at U of 0.46 m/s, 0.54 m/s, and 0.54 m/s, respectively, which corresponded to a flow regime just prior to the transition from sub- to super-critical conditions. After peaking, the BSS estimates decreased to fall back in line with the previously established trend for $U > 0.61$ m/s. Therefore, if using this method in flumes or the field, it is important to identify when conditions transition from sub- to super-critical. If this cannot be done, the Indicator Function method should not be used. With respect to boundary type, BSS estimates for acrylic were larger than sand for U of 0.2 m/s, 0.27 m/s, and 0.46 m/s. For all other velocities, estimates followed the anticipated trend that a rougher substrate produced higher BSS values. The high BSS estimates using this method on rough substrates are likely due to the way velocity was measured, as it relies on a continuously measured and relatively smooth velocity profile to accurately estimate BSS. Further research should be conducted regarding the validity of the Indicator Function method for rough boundaries and in super-critical conditions. **Based on the inconsistent estimates of BSS and limited use in rough bed conditions, the Indicator Function was not used in oil CSS experiments.**

Quadratic Friction Law

The Quadratic Friction Law was applicable for all experimental conditions in this flume. It followed a similar pattern as the Law of the Wall – LP because C_D was derived from z_o . However, the magnitude of the Quadratic Friction Law estimates were smaller because it used \bar{U} rather than calculating BSS from u_w^* . For $U \leq 0.46$ m/s, the average variability for BSS estimates for all substrates was ± 0.18 Pa; when $U \geq 0.54$ m/s the average range increased to ± 2.18 Pa. As velocity increased, the effect of sediment size on BSS estimates was exacerbated, especially for rough substrates, which was attributed to variability associated with z_o . As with the Law of the Wall – LP method, sand BSS estimates were larger than acrylic for $U < 0.77$ m/s, but when 0.77 m/s $\leq U \leq 1.04$ m/s, the acrylic estimates were larger.

Thompson et al. (2006) developed a fitted equation ($\tau_w = 3 * u^2$) to estimate BSS using the Quadratic Friction Law based on experimental data collected in clear water at $z = 15$ cm. To relate values calculated from this research, BSS was adjusted to $z = 15$ cm (Figure 2-13).

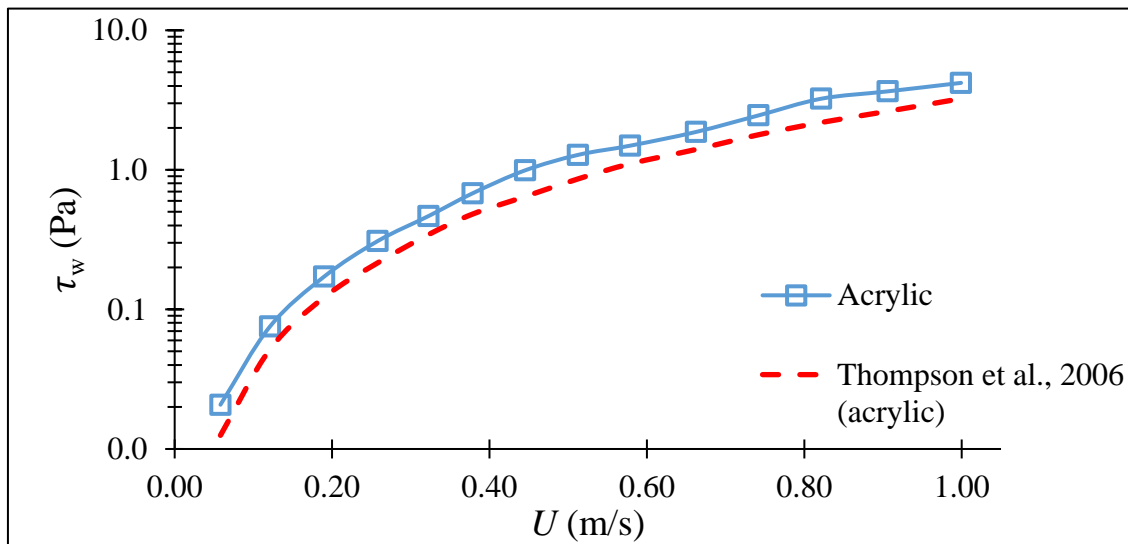


Figure 2-13: Acrylic and sand BSS calculated using the Quadratic Friction Law compared with results from Thompson et al. (2006).

The fitted equation produced slightly lower values than those estimated in this research. For $U < 0.54$ m/s, the difference between measured and predicted values averaged ± 0.12 Pa. When $U > 0.54$ m/s, the average range increased to ± 0.71 Pa, with the largest difference of 1.05 Pa occurring at $U = 0.85$ m/s. The variability in estimates may be due to: (1) the flume configuration (i.e., annular vs. straight), (2) the measured velocity values, or (3) the derived drag coefficients.

The Quadratic Friction Law is a hybrid between local and global estimates because it uses a derived roughness parameter which captures the effect of velocity on drag, while using a global velocity value. **Based on its agreement with literature, its widespread use, and the unique mixture of input parameters, the Quadratic Friction Law was used in oil CSS experiments.**

Chézy/Momentum

The Chézy/Momentum method was valid for all experimental conditions. BSS estimates were based on the ratio of $\frac{R_h}{d_{84}}$ and U , both of which varied as a function of h . The representative roughness components were held constant, and the velocity component increased in a stepwise manner. Therefore, BSS followed the anticipated trend that estimates were largest when water velocity and bed roughness were highest. For $0.06 \text{ m/s} \leq U \leq 1.04 \text{ m/s}$, the medium pebble BSS estimates were largest, followed by fine pebble, sand, and acrylic.

The Chézy/Momentum method can be used when sophisticated velocity measurements are not readily available or when only stream gauge data are available to provide a velocity prediction. Although this method provides a globalized BSS estimate and generally produced higher estimates compared with other methods, it followed the theory that steeper curves are expected with increasing roughness (Bagherimiyab & Lemmin, 2013; Pope et al., 2006). Due to the nature of the equation, BSS continued to increase at a faster rate for higher velocities. **This method was used in oil CSS experiments because it provided consistent BSS estimates for all boundary**

types, applies to riverine environments regardless of flow condition, and uses one-dimensional velocity values that can be readily measured or estimated by stream gauge data.

Manning/Momentum

The Manning/Momentum method was valid for all experimental conditions, and is a good descriptor of river hydraulics for a slowly varying water level (Boufadel et al., 2019). When comparing BSS estimates with respect to substrate type, this method followed the expected trend that a rougher surface causes a higher BSS value. This method is similar to the Chézy/Momentum approach in that it uses a constant roughness parameter and the globalized velocity values. Global estimates do not deviate from the anticipated trend because they are independent of localized turbulence and because velocity does not affect the roughness parameters. However, it provides a reliable BSS estimate that can be predicted using values found in literature and readily measured hydraulic parameters such as depth, cross-sectional area, and average velocity. **Therefore, the Manning/Momentum method was used in oil CSS experiments because it would likely be leveraged to predict an initial estimate of *in-situ* BSS during a response.** The limitation to using global estimates is that they predict BSS to be higher than local methods, especially for rough boundaries. Therefore, when comparing *in-situ* BSS to CSS data it is essential to know how the CSS value was calculated.

2.4.5 Research Limitations and Method Selection

A major limitation to this research is that experiments were conducted for an immobile boundary for non-cohesive sediments, therefore bed forms did not develop and only skin-friction was addressed. Bed forms generally increase drag coefficient estimates and are especially important for sand beds. For example, unrippled sand has a $z_o = 0.04$ mm compared with rippled sand where $z_o = 6$ mm (Soulsby, 1997). Therefore, above the sediment's CSS threshold (i.e., the

critical BSS at which sediment transport occurs), z_0 estimates would likely be larger than those predicted in this research. Using each material's d_{50} and the Shields Diagram, the CSS was estimated to be approximately 0.29 Pa, 4.8 Pa, and 9.6 Pa for sand, fine pebble, and medium pebble, respectively. Based on $\overline{\tau_w} \pm \sigma$ estimates for all valid methods with respect to each boundary type; 0.29 Pa on a static sand bed corresponded to $U > 0.2$ m/s, 4.8 Pa over the fine pebble substrate correlated to $U \sim 0.77$ m/s, and 9.6 Pa with a medium pebble bed related to $U \sim 0.94$ m/s.

Multiple methods were used in this research so that results would be related to literature values and translated from flume-based experiments to the field regardless of instrument availability, boundary type or flow conditions (Table 2-7). Since BSS is not a readily-measured parameter in the field and because it relies on assumed, derived, or measured input values, it was expected that multiple methods would produce a range of BSS estimates (i.e., 2-3 Pa spread) (Wren et al., 2011). A range in BSS values may depend on how and where velocity is measured, characterization of boundary conditions and subsequent roughness parameterization, or the method used to calculate BSS. Therefore, it is important to use global and local methods when quantifying CSS thresholds in the laboratory, so that in the field, any BSS method can be used and appropriately related to CSS values.

Table 2-7: Summary of BSS method scale and application. Note: the bold text indicates the methods used in subsequent CSS experiments.

<i>Method Name</i>	<i>Scale</i>	<i>Reasoning:</i>
Newton's Law of Viscosity	Local	Uses precise near-bed velocity measurements to confirm the presence of a viscous sublayer. This method did not apply to fine pebble and medium pebble substrate at all velocity intervals.
Indicator Function	Local	Further evaluation on the applicability and reliability of the Indicator Function is necessary; compared with the other methods it under predicted BSS over acrylic and sand substrates, fell in line with fine pebble BSS estimates, but greatly overpredicted BSS for medium pebble.
Law of the Wall – LP	Local	Did not apply to $U > 0.61$ m/s. With some exceptions, the Law of the Wall – LP approach produced the highest BSS approximations compared with the other methods. However, the derived z_o proved to be a reliable roughness length and captured the effect of velocity on roughness coefficients and should be used to calculate C_D .
TKE	Local	This method applies to simple and complex flow regimes and all boundary types. Uses 3D instantaneous velocity measurements to relate turbulent fluctuations with BSS. Results produced consistent BSS estimates for all boundary types, similar to literature values without the use of a roughness parameter.
Law of the Wall – Single Point	Local	Applies to all boundary and uniform, steady state flow conditions, and produced reliable local BSS estimates using single point velocity measurements and a readily measurable roughness length.
Quadratic Friction Law	Hybrid	Applies to all boundary and uniform, steady state flow conditions. Results aligned well with literature values, and derived drag coefficients were similar to commonly cited values. Uses local roughness lengths to estimate the drag coefficient, therefore considering the effect of velocity on drag. If necessary, drag coefficients can also be leveraged from literature values. It uses a global velocity value (e.g., depth-averaged velocity), limiting the impact of velocity variability on BSS estimates. BSS approximations agreed with literature values.
Chézy/Momentum	Global	Commonly used method for open channel flow and is applicable to all flow and boundary conditions. It provides a reliable BSS estimate using readily measurable input parameters, and if limited information is available, the depth-slope method can be applied to provide an initial BSS approximation.
Manning/Momentum	Global	Applies to uniform, steady state conditions and is widely used in open channels (e.g., streams, rivers). Uses the free-stream velocity, which can be readily measured. There are multiple methods that relate the particle size to a roughness coefficient. For all substrate types, BSS estimates were consistently within $\overline{\tau_w} \pm \sigma$.

2.4.6 Sensitivity Analysis of BSS Methods

2.4.6.1 Describing Parameter Bounds

A sensitivity analysis was performed on the input parameters used to calculate BSS for methods that rely on derived or measured values (i.e., Law of the Wall – Single Point, the Quadratic Friction Law, Chézy/Momentum, Manning/Momentum). The reference values used in the sensitivity analysis were obtained from results over the sand substrate (Appendix A.10: Sensitivity Analysis Plots).

The upper and lower velocity bounds used in the analysis were $\bar{u}_{z=2cm} \pm \sigma$, $\bar{U} \pm \sigma$, and $U \pm \sigma$ for Law of the Wall – Single Point, Quadratic Friction Law, Chézy/Momentum and Manning/Momentum methods, respectively. Except for the Law of the Wall – Single Point, which uses d_{84} as the characteristic roughness length, the roughness parameters used in the Quadratic Friction Law, Chézy/Momentum and Manning/Momentum were related to one another, and compared as like terms in Table 2-5 (2.4.3 Comparison of Roughness Parameters). The range of the C_D values was then converted to C and n , and used as bounds for the Chézy/Momentum and Manning/Momentum analyses, respectively. For the Law of the Wall – Single Point method the effect of roughness on BSS estimates was evaluated using d_{10} and d_{90} as the lower and upper limits, respectively.

2.4.6.2 Sensitivity Analysis Results

For the Quadratic Friction Law, Chézy/Momentum and Manning/Momentum, if the velocity and characteristic roughness parameters were adjusted by the same amount (e.g., $\pm 10\%$), the effect of velocity was greater than that of the roughness parameter, especially at high velocities. When the velocity changed as a function of σ and over the range of roughness parameters, the

spread in BSS was related to the driving functions in the method's equations, and estimates were more sensitive to roughness parameter than velocity σ .

The effect of velocity was more prominent for the Law of the Wall – Single Point compared with the other three methods because they rely on global velocity values, and the RSD associated with them is smaller than the locally-measured velocity. For example, on a sand substrate, the average RSD for $\bar{u}_{z=2cm}$ was 16% whereas for U and \bar{U} , the average RSDs were 5% and 3%, respectively. The associated variability was expected for $\bar{u}_{z=2cm}$ because near-bed velocity values were subject to excess turbulence caused by boundary roughness, whereas U was measured further from the boundary, therefore, minimally impacted by turbulence due to bed roughness, and \bar{U} is a spatially-averaged value.

For all methods, variability increased as velocity increased resulting in a wider spread of BSS estimates. Using the Law of the Wall – Single Point, when $\bar{u}_{z=2cm} = 0.16$ m/s, the range of BSS was 0.10 Pa to 0.20 Pa, whereas for $\bar{u}_{z=2cm} = 0.81$ m/s, BSS estimates ranged from 2.8 to 4.9 Pa. At the same experimental settings, the Quadratic Friction Law BSS estimates were 0.19 to 0.20 Pa and 4.3 to 4.9 Pa. The Chézy /Momentum estimates were 0.16 to 0.21 Pa and 4.5 to 5.4 Pa, and the Manning/Momentum estimates were 0.15 to 0.19 Pa and 4.3 to 5.1 Pa. The global BSS methods tended to predict higher magnitude BSS estimates, but had a smaller range. For $U < 0.85$, the lowest BSS estimate was calculated by the local method, the Law of the Wall – Single Point, followed by Manning/ Momentum, Chézy /Momentum, and the Quadratic Friction Law. When $U \geq 0.85$, BSS approximations from the Quadratic Friction Law were smaller than those from the Chézy/Momentum method because C_D decreased at high velocities and C remained constant.

The Law of the Wall – Single Point uses d_{84} as the reference characteristic roughness length. As expected, when d_{10} was used as the roughness length, BSS estimates decreased by 69% compared to the reference value, whereas if d_{90} is used BSS increases by 8% relative to the reference value.

For the Quadratic Friction Law, Chézy /Momentum and Manning/Momentum methods, BSS estimates were more sensitive to the variability associated with the roughness parameters than with velocity $U \pm \sigma$. The effect of roughness parameter variability on BSS estimates differed for each method. When using the Manning/Momentum approach, the lower limit had no relative change when compared with the reference value because when compared as like terms, n was the smallest value of all of the roughness parameters for sand. Using the upper roughness limit and the Manning/Momentum approach, estimates increased by 54% relative to the reference value.

When analyzed with respect to the smallest roughness parameter and using the Quadratic Friction Law, BSS decreased on average by 119% relative to the reference value. For the largest roughness parameter at $U < 0.54$ m/s, estimates decreased on average by 4% relative to the reference value; when $U > 0.68$ m/s, approximations were larger by 7% relative to the reference value. The inconsistent effect of the upper roughness limit on BSS estimates occurred because C_D was held constant at 0.0068 for the sensitivity analysis, but the reference value's C_D changed with respect to velocity. This suggested that, when possible, C_D should be derived from the velocity profile rather than using a single value. An averaged C_D value may underestimate the effect of boundary roughness at lower velocities and overestimate drag at higher velocities.

The Chézy/Momentum approach is unique because C follows an inverse relationship with roughness, in that C decreases with increasing boundary roughness. Therefore, if all other factors are held constant, the largest C produces the smallest BSS estimate. The lower limit of C caused

BSS estimates to increase by 30% at all velocity settings relative to the reference value, and the upper limit of C decreased BSS estimates, relative to the reference value, by 54% for all velocities.

Based on findings from this section, assuming uniform, steady state conditions, if BSS is calculated using a local method, then velocity and roughness variability are of equal importance. Global BSS estimates are more sensitive to roughness parameter variability. These findings suggest that bathymetric surveys and characterization of the bed should be a priority when using global methods in the field. Recording near-bed velocity variability is essential to produce accurate ranges of *in-situ* BSS estimates when using local methods. If obtaining sediment cores, performing sieve analyses or conducting bathymetric surveys cannot be accomplished, then BSS should be calculated over a range of sediment sizes representative of *in-situ* conditions until more thorough measurements can be made.

2.5 Conclusion and Future Research

The findings from the hydraulic analysis conducted for CRRC's flume, the evaluation of BSS methods applicable for use in the flume, and the sensitivity analysis on BSS input parameters, are summarized as follows:

Conclusions relevant to the CRRC MacFarlane Flume:

1. The VFD settings (x) were correlated to *in-situ* free-stream velocity (U) for $h = 30.5 \pm 1$ cm by the fitted equation: U (m/s) = $0.0009x^2 + 0.0604x$.
2. The flow regime was classified at each VFD setting for $h = 30.5 \pm 1$ cm (Table 2-3). Flow conditions were considered uniform, steady state at VFD settings 1 to 14 Hz (0.06 m/s to 1.04 m/s). Flow transitioned from sub- to super-critical at VFD settings 8 and 9 Hz (0.54 m/s to 0.61 m/s).
3. For all substrate types, the ADV collected reliable, near-bed velocity profiles for VFD settings 1 to 14 Hz.

Conclusions relevant to external laboratories and field research:

4. The boundary parameters for immobile acrylic, sand, fine pebble, and medium pebble beds were quantified using near-bed velocity measurements and PSD results (Table 2-4). The calculated roughness parameters were then put in terms of C_D and compared as like terms; the range of the values produced were used as the upper and lower roughness parameter limits in the sensitivity analysis (Table 2-5). In the event where only a sieve analysis can be conducted to determine a roughness coefficient in an open channel, use of $z_o = 0.1 * d_{84}$ and Eq. 2-22 as the representative C_D is recommended. Compared to the five other methods used to calculate roughness characteristics, this

approach produced median C_D values for sand, fine pebble, and medium pebble substrates.

5. When using the Quadratic Friction Law to calculate BSS, C_D should be derived from the velocity profile rather than using a single value because it changes as a function of velocity.
6. The effect of *in-situ* water velocity and boundary roughness on BSS estimates was evaluated using eight computational methods. Multiple methods were used so that results could be related to literature values and be translated from flume-based experiments to the field regardless of instrument availability, boundary type or flow conditions. The method application, scale of use, and reason for using the method in future experiments were summarized in Table 2-7. The TKE, Law of the Wall – Single Point, Quadratic Friction Law (using Law of the Wall – LP to calculate C_D), Chézy/Momentum, and Manning/Momentum methods were suitable for use in subsequent oil CSS experiments.
7. If using the Indicator Function method in flumes or the field, it is important to identify when conditions transition from sub- to super-critical. If this cannot be done, the Indicator Function method should not be used. Further research should be conducted to evaluate if adjusting the height of the velocity profile measurement or using a different von Karman constant would improve BSS predictions in super-critical conditions.

Conclusions from the sensitivity analysis:

8. Based on the sensitivity analysis, local BSS estimates were equally sensitive to velocity and roughness variability, whereas the global methods tended to be more sensitive to roughness variability. Therefore, in the event of an oil spill, the first priorities are to

determine the expected velocity range and then to collect sediment cores to determine particle size distribution. Providing a velocity range and knowing the particle size distribution will improve the accuracy of global BSS estimates. As more information becomes available and instruments can be deployed to measure near-bed velocity, then local methods could be used to predict *in-situ* BSS and sediment or oil transport processes.

Further research using a mobile sediment bed in the CRRC flume is recommended to validate the sediment's CSS thresholds estimated from the Shields curve to provide "true" CSS thresholds. The sediment's CSS thresholds should be further refined into incipient motion, bedload transport, and suspended load transport, and the effect of these processes on roughness parameter estimates should be quantified. Additional research should be conducted for fine sediments with cohesive properties (e.g., clays) to evaluate the applicability of BSS methods for a mobile, cohesive bed in the flume. If using a different water depth, then the transitions from sub- to super-critical and laminar to turbulent should be recalculated and the associated VFD settings defined. This change would alter the empirical relationships between VFD setting and free-stream velocity and depth-averaged velocity, and the velocity ranges for which each BSS method is valid.

CHAPTER 3

CRITICAL SHEAR STRESS OF SUNKEN, NO. 6 HEAVY FUEL OIL IN FRESH WATER

3.1 Abstract

A series of flume- and laboratory-based experiments defined and quantified the thresholds of oil transport (sunken, No.6 heavy fuel oil mixed with kaolinite clay (24% by weight, g clay:g oil) in fresh water). When the sunken oil became mobile, the current-induced bed shear stress (BSS) had exceeded a threshold value specific to the oil, known as the critical shear stress (CSS). The oil's CSS was evaluated as a function of water velocity (0.06 to 1.04 m/s by 0.08 ± 0.02 m/s intervals), water temperature ($10 \pm 1.5^\circ\text{C}$, $17.5 \pm 0.5^\circ\text{C}$, $24 \pm 2^\circ\text{C}$), oil condition (fresh, weathered), and sediment median size ($d_{50} = 0.42$ mm, 6.5 mm, 10.6 mm). Based on experimental results, the stages of oil transport were defined and empirical relationships using the oil's kinematic viscosity (ν_o) and sediment d_{50} were developed to predict oil CSS at each transport stage. Additionally, for $\nu_o < 2 \times 10^4$ cSt, multiple thresholds of movement were observed: (1) gravity dispersion, (2) rope formation, (3) ripple formation, (4) break-apart/resuspension. When $\nu_o > 6 \times 10^4$ cSt, transport was more likely to occur as a single event with the oil remaining intact, saltating over the bed in the direction of flow (i.e., oil bedload transport).

3.2 Introduction

When oil is released into water as a non-aqueous phase, the relative density between spilled oil and the receiving water dictates if the oil will float on the water's surface (i.e., floating), be neutrally buoyant and remain in the water column (i.e., submerged), or be negatively buoyant and sink to the bottom (i.e., sunken) (API, 2016b; CRRC, 2007; Michel & Bambach, 2020). Oil spill response tactics have been shaped by the assumption that when spilled into water, most oil will float on the water's surface (CRRC, 2007; Harper et al., 2018). However, non-floating oil spills have been documented in marine and fresh water environments, and because they are less frequent than floating oil spills, testing new response equipment, validating models, and maintaining operational expertise is challenging (CRRC, 2007). Non-floating oils often contain higher concentrations of paraffin waxes, asphaltenes and resins which hinder natural remediation processes, potentially smothering benthic organisms, and introducing them to the chronic exposure of persistent hydrocarbons (Gustitus & Clement, 2017; Martin et al., 2014).

The propensity for the spilled product to float, submerge or sink can change as a function of oil type, *in-situ* environmental conditions (e.g., water temperature, current velocity, wind), weathering processes (e.g., evaporation, dissolution, biodegradation, emulsification), and interaction with sediments, minerals or marine snow (CRRC, 2007; Fitzpatrick et al., 2015a; Gustitus & Clement, 2017; Khelifa et al., 2002; Lee, 2002; Michel & Bambach, 2020; Michel & Galt, 1995; Passow, 2016). For example, during the *T/B DBL-152* spill in 2005, blended slurry oil (API ~ 4 to 4.5°; density, $\rho_o \sim 1.04 \text{ g/cm}^3$) was discharged into the Gulf of Mexico, sank immediately upon entry into the water and was sporadically remobilized by storm events (Beegle-Krause et al., 2006; Michel, 2008). In 1994, during the Morris J. Berman spill of No. 6 heavy fuel oil (HFO) (API ~ 9.5°; $\rho_o \sim 1.004 \text{ g/cm}^3$), the spilled product initially floated, with limited evaporation occurring at the leading edge of the slick which formed tarballs that readily dispersed.

Some of the oil was transported inland where it mixed with sediments through wave action, sank to the bottom, and was stranded in a lagoon. The oil-sediment mixture remained on the seabed overnight, but separated from the sediments and resurfaced throughout the day as water temperatures increased (Petrae, 1995; NRC, 1999).

Depending on *in-situ* turbulence, suspended sediment concentrations and oil viscosity, the oil-sediment mixtures can form microscopic aggregates (<1 mm) or macroscopic agglomerates (>1 mm). This manuscript discusses the transport of macroscopic agglomerates. Macroscopic agglomerates are characterized based on their size. 1 mm to 10 cm are called sand-oil agglomerates (SOA); 10 cm to 1 m sediment-oil patties (SOP), and agglomerates >1 m sunken oil mats (SOM) (Gustitus & Clement, 2017). Pieces of an SOM can break apart into SOAs or SOPs. SOAs and SOPs can be: (1) driven onshore during high energy events causing long-term shoreline oiling, (2) buried and/or exhumed under normal wave events, (3) carried alongshore or downstream under high current velocities, and (4) deposited into low energy environments such as tributary mouths, sheltered lagoons, estuaries, troughs, or deep parts of channels (Dalyander et al., 2014; Dollhopf et al., 2014).

Since the National Research Council's (NRC) call to improve non-floating oil spill response in 1999 (NRC, 1999): (1) new tactics and tools have been developed to monitor, track and contain non-floating oil (Fitzpatrick et al., 2015a; M. Fitzpatrick et al., 2014; Hansen et al., 2014), (2) guidance documents have been published to optimize response operations (API, 2016a; Harper et al., 2018; Michel & Bambach, 2020; NRC, 1999), and (3) development of submerged and sunken oil trajectory models has greatly improved (Dalyander et al., 2014; Echavarria-Gregory & Englehardt, 2015; Englehardt et al., 2010; Jacketti et al., 2020, 2019; Zhao et al., 2016). The techniques used by modelers to predict sunken oil transport have been adapted from sediment

transport theories, research and practice. Specifically, Simecek-Beatty (2007) recommended applying the concept of bed shear stress (BSS) to predict sunken oil transport. BSS is the frictional force exerted by the fluid on the boundary (i.e., force per area), and is used to characterize thresholds of sediment transport as a function of *in-situ* hydrodynamics, skin-friction induced by bed roughness, form drag, and momentum transfer caused by mobilized grains (Nelson et al., 1995; Shields, 1936; Soulsby, 1997). The threshold BSS which causes the sediment (or oil) to move is known as the critical shear stress (CSS) and is a function of the sediment's (or oil's) physical properties (e.g., density, size).

In the event of an oil spill, modelers have relied on surrogate values or previous research to predict the remobilization of sunken oil. In 2004, the hull of the *M/V Athos I* was punctured and over 260,000 gallons of Bachaquero crude oil (API~13.6°; $\rho_o \sim 0.943$ to 0.978 g/cm³) were released into the Delaware River (API, 2016b). As it exited the hull, the jetting action caused the oil to mix with mud and clay resulting in pools of oil near the discharge site, formation of tarballs and tarmats and subsurface transport. Before more data became available about the *M/V Athos I* spilled product, modelers relied on a single reference value (Cloutier et al., 2002) to predict the resuspension of the sunken oil. The reference value provided a lower threshold of movement because the Hibernian crude oil ($\rho_o = 0.875$ g/cm³), upon which it was based, was more buoyant and had a viscosity several orders of magnitude lower than that of the spilled oil (DARRP, 2018; Michel, 2008; NOAA, 2018; Simecek-Beatty, 2007).

Two major spill events occurred in 2010, the Enbridge Line 6b and Deepwater Horizon. In both scenarios, a floating oil weathered or emulsified and then mixed with sediments (e.g., sand, clay) to create a negatively-buoyant oil. These events forced responders to perform impromptu

flume- and field-based experiments to determine the CSS of the spilled product; experimental results were then used to inform model predictions on the transport of the sunken oil.

The Enbridge Line 6b pipeline spill released diluted bitumen (API $\sim 20^\circ$; $\rho_o \sim 0.938 \text{ g/cm}^3$) into Talmadge Creek (MI) which fed into the Kalamazoo River. Some of the oil submerged and was transported with the currents until it reached a low velocity area downstream and deposited (USEPA, 2016). Response and recovery efforts relied on CSS thresholds for clay and silt-sized fine-grained sediment as surrogates for submerged oil ($< 2 \text{ mm}$ droplets) and oiled sediment because oil was deposited in slow moving reaches of the river (Dollhopf et al., 2014). Field-, flume-, and laboratory-based experiments were conducted to support the empirical models used to simulate resuspension, migration, and deposition of the oil-particle aggregates (Fitzpatrick et al., 2015b).

During Deepwater Horizon recovery operations, chronic re-oiling of cleaned beaches drove researchers to investigate and model the subsurface transport of SOAs and SOPs (Dalyander et al., 2014). The authors found that the model was sensitive to CSS thresholds, and uncertainty associated with model prediction could be reduced by more accurate oil CSS estimates. This led to a series of field experiments where the CSS of cm-sized sandy ($> 60\%$ sand by weight), artificial SOAs (aSOA) were placed atop the sea bed ($\rho_o = 1.689 \pm 0.85 \text{ g/cm}^3$) (Dalyander et al., 2015; Michel & Bambach, 2020). BSS was calculated using multiple theories applicable to nearshore coastal environments described by Shields (1936) and extended to a wider range of particle sizes by Soulsby & Whitehouse (1997). Researchers determined that a lower CSS threshold, calculated from an unmodified Shields parameter using SOA properties, was the best predictor of SOA mobility. The authors highlighted the importance of selecting an accurate CSS value, and

recommended that further CSS research be conducted in a laboratory setting “where visibility is improved and the flow conditions can be precisely controlled” (Dalyander et al., 2015).

Although progress has been made to widen the known oil CSS thresholds, no prior published number exists to establish CSS thresholds for HFO. HFO, widely used by ships, has a density (0.95-1.03 g/cm³ at 15°C) that makes it prone to sinking. Its high viscosity increases the propensity to interact and mix with sediments furthering the potential to sink (NOAA Scientific Support Team, 2012). Of 33 globally-recorded sunken oil spills, 16 of the incidents were of heavy refined products (Michel & Hansen, 2017). Results from HFO research could be applied in the event of shipping accidents. Additionally, No. 6 HFO is geographically-relevant to researchers because it is used as fuel source in power plants. For example, a power plant that burns HFO sits alongside the Piscataqua River (NH), which connects Portsmouth Harbor to the Great Bay Estuary. High current velocities (>2 m/s), expansive mudflats, relatively cold water, and a fresh water input increase the risk for a floating oil to submerge and sink.

A series of flume- and laboratory-based experiments were conducted by the Coastal Response Research Center (CRRC) at the University of New Hampshire (UNH) using 100 grams of No.6 HFO on immobile substrates. The aim of this research was to: (1) provide modelers and responders with CSS thresholds of No. 6 HFO over a range of environmental conditions in fresh water to be used as a reference point in the event of a non-floating oil spill, (2) identify factors driving sunken oil transport, and (3) evaluate how boundary roughness impacts an oil’s CSS thresholds. Oil CSS experiments were conducted as a function of water velocity (0.06 to 1.04 m/s by 0.08±0.02 m/s intervals), water temperature (10±1.5°C, 17.5±0.5°C, 24±2°C), oil condition (fresh, weathered), and sediment size (d_{50} = 0.42 mm, 6.5 mm, 10.6 mm).

Results indicated that CSS thresholds were higher at $10\pm 1.5^\circ\text{C}$ due to the increase in oil kinematic viscosity (ν_o) and for larger sediment sizes (i.e., $d_{5o} = 10.6$ mm). Additionally, entire SOPs are likely to move at a single CSS threshold for $\nu_o > 2 \times 10^4$ cSt; when $\nu_o < 2 \times 10^4$ cSt, they exhibit multiple stages of transport. Criteria were developed to convert qualitative video observations into CSS values. For water $> 17.5 \pm 0.5^\circ\text{C}$, the CSS thresholds were defined as: (1) gravity dispersion, (2) rope formation, (3) ripple formation, and (4) oil break apart/resuspension. In the event of a sunken oil spill, modelers and responders can compare *in-situ* BSS values with the oil's CSS thresholds to predict mobility. Based on the sediment sizes present at the boundary, modelers can also compare sediment CSS with oil CSS to determine if burial and exhumation processes are relevant.

3.3 Methods and Materials

3.3.1 Oil Preparation and Properties

Granite Shore Power (Newington, NH) supplied the No. 6 HFO used in the CSS experiments. Half of the oil samples underwent open pan evaporation in a fume hood at $18 \pm 1^\circ\text{C}$ following protocols obtained in Environment Canada (2013) and Fieldhouse et al. (2010) until 5% mass loss was achieved (Eq. 3-1).

$$\%Ev = 1.296 \ln(t) - 3.6183 \quad \text{Eq. 3-1}$$

where: $\%Ev$ = percent mass loss (by weight), t = time spent weathering (hours). The fitted relationship between $\%Ev$ and t was determined from 16 replicate samples ($R^2 = 0.9839$); $\%Ev = 5$ was achieved in ~ 35 days.

The density was measured following ASTM D1298 - 12b (2017a). The density of the fresh ($\rho_{o(F)} = 0.96 \pm 0.001$ g/cm³ at 15°C) and weathered ($\rho_{o(W)} = 0.97 \pm 0.001$ g/cm³ at 15°C) samples indicated that the oil would not readily sink in freshwater. Therefore, kaolinite clay (24% by

weight) was added as a sinking agent to ensure the oil would sink. [N.B., Sand was initially used as the sinking agent, but the mixture separated when injected into water $>17.5\pm 0.5^\circ\text{C}$ (as observed in the Morris J. Berman spill)]. [N.B., The experimental oil will herein be referred to as an “oily” SOM because the mixture was composed $>40\%$ oil by weight (Michel & Bambach, 2020)]. Density measurements for the fresh oil+clay (FC) ($\rho_{o(FC)} = 1.13\pm 0.001 \text{ g/cm}^3$ at 15°C) and weathered oil+clay (WC) ($\rho_{o(WC)} = 1.13\pm 0.001 \text{ g/cm}^3$ at 15°C) samples confirmed that these mixtures would readily sink when injected into fresh water ($\rho_w \sim 0.997$ to 1 g/cm^3) for all experimental conditions.

The complex viscosity of the oil, η_o ($\text{Pa}\cdot\text{s}$), for all four oil mixtures, was measured using a TA Instruments (New Castle, DE) HR-1 Discovery Hybrid Rheometer (DHR) following ASTM D7175-15 (ASTM, 2015a). Viscosity measurements were conducted using a 25 mm diameter oscillating parallel plate geometry with 1 mm gap settings in a temperature sweep mode (-6°C to 12°C or 18°C depending on the instrument’s upper working limit) with tests at strain rates between 0.1 rad/s to 100 rad/s (intervals of 10 rad/s).

To measure viscosities at higher temperatures, a Wells-Brookfield Dial Viscometer (Middleboro, MA) was used following protocols described by Manual No. M/85-150-P700 (Brookfield Engineering, n.d.) The dynamic viscosity, μ_o ($\text{Pa}\cdot\text{s}$), was measured using a Wells-Brookfield Dial Viscometer (model RVT), in cone/plate geometries using the cup-and-cone CP-41 (2mL sample cup, 3° cone angle). As specified by the manufacturer, the range of measurable viscosities is $1.229 \text{ Pa}\cdot\text{s}$ to $24.576 \text{ Pa}\cdot\text{s}$ at shear rates of 20 sec^{-1} and 1 sec^{-1} , respectively. Viscosity readings have a precision of $\pm 1\%$ of the torque reading resulting in a $\pm 1.5\%$ variability in viscosity measurements (Brookfield Engineering, n.d.). Temperature was controlled by a Lauda Super RMS-6 bath circulator (Lauda-Brinkmann, Germany) within $\pm 0.1^\circ\text{C}$ of the test temperature. The

viscosity was analyzed between 15°C and 50°C for all samples, except for the WC mixture which exceeded instrument limitations for samples below 19°C.

3.3.2 Substrate Classification

Sediments sizes chosen for these experiments represented the three most abundant grain size classes found in the upper and lower Mississippi River. The Mississippi is navigable water that has historically experienced sunken oil spills, the most recent spills occurred in 2015 and 2016 (International Maritime Organization, 2014; NOAA ORR, 2019). For the upper and lower Mississippi River, the sediment sizes range from silt to gravel, with the majority of the sediment distribution between ~0.125 mm to greater than 2 mm (Gaines & Priestas, 2013).

Three replicate sieve analyses were conducted to determine the particle size distribution (PSD) for substrates used in the experiments (Table 3-1) (ASTM, 2017b). Based on the Wentworth Grade Scale (Williams et al., 2006) and the median grain size, d_{50} (mm), the substrates were characterized as medium sand (referred to as sand), fine pebble, and medium pebble substrates. [N.B., Using particle size classification from Berenbrock & Tranmer, (2008) and Buffington & Montgomery, (1999) fine pebble and medium pebble can also be referred to as fine gravel and medium gravel].

Table 3-1: Sieve analysis showing the Particle Size Distribution (PSD) and Mean Texture Depth (MTD).

	Sediment Size and MTD (mm)		
	Sand	Fine Pebble	Medium Pebble
d_{10}	0.25	4.60	9.00
d_{25}	0.30	5.50	10.3
d_{50}	0.42	6.50	10.6
d_{84}	1.20	8.50	11.1
d_{90}	1.50	9.00	11.2
MTD	1.40	6.70	8.40

Substrates used in experimental trials were glued to 1.5 m long by 11.5 cm wide metal flashing using contact cement (DAP Products Inc, Baltimore, MD) and centered within the flume’s test segment (See Chapter 2). Macrotexture depth experiments (ASTM E965 – 15) were conducted to determine the mean texture depth (MTD) (ASTM, 2015b). MTDs for sand, fine pebble, and medium pebble were 1.4 mm, 6.7 mm, and 8.4 mm, respectively. The sand MTD can be represented by d_{90} , fine pebble by d_{50} , and medium pebble by d_{10} .

3.3.3 Hydraulic Conditions

3.3.3.1 Recirculating Flume

The oil CSS experiments were conducted in the MacFarlane Flume (Figure 3-1), a bottom to top recirculating flume, owned and operated by the Coastal Response Research Center (CRRC) at the University of New Hampshire (Durham, NH). [N.B., Flume dimensions are the only ones given in English units because that is how the flume was constructed]. The lower tank, 1 ft deep, 4 ft wide, and 16 ft long (30.5 m deep, 1.22 m wide, 4.88 m long), is enclosed on all four sides by acrylic panels. There are two openings in the bottom tank that connect to the upper channel, an entrance and exit, allowing water to be funneled vertically into the upper channel and recirculated back down to the lower tank. The upper channel (1 ft 10 inch deep, 1 ft wide, 13 ft long (55.3 cm

deep, 30.5 cm wide, 3.96 m long)), consists of an open top, acrylic sidewalls, and an acrylic base with zero slope.

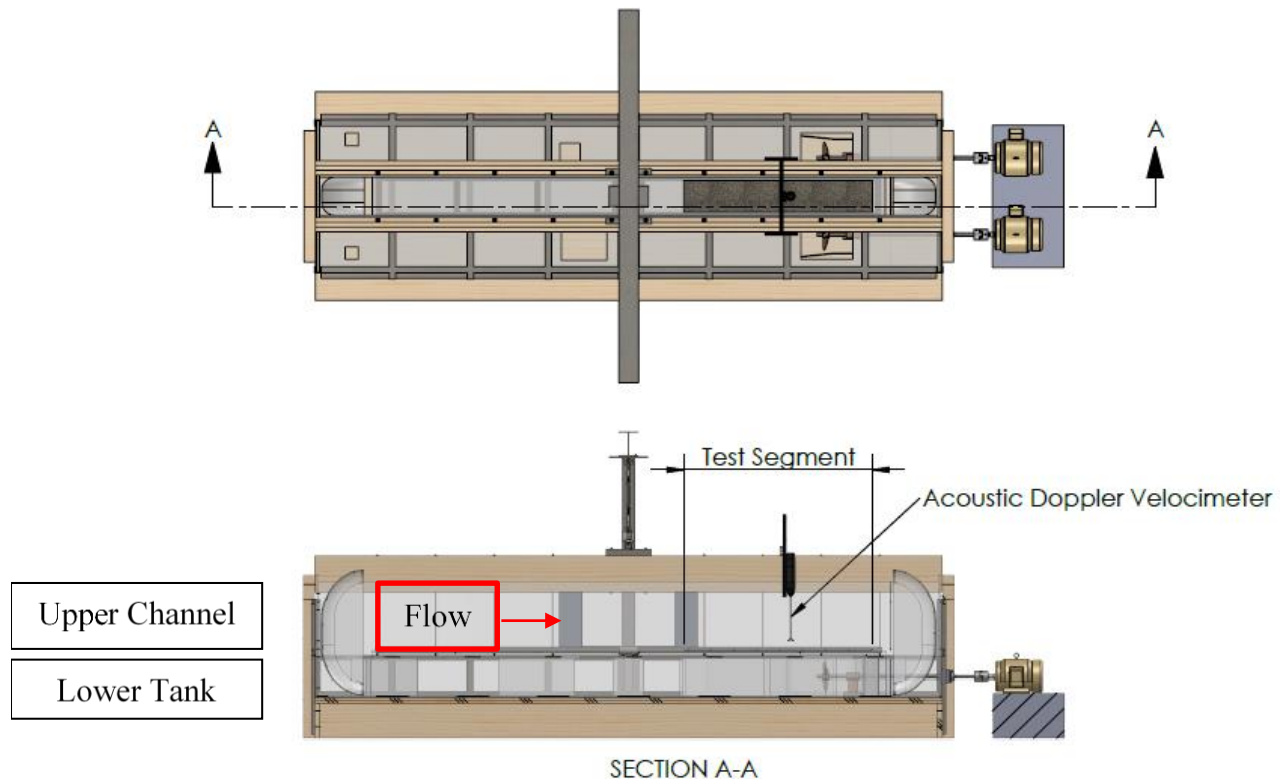


Figure 3-1: Plan view (top) and longitudinal section (bottom) of the MacFarlane Flume.

The water is propelled by two 10 3/8 inch (26.35 cm) propellers, housed in the lower tank, each driven by a 10 hp motor (ABB/Baldor Electric, Fort Smith, AR). Each motor is controlled independently by an ABB variable frequency drive (VFD). Precise motor control ensures experimental reproducibility with respect to *in-situ* flow conditions; at a working water depth (h) of 31 ± 1 cm, flow was considered to be uniform and at steady state for all experimental conditions (See Chapter 2).

3.3.3.2 Velocity Measurements

In-situ free-stream velocity, U (m/s) and depth-averaged velocity, \bar{U} (m/s) were correlated with VFD frequencies, x (Hz), following Eq. 3-2 and Eq. 3-3, respectively (See Chapter 2).

$$U = 0.0009x^2 + 0.0604x \quad \text{Eq. 3-2}$$

$$\bar{U} = 0.0594x \quad \text{Eq. 3-3}$$

where: Eq. 3-2 ($R^2 = 0.9992$) and Eq. 3-3 ($R^2 = 0.9986$) are applicable for $0 \text{ Hz} < x < 14 \text{ Hz}$.

The Vectrino Profiler II (Nortek Scientific; Vangroken, Norway), an acoustic Doppler velocimeter (ADV), measured the instantaneous longitudinal or stream-wise (x), transverse (y), and vertical (z) velocity components (u , v , and w , respectively). Average velocities were denoted using an overbar (e.g., \bar{u}) and fluctuations from the mean are denoted by an apostrophe (e.g., u'). The Vectrino sampled a 30 mm range at a spatial resolution of 1 mm; the sampling range began 40 mm below the center beam to avoid flow field interference (Nortek AS, 2017). The sampling duration for each trial was a minimum of 15 minutes using a sampling rate of 25 Hz (Babaeyan-Koopaei et al., 2002; Pope et al., 2006; van Rijn, 2007). Near-bed velocity measurements were captured 0 to 3 cm above the boundary, where z (cm) was the distance above the boundary. The Vectrino's "Ping Settings" (e.g., ping algorithm, velocity range) were adjusted for each trial based on water velocity and boundary conditions to minimize or eliminate weak spots and optimize the %Corr and SNR (Koca et al., 2017).

Data collected by the Vectrino was exported and evaluated using MatLab (MathWorks, Natick, MA). All raw velocity datasets underwent a two-step filtering process as recommended by the manufacturer. First, the data quality based on %Corr and SNR (using a low pass filter) was evaluated. To maintain the length of the time-series, data points below %Corr < 70 or SNR < 10 were replaced with "Not a Number" (NaN) (Biron et al., 2004). The second step applied a three

pass, despiking filter to each data set. With each pass, \bar{u} , \bar{v} , and \bar{w} , and the standard deviations, σ , were calculated at each sampling depth. Data exhibited a normal (Gaussian) distribution. Outliers were detected and replaced with NaN if outside $\bar{u} \pm 3\sigma_u$, $\bar{v} \pm 3\sigma_v$, and $\bar{w} \pm 3\sigma_w$.

3.3.3.3 BSS Calculations

BSS was calculated using a combination of local and global methods: (1) Turbulent Kinetic Energy (TKE), (2) Law of the Wall – Single Point, (3) Quadratic Friction Law, (4) the Momentum equation using the Chézy resistance coefficient (Chézy/Momentum), and (5) the Momentum equation using Manning’s roughness coefficient (Manning/Momentum). These methods were chosen based on their commonality among field and laboratory experiments, applicability to fluvial and marine current-driven environments, the diversity of necessary velocity measurements, and variability in calculating roughness coefficients. Multiple methods were selected to calculate BSS because the “best method will likely depend on the logistics of deploying field equipment, instrument availability and technical support”(Simecek-Beatty, 2007). Hence, modelers and responders will be able to compare *in-situ* BSS estimates with the CSS thresholds calculated regardless of technology limitations. [N.B., For further explanation as to why these methods were selected see Chapter 2]. For this dissertation research, the term BSS and τ_w were used when describing shear stress for all methods, even for methods evaluating shear stress some elevation (z) above the boundary where $0 \text{ cm} < z < 3 \text{ cm}$).

TKE

To calculate BSS (τ_w), the TKE method uses 3D velocity fluctuations (e.g., u' , v' , w') (Eq. 3-4 to Eq. 3-7).

$$u' = u - \bar{u} \quad \text{Eq. 3-4}$$

$$v' = v - \bar{v} \quad \text{Eq. 3-5}$$

$$w' = w - \bar{w} \quad \text{Eq. 3-6}$$

$$\tau_w = C \left[\frac{1}{2} \right] \rho_w (\overline{(u'^2)} + \overline{(v'^2)} + \overline{(w'^2)}) \quad \text{Eq. 3-7}$$

where: C, a fitting parameter valid for offshore oceanic conditions and rough-bed open channel flow, is 0.19 (Bagherimiyab & Lemmin, 2013; Biron et al., 2004; Pope et al., 2006; Soulsby, 1997; Stapleton & Huntley, 1995; Wren et al., 2017). The TKE method has been used to estimate τ_w in flume and field studies (e.g., riverine, estuarine) under simple and complex flow conditions (Biron et al., 2004; Kim et al., 2000; Nikora & Goring, 2000; Pope et al., 2006; Stapleton & Huntley, 1995). τ_w varies with height above the bed, experiencing a maximum at $0.1 \cdot h$ and decreasing until it reaches the boundary. All τ_w estimates obtained from this method were calculated at $z = 2$ to 3 cm (Bagherimiyab & Lemmin, 2013; Biron et al., 2004). TKE estimates of τ_w are limited by Doppler backscatter and the ADV sampling volume. Backscatter can be a result of increased Doppler noise from positive and negative buoyancy of particles in the sampling volume, small-scale turbulence, acoustic beam divergence, and boundary interference (Kim et al., 2000; Pope et al., 2006).

Law of Wall – Single Point

The single point velocity method, the vertically-averaged form of Law of the Wall, assumes a logarithmic velocity profile and requires information describing the sediment size (e.g., d_{84}) (Eq. 3-8) (Whiting & Dietrich, 1990).

$$\tau_w = \frac{\rho(\bar{u}_z * \kappa)^2}{\ln\left(\frac{10 * z}{d_{84}}\right)^2} \quad \text{Eq. 3-8}$$

where: $\kappa = 0.4$ and \bar{u}_z = average velocity (m/s) at z . This method has been successful in sand-bedded river bends (Dietrich & Smith, 1983) and gravel-bed channels (Whiting & Dietrich, 1990). d_{84} is representative of boundary features that dominate flow resistance because it accounts for the protrusion of larger grains into the flow field (Whiting & Dietrich, 1990). Depending on *in-situ* conditions, the single point average velocity must be based on a minimum sampling duration of 50-100 seconds, at measurements below a height of 2/10ths the flow depth and 2 cm above the bed of coarse sand or fine gravel bed for an immobile boundary (Whiting & Dietrich, 1990; Wilcock, 1996).

Quadratic Friction Law

The Quadratic Friction Law applies to current-driven environments with a steady, uniform, fully turbulent flow regime by quantifying the momentum dissipation due to bottom roughness (Eq. 3-9) (Pope et al., 2006; Soulsby, 1997; Wengrove et al., 2015).

$$\tau_w = \rho_w C_D \bar{U}^2 \quad \text{Eq. 3-9}$$

where: C_D = the drag coefficient (dimensionless). Accurately estimating C_D is challenging due to spatial variability of natural flow regimes and the presence of bed forms (Biron et al., 2004). In many cases, C_D is estimated using a constant value found in literature. For this dissertation, empirical relationships, derived from the velocity profile, used a fitted power-law function to calculate C_D based on the elevation above the bed where velocity goes to zero (z_o) (Eq. 3-10) (Soulsby, 1997).

$$C_D = \alpha \left(\frac{z_0}{h} \right)^\beta \quad \text{Eq. 3-10}$$

where: z_0 was derived from the Law of the Wall – logarithmic profile method, and α (0.0474) and β (1/3) are coefficients that change as a function of bottom substrate material, relative roughness, and bed mobility. α and β were selected based on the Manning-Strickler Law (Strickler, 1923) as it applies to open channel and pipe flow regimes with large relative roughness factors ($\frac{z_0}{h} > 10^{-4}$) (Mehaute & Hanes, 2005). For all experimental conditions in this dissertation research $\frac{z_0}{h} > 10^4$ and experiments were conducted in an open channel.

Chézy/Momentum

The Chézy/Momentum approach is the simplest method to calculate BSS, but it does not capture local, small-scale variations (Biron et al., 2004; Yen, 2002). Because U is the representative velocity component used in calculations, it is referred to as global predictor of BSS (Babaeyan-Koopaei et al., 2002; Yen, 2002). The force balance approach uses the Chézy resistance coefficient (C) to calculate BSS for a section of river with similar hydrologic conditions (i.e., reach-averaged BSS) (Eq. 3-11).

$$C = \sqrt{8g * \left[1.2 + 2.03 \log \left(\frac{R_h}{d_{84}} \right) \right]^2} \quad \text{Eq. 3-11}$$

where R_h = hydraulic radius; R_h is calculated from the channel's cross-sectional area (A) and wetted perimeter (P_w) using $R_h = \frac{A}{P_w}$. This method is generally applied to open channel flow (e.g., rivers, streams) under steady, uniform, and non-uniform hydraulic conditions. C was estimated using an empirical relationship, originally developed to calculate the Darcy-Weisbach friction factor, f , by relating d_{84} and R_h (Elger et al., 2013; Leopold & Wolman, 1957; Limerinos, 1970).

Eq. 3-11 was modified to directly calculate C , from $C = \sqrt{\frac{8g}{f}}$ (Chaudhry, 2008; Elger et al., 2013).

For the purpose of this dissertation research, the slope of the energy grade line or friction slope, S_f , was used because it applies to uniform and non-uniform conditions (Eq. 3-12).

$$S_f = \frac{\left(\frac{U}{C}\right)^2}{R_h} \quad \text{Eq. 3-12}$$

τ_w was calculated by substituting Eq. 3-12 into Eq. 3-13 and multiplying by the specific weight of water, γ_w (N/m³).

$$\tau_w = \gamma_w R_h S_f \quad \text{Eq. 3-13}$$

Manning/Momentum

The Manning formula is commonly used to estimate stream flow, velocity, or friction slope in open channels (Yen, 2002). For this research, U was known and the Manning formula was used to calculate S_f for uniform, steady state conditions (Eq. 3-14) (Limerinos, 1970).

$$S_f = \left(\frac{U * n}{R_h^{2/3}}\right)^2 \quad \text{Eq. 3-14}$$

where: n = Manning's roughness parameter quantifies friction and form losses and varies with water discharge and bed material size (U.S. Army Corp of Engineers, 1993). n has commonly been used to represent cross-sectional and reach resistance coefficients (Yen, 2002). Seven methods were used to estimate n based upon the PSD. Of the seven estimates, the median value was selected for use in BSS calculations (see Appendix A.5: Estimating Manning's n). τ_w was calculated by substituting Eq. 3-14 into Eq. 3-13.

3.3.4 Oil CSS Experiments

Experiments were designed using the JMP 15 statistical software (SAS Institute; Cary, NC) to create a randomized, custom design that captured potential interaction between the main and quadratic effects (Table 3-2). Additionally, four replicates and three center points were included in the design as indicators of reproducibility, and to identify experimental variability between oil CSS thresholds under identical conditions. Because the oil was a non-Newtonian fluid, and viscosity changes with temperature, the temperature center points were included in the experimental design to document any curvature in the measured responses (i.e., to highlight temperatures' non-linear influence on viscosity). The experimental design for this research was developed so that results could be compared to Cloutier et al. (2002) which used a step-wise increase in velocity by ~0.07 m/s intervals.

Table 3-2: Summary of experimental conditions.

Trial Number	Oil Condition	Water Temperature (°C)	Boundary Type
1 ^a	Fresh Oil+Clay	8.6	Sand
2 ^a	Fresh Oil+Clay	9.9	Sand
3 ^b	Fresh Oil+Clay	24	Sand
4 ^b	Fresh Oil+Clay	25	Sand
5 [*]	Weathered Oil+Clay	7.2	Sand
6 ⁺	Weathered Oil+Clay	10	Sand
7	Weathered Oil+Clay	17	Sand
8	Weathered Oil+Clay	24	Sand
9 ^c	Fresh Oil+Clay	10	Fine Pebble
10 ^c	Fresh Oil+Clay	10	Fine Pebble
11	Fresh Oil+Clay	25	Fine Pebble
12	Weathered Oil+Clay	10	Fine Pebble
13	Weathered Oil+Clay	18	Fine Pebble
14	Weathered Oil+Clay	25	Fine Pebble
15	Fresh Oil+Clay	9.5	Medium Pebble
16	Fresh Oil+Clay	18	Medium Pebble
17	Fresh Oil+Clay	22	Medium Pebble
18	Weathered Oil+Clay	11	Medium Pebble
19 ^d	Weathered Oil+Clay	25	Medium Pebble
20 ^d	Weathered Oil+Clay	25	Medium Pebble

^{a,b,c,d} Replicate experiments

^{*} Water temperature was below experimental setting of $10 \pm 1.5^\circ\text{C}$ and therefore trial was redone (Trial 6), however, results from Trial 5 were retained and analyzed in the results.

⁺ Trial 5 redo.

Prior to each experiment, residual oil was removed from the upper channel using CitraSolve (Citra Solve, LLC; Danbury, CT), followed by liquid Dawn dish soap (Procter & Gamble; Cincinnati, OH), and rinsed using warm tap water. The upper channel and test segment were dried and disinfected using rubbing alcohol. Prior to filling the flume with water, the substrate was centered within the test segment and adhered to the bottom. As the flume filled with water, the temperature was adjusted based on the experimental condition, and GoPro cameras and the Vectrino were secured into place and tested. *In-situ* water temperature was held constant ($\pm 1^\circ\text{C}$) for the duration of each experiment. The oil was then added (99 ± 6 g) into quiescent water via subsurface injection. The actual oil mass applied to the substrate was determined

gravimetrically by weighing the syringe used before and after injection. Based on the oil mass injected and the substrate type, the diameter of the SOP ranged between 10 cm and 13 cm, classifying this experimental oil as an oily SOP (Gustitus & Clement, 2017).

The water remained at zero velocity for a minimum of two minutes. It was then increased to the lowest velocity setting ($U = 0.06 \pm 0.01$ m/s). The velocity was held constant for 15 minutes and then increased step-wise by 0.08 ± 0.02 m/s until: (1) all of the oil had eroded from the substrate, or (2) a maximum velocity of 1.04 m/s was reached. An overhead flashing light was used to indicate that the velocity was being increased to the next interval; this allowed the overhead and side-view video recordings to be synchronized during data post-processing. Once the velocity was increased and the test segment reached steady state (~15 seconds), the Vectrino began measuring instantaneous velocity; velocity measurements were then used to calculate *in-situ* BSS.

The video recordings and photographs were compiled and edited using Adobe Premiere Pro and Adobe Photoshop, respectively. Two responses were measured to evaluate the SOP's movement: (1) the number of oil droplets or pieces of oil (type II erosions) that broke away from the SOP, and (2) spreading of oil along the bottom (i.e., SOP footprint). Cloutier et al. (2002) characterized oil droplets which detached from oil stranded on their flume base as type II erosions. They defined the CSS threshold as “the threshold velocity under which visual deformation and erosion of the [oil's] surface take place”. After compiling the videos for each experimental trial, the number of type II erosions were counted for each velocity interval. In this research, type II erosions were counted when they left the field of view of both cameras.

The spreading distance along the bottom was quantified using overhead and side-view images of the oil at the end of each velocity interval. The area of substrate covered by the oil's footprint was measured using Adobe Photoshop's pixel count and converted to cm^2 using an *in-*

situ scale. Additionally, the oil's dimensions (e.g., length, width, thickness) were measured at the end of each velocity interval.

3.4 Results

Laboratory experiments were conducted to measure the physical parameters of the experimental oil (i.e., ρ_o, μ_o), and the substrates' boundary roughness was characterized by a sieve analysis and MTD experiments. A series of flume-based experiments (20 trials) were conducted over a range of environmental conditions (i.e., water velocity, water temperature, sediment size) to determine the oil's CSS. Instantaneous, 3D velocity measurements were collected using the Vectrino and used to calculate τ_w using five methods. Side-view and overhead video recordings captured the oil's behavior. Videos were compiled and correlated to each velocity interval; videos and images were used to define the thresholds of oil movement. The SOP's CSS thresholds were determined based on the thresholds of movement and *in-situ* τ_w estimates.

3.4.1 Viscosity Analysis

The measured viscosity values of FC and WC oil samples collected using the Wells-Brookfield viscometer (number of replicates at each test condition, n=2 to 3), were plotted with respect to temperature (Figure 3-2) (Appendix B.1: Fresh & Weathered Brookfield Viscosity).

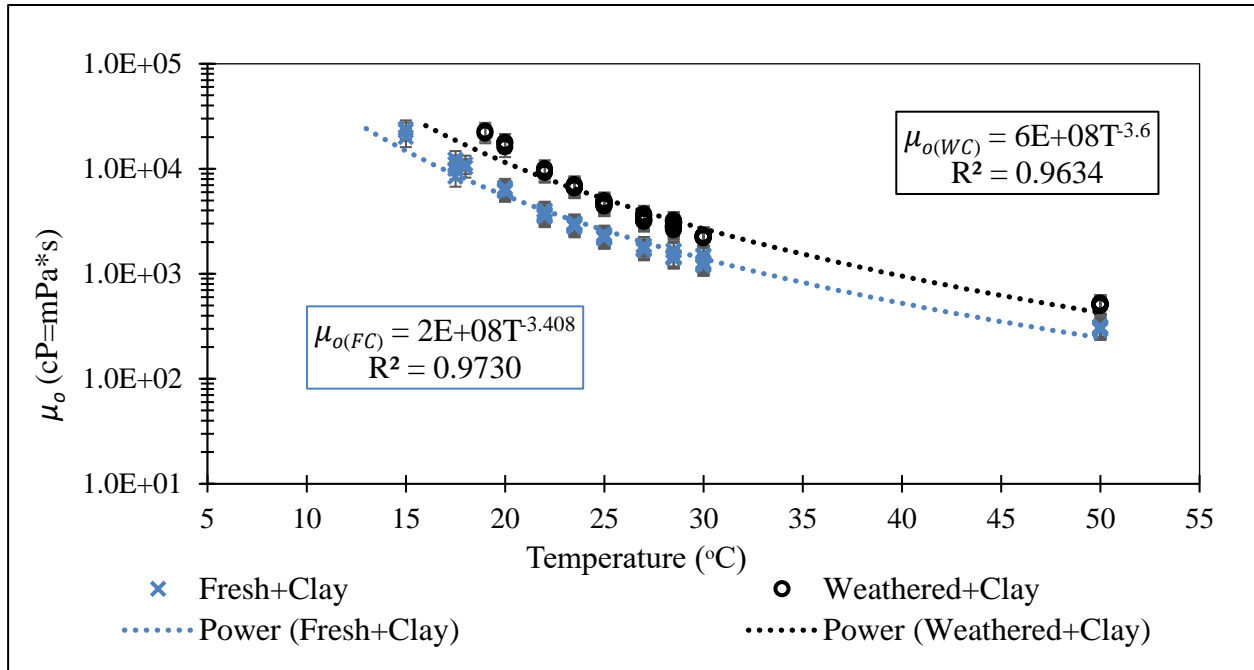


Figure 3-2: Wells-Brookfield viscosity measurements for FC and WC oil.

Two fitted relationships were developed based on $\bar{\mu}_{o(FC)}$ and $\bar{\mu}_{o(WC)}$ (mPa*s = cP) to predict viscosities outside the working range of the instrument for FC oil < 15°C (Eq. 3-15; $R^2=0.9730$) and WC oil < 19°C (Eq. 3-16; $R^2=0.9634$).

$$\bar{\mu}_{o(FC)} = 2E + 8(T)^{-3.408} \quad \text{Eq. 3-15}$$

$$\bar{\mu}_{o(WC)} = 6E + 8(T)^{-3.6} \quad \text{Eq. 3-16}$$

where: T = temperature (°C) and Eq. 3-15 and Eq. 3-16 apply for $5^\circ\text{C} < T < 50^\circ\text{C}$. This relationship was verified with measurements made using the DHR for $T < 10^\circ\text{C}$ (Appendix B.2: DHR and Brookfield Viscosity). HFO is a viscoelastic material which exhibits shear-thinning behavior, a decrease in viscosity as shear rate increases, for temperatures $< 50^\circ\text{C}$. The DHR viscosity measurements showed exacerbated effects at lower temperatures ($< 18^\circ\text{C}$). Weathered oils have a higher viscosity than their fresh counterparts, this has been document in many spill responses (e.g., Enbridge Line 6b) (USEPA, 2016), observed through laboratory experiments (Environment

Canada, 2013), and modeled (Etkin et al., 2007). As expected, the WC oil samples were more viscous at all temperatures when compared with those of FC.

The variability associated with the Wells-Brookfield viscosity measurements, from which the fitted equation was calculated, was evaluated using JMP statistical software's variability/attribute gauge chart. The viscoelastic material exhibited different viscosities based on the applied shear rate at a single temperature, thus creating a spread in viscosity data with respect to temperature. Results from the variability analyses indicated that sampling variability increased as temperature decreased and quantified the associated σ along with other statistical parameters (e.g., 95% confidence interval). The highest RSD based on these results was 20%, henceforth, error bars associated with viscosity were set to 20% (Appendix B.3: Wells-Brookfield Viscosity Variability).

v_o (cSt) was calculated over the experimental temperature range using the measured ρ_o and μ_o , where $v_o = \left(\frac{\mu_o}{\rho_o}\right)$ (Figure 3-3). Responders can estimate if a floating oil has the potential to form SOM's based on the v_o . Typically, estimate an upper and lower limit of SOM formation at 10,000 cSt and 100,000 cSt, respectively (Michel & Bambach, 2020). Based on the thresholds identified by Michel & Bambach (2020), SOM formation for the HFO in this research would most likely occur in water temperatures between 10°C and 17.5±0.5°C.

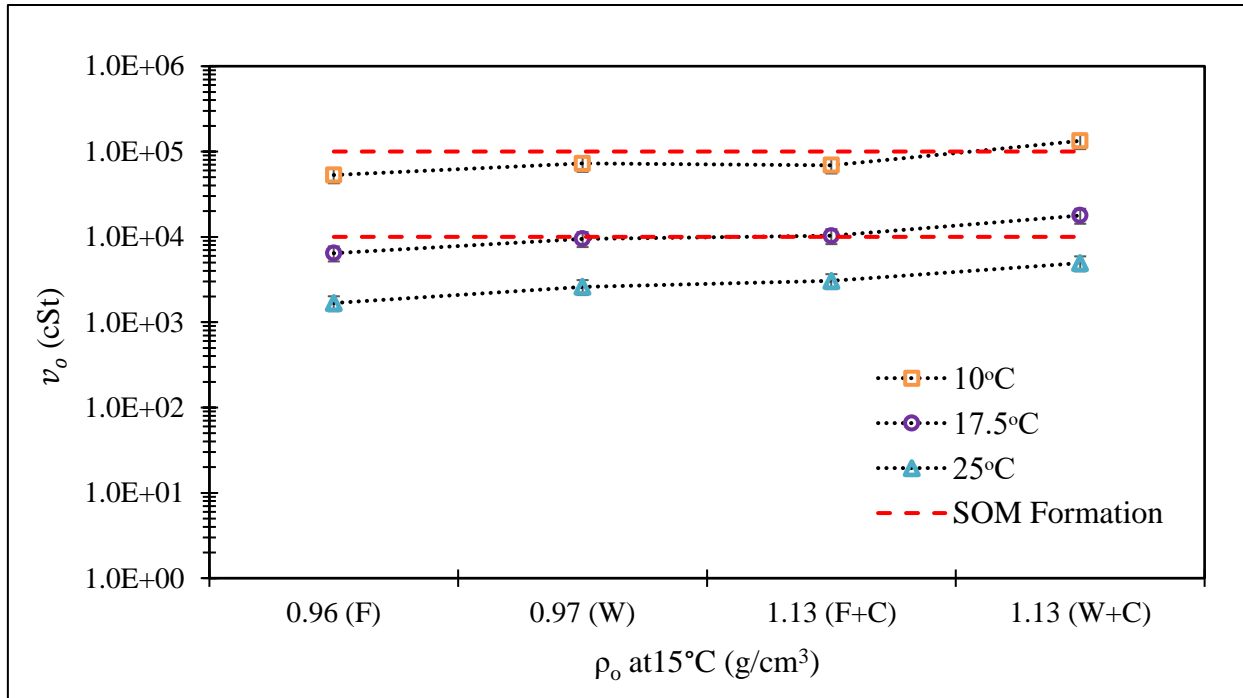


Figure 3-3: Formation of SOP based ρ_o and v_o for all oil conditions and experimental temperature range.

3.4.2 Oil CSS Experiments

3.4.2.1 Defining Thresholds of Oil Movement

The criteria describing the oil's CSS thresholds was developed based on the measured responses, spreading of the oil, number of type II erosions, and SOP dimensions (i.e., width, length, thickness). To characterize the thresholds of movement and quantify the corresponding critical velocity, the overhead and side view area measurements and number of type II erosions were plotted with respect to U . The criteria describing the thresholds of movement was defined based on observations from this research, the literature, and historic spill events. The thresholds of movement were different for cold water trials (i.e., $10 \pm 1.5^\circ\text{C}$) compared with warmer water trials (i.e., $>17.5 \pm 0.5^\circ\text{C}$). $10 \pm 1.5^\circ\text{C}$ tests often exhibited a single threshold of movement that

transported a majority of oil at one time (Figure 3-4) (Appendix B.4: Plots of Measured Responses).

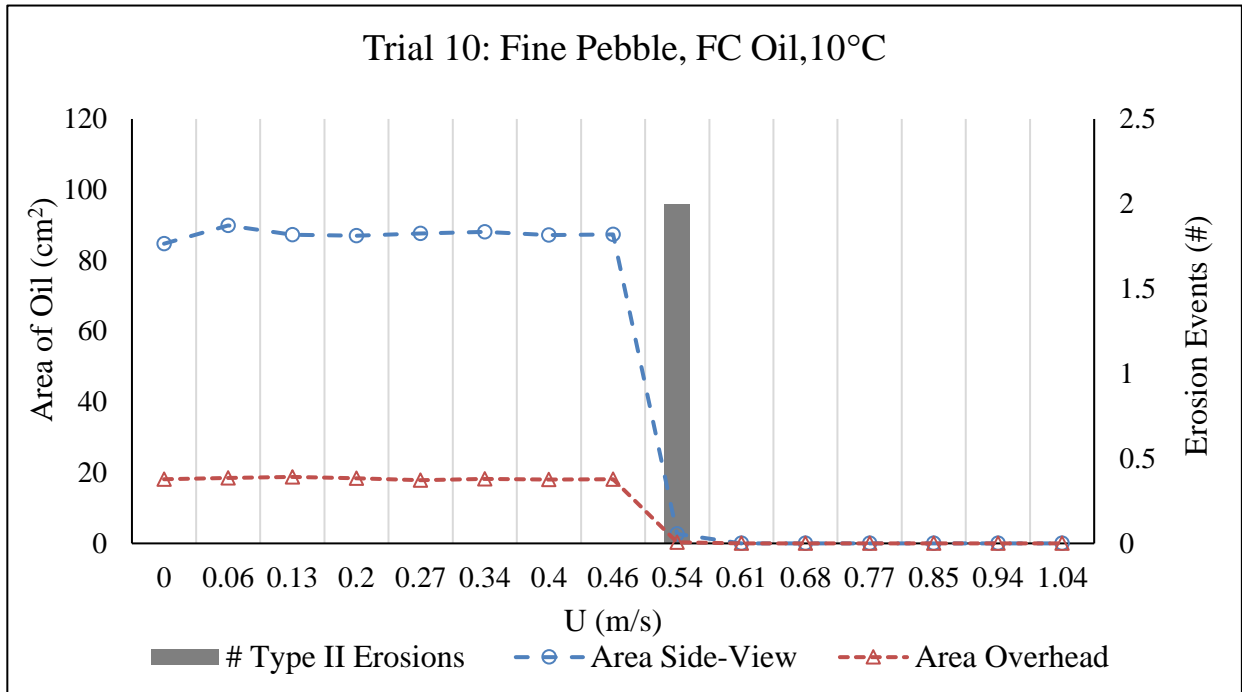


Figure 3-4: Area of oil and number of erosions for FC oil on fine pebble substrate at 10°C.

Figure 3-4 is representative of most $10 \pm 1.5^\circ\text{C}$ trials, with the area of the SOP remaining constant, and suddenly decreasing to zero at a corresponding erosion event. That particular trial had a total of two erosion events that took place at $U=0.54$ m/s: one was a small droplet or piece of oil that occurred just prior to the second where the remaining SOP left the substrate. In all nine cold water trials, a type II erosion that resuspended a piece or droplet of oil occurred before a significant portion of the SOP mobilized. For eight of the nine trials, the type II erosion was driven by current velocity, whereas in one trial, the type II erosion happened just after the oil was injected at zero velocity. By referring to the area measurements, a distinction could be made between the type II erosion threshold and an erosion event which caused the entire SOP to mobilize. Based on trends identified after plotting the measured responses, two thresholds of oil transport were defined for cold water trials: (1) type II erosions, and (2) bedload transport (Table 3-3). SOP bedload

transport was established as a single event that transported a significant portion or the entire SOP. The SOP, which remained intact rather than breaking into small pieces, bounced along the bottom. For trials where the type II erosion event and bedload transport threshold occurred at different velocities, the SOP bedload transport threshold could be differentiated from a type II erosion event that removed a single droplet or small piece of oil by an immediate decline in the oil's area on the substrate.

Table 3-3: Criteria of oil CSS threshold for $v_o > 6 \times 10^4$ cSt. [N.B., The $v_o > 6 \times 10^4$ cSt threshold is based on experimental data and future experiments should be conducted to resolve these ranges as the criteria may apply to a broader viscosity range].

Applicable for $v_o > 6 \times 10^4$ cSt: A single threshold event often results in substantial mass transport.			
Threshold	What would happen in the field	Dominant force affecting the oil (resulting transport process)	CSS threshold determined by assessing SOP length (X), width (Y), area measurements, and number of erosions from overhead and side view images and videos).
Type II Erosions	Oil at the water's surface, oil droplets in the water column, or oil droplets lodged in pore spaces.	Buoyancy or water velocity (oil pieces/droplets transport as bedload or suspended load)	Any piece of oil or oil droplet leaving the SOP due to buoyancy or water velocity.
Bedload Transport	Majority of SOP no longer present on the substrate; remnants of oil may be visible on sediments. Segmentation of SOP into smaller pieces, with droplets stuck in pore spaces on the bed or transporting with water currents.	Water velocity (SOP bedload transport)	Identified by a reduction in oil area due to mass loss (i.e., reduction in area and corresponding spike in erosion events).

A higher number of type II erosion events occurred in the $>17.5\pm 0.5^\circ\text{C}$ trials than in the $10\pm 1.5^\circ\text{C}$ counterpart (Figure 3-5). [N.B., Erosion event (#) axis scale is different than Figure 3-4].

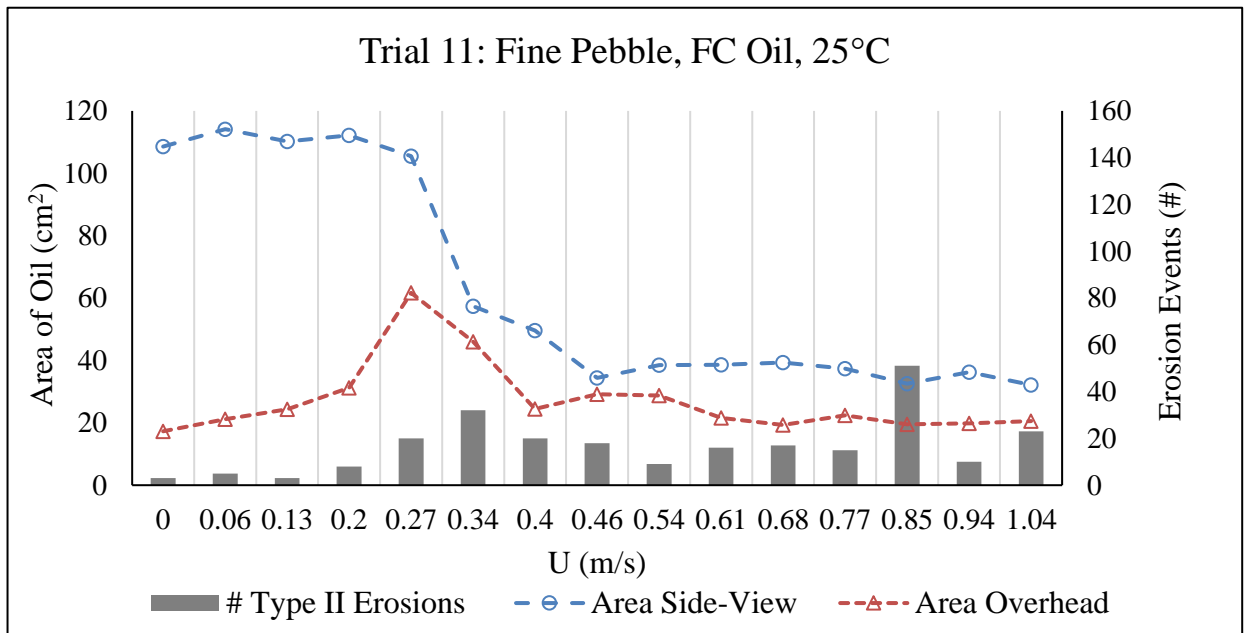


Figure 3-5: Area of oil and number of erosions for FC oil on fine pebble substrate at 25°C.

This particular trial had 250 cumulative type II erosions, with a maximum number of erosions (51) occurring at $U = 0.85$ m/s. Unlike the $10\pm 1.5^\circ\text{C}$ trials, type II erosions occurred in all 11 warm water trials when $U = 0$ m/s. In general, the number of type II erosion events increased as temperature increased for all substrate sizes. Based on the fact that type II erosions occurred in all of the warm water trials in stagnant water, this threshold of movement will not be displayed in future plots.

For the fine pebble, 25°C, FC trial, the side view area remained constant, while the overhead increased to a maximum, until both area measurements simultaneously declined when $U = 0.34$ m/s. This pattern was common for most warm water experiments on sand and fine pebble substrates, whereas on medium pebble substrates, the peak was less distinct and area measurements often declined as velocity increased. For sand and fine pebble substrates, the area of oil increased with increasing velocity until it reached a peak; the side view maximum generally occurred at a

velocity interval before the overhead area maximum. Once the maximum was reached, the trend was similar to that for the medium pebble, and area declined as velocity increased.

The thresholds of movement for warm water trials were divided into three categories: (1) gravity spreading, (2) advective spreading (i.e., migration along the bed), and (3) SOP break-apart/resuspension (Table 3-4). Using the width and length measurements collected from the overhead camera, gravity spreading was classified by proportional spreading in the x - and y -dimensions. Gravity spreading on the sand and fine pebble substrates for FC occurred when $U < 0.06$ m/s and for WC at $U < 0.13$ m/s. On the medium pebble substrate, gravity spreading occurred at $U < 0.20$ m/s and $U < 0.13$ m/s for FC and WC, respectively. Advective spreading was divided into two subcategories, a lower threshold classified as rope formation (Figure 3-6) and an upper threshold termed ripple formation (Figure 3-7).



Figure 3-6: Rope formation (red box) at $U=0.13$ m/s during Trial 4 (FC oil, 25°C, sand).



Figure 3-7: Ripple formation (red arrows) at $U=0.27$ m/s during Trial 8 (WC oil, 24°C, sand).

Rope formation was characterized using the length and width dimensions, and the overhead and side view area measurements. Preliminary rope formation coincided with a slight increase in oil area followed by a rapid increase in either the width or length of the SOP. On sand and fine pebble, rope formation was readily observable by an increase in the width, while the length remained constant or decreased. On the medium pebble substrate, the length increased, while the width remained constant. Ripple formation was identified by oil waves developing at the downstream side of the SOP which proceeded to propagate down its length causing oil to actively migrate in the direction of flow. Ripple formation was first identified when reviewing the video recordings and later confirmed by the side view and overhead area measurements. Formation of oil waves led to the elongation of the SOP which often corresponded with a rapid increase or peak in area or length measurements.

The SOP break-apart/resuspension threshold was identified by a peak in type II erosion (Figure 3-8) events that corresponded with a decline in oil area. This threshold was confirmed by comparing images of the oil at the end of each velocity interval. The SOP was deemed “broken apart” if the SOP was no longer present on the substrate or was not a continuous mass. It would

be challenging for responders to recover the broken-apart/resuspended SOP. With the exception of FC oil on sand at 25°C, as velocity increased the oil continued to fragment and break into smaller droplets. Type II erosions that took place at low velocities ($U < 0.13$ m/s) occurred randomly throughout the SOP footprint. Type II erosions that occurred as a consequence of advective spreading, separated from the leading edge of the SOP.



Figure 3-8: Type II erosion (red circle) at $U=0.2$ m/s during Trial 17 (FC oil, 22°C, medium pebble).

Table 3-4: Criteria of oil CSS thresholds for $v_o < 2 \times 10^4$ cSt. [N.B., The $v_o < 2 \times 10^4$ cSt threshold is based on experimental data and future experiments should be conducted to resolve these ranges as the criteria may apply to a broader viscosity range].

Applicable for $v_o < 2 \times 10^4$ cSt: SOP transports in multiple stages.			
Threshold	What would happen in the field?	Dominant force affecting the oil (resulting transport process)	CSS threshold determined by assessing SOP length (X), width (Y), area measurements, and number of erosions from overhead and side view images and videos).
Gravity Spreading	Length and width of SOP increase proportionally.	Gravity (an increase in SOP diameter)	Used overhead images at the end of each velocity interval to measure the length and width of SOP.
Rope Formation	On sand and fine pebble, the width of SOP is greater than the length (beginning of oil rope formation). On medium pebble, length increasing at faster rate than the width.	Water velocity (bedload transport)	Width > length or length > width using overhead measurements; SOP does not spread against the current.
Ripple Formation	Oil ripples developing on top surface of the SOP. Migrating ripples drive SOP to lengthen in the direction of flow along the bed.	Water velocity (suspended load transport & bedload transport)	Ripples developed in the downstream side of the footprint and migrate the length of the SOP. Ripple formation drives oil lengthening and causes type II erosions from leading edge of SOP.
Type II Erosions	Surface oiling, oil droplets in the water column, or oil droplets lodged in pore spaces.	Buoyancy or water velocity (oil pieces/droplets transport as bedload or suspended load)	Any piece of oil or oil droplet leaving the SOP due to buoyancy or water velocity.
Break-Apart/Resuspension	Majority of SOP no longer present on the substrate; remnants of oil may be visible on sediments. Segmentation of SOP into smaller pieces, with droplets stuck in pore spaces on the bed or transporting with water currents.	Water velocity (SOP bedload transport)	Identified by a reduction in oil area due to mass loss (i.e., reduction in area and corresponding spike in erosion events).

For low velocity erosions, the oil droplets tended to rise to the surface, whereas erosions coinciding with advective spreading remained suspended in the water column. Unlike the $10\pm 1.5^\circ\text{C}$ trials, in warm water conditions the SOP did not remain intact at the break-apart/resuspension threshold, but rather fragmented into many droplets which then became: (1) lodged in pore spaces on the substrate, (2) saltated along the bed, or (3) suspended into the water column.

The pattern of erosion events as velocity increased differed with respect to substrate size for water temperatures $>17.5\pm 0.5^\circ\text{C}$. On the sand substrate, the number of erosions increased with velocity until it reached a peak and then declined as velocity continued to increase. For fine pebble experiments, erosion events increased with respect to increasing velocity until reaching a maximum and plateaued around that value even as velocity continued to increase. For medium pebble, erosion events reached local maxima, but steadily increased as velocity increased. For all medium pebble trials, the highest number of erosions occurred when $U > 0.94$ m/s. For rougher substrates, some oil stayed within pore spaces at high velocities ($U \sim 1.04$ m/s), thus providing a continuous source of oil droplets to the environment.

Regardless of boundary type, for trials with water temperatures $>17.5\pm 0.5^\circ\text{C}$, the side view areas tended to peak at a velocity interval below the overhead areas. This occurred because the oil's thickness reached a maximum value at a lower velocity than the length. This suggested that the oil gets thicker before it lengthens.

3.4.2.2 Converting Critical Velocity to CSS

Once the critical thresholds were defined, the corresponding critical velocity interval was determined and used to calculate CSS based on the *in-situ* hydraulic and boundary conditions specific to each trial. Over the 15 minute period for each velocity interval, the arithmetic average

of BSS ($\overline{\tau_w}$) was calculated using the five approaches (See Section 3.3.3.3 BSS Calculations) (Figure 3-9).

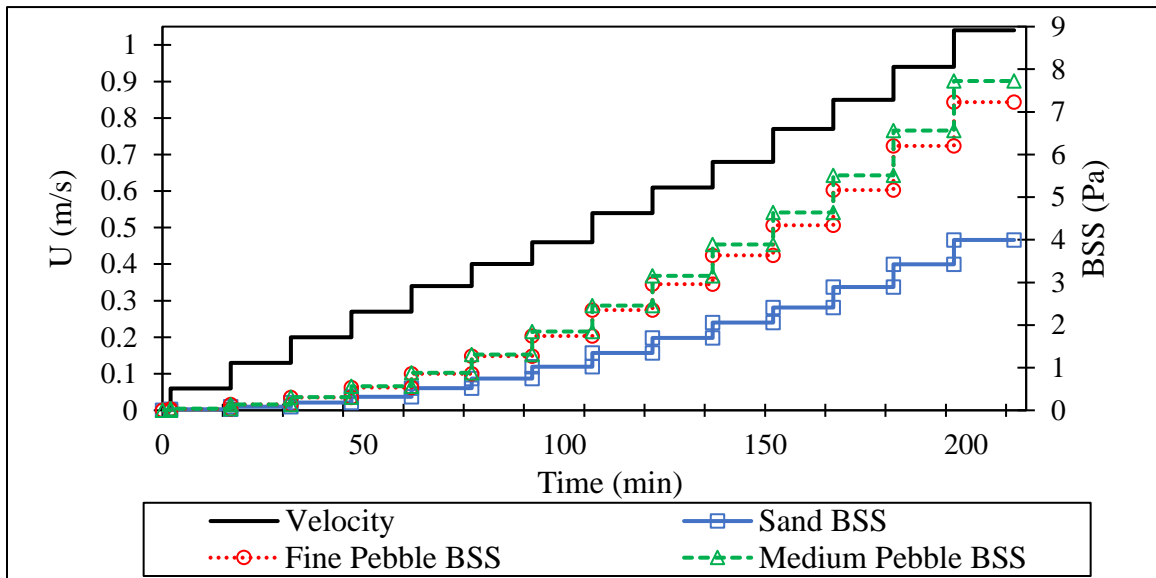


Figure 3-9: Relation between velocity (m/s) and average BSS (Pa) on sand, fine pebble, and medium pebble substrates.

The CSS values for all applicable thresholds are summarized for the 20 trials (Table 3-5). In the event of an HFO spill, modelers could select the oil CSS threshold(s), determined from this research, that represent *in-situ* spill conditions, to predict the transport of the sunken oil. The primary factors driving the oil's thresholds of movement were evaluated for rope formation, ripple formation, and SOP break-apart/resuspension using the standard least squares model in the JMP statistical software. SOP break-apart and SOP bedload transport (SOP break-apart/resuspension) were evaluated together because both thresholds were based on the underlying assumption that the SOP was no longer recoverable in the location where it was initially stranded. Based on model outputs, d_{50} was identified as a statistically significant parameter for the model (i.e., $p < 0.05$) when predicting rope formation, ripple formation, and SOP break-apart/resuspension. Additionally, the $\log(v_o)$ was significant for the model for ripple formation and SOP break-apart/resuspension.

Table 3-5: Summary of results for all of the oil CSS experimental trials.

Trial Number	Sediment d_{50} (mm)	Water Temperature ($^{\circ}$ C)	Oil Kinematic Viscosity (cSt)	Gravity Spreading CSS (Pa)	Rope Formation CSS (Pa)	Ripple Formation CSS (Pa)	Type II Erosion CSS (Pa)	Break-Apart/Resuspension CSS (Pa)
1	0.42	8.6	115,018	-	-	-	0.34 \pm 0.11	1.4 \pm 0.41
2	0.42	9.9	70,952	-	-	-	1.0 \pm 0.17	1.0 \pm 0.17
3	0.42	24	3,773	0.02 \pm 0.01	0.09 \pm 0.03	0.19 \pm 0.07	0.02 \pm 0.01	0.19 \pm 0.07
4	0.42	25	3,206	0.02 \pm 0.01	0.08 \pm 0.03	0.19 \pm 0.04	0.02 \pm 0.01	0.19 \pm 0.04
5	0.42	7.2	431,742	-	-	-	0.33 \pm 0.12	1.3 \pm 0.43
6	0.42	10	132,662	-	-	-	0.08 \pm 0.02	0.53 \pm 0.1
7	0.42	17	18,001	0.08 \pm 0.03	0.18 \pm 0.06	0.31 \pm 0.12	0.02 \pm 0.01	0.48 \pm 0.2
8	0.42	24	6,159	0.07 \pm 0.03	0.18 \pm 0.04	0.26 \pm 0.07	0.02 \pm 0.004	0.52 \pm 0.11
9	6.5	10	63,058	-	-	-	1.7 \pm 0.5	1.7 \pm 0.5
10	6.5	10	62,024	-	-	-	2.3 \pm 0.65	2.3 \pm 0.65
11	6.5	25	3,058	0.03 \pm 0.01	0.03 \pm 0.01	0.49 \pm 0.16	0.03 \pm 0.01	0.53 \pm 0.12
12	6.5	10	113,269	-	-	-	0.83 \pm 0.21	1.6 \pm 0.46
13	6.5	18	15,481	0.14 \pm 0.03	0.32 \pm 0.07	0.88 \pm 0.21	0.04 \pm 0.01	1.4 \pm 0.25
14	6.5	25	4,761	0.03 \pm 0.02	0.13 \pm 0.03	0.82 \pm 0.22	0.03 \pm 0.02	1.3 \pm 0.3
15	10.5	9.5	83,095	-	-	-	3.8 \pm 1.21	11 \pm 3.39
16	10.5	18	9,524	0.17 \pm 0.03	0.66 \pm 0.11	1.0 \pm 0.2	0.04 \pm 0.01	2.0 \pm 0.48
17	10.5	22	4,629	0.28 \pm 0.1	0.53 \pm 0.16	0.77 \pm 0.34	0.03 \pm 0.02	1.3 \pm 0.37
18	10.5	11	105,816	-	-	-	0.89 \pm 0.35	8.0 \pm 4.2
19	10.5	25	4,969	0.11 \pm 0.08	0.55 \pm 0.17	0.84 \pm 0.34	0.03 \pm 0.02	2.3 \pm 0.8
20	10.5	25	4,898	0.14 \pm 0.05	0.53 \pm 0.22	0.93 \pm 0.26	0.04 \pm 0.01	2.5 \pm 0.81

Based on these findings, the oil's CSS thresholds were plotted with respect to v_o for experiments conducted on sand (Figure 3-10), fine pebble (Figure 3-11), and medium pebble (Figure 3-12) substrates. The horizontal error bars represent the 20% RSD associated with viscosity measurements. The vertical error bars correspond to $\overline{\tau_w} \pm \sigma_{\overline{\tau_w}}$. Dalyander et al. (2015) noted the importance of burial and exhumation processes influencing the fate and behavior of SOPs which can take place within the order of 10 minutes. Based on their finding and because sediments were glued to the boundary in this dissertation research, a range of sediment CSS thresholds corresponding to the substrate's PSD, were plotted to compare sediment mobility with oil mobility (Berenbrock & Tranmer, 2008). The fitted relationships and associated R^2 for each of the thresholds in Figure 3-10 to Figure 3-12 are summarized in Table 3-6.

For experiments conducted $>17.5 \pm 0.5^\circ\text{C}$, CSS progressively increased from gravity spreading to rope formation, ripple formation, and break-apart thresholds. Regardless of substrate type, trials conducted at $24 \pm 2^\circ\text{C}$ had the smallest CSS for rope formation, ripple formation, and break-apart/resuspension thresholds. Additionally, CSS thresholds increased as water temperature decreased. Out of the 20 trials, two trials (replicates) conducted on the sand substrate using FC oil at $24 \pm 2^\circ\text{C}$ had the same CSS for ripple formation and break-apart/resuspension thresholds. The thresholds of movement, especially for rope formation, were most clearly observable on the sand substrate, and became less distinct as substrate size increased.

Regardless of substrate type, the highest CSS value that initiated SOP break-apart/resuspension was not observed for the most viscous oil. For the sand substrate, CSS was largest for $v_o \sim 115,000$ cSt (maximum $v_o = 431,724$ cSt). For fine pebble, it occurred at $v_o \sim 62,000$ cSt (maximum $v_o = 113,269$ cSt). On medium pebble it was at $v_o \sim 83,000$ cSt (maximum

$\nu_o = 105,816$ cSt). The results from this research identified the factors significant to predicting oil CSS thresholds are ν_o and d_{50} .

For the medium pebble at 9.5°C with FC oil, the SOP did not partially or fully mobilize at the CSS; this was the only case where the majority of the SOP remained on the substrate for $U = 1.04$ m/s. The WC trial under the same experimental conditions, did exhibit SOP bedload transport at $U = 1.04$ m/s. To capture the increased CSS for the FC trial, the FC CSS was represented in the results as the upper BSS threshold when $U = 1.04$ m/s (i.e., $\overline{\tau_w} \pm \sigma_{\overline{\tau_w}} = 11$ Pa). Further research should be conducted to determine the true CSS value for this experimental condition (i.e., FC oil, at $10 \pm 1.5^\circ\text{C}$, medium pebble).

The lines of best fit correlated fairly well with data ($R^2 > 0.6467$) (Table 3-6) except for the medium pebble, gravity spreading threshold ($R^2 = 0.0180$) which showed a decline in CSS with increasing viscosity and may be a result of the oil filling in pore spaces rather than spreading (Figure 3-12). This decline suggests that the slightly less viscous oils required a higher threshold of movement as they tended to fill in the open pore spaces and be shielded from the flow field by the medium sized pebbles. Polynomial equations were initially used to describe the fine pebble and medium pebble break-apart/resuspension thresholds as it had a better fit and captured the non-linear nature of transport due to the shear-thinning fluid. However, if a ν_o outside of the experimental data range was used, the predicted CSS became a negative value which is not probable. Therefore, the natural log equations were selected to reflect the anticipated transport patterns more accurately.

For water temperatures of $10 \pm 1.5^\circ\text{C}$, the thresholds of movement no longer followed the gravity spreading \rightarrow rope formation \rightarrow ripple formation \rightarrow break-apart/resuspension pattern (i.e., the validity of the fitted equations failed for gravity spreading, rope formation, and ripple

formation when $\nu_o > 2 \times 10^4$ cSt). Based on the experimental conditions and results, the break-apart/resuspension fitted equations were valid for $\nu_o < 431,000$ cSt on sand, $\nu_o < 115,000$ cSt on fine pebble, and $\nu_o < 106,000$ cSt for medium pebble.

The oil CSS values were converted to the corresponding dimensionless shear stress (*Oil* τ^*) and grain Reynolds number (*Oil* Re^*) using Eq. 3-17 and Eq. 3-18, respectively. These values were then plotted for the gravity spreading, rope formation, ripple formation, and break-apart/resuspension thresholds in the form of a Shield's Curve (Figure 3-13).

$$Oil \tau^* = \frac{\overline{\tau_w}}{g(\rho_o - \rho_w)d_{50}} \quad \text{Eq. 3-17}$$

$$Oil Re^* = \frac{u_w^* d_{50}}{\nu_o} \quad \text{Eq. 3-18}$$

where: $\overline{\tau_w}$ = threshold BSS for oil transport (i.e., oil CSS) (Pa), g = gravity (m/s^2), ρ_o = oil density (kg/m^3), d_{50} = median grain size (m), u_w^* = friction velocity (m/s) using $u_w^* = \sqrt{\frac{\overline{\tau_w}}{\rho_w}}$, and ν_o = kinematic viscosity of oil (m^2/s).

Figure 3-13 is analogous to a sediment Shield's Curve in that each threshold is represented by a fitted line that corresponds to a threshold of movement. When values fall above the threshold line then that threshold has been exceeded and oil transport was likely initiated. Alternatively, when values fall below the line, that transport threshold has not been reached.

ν_o is the fundamental parameter controlling *Oil* Re^* and $\overline{\tau_w}$ is the primary value driving *Oil* τ^* . Smaller *Oil* Re^* values represent cold water experiments (i.e., higher oil viscosity) and larger *Oil* Re^* values indicate warmer trials (i.e., lower oil viscosity). The larger *Oil* τ^* associated with the smaller *Oil* Re^* suggests that more viscous oils require larger oil CSS values to achieve that transport threshold. The equations shown in Figure 3-13 are valid only within the experimental range from this research, $3 \times 10^{-5} < Oil Re^* < 10^{-1}$ and $3 \times 10^{-3} < Oil \tau^* < 10^1$.

As would be expected, the stages are staggered with gravity spreading requiring the lowest $Oil \tau^*$, followed by rope formation, ripple formation, and the largest $Oil \tau^*$ required for break-apart/resuspension. The break-apart/resuspension fitted equation diverges from the data points as $Oil Re^*$ approaches 10^{-1} . This divergence was likely due to the influence of sediment size on oil CSS and the type of equation selected to represent this threshold. As with the other curves and associated equations, further research should be conducted to refine these relationships, especially towards the edge of the validity range, as they are representative of one oil type on an immobile bed.

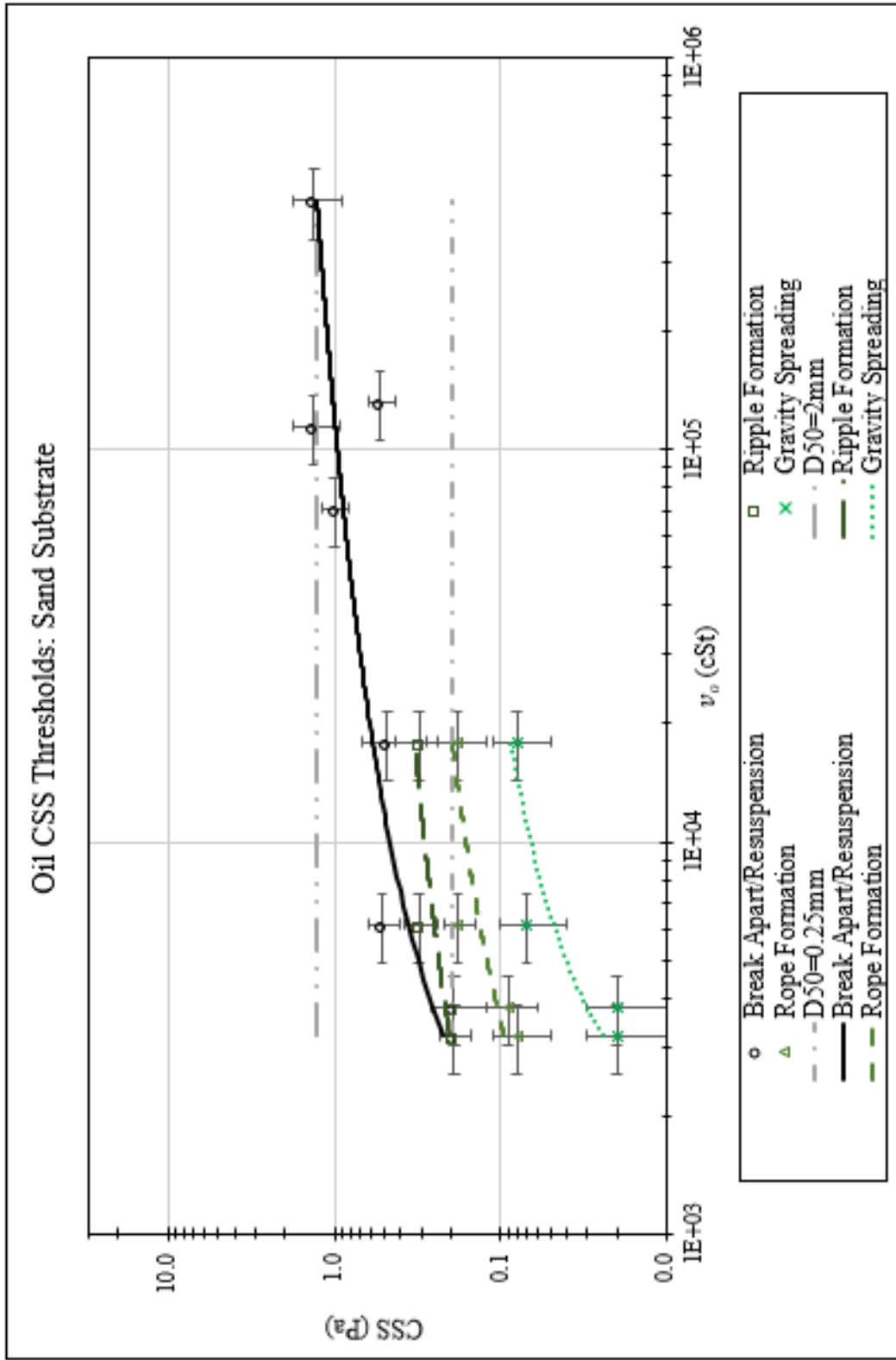


Figure 3-10: Gravity spreading, rope formation, ripple formation, and SOP break-apart/resuspension CSS thresholds and sediment CSS values on sand substrate.

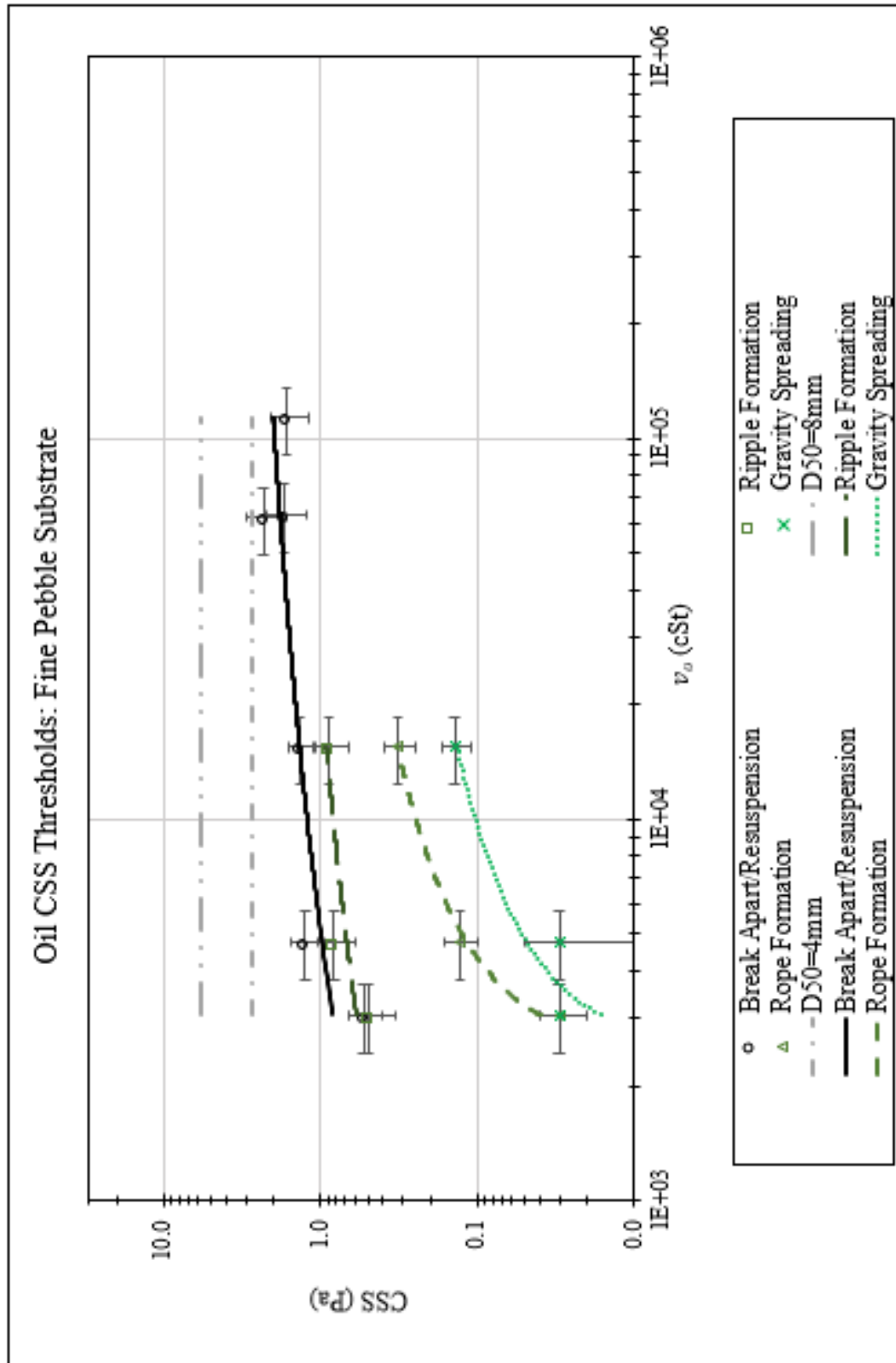


Figure 3-11: Gravity spreading, rope formation, ripple formation, and SOP break-apart/resuspension CSS thresholds and sediment CSS values on fine pebble substrate.

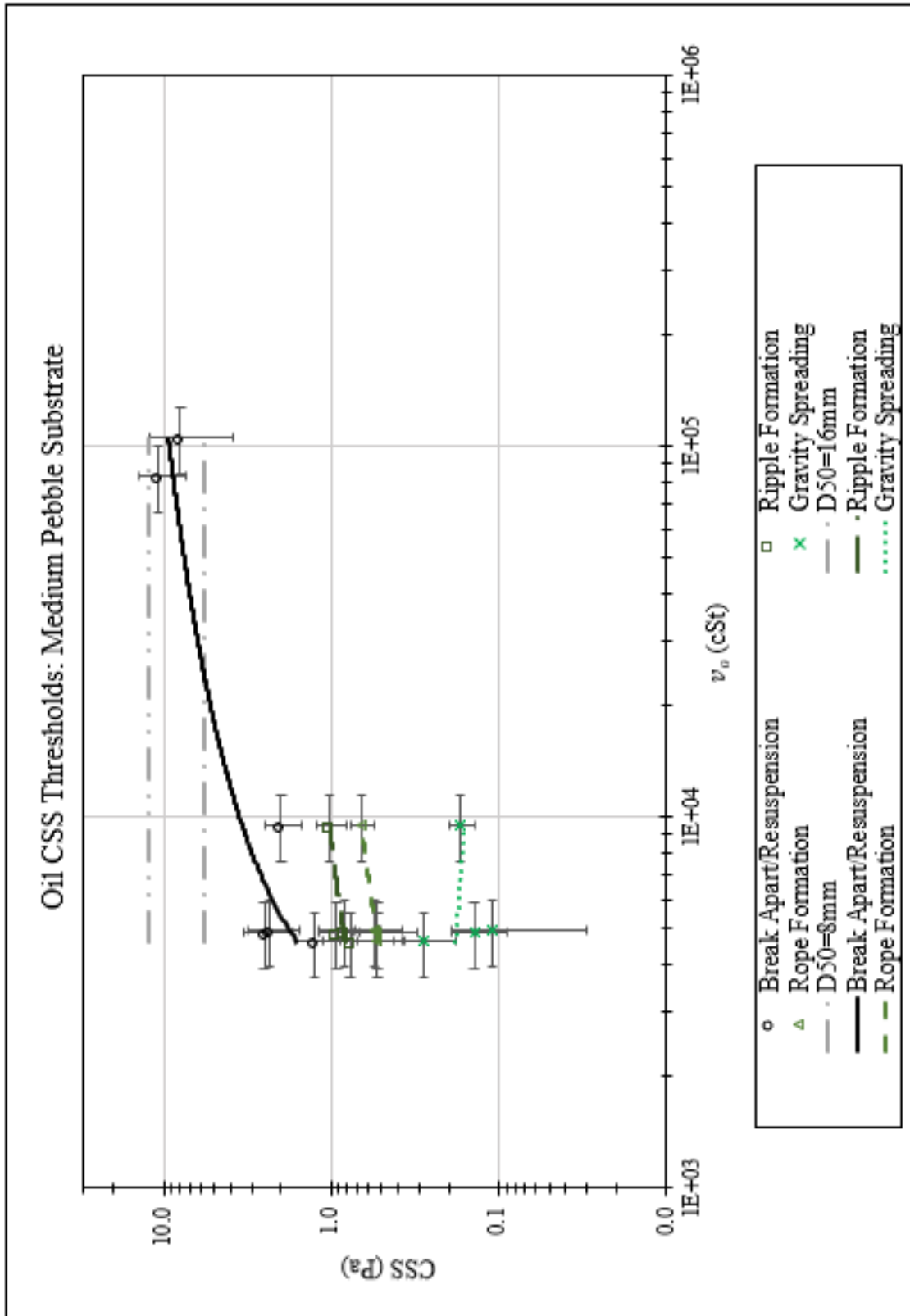


Figure 3-12: Gravity spreading, rope formation, ripple formation, and SOP break-apart/resuspension CSS thresholds and sediment CSS values on medium pebble substrate.

Table 3-6: Fitted equations for gravity spreading, rope formation, ripple formation, and SOP break-apart/resuspension CSS thresholds.

Threshold of Movement	Sand	Fine Pebble	Medium Pebble
Gravity Spreading	CSS = $0.0365\ln(v_o) - 0.2705$ $R^2 = 0.7871$	CSS = $0.0731\ln(v_o) - 0.57$ $R^2 = 0.9302$	CSS = $-0.029\ln(v_o) + 0.4277$ $R^2 = 0.0180$
Rope Formation	CSS = $0.0584\ln(v_o) - 0.3762$ $R^2 = 0.6826$	CSS = $0.1752\ln(v_o) - 1.3663$ $R^2 = 0.9938$	CSS = $0.1818\ln(v_o) - 1.0057$ $R^2 = 0.9869$
Ripple Formation	CSS = $0.0732\ln(v_o) - 0.3876$ $R^2 = 0.6759$	CSS = $0.2014\ln(v_o) - 1.0251$ $R^2 = 0.6467$	CSS = $0.2654\ln(v_o) - 1.4063$ $R^2 = 0.6934$
Break-Apart/Resuspension	CSS = $0.2153\ln(v_o) - 1.52$ $R^2 = 0.7211$	CSS = $0.3248\ln(v_o) - 1.7736$ $R^2 = 0.6745$	CSS = $2.503\ln(v_o) - 19.519$ $R^2 = 0.8839$

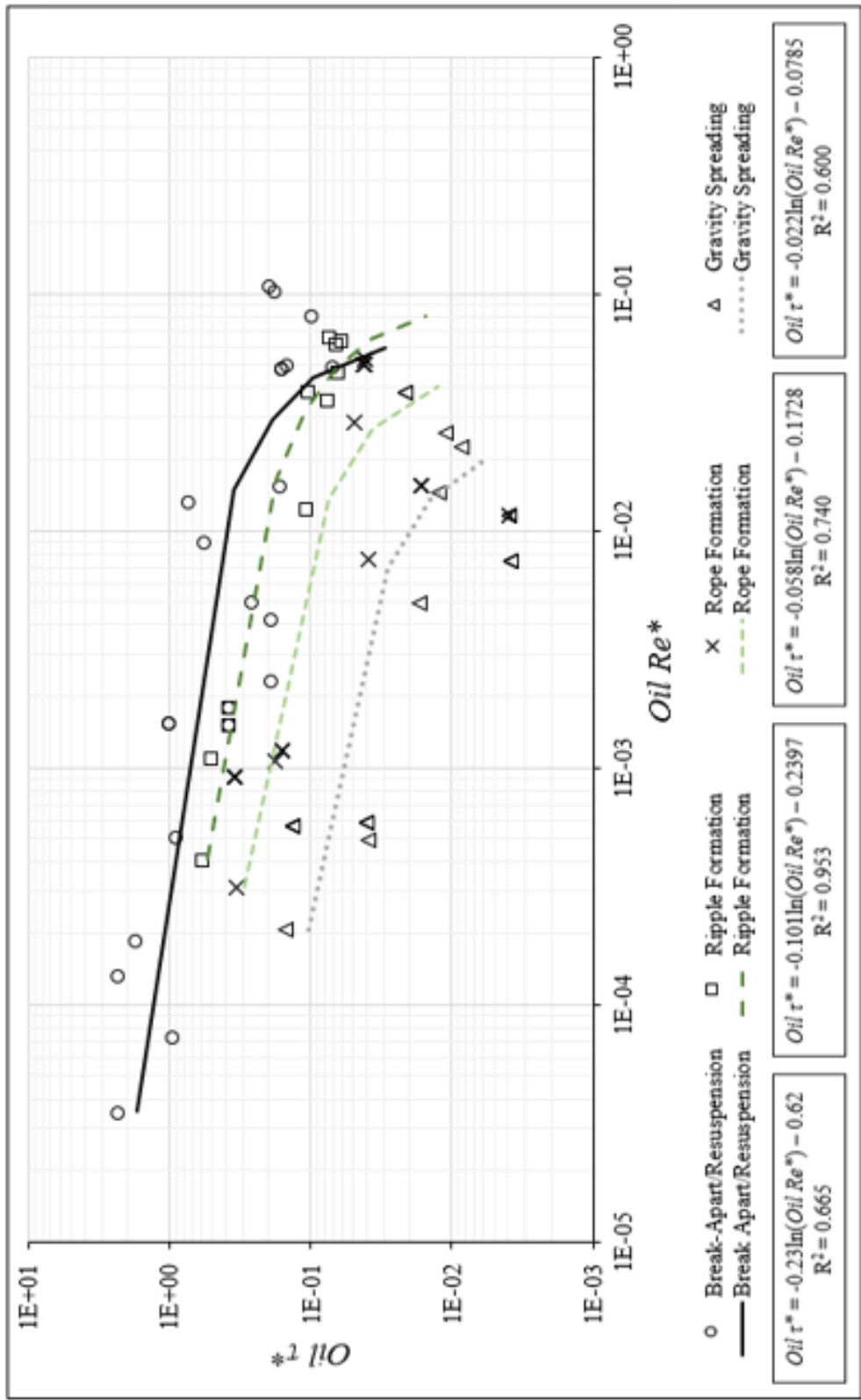


Figure 3-13: Results from the oil CSS experiments presented in the form of a Shield's Curve.

3.4.2.3 Experimental Variability

Based on the four replicates, experimental variability was higher for $10\pm 1.5^\circ\text{C}$ trials than trials with water temperatures $>17.5\pm 0.5^\circ\text{C}$. For example, FC oil on the sand substrate reached its CSS SOP break-apart/resuspension threshold at 1.4 ± 0.4 Pa and 1.0 ± 0.2 Pa. [N.B., The higher CSS threshold is associated with a slightly colder water temperature (e.g., 8.6°C vs. 9.9°C)]. This was expected because v_o is lower at a colder temperature, thus increasing the SOP's resistance to deformation. $24\pm 2^\circ\text{C}$ replicates on sand using FC oil, had CSS values of 0.2 ± 0.07 Pa and 0.2 ± 0.04 Pa; the temperature for one of the replicates was also slightly lower (i.e., 24°C vs. 25°C). Although the oil was completely eroded from the substrate by the end of the 0.20 m/s velocity interval for both replicates, fewer erosions occurred at $U < 0.20$ m/s and the SOP took longer to erode once at $U = 0.20$ m/s for the 24°C than the 25°C replicate.

$10\pm 1.5^\circ\text{C}$ replicates were conducted on the fine pebble substrate using FC oil. The SOP break-apart/resuspension thresholds occurred at 1.7 ± 0.5 Pa and 2.3 ± 0.7 Pa. The lower CSS threshold had a larger initial average oil thickness (h_o) of 1.6 cm compared with 1.3 cm. For the $24\pm 2^\circ\text{C}$ replicates on medium pebble substrate using WC oil, the CSS break-apart/resuspension thresholds were 2.33 ± 0.8 Pa and 2.51 ± 0.8 Pa. In this case, h_o was smaller (i.e., 0.9 cm vs. 1.2 cm) for the lower CSS threshold. h_o was not a statistically significant parameter for predicting oil CSS thresholds for the oil type, weathering state, quantity, and variables (e.g., temperature, water velocity) evaluated in these experiments.

3.5 Discussion

3.5.1 Oil CSS Experiments

The findings from this research suggest that the thresholds for oil movement should be defined differently when predicting the transport of sunken oils with high viscosity compared with low viscosity. Based on the experimental test conditions and oil type used, the viscosity threshold for oil transport of low and high viscosity oils was defined as $v_o < 18,000$ cSt and $v_o > 62,000$ cSt, respectively (herein referred to as $v_o < 2 \times 10^4$ cSt and $v_o > 6 \times 10^4$ cSt). When $v_o < 2 \times 10^4$ cSt, the SOP will likely be broken into multiple pieces and move in stages. For $v_o > 6 \times 10^4$, the SOP is likely to remain intact and erode all at once. Because no experiments were conducted on oil viscosities between the high and low viscosity threshold limits, future experiments should be conducted to resolve these ranges. The results also indicated that the oil's CSS increased as a function of bottom roughness. The substrate's d_{50} and v_o were statistically significant when predicting SOP movement.

In $10 \pm 1.5^\circ\text{C}$ trials, the lowest SOP bedload transport CSS (0.53 ± 0.1 Pa) occurred on the sand substrate with WC oil. The highest observed CSS (10.8 ± 3.4 Pa) occurred for FC oil on medium pebble substrate at 9.5°C . Because the SOP did not fully erode this suggests the CSS is likely > 11 Pa.

For $> 17.5 \pm 0.5^\circ\text{C}$ experiments, the lowest CSS for rope formation (0.08 ± 0.03 Pa) and SOP break-apart/resuspension (0.19 ± 0.04 Pa) occurred for FC oil at 24.7°C on sand. Initial SOP transport at 0.08 Pa corresponded to a critical velocity of 0.13 m/s; this value agreed with the 0.1 m/s threshold identified as sufficient for resuspending submerged oil in rivers (API, 2016b). Alternatively, the largest CSS values for rope formation (0.53 ± 0.22 Pa) and SOP break-apart/resuspension (2.5 ± 0.81 Pa) occurred for WC oil at 25.1°C on medium pebble substrate.

The experimental BSS range was chosen to represent as wide of a range as possible, while maintaining uniform, steady state conditions. Because BSS is highly dependent on current velocity which fluctuates in the natural environment (e.g., flood, storm conditions), a wide range of values is expected. Fluctuations in current velocity affects sediment transport mechanisms (e.g., suspended vs. bedload transport), the presence of bed forms, channel geometry, and boundary roughness (Berenbrock & Tranmer, 2008). For example, in the Great Bay Estuary (NH), a shallow estuary with muddy-sand sediments, the maximum BSS observed under non-storm conditions was 0.10 Pa, whereas in storm conditions it peaked at 0.58 Pa (Wengrove et al., 2015). In Solfatara Creek (Yellowstone National Park, WY), for a gravel bed channel (5.2 m wide, 0.4 m deep) the local BSS was mapped over a midchannel bar and values ranged between 0 to 10 Pa along a 20 m reach (Whiting & Dietrich, 1990). The potential environmental variability highlights the importance of determining *in-situ* sediment sizes, current velocities, and water temperatures throughout response and recovery operations to predict SOP transport.

3.5.2 Caveats to Research Findings

Because the sediments were adhered to the boundary, they could not transport, therefore subsequent contributions to BSS (e.g., form drag, suspended sediment interactions) were not considered (Soulsby, 1997). When applying this research to mobile boundaries, the contribution of form drag to and the effect of suspended sediment concentration on BSS should be considered. The CSS for sand, fine pebble, and medium pebble were approximately 0.29 Pa, 4.8 Pa, and 9.6 Pa, respectively. Because the oil remained submerged for the duration of each experimental trial, the thresholds can only be applied to submerged conditions (e.g., not an area exposed at low tide).

3.5.3 Factors Driving SOP Transport

3.5.3.1 Oil's Kinematic Viscosity

Based on experimental and model results, ν_o was identified as a statistically significant factor when predicting CSS thresholds for advective spreading and break-apart/resuspension. This result was expected because viscosity is a driving parameter when predicting droplet size distribution of floating oil slicks in turbulent conditions (Delvigne & Sweeney, 1988; Zhao et al., 2014), and a shoreline's capacity to retain oil (Etkin et al., 2007). Cloutier et al. (2002) credited the lack of type II erosions at 4°C to the increase in oil viscosity at cold temperatures.

Regardless of substrate type, the highest break-apart/resuspension CSS value was not associated with the most viscous oil or coldest temperature. For $10 \pm 1.5^\circ\text{C}$ trials, FC SOPs tended to have a higher SOP bedload transport CSS than their WC counterparts. Alternatively, for $>17.5 \pm 0.5^\circ\text{C}$ trials, WC SOPs had a higher SOP break-apart CSS than FC oil. This inflection may be attributed to the oil's shear-thinning properties, thus reducing the viscosity of oil at higher shear rates. Shear rate can be calculated from the rate of change in the velocity profile over the height for which velocity is measured. Higher current velocities generally result in higher shear rates. Based on the concept of shear thinning, at higher velocities the viscosity of oil may be reduced further. Because WC oil is more viscous than FC oil, the effect of shear-thinning may be exacerbated for warmer temperatures. The addition of clay to the fresh and weathered oil resulted in a more viscous oil. The weathered only had similar viscosities to the FC oil, whereas WC oil was more viscous than fresh oil, weathered oil, and FC oil.

The viscoelastic nature of heavy fuels is due to the complex compounds (e.g., asphaltenes, resins, wax crystals) present in the oil, and the temperature-dependent internal interaction of molecules (e.g., van der Waals, hydrogen bonding, π -stacking) (Abivin et al., 2012). Abivin et al.

(2012) also attributed the elastic tendencies at low temperatures to the reduction of thermal energy which draws the molecules together increasing the material's internal friction causing the oil to act as a solid rather than a liquid. For heavy oils, the asphaltene content has been used to predict the dynamic viscosity (Luo & Gu, 2007) and other viscoelastic properties using the Williams-Landel-Ferry model over a wide range of temperatures (Abivin et al., 2012).

3.5.3.2 Sediment Size

For all of the thresholds of movement, the substrate's d_{50} was a statistically significant parameter for predicting sunken oil transport. Experimental results showed that oil CSS thresholds increased with increasing boundary roughness (i.e., oil stranded on a sand stream bed would require a lower CSS than if stranded on a gravel bed under the same environmental conditions).

Burial and exhumation processes were evaluated by plotting the sediment's CSS with oil CSS. On sand, rope formation was initiated prior to sediment incipient motion ($d_{50}=0.25$ mm) for all trials with water temperature $>17.5\pm 0.5^\circ\text{C}$. At the warmest conditions ($\sim 25^\circ\text{C}$), the oil reached ripple formation and break-apart/resuspension thresholds before incipient motion began. This suggested that the SOP may move before being buried by the surrounding sand. Alternatively, because the oil CSS increased as oil viscosity increased, burial and exhumation processes should be considered an important factor on sand substrates when $\nu_o > 6 \times 10^3$ cSt.

For fine pebble experiments, all oil CSS thresholds were smaller than the corresponding sediment CSS thresholds ($d_{50}= 4$ mm). When oil CSS thresholds are compared to smaller sediment's CSS ($d_{50}= 0.25$ mm), incipient motion would begin before ripple formation or break-apart/resuspension CSS thresholds. Hence, burial and exhumation processes for the smaller sediment fraction would be important considerations when predicting the location of SOPs. A similar pattern is true for medium pebble substrates, however in this case, for all temperature

conditions, the rope formation threshold is larger than sediment CSS ($d_{50} = 0.25$ mm) by ~ 0.3 Pa. Although it may be inferred that the oil would not be buried by sediments in some of these cases, in the natural environment, sediment distribution is not uniform with smaller sediments co-occurring. If there is co-occurrence, the SOP may be covered by smaller sediments before it can erode, potentially burying it until a flood event remobilizes the smaller sediments.

In the case where sediments become mobile before the oil, the CSS thresholds determined in this research may underestimate the oil's CSS due to the SOP being buried or because SOP density increases as a result of sediments (i.e., silt, sand, clay) adhering. Alternatively, an unstable bed may result in premature oil mobility being driven by movement of surrounding sediments, thus initiating oil transport at lower CSS thresholds. In the case where an active layer of transport or bed forms exist, the shear stress components related to those processes should be considered. For example, Cloutier et al. (2002) found that oil erosion rates were highest at moderate suspended sediment concentrations (SSC) (200-250 mg/L), and that oil erosion rates decreased when SSC increased to >250 mg/L. It is recommended that further research be conducted to evaluate the effect of a mobile bed on oil CSS thresholds.

3.5.4 Comparison to Literature

Cloutier et al. (2002) is the only published research that evaluated the CSS of sunken oil in its fluid form; other oil CSS experiments have been conducted using aSOAs (Dalyander et al., 2015) and microscopic aggregates known as oil-particle aggregates (OPAs) (Hayter et al., 2015). Cloutier et al. (2002) used an annular flume to analyze the transport of weathered Hibernia Crude ($\mu_o \sim 4003$ mPa*s at 15°C) at 4°C and 13°C in clear sea water on a smooth (acrylic) boundary. Minor erosion thresholds (i.e., type I erosions (non-visible droplet formation or dissolution)) were determined by an increase in oil concentrations without visual erosion of the oil surface. Type II

erosions were defined using visual deformation of the slick, specifically by three types of movement: disturbance of the slick surface, ripple formation, and suspension of visible oil droplets. None of the Hibernia crude eroded even at the strongest current velocity (0.75 m/s) at 4°C, whereas, at 13°C, the type I erosions were observed at a CSS of 0.52 Pa to 1.88 Pa. Type II erosions occurred at a CSS of 5.0 Pa and critical velocity of 0.55 m/s. To adequately compare findings from this dissertation research and Cloutier et al. (2002) experimental trials conducted at for 24±2°C can be used because a similar viscosity to Hibernia crude was achieved for FC oil ($\mu_o \sim 4071$) at 23.8 °C and WC oil ($\mu_o \sim 4002$ mPa*s) at 27.4°C. Additionally, because water column concentrations of oil were not measured in this experiment, only the type II erosion threshold identified by Cloutier et al. (2002) can be compared.

The range of CSS values for ripple formation to SOP break-apart/resuspension thresholds on sand, fine pebble, and medium pebble occurred between 0.12–0.63 Pa, 0.33–1.55 Pa, and 0.43–3.32 Pa, respectively. FC/WC oil CSS ranges for all substrate types were well below the type II erosion threshold identified for Hibernia crude (5.0 Pa). This disparity between CSS thresholds for FC/WC No. 6 HFO and Hibernia crude may be attributed to a number of factors. First, Hibernia crude was injected into the flume before it was filled with water; this provided ample time for the oil to spread to a thickness of 2 mm. A thinner slick is less exposed to bulk flow; therefore, a higher critical velocity may be required to erode the oil. Secondly, Hibernia CSS was evaluated on an acrylic, smooth boundary, and because acrylic is derived from petroleum products, the oil has a higher propensity to stick to the acrylic bed compared with a sediment boundary. Cloutier et al. (2002) did address the limitations of using a smooth boundary, speculating that a reduced erosion rate was due to turbulence suppression, and that in the natural environment, “bed roughness would increase turbulence levels in the water column, therefore, enhancing

fluid/sediment interaction with the seabed and the erosion rates of oils”. The reduced CSS threshold identified in this research supports that statement, and therefore by conducting sunken oil transport experiments on an acrylic boundary, the CSS threshold may be inflated when compared with experiments on rougher (non-oleophilic) substrates.

Lastly, the configuration of the flume (annular vs. straight) or the methods used to calculate BSS could have contributed to the higher CSS threshold for a less viscous oil. As with sediment transport research, a major challenge is defining CSS thresholds consistently between research groups and using similar investigative methodologies so that research results can be compared (Buffington & Montgomery, 1997).

Findings from the aSOA CSS experiments (Dalyander et al., 2015) could only be qualitatively compared with results from this research because the Dalyander et al. (2015) experiments were in wave-dominated regimes on mobile sand substrates. They found that the smaller the aSOA, the lower the CSS required to mobilize it. Hence, when using the empirically-derived equations from this dissertation research to predict sunken oil transport in the field, it should be noted that an SOP < 10 cm may mobilize at a lower CSS than identified and an SOP larger than 13 cm may have a higher CSS range.

A short-coming of this dissertation research is the inability to determine how the oil and mobile sediment would interact. Further research should be conducted to evaluate the impacts of a mobile bed on oil CSS and how sediment mobility changes with the addition of oil.

3.6 Conclusions and Future Research

The CSS thresholds for fresh and weathered No. 6 HFO mixed with kaolinite clay (24% by weight, g oil: g clay) were determined under variable environmental conditions. By a series of laboratory- and flume-based experiments, historic spill events, and literature, criteria defining the

thresholds of movement were developed for 10 – 25°C that can be applied to sunken oil spills. In the event of a non-floating oil spill, where the spilled product sinks and strands on the bottom, results from this research could be used to inform response operations.

The major findings from this research are: (1) oil kinematic viscosity (ν_o) and the median grain size (d_{50}) are two measurable parameters that can be used to predict oil CSS; (2) oil CSS increases as d_{50} increases; (3) for $\nu_o < 2 \times 10^4$ cSt, there are multiple thresholds of movement and the number of visible oil droplets leaving the SOP increases; and (4) for $\nu_o > 6 \times 10^4$ cSt, transport is more likely to occur as a single event with the SOP remaining intact. Using these CSS thresholds and the factors driving SOP transport, an Excel-based tool was developed (See Chapter 4) so that responders can input environmental conditions (i.e., water temperature, water velocity, sediment type) and properties of the spilled product (i.e., oil viscosity, oil density) to predict if the environmental conditions are sufficient to initiate rope formation, ripple formation, break-apart/resuspension thresholds and to compare SOP transport with sediment mobility.

A limitation of this research was conducting experiments on an immobile bed (i.e., glued substrate). Therefore, future research should be conducted on mobile boundaries (i.e., non-glued substrate) to determine the relationship between oil and sediment mobility and evaluate sediment uptake or adherence of sediments by the SOPs. Experiments should be performed in cohesive sediments and mixed beds to determine how the size class of sediments controls CSS thresholds. Although this research can be used to represent No. 6 HFO/Bunker C sunken oils, a wider range of oil's (i.e., with different viscosities and densities) should be tested under cold and warm water conditions. Regardless of the approach, an oil's physical properties (e.g., density, viscosity) should be measured over the range of experimental conditions because temperature controls many of the physical properties important to predicting its fate and transport.

CHAPTER 4

SUNKEN OIL TRANSPORT TOOL

4.1 Abstract

The multi-year process of developing a prototype sunken oil transport tool (SOTT) is described in this paper including : (1) discussions between the Coastal Response Research Center (CRRC) and the National Oceanic and Atmospheric Administration's (NOAA) Office of Response and Restoration (OR&R) regarding responders' needs, (2) development and structure of the SOTT, (3) algorithms and relationships used in the SOTT, and (4) application of the SOTT to the Enbridge Line 6b (i.e., Kalamazoo River) spill as a case study. The SOTT was developed from experimentally-derived oil transport equations using sunken No. 6 heavy fuel oil mixed with kaolinite clay, and is valid for current-driven flow regimes with uniform, steady state conditions. The SOTT allows responders to input *in-situ* environmental conditions and properties of the spilled oil to predict if oil could transport along the bed, be resuspended into the water column, or be buried by sediments. Findings from the case study suggest that this tool provides an estimate of sunken oil transport that could be used to assist response operations during a sunken oil spill.

4.2 Introduction

Following two major non-floating oil spill events, the 2004 (*Athos I*) and 2005 (*Tank/Barge DBL-152*), the National Oceanic and Atmospheric Administration's (NOAA) Office of Response and Restoration (OR&R) and the Coastal Response Research Center (CRRC) partnered to host a workshop focused on non-floating oil spill response. Specifically, workshop participants discussed the state-of-practice, challenges and knowledge gaps associated with non-floating oil spill response. Non-floating oil was defined as submerged oil (i.e., neutrally buoyant oil in the water column) or sunken oil (i.e., negatively buoyant oil that sinks to the bottom) (CRRC, 2007). Over the past 13 years, CRRC has funded research projects to improve sunken oil modeling (Englehardt et al., 2010); built two flumes specifically designed to study the transport of sunken oil (Gloekler et al., 2017; Watkins, 2015) and optimize detection techniques for non-floating oils (Verfaillie et al., 2021); and performed flume studies to support OR&R's response during a 2015 slurry oil spill in the Mississippi River (*Apex 3508*) (NOAA, 2015).

In 2017, based on the research needs identified by the U.S. Interagency Coordinating Committee on Oil Pollution Research (ICCOPR, 2015), OR&R and CRRC shifted their focus from flume-based experiments on smooth boundaries to the effect of boundary roughness and sediment dynamics on sunken oil transport. Based on multiple discussions with OR&R, CRRC proposed a series of laboratory- and flume-based experiments to determine: (1) what factors control sunken oil transport, (2) under what *in-situ* environmental conditions sunken oil will resuspend or move along the bottom in a current-driven flow regime, and (3) the critical shear stress (CSS) associated with an oil's stages of transport.

The research on No. 6 heavy fuel oil (HFO) was divided into three phases: (1) a benchtop analysis of the oil's properties (density and viscosity) and sensitivity analysis to evaluate the relative importance of the input parameters on bed shear stress (BSS) estimates; (2) flume

experiments to evaluate the transport as a function of bottom roughness, water velocity, water temperature, and oil condition; and (3) development of a tool that can be used by oil spill responders to predict whether *in-situ* conditions are sufficient to mobilize sunken oil.

The first phase was necessary to establish oil density-temperature and oil viscosity-temperature relationships and characterize the particle size distribution (PSD) of the three substrates used in the second experiments. That phase quantified the applied BSS, the frictional force exerted by the fluid on the boundary (i.e., force per area), that would mobilize the sunken oil (i.e., the CSS). The oil's CSS was significantly influenced by the oil's kinematic viscosity and substrate sediment median grain size (d_{50}), and the stages of transport were different in cold water (e.g., $<11^\circ$) and warmer water (e.g., $>17.5^\circ$). Using the empirically-derived relationships, a sunken oil transport tool (SOTT) was developed. A reference curve was created and a catalogue of images was compiled from the No. 6 HFO CSS experiments as supplemental information (Appendix C.1: Catalogue of Sunken Oil Images).

The prototype SOTT does not replace complex trajectory models (e.g., NOAA's GNOME, RPS OILMAP/SIMAP) as it uses one-dimensional current information and was only calibrated from mesoscale experiments. For more detailed descriptions of sunken oil nomenclature, behavior, available response technologies, and model descriptions see recent publications by API (2016), Gustitus & Clement (2017), Jacketti et al. (2020), and Michel & Bambach (2020).

This paper describes the: (1) discussions between CRRC and OR&R regarding responders' needs, (2) development of the SOTT, (3) algorithms and relationships used in the SOTT, and (4) application of the SOTT using the Enbridge Line 6b (i.e., Kalamazoo River) spill as a case study.

4.3 Methods: Tool Development

4.3.1 Stakeholder Engagement

In June 2020, the results of the BSS/CSS flume studies with No.6 HFO were presented to OR&R's scientific support coordinators, modelers, and assessment and restoration (ARD) experts, so that the research could be leveraged into an operational tool. From this discussion, multiple types of response- and recovery-oriented questions to be answered by the SOTT were defined:

1. What are the clean-up termination endpoints?
2. Will the sunken oil remain as a continuous mat or break into smaller pieces?
3. Where should responders look for the sunken oil?
4. What field data can responders provide to modelers to inform decision-making?
5. Will the sunken oil be buried and exhumed over time?

In coordination with the USCG Region 1 NOAA scientific support coordinator, the stages of oil transport were outlined and criteria defining the oil's thresholds of movement, using language specific to spill response, were developed from observations during the oil CSS flume experiments. The criteria were different for oil kinematic viscosities (ν_o) $>6 \times 10^4$ cSt (Table 4-1) compared to $\nu_o < 2 \times 10^4$ cSt (Table 4-2) environments. [N.B., For a more detailed explanation of how the thresholds were defined, see Chapter 3].

Images of type II erosions (Figure 4-1a), rope formation (Figure 4-1b), and ripple formation (Figure 4-1c) are shown along with a more detailed Catalogue of Sunken Oil Images in Appendix C.1.

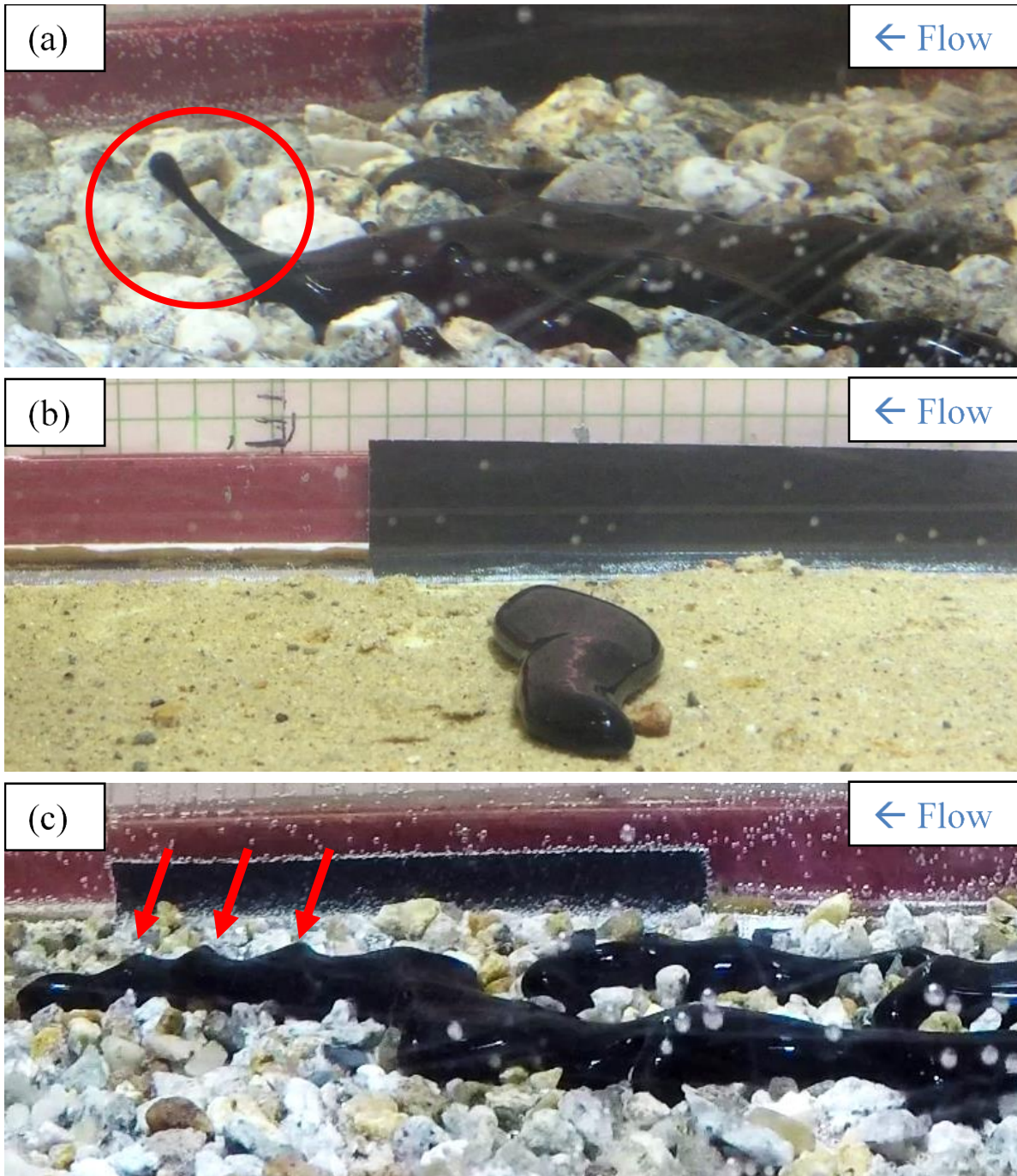


Figure 4-1: Representative images of (a) type II erosions (red circle), (b) rope formation, and (c) ripple formation (red arrows) of oil on medium pebble, sand, and fine pebble substrates, respectively.

Table 4-1: Criteria describing the thresholds of oil movement applicable for $v_o > 6 \times 10^4$ cSt (typical of Alberta bitumen at $\sim 33^\circ\text{C}$). [N.B., The $v_o > 6 \times 10^4$ cSt threshold is based on experimental data and future experiments should be conducted to resolve these ranges as the criteria may apply to a broader viscosity range].

Applicable for $v_o > 6 \times 10^4$ cSt: A single threshold event often results in substantial mass transport.			
Threshold	What would happen in the field	Dominant force affecting the oil (resulting transport process)	CSS threshold determined by assessing SOP length (X), width (Y), area measurements, and number of erosions from overhead and side view images and videos).
Type II Erosions (i.e., an event when a piece or droplet of oil is removed from the large oil mass)	Oil at the water's surface, oil droplets in the water column, or oil droplets lodged in pore spaces.	Buoyancy or water velocity (oil pieces/droplets transported as bedload or suspended load)	Any piece of oil or oil droplet leaving the SOP due to buoyancy or water velocity.
Bedload Transport (i.e., a single event which transports a significant portion or the entire oil mass)	Majority of SOP no longer present on the substrate; remnants of oil may be visible on sediments. Segmentation of SOP into smaller pieces, with droplets stuck in pore spaces on the bed or transporting with water currents.	Water velocity (SOP bedload transport)	Identified by a reduction in oil area due to mass loss (i.e., reduction in area and corresponding spike in erosion events).

Table 4-2: Criteria describing the thresholds of oil movement applicable for $v_o < 2 \times 10^4$ cSt (typical of fresh No.6 HFO at $\sim 13^\circ\text{C}$). [N.B., The $v_o < 2 \times 10^4$ cSt threshold is based on experimental data and future experiments should be conducted to resolve these ranges as the criteria may apply to a broader viscosity range].

Applicable for $v_o < 2 \times 10^4$ cSt: SOP transports in multiple stages.		CSS threshold determined by assessing SOP length (X), width (Y), area measurements, and number of erosions from overhead and side view images and videos).	
Threshold	What would happen in the field?	Dominant force affecting the oil (resulting transport process)	Used overhead images at the end of each velocity interval to measure the length and width of SOP.
Gravity Spreading	Length and width of SOP increase proportionally.	Gravity (an increase in SOP diameter)	Width > length or length > width using overhead measurements; SOP does not spread against the current.
Rope Formation	On sand and fine pebble, the width of SOP is greater than the length (beginning of oil rope formation). On medium pebble, length increasing at faster rate than the width.	Water velocity (bedload transport)	Ripples developed in the downstream side of the footprint and migrate the length of the SOP. Ripple formation drives oil lengthening and causes type II erosions from leading edge of SOP.
Type II Erosions	Oil at the water's surface or as oil droplets in the water column, or oil droplets lodged in pore spaces.	Buoyancy or water velocity (oil pieces/droplets transport as bedload or suspended load)	First oil droplet leaving SOP; occurred in all trials when free stream velocity (U) < 0.13 m/s.
Break-Apart/Resuspension	Majority of SOP no longer present on the substrate; remnants of oil may be visible on sediments. Segmentation of SOP into smaller pieces, with droplets stuck in pore spaces on the bed or transporting with water currents.	Water velocity (SOP bedload transport)	Identified by a reduction in oil area due to mass loss (i.e., reduction in area and corresponding spike in erosion events).

As recommended by OR&R, the concept of the SOTT was socialized throughout the spill response community. First, CRRC conducted an interagency (e.g., United States Geological Survey (USGS), U.S. Army Corp of Engineers) meeting in August 2020 with representatives from the Inland Riverine Oil Spill (IROS) collaborative. The focus of IROS is to bring together groups conducting research and developing oil spill response tools specific to rivers. Members from this group agreed with the substrate sizes and BSS range used in the flume experiments and encouraged further development of the SOTT. The group was especially interested in the documentation (e.g., pictures, videos) used to describe the stages of oil movement and the criteria describing the thresholds. IROS representatives noted this tool would be helpful in small rivers where bathymetry data is not available, and assumptions need to be made about hydraulics, bed type, and other *in-situ* conditions.

Preliminary findings were also presented to >150 participants watching NOAA's "*You don't know what you don't know*" webinar series in September 2020. Participants at the webinar represented groups from oil spill response organizations, industry, international governments (e.g., Environment Canada), academia, and the USCG. Based on input from multiple stakeholder groups and discussions with OR&R from 2017-2020, the development of the SOTT prototype was encouraged. The SOTT, developed in Excel to provide a user-friendly interface in a platform (no Wi-Fi connectivity required), provides oil spill responders with an initial "best estimate" of the extent of sunken oil transport.

4.3.2 SOTT Structure

The SOTT was developed using empirical relationships established from flume-based experiments in a sustained current-driven environment over an immobile boundary. Hence, the SOTT does not apply to wave-dominated flow regimes (e.g., surf zone) and only accounts for skin-

friction-induced BSS. The relationships were developed for sediment-oil patties (SOP) with an initial diameter of ~10 cm (Gustitus & Clement, 2017) stranded on top of an immobile sediment bed. A flow chart (Figure 4-2) was developed to illustrate the major processes used in the SOTT to predict oil transport by referencing the relevant equations, tables, and figures discussed in this chapter. This figure can be referenced by the SOTT user in the sheet titled “5_Flow Chart”.

Upon opening the Excel spreadsheet, the user selects the “1_Questionnaire” tab before continuing, reads the instructions and then answers a series of questions. The questions ensure the SOTT applies to the *in-situ* conditions under evaluation; the SOTT assumes uniform, steady state conditions and is limited to a current-driven environment. Therefore, if the user enters “Yes” when asked if the oil spilled in a wave-dominated environment (e.g., surf zone), the user would be warned that the SOTT does not apply (Table 4-3). [N.B., The SOTT does not physically lock the user out, however, if any assumptions do not apply then results from the SOTT are invalid]. Alternatively, if the *in-situ* conditions follow SOTT assumptions, then the user is alerted by a green-bar showing the word “Applicable” and may continue to the “2_Input” tab (Table 4-4).

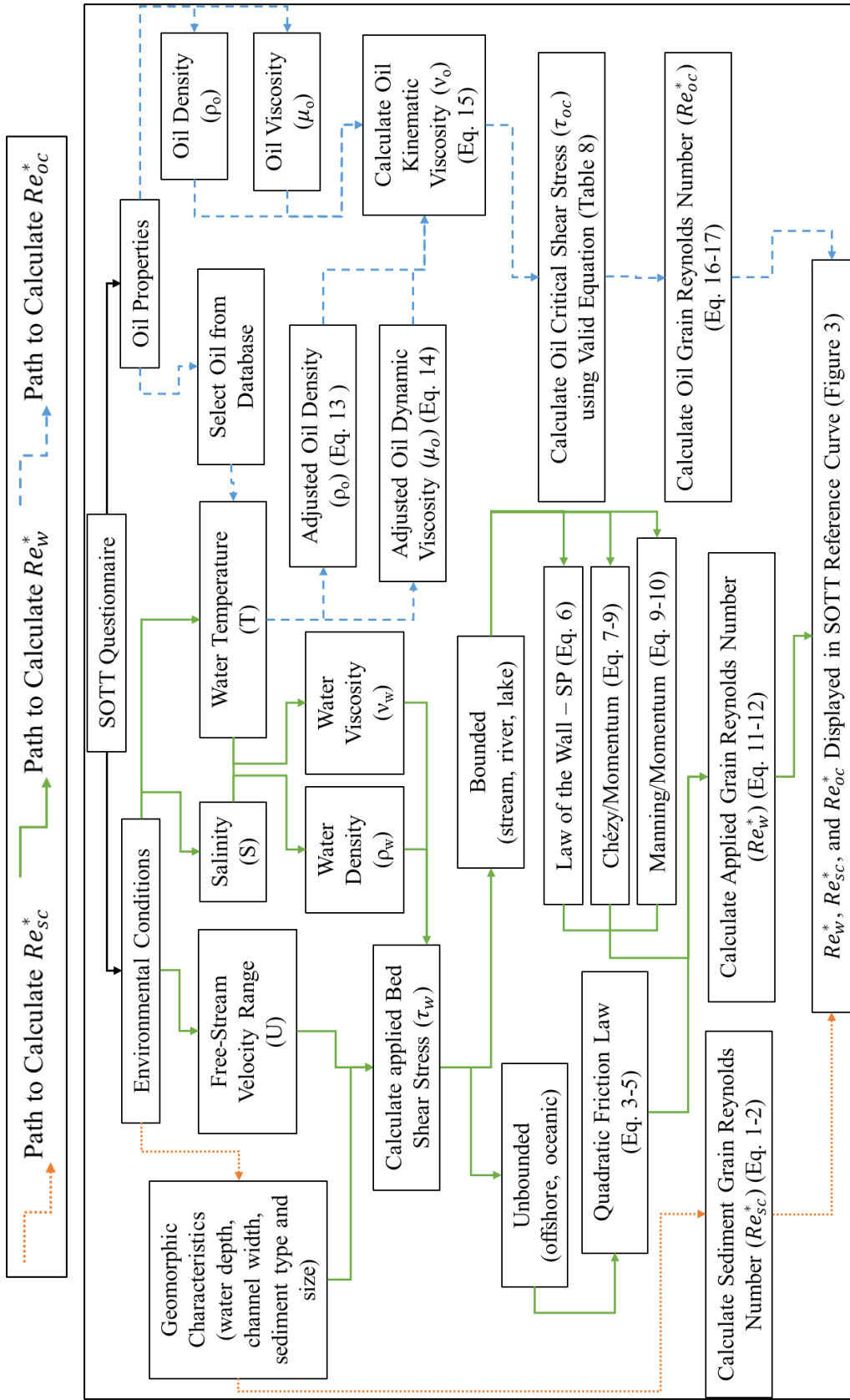


Figure 4-2: Overview of the SOTT structure showing the major processes by referencing the relevant equations, tables, and figures discussed in this chapter.

Table 4-3: Example of a scenario that does not follow all SOTT assumptions and warns the user the SOTT is not applicable.

Step 1: Instructions		
Read the instructions below:		
Answer the following questions to determine if the Sunken Oil Transport Tool (SOTT) is applicable to your spill scenario. At the end of Step 2, if the bar at the end reads "Applicable" and is green, continue on to Step 3. If it reads "N/A" and is red, the SOTT is not applicable to your conditions.		
Step 2: SOTT Applicability		
Answer the following questions:	Answers (Yes/No)	
	SOT Applicable	SOT Applicability
Did oil sink to the bottom of a water body?	Yes	Applicable
Did the spill occur in a river, stream, or lake?	Yes	Applicable
Did the spill occur in a marine, tidally driven environment?	Yes	Applicable
Is the oil in a shallow, wave-dominated environment (e.g., surf zone)?	Yes	N/A
Has the stranded oil continuously been submerged?	Yes	Applicable
Are hydraulic conditions uniform (i.e., is the water level constant)?	Yes	Applicable
Is flow at steady state (i.e., is velocity constant over time)?	Yes	Applicable
N/A		

Table 4-4: Example of a scenario that follows SOTT assumptions and can be used to predict sunken oil transport.

Step 1: Instructions		
Read the instructions below:		
Answer the following questions to determine if the Sunken Oil Transport Tool (SOTT) is applicable to your spill scenario. At the end of Step 2, if the bar at the end reads "Applicable" and is green, continue on to Step 3. If it reads "N/A" and is red, the SOTT is not applicable to your conditions.		
Step 2: SOTT Applicability		
Answer the following questions:	Answers (Yes/No)	SOT Applicability
Did oil sink to the bottom of a water body?	Yes	Applicable
Did the spill occur in a river, stream, or lake?	Yes	Applicable
Did the spill occur in a marine, tidally driven environment?	Yes	Applicable
Is the oil in a shallow, wave-dominated environment (e.g., surf zone)?	No	Applicable
Has the stranded oil continuously been submerged?	Yes	Applicable
Are hydraulic conditions uniform (i.e., is the water level constant)?	Yes	Applicable
Is flow at steady state (i.e., is velocity constant over time)?	Yes	Applicable
Applicable		

4.3.2.1 Environmental Calculations

The SOTT allows the user to define the *in-situ* environmental conditions (e.g., water temperature, salinity, current velocity range, sediment type) from a series of drop-down menus and individual input parameters (Table 4-5).

Based on the input salinity and temperature, the water density (Millero et al., 1980) and water viscosity (El-Dessouky & Ettouney, 2002) are calculated. Water density is not adjusted for depth; however, the overall effect of depth on water density and, hence, BSS estimates is negligible. For example, using a water temperature of 5°C, salinity of 35 ‰, and assuming pressure of 0 Pa, the calculated water density is 1027.7 kg/m³. Using the same input parameters, but adjusting pressure to a depth of 30 m (304,600.5 Pa), the calculated water density increases slightly to 1027.85 kg/m³. Using the Oceanic (offshore) methods to calculate τ_w , assuming velocity remains constant at 1 m/s, a density of 1027.7 and 1027.85 kg/m³ result in a 0.001 Pa difference in τ_w which is negligible.

To calculate applied BSS (τ_w), the user must enter the free-stream velocity range (U_{\min} and U_{\max}), the water depth (h), and sediment type. For rivers/streams/lakes, the channel width (b) is also a required input parameter. Depending on the water body type, τ_w is calculated using one or more of the following methods: Quadratic Friction Law, Law of the Wall – Single Point, the Chézy/Momentum, and the Manning/Momentum. [N.B., The subscript “w” designates water (e.g., τ_w, μ_w), “s” represents “sediment” (e.g., Re_s^*), “o” indicates “oil” (μ_o), and “c” denotes the critical threshold (e.g., Re_{sc}^*, τ_{oc})].

Table 4-5: An example of the environmental data input parameters used in the SOTT.

Step 3: Input Environmental Conditions					
Environmental Subcategories	Input Name (Symbol)	Input Value	Units	Notes	
Water Properties	Water Body Type	Ocean (offshore)	-	<--Select water body type of spill location from drop-down menu	
	Water Temperature (T)	15	°C	<-- If unknown, use Temp_Salinity_RefValues	
	Water Salinity (S)	33	ppt	<-- If unknown, use Temp_Salinity_RefValues	
	Minimum Free-stream Velocity (U_{min})	0.05	m/s	<-- Average velocity just below the surface (time averaged for 60 seconds)	
	Maximum Free-stream Velocity (U_{max})	2	m/s	<-- Average velocity just below the surface (time averaged for 60 seconds)	
	Water Depth (h)	30	m		
Geomorphic Characteristics	Channel Width (b)	10	m		
	Sediment Type	Very fine sand	-	<-- Select <i>in-situ</i> sediment type from drop-down menu	

Sediment Type & Characteristics

For each of the sediment types available in the drop-down menu, there is an associated sediment size range (d_{50}) and CSS (τ_{sc}) (Table 4-6) (Berenbrock & Tranmer, 2008).

Table 4-6: Particle size range and associated CSS range used as input in the SOTT.

Classification Name	Particle Size Range		Particle Critical Shear Stress Range	
	Min d_{50}	Max d_{50}	Min τ_{sc}	Max τ_{sc}
Sediment Type	(mm)		(N/m ²)	
Coarse cobble	128	256	112	223
Fine cobble	64	128	53.8	112
Very coarse gravel	32	64	25.9	53.8
Coarse gravel	16	32	12.2	25.9
Medium gravel	8	16	5.7	12.2
Fine gravel	4	8	2.7	5.7
Very fine gravel	2	4	1.3	2.7
Very coarse sand	1	2	0.47	1.3
Coarse sand	0.5	1	0.27	0.47
Medium sand	0.25	0.5	0.194	0.27
Fine sand	0.125	0.25	0.145	0.194
Very fine sand	0.0625	0.125	0.11	0.145
Coarse silt	0.031	0.0625	0.083	0.11
Medium silt	0.0156	0.031	0.063	0.0826
Fine silt	0.0078	0.0156	0.0378	0.063

The τ_{sc} range is transformed into the critical friction velocity (u_{sc}^*) (Eq. 4-1) and then the range is converted into the critical grain Reynold's Number (Re_{sc}^*) (Eq. 4-2) using the associated d_{50} range.

$$u_{sc}^* = \sqrt{\frac{\tau_{sc}}{\rho_w}} \quad \text{Eq. 4-1}$$

$$Re_{sc}^* = \frac{u_{sc}^* * d_{50}}{\nu_w} \quad \text{Eq. 4-2}$$

The sediment's d_{50} is also used to calculate the Law of the Wall's characteristic roughness length, z_o , (Eq. 4-3) (Soulsby, 1997).

$$z_o = \frac{d_{50}}{12} \quad \text{Eq. 4-3}$$

As described in the next section (4.3.2.2 Calculating BSS), the d_{50} and z_o ranges are used to calculate the roughness coefficients C_D , C , n for the Quadratic Friction Law, Momentum/Chézy, and Momentum/Manning equations, respectively.

4.3.2.2 Calculating BSS

For this dissertation research, the term BSS and τ_w were used when describing shear stress for all methods, even for methods evaluating shear stress some elevation (z) above the boundary where $0 \text{ cm} < z < 3 \text{ cm}$.

Quadratic Friction Law

The Quadratic Friction Law uses C_D to quantify drag associated with bed roughness or bed forms. Because C_D varies depending on the relative roughness ($\frac{z_o}{h}$) and water body type (e.g., river, offshore oceanic) (Soulsby, 1997), the fitted parameters, α and β , are condition specific. For example, if C_D is calculated (Eq. 4-4) for shallow water flow ($10^{-7} < \frac{z_o}{h} < 10^{-2}$), over bed forms in coastal waters, $\alpha=0.019$ and $\beta=0.208$ (Dawson et al., 1983). For flat mobile or immobile beds of sand with steady flows in flumes or oceanic environments, $\alpha=0.0415$ and $\beta=0.286$ (Soulsby, 1997). Alternatively, in open channel flow, such as rivers or streams ($\frac{z_o}{h} > 10^{-4}$), C_D is calculated using $\alpha=0.047$ and $\beta=0.33$ (Eq. 4-4) (Soulsby, 1997; Strickler, 1923).

$$C_D = \alpha \left(\frac{z_o}{h} \right)^\beta \quad \text{Eq. 4-4}$$

Because the Dawson et al. (1983) and Soulsby (1997) approaches were derived in oceanic and coastal waters, when the user selects “Oceanic (offshore)” or “Estuary” in the SOTT the arithmetic mean of C_D is then used to calculate BSS (Eq. 4-5). When the SOTT user selects

“River/Stream/Lake”, the Manning-Strickler specific α and β coefficients are used to calculate C_D (Eq. 4-4).

$$\tau_w = \rho_w C_D \bar{U}^2 \quad \text{Eq. 4-5}$$

where ρ_w = water density (kg/m³) and \bar{U} = depth averaged velocity (m/s), which is assumed to be $0.8*U$ for $h < 2$ m, and $0.85*U$ for $h > 2$ m.

Law of the Wall – Single Point

The Law of the Wall – Single Point uses readily measurable parameters to directly calculate BSS (Eq. 4-6) and applies to sand- and gravel-bedded rivers (Dietrich & Smith, 1983; Whiting & Dietrich, 1990; Wilcock, 1996). The equation calls for d_{84} as the representative sediment size, but due to the limited data available for d_{84} ranges with associated τ_{sc} , the comprehensive data set for d_{50} from Berenbrock & Tranmer, (2008) was used in the SOTT. Using the PSD from Chapter 2 and holding all other parameters constant, replacing d_{50} with d_{84} reduces τ_w for sand, fine pebble, and medium pebble substrates by 44%, 17%, and 3%, respectively. [N.B., As these reduction calculations are specific to the PSD measured in Chapter 2, the effect on τ_w would vary depending on the *in-situ* PSD, grain uniformity, water body type, and hydraulic regime]. The reduction in τ_w for sand is larger than fine and medium pebble because the relative change from d_{50} to d_{84} is greater for sand. To minimize the impact of using d_{50} vs d_{84} in the SOTT, τ_w is calculated using the range of d_{50} (min to max) for the selected sediment type (Table 4-6).

$$\tau_w = \frac{\rho_w (\bar{u}_z * \kappa)^2}{\ln \left(\frac{10 * z}{d_{50}} \right)^2} \quad \text{Eq. 4-6}$$

where $\kappa = 0.4$ (von Karman Constant), z = elevation above the bed (m), and \bar{u}_z = near-bed velocity (m/s), calculated using the relationship $\bar{u}(z) = \left(\frac{z}{0.32h} \right)^{1/7} * \bar{U}$ (Soulsby, 1997). For all calculations, \bar{u}_z is adjusted to $z = 3$ cm because the method requires velocity measurements to be

below 2/10ths of the flow depth and 2 cm above the bed of coarse sand or fine gravel for an immobile boundary (Whiting & Dietrich, 1990; Wilcock, 1996).

Chézy/Momentum

The Chézy, C , is estimated using an empirical relationship, originally developed to calculate the Darcy-Weisbach friction factor (f) by relating the inverse of relative roughness to the friction factor (Elger et al., 2013; Leopold & Wolman, 1957; Limerinos, 1970). Eq. 4-7 was modified to directly calculate C , using $C = \sqrt{\frac{8g}{f}}$ (Chaudhry, 2008; Elger et al., 2013).

$$C = \sqrt{8g * \left[1.2 + 2.03 \log \left(\frac{R_h}{d_{50}} \right) \right]^2} \quad \text{Eq. 4-7}$$

where g = gravity (m/s^2), R_h = hydraulic radius (m), and d_{50} = median grain size (m). The equation normally uses d_{84} , but as previously described, the SOTT uses a range of d_{50} for each sediment class because limited data was available for d_{84} and the associated τ_{sc} . Using the PSD from Chapter 2 and holding all other parameters constant, replacing d_{50} with d_{84} reduces τ_w for sand, fine pebble, and medium pebble substrates by 39%, 14%, and 2.6%, respectively. As with the Law of the Wall – Single Point, C is calculated using a representative sediment size range based on the selected sediment type. Following Eq. 4-8, C is used to estimate friction slope, S_f , and S_f is substituted into the Eq. 4-9 to calculate BSS.

$$S_f = \frac{\left(\frac{U}{C} \right)^2}{R_h} \quad \text{Eq. 4-8}$$

$$\tau_w = \gamma_w R_h S_f \quad \text{Eq. 4-9}$$

where γ_w = specific weight of water (N/m^3), and U = free-stream velocity (m/s).

Manning/Momentum

Manning's, n , is estimated by $n = K_u d_{50}^{1/6}$, where K_u is a coefficient derived by fitting empirical relationships to flume or field data. Three methods are used in the SOTT to estimate K_u (Chow, 1959; Anderson et al., 1970; Strickler, 1923). The median n value of the three methods is used to calculate S_f (Eq. 4-10) to avoid averaging them as they are independent empirically derived values.

$$S_f = \left(\frac{U * n}{R_h^{2/3}} \right)^2 \quad \text{Eq. 4-10}$$

where $K_u = 0.0417$, $K_u = 0.0482$, and $K_u = 0.0474$ based on Chow (1959), Anderson et al. (1970), and Strickler (1923), respectively. S_f is then substituted into Eq. 4-9 to estimate BSS.

Depending on the hydraulic regimes (e.g., open channel vs. offshore oceanic), an arithmetic mean $\overline{\tau_w}$ of the valid methods is used in subsequent calculations. For river/streams, $\overline{\tau_w}$ is estimated from the Quadratic Friction Law (using Strickler (1923) α and β), Law of the Wall – Single Point, the Chézy/Momentum, and Manning/Momentum approaches. In oceanic (offshore) or estuarine environments, $\overline{\tau_w}$ is calculated using the Dawson et al. (1983) and Soulsby (1997) Quadratic Friction Law approaches.

4.3.2.3 Calculating Re_w^*

$\overline{\tau_w}$ is used to calculate the *in-situ* friction (shear) velocity, u_w^* (m/s), (Eq. 4-11) and the corresponding grain Reynold's number, Re_w^* , (Eq. 4-12). Re_w^* represents the SOTT estimated *in-situ* τ_w which is controlled by the user's selected environmental conditions (e.g., water velocity, temperature, sediment type). This value will be used in the reference curve to relate the critical thresholds of movement for oil and sediment to determine if *in-situ* conditions are sufficient to mobilize them.

$$u_w^* = \sqrt{\frac{\tau_w}{\rho_w}} \quad \text{Eq. 4-11}$$

$$Re_w^* = \frac{u_w^* * d_{50}}{\nu_w} \quad \text{Eq. 4-12}$$

where ρ_w = density of water (kg/m³), ν_w = water kinematic viscosity (m²/s), and d_{50} = median grain size (m). Along with the range of Re_{sc}^* (i.e., the critical grain Reynolds Number of the selected sediment), a range of Re_w^* is displayed in the SOTT reference curve.

4.3.2.4 Oil Property Calculations

The user then enters the spilled oil's properties (e.g., API, density, viscosity) or selects a proxy oil from the SOTT's oil database (Table 4-7). The database was developed using oil types from NOAA's Automated Data Inquiry for Oil Spills (ADIOS2) model (Lehr et al., 2002). Oils were added to the SOTT database if the API <15° (i.e., oils most likely to sink) and at least two datapoints for oil viscosity and density were available. A minimum of two reference datapoints, at two temperatures for each oil type, were required so that oil density (K_t) and oil viscosity (C_T) coefficients could be calculated using measured values. K_t and C_T are used in the SOTT to adjust oil density and viscosity to the user's selected water temperature; it is assumed that K_t and C_T are do not vary with temperature. [N.B., This assumption was necessary based on available equations, but should be further investigated especially C_T for high viscosity oils in water temperatures near their pour point].

The oil's density, ρ_o , (Eq. 4-13) is calculated at the user's selected water temperature using formulas from NOAA's ADIOS2 technical manual and K_t . [N.B., They are not adjusted for emulsification or weathering.]

$$\rho_o = \rho_1(1 - K_t(T_2 - T_1)) \quad \text{Eq. 4-13}$$

where ρ_1 is the density (kg/m³) at temperature, T_1 (°C), from the database, and T_2 (°C) is the user's selected water temperature.

The oil's dynamic viscosity, μ_o , (Eq. 4-14), is also calculated at the user's selected water temperature using equations from NOAA's ADIOS2 technical manual and C_T .

$$\ln\left(\frac{\mu_o}{\mu_1}\right) = C_T\left(\frac{1}{T_2} - \frac{1}{T_1}\right) \quad \text{Eq. 4-14}$$

where μ_1 is the dynamic viscosity (cP) at temperature, T_1 (°K), from the database, and T_2 (°K) is the user's selected water temperature.

ρ_o and μ_o are used to calculate the oil's kinematic viscosity, ν_o , (m²/s) (Eq. 4-15).

$$\nu_o = \frac{\mu_o}{\rho_o} \quad \text{Eq. 4-15}$$

4.3.2.5 Calculating Oil CSS

Based on a series of flume-based experiments, using No. 6 HFO, multiple empirical relationships were developed using ν_o (cSt) and d_{50} to estimate the oil's CSS (τ_{oc}) for gravity spreading, rope formation, ripple formation, and break-apart/resuspension thresholds (See Chapter 3). τ_{oc} (Pa) is calculated using the sand equations for $d_{50} < 6.5$ mm, fine pebble equations when $6.5 \text{ mm} < d_{50} < 10.5$ mm, and medium pebble when $d_{50} > 10.5$ mm (Table 4-8).

To be conservative in predicting oil transport and avoid overpredicting τ_{oc} , because τ_{oc} increases with increasing d_{50} , the SOTT uses the sediment's lower d_{50} value as a threshold to determine which empirical relationship is used. Because the equations relating ν_o to τ_{oc} were developed from the oil CSS experiments (See Chapter 3), the fitted relationships are bounded by the conditions they were derived from. The fitted equations for gravity spreading, rope formation, and ripple formation are valid for $\nu_o < 2 \times 10^4$ cSt on all sediment types. The break-

apart/resuspension fitted equations are valid for $\nu_o < 431,000$ cSt on sand, $\nu_o < 115,000$ cSt on fine pebble, and $\nu_o < 106,000$ cSt for medium pebble. Note that the medium pebble's gravity spreading equation shows a decline in τ_{oc} as ν_o . This decline suggests that the slightly less viscous oils required a higher threshold of movement as they tended to fill in the open pore spaces and be shielded from the flow field by the medium sized pebbles. Using the rope formation τ_{oc} as a lower threshold of movement and the break-apart/resuspension, τ_{oc} as an upper threshold, τ_{oc} was converted to the oil's critical friction (shear) velocity, u_{oc}^* , (Eq. 4-16) and the oil's critical grain Reynold's number, Re_{oc}^* (Eq. 4-17).

$$u_{oc}^* = \sqrt{\frac{\tau_{oc}}{\rho_w}} \quad \text{Eq. 4-16}$$

$$Re_{oc}^* = \frac{u_{oc}^* * d_{50}}{\nu_w} \quad \text{Eq. 4-17}$$

The range of Re_{sc}^* and Re_w^* are plotted with the predicted upper and lower Re_{oc}^* estimates on the SOTT reference curve.

Table 4-7: Oil properties or selection of a proxy oil as input parameters used in the SOTT.

Step 4: Input Oil Properties				
Oil Subcategories	Input Name (Symbol)	Oil Name (API*)	Units	Notes
Proxy Oil	Oil Name	High Viscosity Fuel Oil (B)		<--If no information about <i>in-situ</i> oil is available, select a proxy
	API Gravity (API)	N/A	°	<--API Gravity of <i>in-situ</i> spilled oil
Spilled Oil	Oil Density (ρ_o)	N/A	g/cm ³	<-- Density of oil at <i>in-situ</i> water temperature
	Oil Viscosity (μ_o)	N/A	cP	<-- Dynamic viscosity of oil at <i>in-situ</i> water temperature

Table 4-8: Empirically-derived equations of oil CSS from the flume-based experiments.

Threshold of Movement	Sand ($d_{50} < 6.5$ mm)	Fine Pebble (6.5 mm < $d_{50} < 10.5$ mm)	Medium Pebble (10.5 mm < $d_{50} < 16$ mm)
Gravity Spreading	$\tau_{oc} = 0.0365 \ln(v_o) - 0.2705$ $R^2 = 0.7871$	$\tau_{oc} = 0.0731 \ln(v_o) - 0.57$ $R^2 = 0.9302$	$\tau_{oc} = -0.029 \ln(v_o) + 0.4277$ $R^2 = 0.0180$
Rope Formation	$\tau_{oc} = 0.0584 \ln(v_o) - 0.3762$ $R^2 = 0.6826$	$\tau_{oc} = 0.1752 \ln(v_o) - 1.3663$ $R^2 = 0.9938$	$\tau_{oc} = 0.1818 \ln(v_o) - 1.0057$ $R^2 = 0.9869$
Ripple Formation	$\tau_{oc} = 0.0732 \ln(v_o) - 0.3876$ $R^2 = 0.6759$	$\tau_{oc} = 0.2014 \ln(v_o) - 1.0251$ $R^2 = 0.6467$	$\tau_{oc} = 0.2654 \ln(v_o) - 1.4063$ $R^2 = 0.6934$
Break-Apart/Resuspension	$\tau_{oc} = 0.2153 \ln(v_o) - 1.52$ $R^2 = 0.7211$	$\tau_{oc} = 0.3248 \ln(v_o) - 1.7736$ $R^2 = 0.6745$	$\tau_{oc} = 2.503 \ln(v_o) - 19.519$ $R^2 = 0.8839$

4.3.2.6 SOTT Uncertainty

The uncertainty associated with the effects of shear rate on oil viscosity and sample variability for No. 6 HFO at temperatures $>10^{\circ}\text{C}$ is quantified as $\pm 20\%$ of μ_o over the range of temperatures and shear rates tested (See Chapter 3). The upper bound ($\mu_{upper} = 1.2\mu_o$) and the lower bound ($\mu_{lower} = 0.8\mu_o$) values are used to calculate oil CSS, u_{oc}^* , and the Re_{oc}^* range. The minimum Re_{oc}^* , calculated from μ_{upper} and μ_{lower} , is used as an uncertainty bound for rope formation and maximum Re_{oc}^* represents the break-apart/resuspension thresholds. The uncertainty bounds are overlaid with the predicted Re_{oc}^* range of the input oil in the reference curve.

If the SOTT is used at temperatures $<10^{\circ}\text{C}$ the shear-thinning effect for oils (e.g., No.6 HFO) becomes more prominent, but is not captured because μ_o is adjusted only to temperature using the Arrhenius-type equation (Eq. 4-15) and not based on shear rate. There is a potential for the SOTT to underpredict τ_{oc} at high shear velocities as the shear-thinning fluid would have a lower τ_{oc} . Therefore, potentially underpredicting oil transport. Additionally, the viscoelastic nature may be more pronounced for lower temperatures and may not be accurately captured using the Arrhenius-type equation thus potentially underestimating μ_o for more viscous, weathered oils. Because many transport processes rely on μ_o , characterization of μ_o over wide temperature ranges and at multiple shear rates should be considered in future research to improve model predictions. It is recommended that further research be done to quantify shear-thinning effects, especially near the oil's pour point, of heavy crude or refined products, weathered, and emulsified oils to develop an empirical relationship over a range of shear rates (0.1 to 16 Hz) and environmentally relevant temperatures (0 to 35°C) to ensure μ_o is accurately predicted.

4.3.2.7 SOTT Reference Curve

Based on the input parameters selected by the user, the reference curve provides a visual representation of how the estimated *in-situ* τ_w (i.e., applied BSS) compares with *in-situ* τ_{sc} (i.e., sediment incipient motion threshold) and the predicted τ_{oc} range (i.e., oil CSS thresholds) (Figure 4-3). The results displayed the τ_{oc} (Table 4-9) and reference curve (Table 4-10) values; these are summarized for the SOTT user in the “4_Summary Tables” tab.

Based on the fact that v_o is a significant factor used to estimate oil transport (see Chapter 3), Re_{oc}^* is plotted with respect to v_o , and Re_w^* and Re_{sc}^* are plotted over the range of v_o valid to the SOTT. The errors bars in the reference curve show the τ_{oc} variability based on $v_o \pm 20\%$ because exact v_o measurements at the *in-situ* temperature are challenging to obtain and the SOTT relies heavily on this parameter.

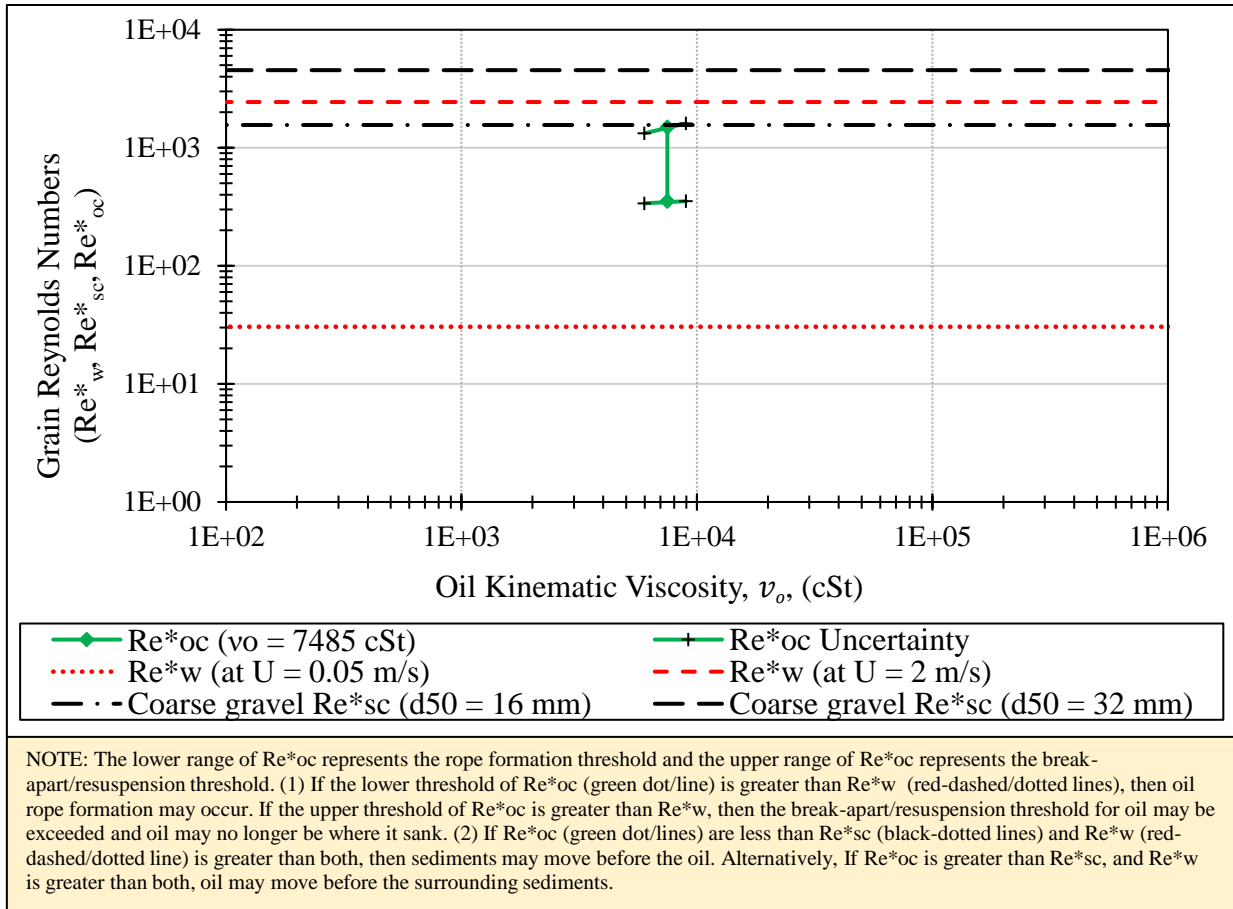


Figure 4-3: Example of the SOTT output displayed as a reference curve.

Table 4-2: Example of the τ_{oc} summary table.

Oil Critical Shear Stress (τ_{oc}) Summary Table	
Transport Threshold	τ_{oc} (Pa)
Rope Formation	0.616
Ripple Formation	0.96
Break-Apart/Resuspension	2.81

Table 4-3: Example of the sediment and oil transport summary table.

Sediment and Oil Transport Summary Table		U (m/s) = 0.05	U (m/s) = 2
Oil Kinematic Viscosity (cSt)	7485	No Oil Movement	Oil Break-Apart/Resuspension
Sediment Type & Size	Coarse gravel		
d50 (mm)	16	No Sediment Transport	Sediment Incipient Motion
d50 (mm)	32	No Sediment Transport	No Sediment Transport

The SOTT output is plotted so that responders can evaluate a range of conditions which may cause sunken oil transport. Alternatively, the responder could input information about the spill scenario and then tune the SOTT to determine at over what velocity the oil may migrate along the bed, break-apart into non-recoverable droplets, or become buried by surrounding sediments (See example in Section 4.4.1 Kalamazoo River Case Study).

In general, Re^* increases for higher current velocities, larger sediment sizes, or increased water viscosity. In the reference curve, the lower and upper ranges of Re_{oc}^* represents the rope formation threshold and break-apart/resuspension thresholds, respectively. If the lower threshold of Re_{oc}^* is greater than Re_w^* , then oil rope formation may occur. If the upper threshold of Re_{oc}^* is greater than Re_w^* , then the break-apart/resuspension threshold for oil may be exceeded and oil may no longer be where it sank. If the range of Re_{oc}^* is less than Re_{sc}^* , and Re_w^* is greater than both, then sediments may move before the oil. Alternatively, if Re_{oc}^* is greater than Re_{sc}^* , and Re_w^* is greater than both, oil may move before the surrounding sediments.

As shown in Figure 4-3, Re_{oc}^* and Re_{sc}^* are greater than the lower Re_w^* threshold, suggesting that the applied τ_w at $U = 0.05$ m/s is unlikely to cause bulk oil or sediment transport. If Re_{oc}^* is less than the upper Re_w^* and the range of Re_{sc}^* , the applied τ_w at $U = 2$ m/s may cause oil to resuspend or break-apart prior to incipient motion of the surrounding sediment. If the Re_{sc}^* thresholds are below Re_{oc}^* , this would imply that the surrounding sediment may mobilize prior to oil transport and burial and exhumation processes could occur. [N.B. The SOTT only accounts for the sediment type and associate size range selected by the user. Therefore, if a smaller sediment fraction is present *in-situ*, then burial/exhumation of oil may occur before the SOTT indicates].

4.4 Results and Discussion

4.4.1 Kalamazoo River Case Study

4.4.1.1 Spill Description

The Enbridge Line 6b pipeline spilled 843,000 gallons of diluted bitumen (Cold Lake Bitumen (CLB), API=9.5°) into a wetland during July 2010 in Marshall, MI (Fitzpatrick et al., 2015b; USEPA, 2016). The spill occurred during a flood and caused the oil to travel from the wetland into Talmadge Creek and the Kalamazoo River, where it proceeded to deposit along 38 miles and enter Morrow Lake. Due to the nature of the oil spilled, the increased turbulence, and high suspended sediment concentration, the initially buoyant oil mixed with river sediment and submerged so responders could not see it. The fraction of oil that remained on the water's surface weathered over time and the diluent evaporated. This caused the floating oil's density to increase, and it submerged and interacted with suspended sediments. The weathered and sediment-laden oil transported with the currents until it reached low velocity areas (<0.3 m/s) and deposited on the river bed in channel margins, backwaters, side channels, and oxbows (Fitzpatrick et al., 2015b).

Response operations and oil spill modelers worked to develop hydrodynamic and sediment transport models representative of *in-situ* conditions. New techniques were developed to detect sunken oil (e.g., probing the bottom with poles (i.e., poling)), determine the water depth, and identify oil depositional areas (Fitzpatrick et al., 2015b). Sediment cores were collected to determine sediment type, and sediment layering structure and develop a grain size distribution. The river bottom bathymetry was mapped using LIDAR. Flume studies used the sediment collected from depositional areas to estimate the erosion rates and τ_{sc} of *in-situ* sediment or τ_{oc} of the sediment/oil mixtures. $\tau_{oc} = 0.4$ Pa was calculated as the erosion threshold for the sediment-oil mixture (Perkey et al., 2014; Waterman et al., 2015). Laboratory studies evaluated

resuspension of oil-particle aggregates (OPAs) which were then incorporated into an existing sediment transport model (e.g., SEDZLJ) (Hayter et al., 2015). Because depositional areas of oil were associated with fine grained soft sediments, modelers used the τ_{sc} of silt-sized sediments, $\tau_{sc} = 0.05$ Pa, as a proxy for OPAs (Dollhopf et al., 2014; Fitzpatrick et al., 2015b).

4.4.1.2 SOTT Inputs

To accurately model the Enbridge Line 6b oil spill, environmental conditions (e.g., water temperature) and riverine characteristics (e.g., width, depth) were obtained from literature. Using a $b:h$ of 40 and a river width, b , of 22.86 m (75 ft), a water depth, h , of 0.57 m (1.88 ft) was calculated and used for all of the scenarios (Fitzpatrick et al., 2015b). Dollhopf et al. (2014) noted that the submerged oil aggregated with fine-grained soft sediment (silt, clay, and organic accumulations). Coarse silt (d_{50} range = 0.031 to 0.0625 mm) was selected as the sediment type for all SOTT simulations. Flume studies determined that typical τ_{sc} values in the Kalamazoo River were between 0.10 and 0.15 Pa (Waterman et al., 2015). The coarse silt used in the SOTT had an associated τ_{sc} range of 0.083 to 0.11 Pa. Because oil density and viscosity are influenced by temperature, and viscosity is a factor driving sunken oil transport, two temperatures were evaluated for this case study. An upper temperature limit of 22.2°C (72 °F) was used to represent summer water temperatures at the time of the spill (Fitzpatrick et al., 2015b), and 15.6°C (60°F) was selected as the lower limit because poling operations were terminated for temperatures below that (Dollhopf et al., 2014; USEPA, 2016).

There is a higher relative concern of weathered diluted bitumen sinking as compared to fresh diluted bitumen (NASEM, 2016). Additionally, the associated response to a sunken/submerged oil is “more complex” and the recovery is “less effective”. The focus of the SOTT is on sunken oil transport, therefore, two weathered Cold Lake bitumen (CLB) oils (Percent

Evaporation (%Ev) =16.9 and 25.3) were selected as representative to capture the influence of weathering state and its effects on physical properties. CLB (%Ev=16.9) was included in the analysis because King et al. (2014) conducted laboratory- and flume-based experiments to study the effect of weathering (e.g., evaporation, photo-oxidation) on floating CLB, and found that the density remained below 1.00 g/cm^3 even after 300 hours of weathering. This suggests that the oil was not dense enough to sink without the incorporation of sediment, but may be the most representative oil condition for the Kalamazoo River spill simulations.

The dynamic viscosity and density of the weathered CLB (Table 4-11) were parameterized by Environment Canada (2013). The values were adjusted based on the SOTT input temperatures (16°C and 22°C). Four scenarios were simulated for the case study (Table 4-12). To show how the SOTT can be tuned to predict the velocity range that would initiate oil transport, a velocity range was not chosen as an input parameter, but is presented in the output.

Table 4-11: SOTT input parameters used for the Kalamazoo River oil spill case study.

Temperature (°C)	Oil Type (%Ev)	ρ_o (g/cm ³)	μ_o (cP)	ν_o (cSt)
16	CLB (16.9)	0.981	16,996	17,325
22	CLB (16.9)	0.977	7,690	7,871
16	CLB (25.3)	1.003	337,907	336,896
22	CLB (25.3)	0.999	70,569	70,640

Table 4-12: Summary table describing Kalamazoo River dimensions, water temperature, and oil condition for each SOTT scenario.

Scenario Number	h (m)	b (m)	Water Temperature (°C)	Oil Type (%Ev)
1	0.57	22.86	16	CLB (16.9%)
2	0.57	22.86	22	CLB (16.9%)
3	0.57	22.86	16	CLB (25.3%)
4	0.57	22.86	22	CLB (25.3%)

4.4.1.3 SOTT Results

Oil CSS Predictions

After inputting the scenario-related parameters, the velocity range was tuned to find the critical velocity (U_c) associated with oil rope formation and break-apart/resuspension (Table 4-13). In the event of a spill, responders can gain an initial “best estimate” as to the range of current velocities that may initiate oil transport along the bed or resuspension into the water column. The minimum Re_{oc}^* , corresponding to τ_{oc} for rope formation, and maximum Re_{oc}^* , representing τ_{oc} for break-apart/resuspension, were calculated (when valid) for Scenarios 1-4 (Table 4-14). All valid τ_{oc} estimates for rope formation, ripple formation, and break-apart/resuspension thresholds are presented in Figure 4-4. [N.B., Rope formation indicated with an open symbol, ripple formation by a symbol with horizontal hatched lines, and the break-apart/resuspension symbol with a solid fill].

Table 4-13: SOTT results summarizing U_c for each scenario.

Scenario Number (Description)	Rope Formation U_c (m/s)	Break-Apart/Resuspension U_c (m/s)
1 (16°C & 16.9%Ev)	0.44	0.75
2 (22°C & 16.9%Ev)	0.38	0.60
3 (16°C & 25.3%Ev)	N/A	1.1
4 (22°C & 25.3%Ev)	N/A	0.95

Table 4-14: SOTT results summarizing the predicted oil τ_{oc} thresholds and the range of Re_{oc}^* for each scenario.

Scenario Number (Description)	Parameter (units)	Rope Formation	Ripple Formation	Break-Apart/ Resuspension
1 (16°C & 16.9%Ev)	τ_{oc} (Pa)	0.19±0.01	0.33±0.02	0.58±0.05
	Minimum Re_{oc}^*	0.39	0.50	0.67
	Maximum Re_{oc}^*	0.78	1.01	1.34
2 (22°C & 16.9%Ev)	τ_{oc} (Pa)	0.14±0.01	0.27±0.02	0.41±0.05
	Minimum Re_{oc}^*	0.39	0.52	0.65
	Maximum Re_{oc}^*	0.79	1.05	1.31
3 (16°C & 25.3%Ev)	τ_{oc} (Pa)	N/A	N/A	1.22±0.05
	Minimum Re_{oc}^*	N/A	N/A	0.97
	Maximum Re_{oc}^*	N/A	N/A	1.96
4 (22°C & 25.3%Ev)	τ_{oc} (Pa)	N/A	N/A	0.88±0.05
	Minimum Re_{oc}^*	N/A	N/A	0.98
	Maximum Re_{oc}^*	N/A	N/A	1.97

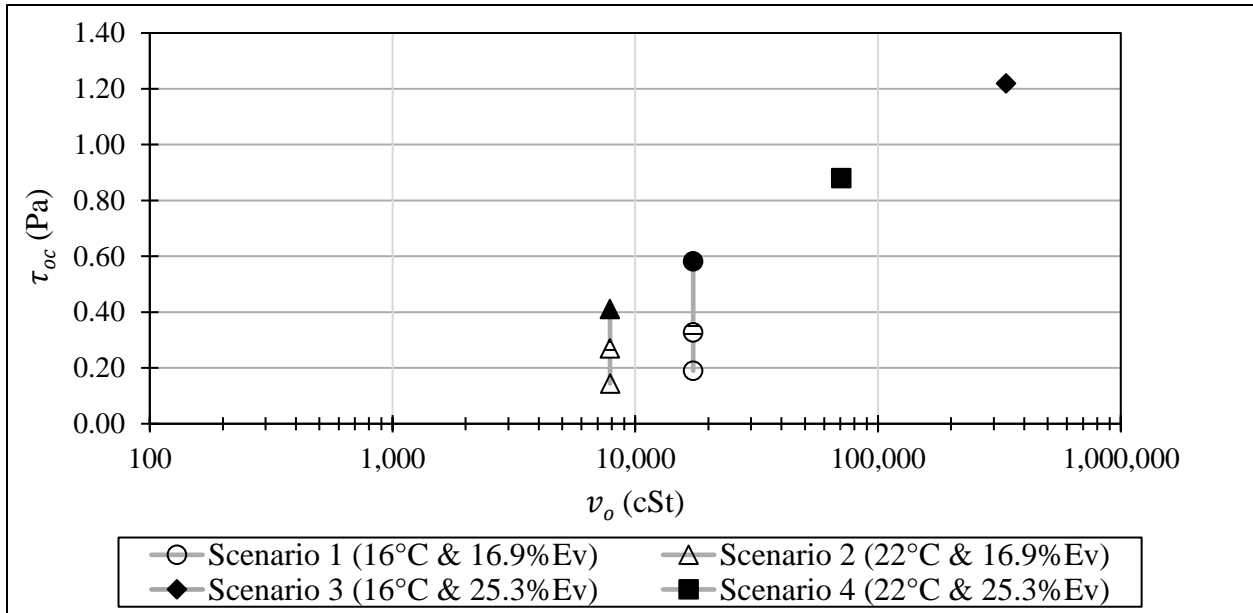


Figure 4-4: Comparison of scenario's valid oil CSS thresholds with respect to ν_o .

The ν_o values of CLB (25.3%) at 16°C and 22°C were outside of the applicable viscosity range, thus invalidating τ_{oc} predictions of rope formation and ripple formation for Scenarios 3 and 4. Therefore, U_c , τ_{oc} , and the Re_{oc}^* range, for these scenarios are only presented for the resuspension/break-apart threshold.

The SOTT results showed that Scenario 2 had the lowest predicted τ_{oc} for all thresholds, and the smallest spread in τ_{oc} values. Scenario 1 results predicted slightly higher τ_{oc} values for all thresholds and the range of predicted τ_{oc} values was wider because the oil was more viscous due to the colder temperature. Scenario 4 had the second largest predicted τ_{oc} and Scenario 3 had the largest break-apart/resuspension because a more weathered oil has a higher viscosity and the impact of water temperature on viscosity is greater. As expected, the more viscous oils (due to evaporation and compounded by cold water temperatures) had the highest predicted τ_{oc} . Because τ_{oc} was used to calculate U_c , the same pattern is true for the magnitude and range of U_c thresholds.

The uncertainty in SOTT predictions (shown as error bars for the τ_{oc} ranges in the reference curve) comes from the assumed ν_o , the empirical relationship used to adjust it based on water

temperature, and the fitted relationship used to calculate τ_{oc} . The fitted relationship was developed by corresponding the oil's movement to U_c and calculating τ_{oc} based on U_c .

Five methods were used to calculate applied τ_w , and the mean of the five methods ($\overline{\tau_w}$) was designated as the τ_{oc} . The variability associated with $\overline{\tau_w}$ was captured using ± 1 standard deviation (σ) from the mean (See Chapter 3 for true CSS values). The spread in estimates of 2-3 Pa is expected, especially at high velocities (~ 0.7 m/s) because τ_w is difficult to estimate as it relies on assumed, derived, or measured input values (Wren et al., 2011). The variability in τ_w may also depend on how and where velocity is measured, the characterization of boundary conditions and subsequent roughness parameterization, relative roughness, or the method used to calculate it.

To determine the largest source of uncertainty for the SOTT, the variability in τ_{oc} estimates associated with $v_o \pm 20\%$ and variability in τ_w calculated from flume trials were compared. For example, Scenario 1 (16°C & 16.9%Ev) assumed $v_o = 17,325$ cSt. When comparing the uncertainty associated with $v_o \pm 20\%$ on the rope formation, ripple formation, and break-apart/resuspension τ_{oc} , the error bars accounted for ± 0.01 Pa, ± 0.02 Pa, and ± 0.05 Pa, respectively. In a flume trial on sand with $v_o = 18,001$ cSt; the corresponding $\tau_{oc} \pm \sigma$ for rope formation, ripple formation, and break-apart/resuspension thresholds were 0.18 ± 0.06 , 0.31 ± 0.12 , and 0.48 ± 0.2 Pa, respectively.

It is clear that the method uncertainty associated with estimating τ_{oc} is larger than the uncertainty caused by $v_o \pm 20\%$. Therefore, to capture variability when predicting τ_{oc} thresholds using the SOTT, it is important to compare results with τ_{oc} ranges for similar oil viscosities and sediment sizes determined from flume-based experiments (See Table 3-5 in Chapter 3 in for a summary of τ_{oc} values). Dalyander et al. (2015) found that the uncertainty associated with τ_w was less influential than τ_{oc} in predicting the transport of sand-oil agglomerates in low energy

environments, but the uncertainty associated with high energy environments propagated “through to τ_w and potentially dominate(d) the uncertainty in choice of τ_{oc} ”. Therefore, to minimize SOTT uncertainty, spatially- and temporally-varying *in-situ* measurements of U should be used, if available, to estimate the anticipated range of τ_w estimates and compared with τ_{oc} . In addition, accurate estimates of v_o at the *in-situ* water temperature will reduce uncertainty associated with τ_{oc} and improve the SOTT’s prediction of oil transport.

Comparing Oil and Sediment Mobility

To compare predicted oil mobility with the anticipated range of sediment transport thresholds, the four reference curves, displaying SOTT results, are presented below (Figure 4-5 to Figure 4-8). Based on the prediction that typical sediment τ_{sc} in the Kalamazoo River ranges between 0.10 and 0.15 Pa (Waterman et al., 2015), Scenario 2 was the only one with a τ_{oc} value (0.14 Pa) within the τ_{sc} range. This suggests that migration of oil along the bed may have initiated, for the assumed conditions, prior to the oil being buried by the silt/clay fraction in the river. For all other scenarios, the silt/clay would likely have moved prior to oil migration or resuspension, potentially burying, or coating the oil. For Scenario 2, at $U_c = 0.38$ m/s, the Re_{sc}^* for $d_{50}=0.031$ mm was smaller than the minimum Re_{oc}^* , therefore, incipient motion of the smallest fraction of sediment would likely occur prior to oil rope formation. Similarly, at $U_c = 0.60$ m/s, the sediment would likely move prior to oil reaching the break-apart/resuspension threshold.

In Scenario 1, when $U_c = 0.44$ m/s, the smallest fraction of sediment ($d_{50}=0.031$ mm) would likely undergo incipient motion before the oil started to migrate along the bed. At $U_c=0.75$ m/s, the oil’s break-apart/resuspension threshold, the entire sediment range would likely be moving as bedload or suspended load transport.

Scenarios 3 and 4 are different from Scenarios 1 and 2 because the τ_{oc} values are larger. Therefore, even the largest sediment fraction ($d_{50} = 0.0625$ mm) would likely be mobilized at or slightly below the rope formation U_c threshold. For Scenario 3 ($U_c = 0.6$ m/s) and Scenario 4 ($U_c = 0.5$ m/s), the smaller sediment fraction would likely already be in motion prior to oil movement thus causing the oil to be buried or coated with silt/clay. At the oil's break-apart/resuspension threshold in Scenario 3 ($U_c = 1.1$ m/s) and Scenario 4 ($U_c = 0.95$ m/s), the bed would likely be unstable due to silt/clay's relatively low τ_{sc} , thus increasing the importance of burial and exhumation processes when locating the oil.

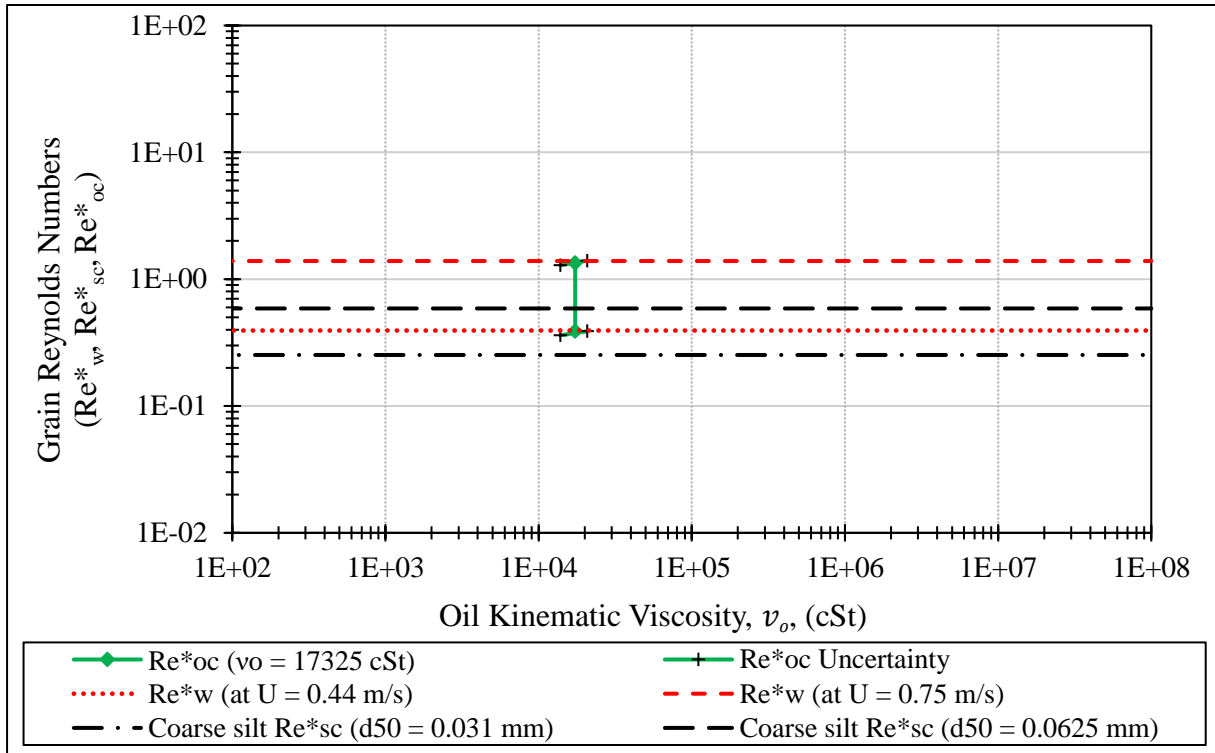


Figure 4-5: SOTT reference curve from Scenario 1.

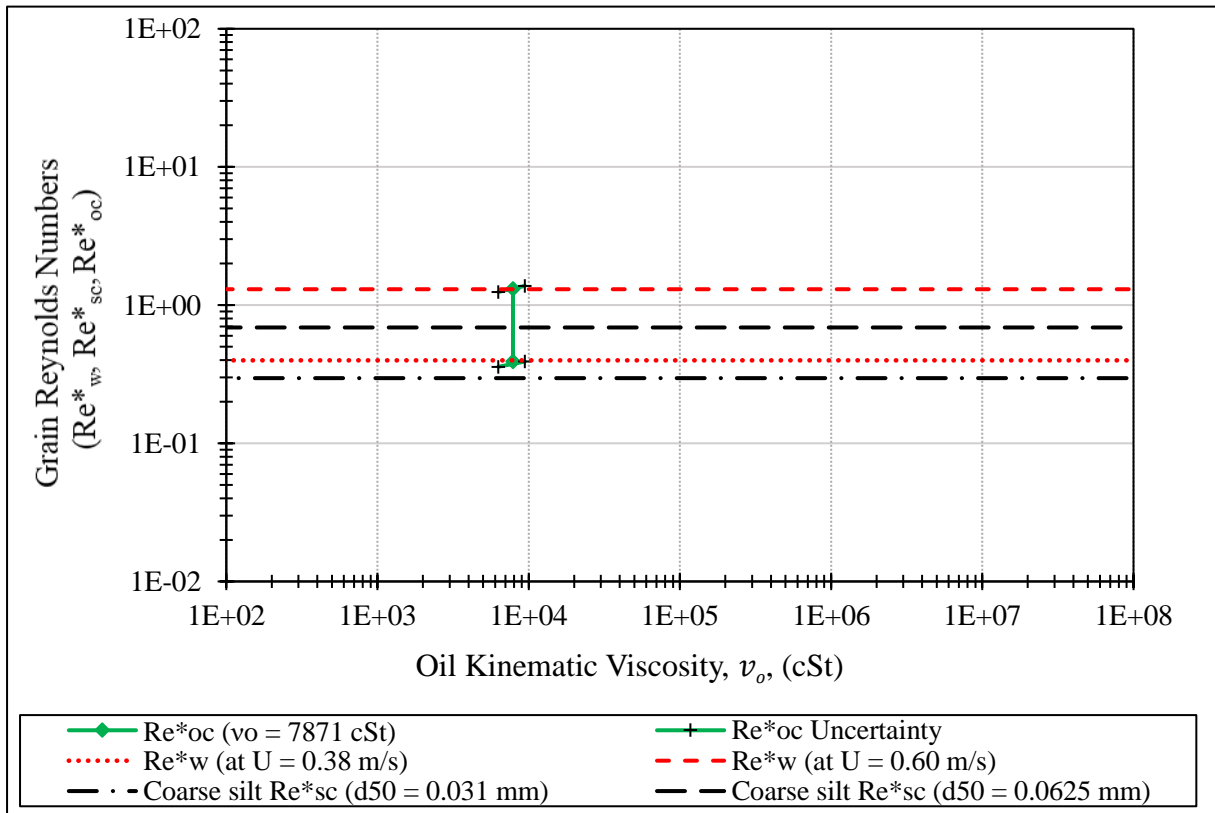


Figure 4-6: SOTT reference curve from Scenario 2.

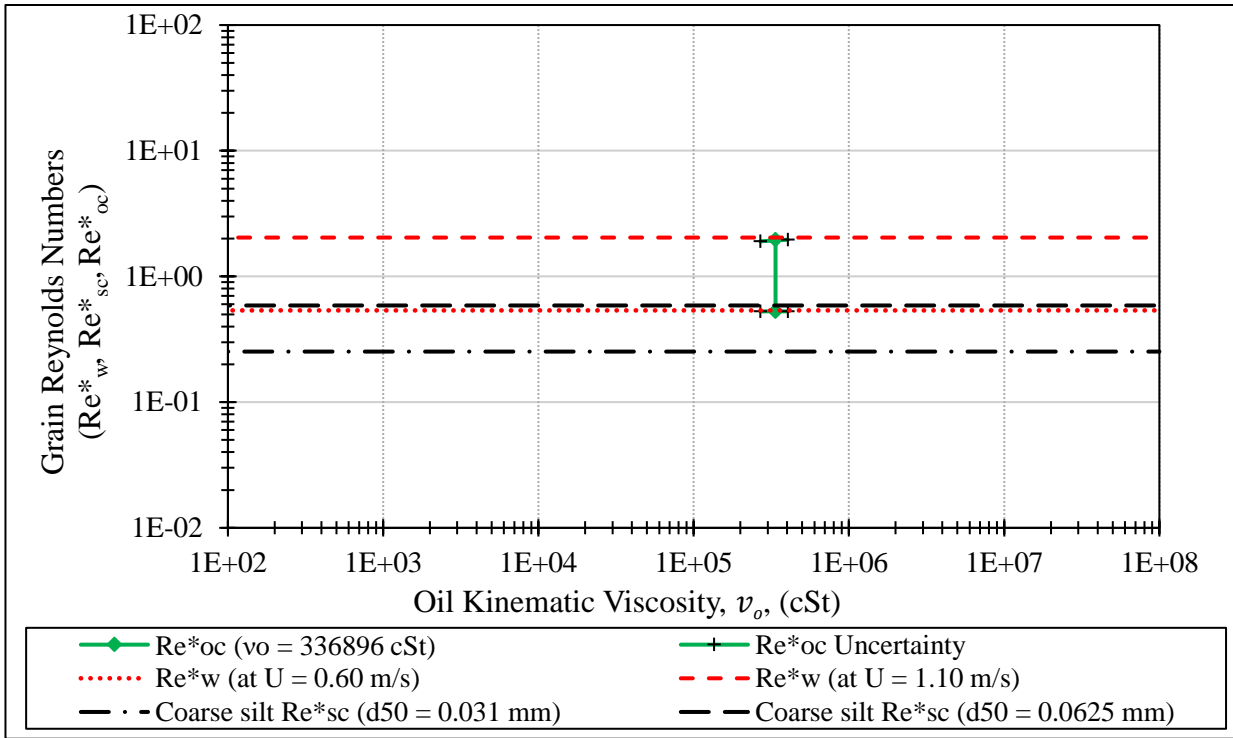


Figure 4-7: SOTT reference curve from Scenario 3.

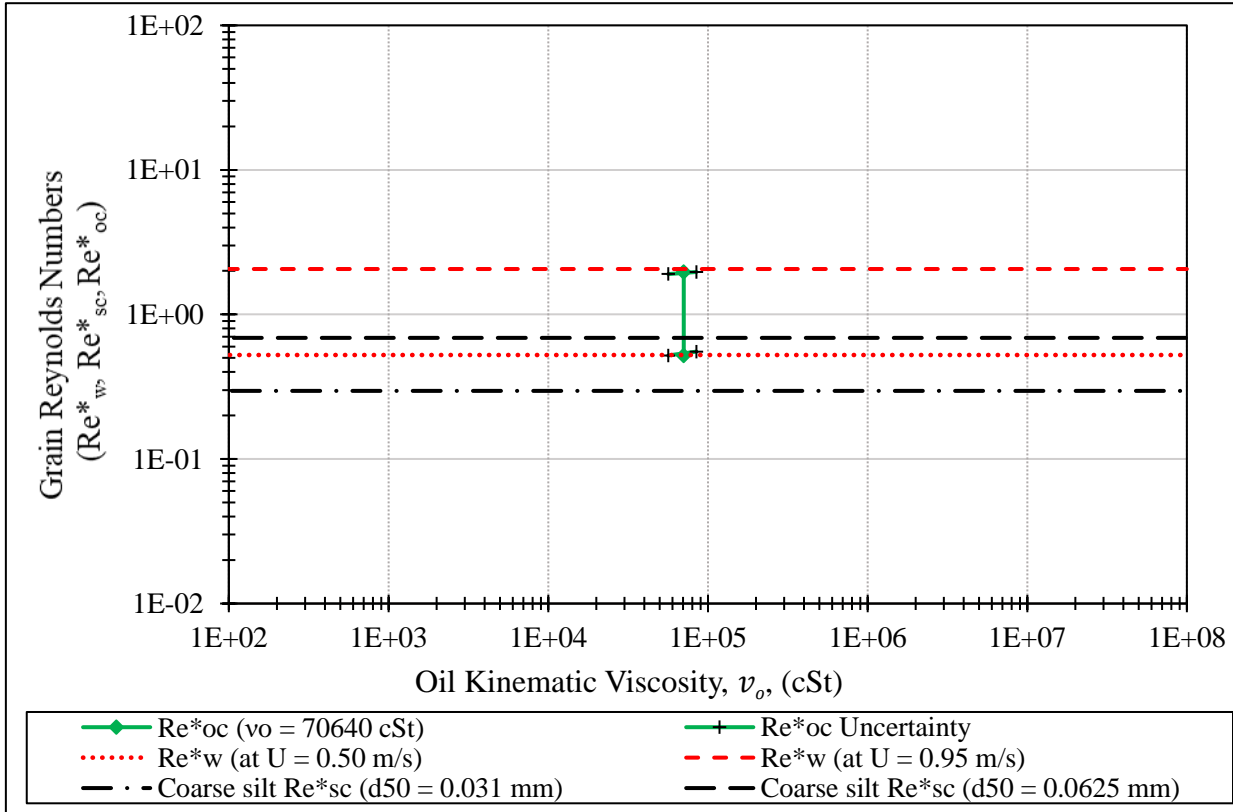


Figure 4-8: SOTT reference curve from Scenario 4.

4.4.1.4 Comparison to Literature

Scenario 2 (22°C & 16.9%Ev) most closely represents the Kalamazoo River spill conditions. The SOTT rope formation, ripple formation, and break-apart/resuspension τ_{oc} predictions for this scenario were 0.14 Pa, 0.27 Pa, and 0.41 Pa, respectively. Laboratory- (Perkey et al., 2014) and field- (Waterman et al., 2015) flume studies were conducted on Kalamazoo River oiled sediment “to identify erosion parameters that can be implemented in a numerical hydrodynamic and sediment transport model to represent erosional characteristics of oiled sediment in depositional areas of the Kalamazoo River” (Waterman et al., 2015). Perkey et al. (2014) determined the erosion τ_{sc} (i.e., displacement of the sediment surface) for the top 5 cm of a river sediment core to be between 0.1 and 1.6 Pa. Waterman et al. (2015) evaluated oiled sediment erosion thresholds at five locations within depositional areas of the Kalamazoo River. They determined the typical τ_{sc} fell between 0.10 and 0.15 Pa with values ranging up to 0.67 Pa. Provided all available information, a conservative τ_{oc} threshold of 0.4 Pa was used to model the sunken oil erodibility for the river (Fitzpatrick et al., 2015b).

The SOTT predicted rope formation τ_{oc} (0.14 Pa) fell within measured Waterman et al. (2015) erosion τ_{oc} (0.1 to 0.15 Pa). The SOTT estimated ripple formation τ_{oc} (0.27 Pa) was slightly larger. The SOTT predicted break-apart/resuspension τ_{oc} (0.41 Pa) compared well with the sunken oil erosion τ_{oc} used in the Kalamazoo River models (Fitzpatrick et al., 2015b). The 0.01 Pa variation between the measured τ_{oc} and the SOTT predicted break-apart/resuspension τ_{oc} suggests that this tool provides a reasonable estimate of sunken oil transport and could have been used to assist decision-makers during the Kalamazoo River spill response.

4.4.2 Application to Sunken Oil Spill

In the event of a sunken oil spill, responders could use the SOTT as an initial estimate of sunken oil transport using data from the *in-situ* environmental conditions (e.g., current velocity, sediment type), open-source databases (e.g., NOAA's ERMA, USGS Stream Stats) or the literature to predict the range of τ_w . As more information becomes available during the spill, and *in-situ* conditions can be measured (e.g., current velocity, substrate type, water temperature) predictions of sunken oil transport can be refined. The Kalamazoo River case study provided one way in which the SOTT could be tested to predict the critical velocity required to transport the oil. If the *in-situ* velocity range is known, then the SOTT could be tuned to evaluate the effects of diurnal temperature fluctuations, the effect of oil weathering on the viscosity range, or the influence of bed roughness (i.e., sediment size) on the transport of sunken oil. Because the SOTT uses generalized assumptions to adjust U to \bar{U} and $\bar{u}(z)$, more accurate estimates of τ_w may be calculated using external sources with the capability of using direct measurements of \bar{U} and $\bar{u}(z)$ or different methods (e.g., Turbulent Kinetic Energy) to compare with oil CSS estimates.

Based on results from the sensitivity analysis conducted in Chapter 2, when using global methods (e.g., Chezy/Momentum, Manning/Momentum), τ_w estimates are more sensitive to roughness parameter variability, whereas local methods (e.g., Law of the Wall – Single Point) require accurate estimates of near-bed velocity and velocity fluctuations. Therefore, bathymetric surveys and characterization of the bed should be a priority when using these global methods in the field. Recording near-bed velocity variability is essential to produce accurate ranges of *in-situ* τ_w estimates when using local methods. In those spills where a sieve analysis using sediment cores or bathymetric surveys is not possible, τ_w can be calculated over the anticipated range of sediment types and sizes.

4.5 Conclusions and Future Research

This chapter described the multi-year process of developing a prototype sunken oil transport tool (SOTT). The methods and data used to predict sunken oil transport and a case study using an actual spill application of the tool and interpretation of results were discussed. The process began through a series of meetings facilitated by CRRC with OR&R to identify the relevant questions asked by responders in the event of a sunken oil spill to improve response decision-making. CRRC and OR&R developed laboratory- and flume-based experiments to answer the identified response questions and minimize knowledge gaps. The experiments identified the factors driving sunken oil transport. Empirical relationships were developed to relate oil viscosity to CSS thresholds.

The results from the oil CSS experiments were discussed by spill responders from multiple agencies (e.g., U.S. Army Corps, USGS) that provided feedback as to how the data should be used and visualized in the SOTT. In the event of a sunken oil spill, responders can input the spilled oil's characteristics (i.e., density, viscosity) and *in-situ* environmental conditions (i.e., water velocity, density, sediment size) to evaluate if oil will likely transport along the bottom, mobilize into the water column, or be buried by sediments. SOTT results could: (1) help inform placement of response assets, (2) relevant response techniques (e.g., poling operations, water column snare/pom-pom configurations), and (3) direct where responders look for sunken oil (e.g., downstream, where the oil sank).

In the event of a spill, an accurate estimate or range of the spilled oil's kinematic viscosity (for fresh and weathered conditions) at the *in-situ* water temperature should be used in the SOTT. Ideally, viscosity would be measured directly, but if instruments are unavailable, then a range of viscosities can be obtained using an existing database (e.g., ADIOS, Environment Canada). The environmental conditions can be initially estimated using values found in literature or

environmental databases (e.g., AXIOM, ERMA). To improve the accuracy of oil and sediment transport predictions throughout the spill event, values from the literature and databases should be replaced with *in-situ* measurements of water velocity (near-bed and depth-averaged) and grain size distribution.

Relationships used in the SOTT were developed from oil CSS experiments conducted on a glued (immobile) boundary. Therefore, further research should be conducted to understand how mobile sediment and an unstable bed would impact oil CSS thresholds. Experiments were conducted using No. 6 HFO mixed with clay, therefore, further research should be conducted using other oils with the propensity to sink in fresh water environments (e.g., diluted bitumen) over a wide temperature range to capture the non-linear influence of oil viscosity. Additionally, further improvements to the SOTT could include integrating direct measurements of *in-situ* velocity profiles from acoustic doppler current profilers to calculate BSS (e.g., Turbulent Kinetic Energy Method).

A database could be developed that would allow responders to query information from the catalogue of sunken oil experimental images and videos. Key name searches could be based on the input criteria (e.g., oil properties, environmental conditions), and would direct users to relevant images of sunken oil that could be compared to visual observations of the spilled oil obtained *in-situ* by remotely operated vehicles or diver observations.

CONCLUSIONS AND RECOMMENDATIONS

5.1 Conclusions

This section summarizes the major conclusions developed from this dissertation research, highlights their significance, and recommends future research to fill relevant knowledge gaps. The overarching objective of this dissertation was to define the stages of transport using sunken, No. 6 HFO, quantify the oil's CSS at those thresholds, and develop a tool using the experimental data that can be used by responders to predict if *in-situ* environmental conditions are sufficient to mobilize sunken oil.

To accomplish the research objectives, a comprehensive hydraulic analysis (See Chapter 2) was necessary as it had never been done for the newly-constructed MacFarlane Flume. [N.B., Findings from the hydraulic analysis are not described in detail here unless directly related to predicting sunken oil transport]. The hydraulic analysis was necessary to quantify baseline flow conditions, identify instrument limitations, and determine which BSS methods were valid under various flow regimes. Findings from Chapter 2 provided the foundation for all BSS calculations and methods used in the oil CSS experiments and to develop the SOTT.

Based on the sensitivity analysis (See Chapter 2), local BSS estimates were equally sensitive to velocity and roughness variability, whereas the global methods tended to be more sensitive to roughness variability alone. Therefore, in the event of an oil spill, the first priorities are to determine the expected velocity range and then to collect sediment cores to determine particle size distribution (PSD). Providing a velocity range and knowing the PSD will improve the accuracy of global BSS estimates. If more information becomes available and instruments can be deployed to measure near-bed velocity, then local methods could be used to predict *in-situ* BSS and more accurately predict sediment or oil transport processes.

From the oil CSS experiments (See Chapter 3), the driving factors used to predict sunken oil transport were the oil's kinematic viscosity (ν_o) and the median sediment size (d_{50}). Empirical relationships using ν_o and d_{50} were developed to predict an oil's CSS for multiple stages of movement. These are two measurable parameters that can be leveraged in a spill event to predict sunken oil transport thresholds. Additionally, for $\nu_o < 2 \times 10^4$ cSt, there are multiple thresholds of movement and the number of oil droplets leaving the oil increases. When $\nu_o > 6 \times 10^4$ cSt, transport is more likely to occur as a single event with the oil remaining intact, resulting in bedload transport in the direction of flow.

The SOTT provides a user-friendly platform for responders to input the *in-situ* environmental conditions (i.e., water velocity, density, sediment size) and oil properties (i.e., density, viscosity) to predict sunken oil transport. SOTT results are presented in the form of a reference curve and summary tables so that responders can predict if oil may be transported along the bottom, resuspended into the water column, or buried by sediments. SOTT results could help inform placement of response assets, evaluate relevant response techniques (e.g., poling operations, water column snare/pom-pom configurations), and direct where responders look for the sunken oil (e.g., downstream, where the oil sank).

5.2 Significance

Prior to this research, there was limited experimentally-derived data available for oil spill response operations regarding the CSS of sunken oils. This research provides the CSS of No. 6 HFO, a commonly-transported oil with a propensity to sink, over a range of environmentally-relevant conditions and oil viscosities. The empirically-derived equations could be incorporated into existing models or used by oil spill modelers to predict the trajectory of sunken oil more accurately. The SOTT provides a user-friendly, open-source tool that is readily available to oil

spill responders in the event of a sunken oil spill. Understanding the range of environmental conditions that may cause oil to move can help locate the oil, estimate if it has been buried by sediments, and direct the type and placement of response assets.

5.3 Recommendations for Future Research

Recommended future research projects specific to CRRC's flume:

- Conduct experiments on mobile sediments to validate the applicability of estimating the sediment's CSS thresholds using the Shields curve.
- Re-evaluate all hydrodynamic conditions in case of using a different water depth. The transitions from sub- to super-critical and laminar to turbulent should be recalculated and the associated VFD settings defined. This change would alter the empirical relationships between VFD setting and free-stream velocity and depth-averaged velocity, and the velocity ranges for which each BSS method is valid.

Recommended future research projects relevant to external laboratories and field research:

- Evaluate the effects of current velocity on sinking mechanisms to determine the variability in size, shape, thickness, and morphology of the oil once settled to the bed.
- Using variable stranding patterns, conduct experiments to evaluate the impacts of morphology, thickness, size, and shape on CSS thresholds.
- Assess the influence of sloping beds or bedforms on CSS values and compare the thresholds of movement determined in this dissertation for a zero-sloping bed. Specifically for the gravity spreading, rope formation, and ripple formation thresholds as a downward sloping bed (in the direction of flow) would initiate movement for low viscosity oils in environments with no or minimal velocity present. Therefore, potentially reducing the CSS required to initiate oil transport. Alternatively, how would

the CSS of the oil change once it is trapped in a local bedform or offshore trench, and how would these values compare with CSS of oil on a zero-sloping bed.

- Conduct experiments on a mobile bed (i.e., non-adhered substrate) to determine the relationship between oil and sediment mobility, and to evaluate sediment uptake or adherence of sediments to the oil. Experiments should be performed with cohesive sediments and with heterogenous mixed beds to determine what size class of sediments controls CSS thresholds.
- Characterize oil viscosity for heavy refined or crude products over a wide temperature (e.g., 0 to 35°C) and shear rate (e.g., 0.01 to 16 Hz) ranges to establish oil-specific relationships. Establish temperature-viscosity relationships for various oil types and weathering states to allow modelers to adjust oil viscosity more accurately to *in-situ* temperatures, thus improving oil spill trajectory and fate modeling.
- Compile the images, videos, experimental properties, and oil thresholds from this research into a database, so that responders can obtain information in a single location. Queries could be based on the input criteria (e.g., oil properties, environmental conditions), and direct users to relevant images of sunken oil to compare with visual observations of the *in-situ* oil obtained by remotely operated vehicles or diver observations.
- Using the SOTT, conduct an additional sensitivity analysis on the various input parameters. Further refine the influence of the mechanistic factors potentially driving transport.

LIST OF REFERENCES

- Abivin, P., Taylor, S. D., & Freed, D. (2012). Thermal behavior and viscoelasticity of heavy oils. *Energy & Fuels*, 26(6), 3448–3461. <https://doi.org/10.1021/ef300065h>
- Aldridge, B. N., & Garrett, J. M. (1973). *Roughness coefficients for stream channels in Arizona* (p. 87) [Open-File Report]. United States Department of the Interior Geologic Survey. <https://pubs.usgs.gov/of/1973/0003/report.pdf>
- Anderson, A. G., Paintal, A. S., & Davenport, J. T. (1970). *Tentative design procedure for riprap-lined channels*. Highway Research Board, Division of Engineering, National Research Council.
- API, American Petroleum Institute. (2016a). *Sunken oil detection and recovery operational guide* (pp. 1–36). API Publishing Services.
- API, American Petroleum Institute. (2016b). *Sunken oil detection and recovery report* (p. 126). API Publishing Services.
- ASTM. (2015a). *Test method for determining the rheological properties of asphalt binder using a dynamic shear rheometer (ASTM D7175-15)*. ASTM International: D04 Committee. <https://doi.org/10.1520/D7175-15>
- ASTM. (2015b). *Test method for measuring pavement macrotexture depth using a volumetric technique (E965 – 15)*. ASTM International. <https://doi.org/10.1520/E0965-15>
- ASTM. (2017a). *Test method for density, relative density, or API gravity of crude petroleum and liquid petroleum products by hydrometer method (ASTM D1298—12b)*. ASTM International. <https://doi.org/10.1520/D1298-12BR17>
- ASTM. (2017b). *Test methods for particle-size distribution (gradation) of soils using sieve analysis (ASTM D6913-04 2009)*. ASTM International. https://doi.org/10.1520/D6913_D6913M-17
- Babaeyan-Koopaei, K., Ervine, D. A., Carling, P. A., & Cao, Z. (2002). Velocity and turbulence measurements for two overbank flow events in River Severn. *Journal of Hydraulic Engineering*, 128(10), 891–900. [https://doi.org/10.1061/\(ASCE\)0733-9429\(2002\)128:10\(891\)](https://doi.org/10.1061/(ASCE)0733-9429(2002)128:10(891))
- Bagherimiyab, F., & Lemmin, U. (2013). Shear velocity estimates in rough-bed open-channel flow. *Earth Surface Processes and Landforms*, 38(14), 1714–1724. <https://doi.org/10.1002/esp.3421>
- Beegle-Krause, C., Barker, C., Watabayashi, G., & Lehr, W. J. (2006). Long-term transport of oil from T/B DBL-152: lessons learned for oils heavier than seawater. *Environment Canada Arctic and Marine Oil Spill Program Technical Seminar (AMOP) Proceedings*. AMOP.

- Berenbrock, C., & Tranmer, A. W. (2008). *Simulation of flow, sediment transport, and sediment mobility of the Lower Coeur d'Alene River, Idaho* (Scientific Investigations Report No. 2008–5093. U.S. Geological Survey. <https://pubs.usgs.gov/sir/2008/5093/pdf/sir20085093.pdf>
- Biron, P. M., Robson, C., Lapointe, M. F., & Gaskin, S. J. (2004). Comparing different methods of bed shear stress estimates in simple and complex flow fields. *Earth Surface Processes and Landforms*, 29(11), 1403–1415. <https://doi.org/10.1002/esp.1111>
- Boudreau, B. P., & Jorgensen, B. B. (2001). *The benthic boundary layer: Transport processes and biogeochemistry*. Oxford University Press.
- Boufadel, M. C., Fitzpatrick, F., Cui, F., & Lee, K. (2019). Computation of the mixing energy in rivers for oil dispersion. *Journal of Environmental Engineering*, 145(10), 06019005. [https://doi.org/10.1061/\(ASCE\)EE.1943-7870.0001581](https://doi.org/10.1061/(ASCE)EE.1943-7870.0001581)
- Brookfield Engineering. (n.d.). *Brookfield dial viscometer: Opening instructions (Manual No. M/85-150-P700)*. Brookfield Engineering Laboratories, INC. Retrieved February 16, 2019. <https://www.brookfieldengineering.com>
- Buffington, J. M., & Montgomery, D. R. (1997). A systematic analysis of eight decades of incipient motion studies, with special reference to gravel-bedded rivers. *Water Resources Research*, 33(8), 1993–2029. <https://doi.org/10.1029/96WR03190>
- Buffington, J. M., & Montgomery, D. R. (1999). A Procedure for classifying textural facies in gravel-bed rivers. *Water Resources Research*, 35(6), 1903–1914. <https://doi.org/10.1029/1999WR900041>
- Buscombe, D., & Conley, D. C. (2012). Effective shear stress of graded sediments. *Water Resources Research*, 48(5). <https://doi.org/10.1029/2010WR010341>
- Chaudhry, H. M. (2008). *Uniform Flow* (2nd ed.). Springer.
- Chow, V. T. (1959). *Open Channel Hydraulics*. Prentice-Hall.
- Cloutier, D., Amos, C. L., Hill, P. R., & Lee, K. (2002). Oil erosion in an annular flume by seawater of varying turbidities: A critical bed shear stress approach. *Spill Science & Technology Bulletin*, 8(1), 83–93. [https://doi.org/10.1016/S1353-2561\(02\)00115-9](https://doi.org/10.1016/S1353-2561(02)00115-9)
- Conmy, R.N., DiPinto, L., Kukulya, A., Garcia-Pineda, O., Tulis, D., Sundaravadivelu, D., Gloekler, M., Hall, A., Fischell, E., Gomez-Ibanez, D. (2021). Advances in underwater oil plume detection capabilities. *Proceedings of the International Oil Spill Conference, USA*.
- CRRC. (2007). *Submerged oil – State of the practice and research needs* (p. 29+ appendix). Coastal Response Research Center (CRRC).

- Dalyander, P. S., Long, J. W., Plant, N. G., & Thompson, D. M. (2014). Assessing mobility and redistribution patterns of sand and oil agglomerates in the surf zone. *Marine Pollution Bulletin*, 80(1), 200–209. <https://doi.org/10.1016/j.marpolbul.2014.01.004>
- Dalyander, P. S., Plant, N. G., Long, J. W., & McLaughlin, M. (2015). Nearshore dynamics of artificial sand and oil agglomerates. *Marine Pollution Bulletin*, 96(1), 344–355. <https://doi.org/10.1016/j.marpolbul.2015.04.049>
- DARRP, NOAA. (2018). *M/T Athos I*. <https://darrp.noaa.gov/oil-spills/mt-athos-i>
- Dawson, G. P., Johns, B., & Soulsby, R. L. (1983). Chapter 6: A numerical model of shallow-water flow over topography. In B. Johns (Ed.), *Elsevier Oceanography Series* (Vol. 35, pp. 267–320). Elsevier. [https://doi.org/10.1016/S0422-9894\(08\)70504-X](https://doi.org/10.1016/S0422-9894(08)70504-X)
- Delvigne, G. A. L., & Sweeney, C. E. (1988). Natural dispersion of oil. *Oil and Chemical Pollution*, 4(4), 281–310. [https://doi.org/10.1016/S0269-8579\(88\)80003-0](https://doi.org/10.1016/S0269-8579(88)80003-0)
- Dietrich, W. E., & Smith, J. D. (1983). Influence of the point bar on flow through curved channels. *Water Resources Research*, 19(5), 1173–1192. <https://doi.org/10.1029/WR019i005p01173>
- Dollhopf, R. H., Fitzpatrick, F. A., Kimble, J. W., Capone, D. M., Graan, T. P., Zelt, R. B., & Johnson, R. (2014). Response to heavy, non-floating oil spilled in a great lakes river environment: A multiple-lines-of-evidence approach for submerged oil assessment and recovery. *International Oil Spill Conference Proceedings, 2014*(1), 434–448. <https://doi.org/10.7901/2169-3358-2014.1.434>
- Echavarria-Gregory, A. M., & Englehardt, J. D. (2015). A predictive Bayesian data-derived multi-modal Gaussian model of sunken oil mass. *Environmental Modelling & Software*, 69, 1–13.
- El-Dessouky, H. T., & Ettouney, H. M. (2002). *Fundamentals of Salt Water Desalination*. Elsevier. <https://doi.org/10.1016/B978-0-444-50810-2.X5000-3>
- Elger, D., Williams, B., Crowe, C., & Roberson, J. (2013). *Engineering Fluid Mechanics* (10th ed.). John Wiley & Sons, Inc.
- Englehardt, J. D., Echavarria-Gregory, A. M., & Avellaneda, P. M. (2010). *Development of a predictive Bayesian data-derived multimodal Gaussian model of sunken oil mass location and transport* (Final Report NOAA Grant Number: NA04NOS4190063, Project Number: 08-088). Coastal Response Research Center. https://crrc.unh.edu/sites/crrc.unh.edu/files/final_report_univ_miami_sosim_development.pdf

- Environment Canada. (2013). *Properties, composition and marine spill behaviour, fate and transport of two diluted bitumen products from the Canadian oil sands* (Technical Report No. En84-96). Environment Canada, Emergencies Sciences and Technology; Fisheries and Oceans Canada, Center for Offshore Oil, Gas and Energy Research; Natural Resources Canada.
- Etkin, D. S., French McCay, D., & Michel, J. (2007). *Review of the state-of-the-art on modeling interactions between spilled oil and shorelines for the development of algorithms for oil spill risk analysis modeling* (MMS Contract 0106PO39962). MMS OCS Study.
- Fieldhouse, B. G., Hollebone, B. P., Singh, N. R., Tong, T. S., & Mullin, J. V. (2010). Artificial weathering of oils by rotary evaporator. *Proceedings of the 33rd AMOP Conference, CA*, 159–180.
- Fitzpatrick, F. A., Boufadel, M. C., Johnson, R., Lee, K., Graan, T. P., Bejarano, A. C., Zhu, Z., Waterman, D., Capone, D. M., Hayter, E., Hamilton, S. K., Dekker, T., Garcia, M. H., & Hassan, J. S. (2015a). *Oil-particle interactions and submergence from crude oil spills in marine and freshwater environments—Review of the science and future science needs* (Open File No. 2015–1076). U.S. Department of the Interior, U.S. Geological Survey. <http://dx.doi.org/10.3133/ofr20151076>
- Fitzpatrick, F. A., Johnson, R., Zhu, Z., Waterman, D., McCulloch, R. D., Hayter, E. J., Garcia, M. H., Boufadel, M., Dekker, T., Hassan, J. S., Soong, D. T., Hoard, C. J., & Lee, K. (2015b). Integrated modeling approach for fate and transport of submerged oil an oil-particle aggregates in a freshwater riverine environment. *Proceedings of the 10th Federal Interagency Sedimentation Conference (SEDHYD2015)*, USA.
- Fitzpatrick, M., Tebeau, P. A., & Hansen, K. A. (2014). *Development of bottom oil recovery systems—Final project report*. [Report No. CG-D-09-13]. USCG Research and Development Center.
- Gaines, R. A., & Priestas, A. M. (2013). *Particle size distribution of bed sediments along the Mississippi river, Grafton, Illinois, to head of passes, Louisiana, November 2013*. (MRG&P Report No. 7). United States Army Corp of Engineers , Coastal and Hydraulics Laboratory, Engineer Research and Development Center.
- Garcia, M. H. (2000). The legend of A.F. Shields. *Journal of Hydraulic Engineering*, 125, 718–723.
- Gloekler, M. D., Ballestero, T. P., Dave, E. V., Gaudreau, I. P., Watkins, C. B. R., & Kinner, N. E. (2017). Movement and erosion of Alberta bitumen along the bottom as a function of temperature, water velocity and salinity. *Proceedings of the International Oil Spill Conference, USA*, 2306–2326. <https://doi.org/10.7901/2169-3358-2017.1.2306>
- Gustitus, S. A., & Clement, T. P. (2017). formation, fate, and impacts of microscopic and macroscopic oil-sediment residues in nearshore marine environments: A critical review. *Reviews of Geophysics*, 55(4), 1130–1157. <https://doi.org/10.1002/2017RG000572>

- Hansen, K. A., Guidroz, L., Hazel, B., Fitzpatrick, M., & Johnson, G. W. (2014). Sunken oil recovery system recommendations. *Proceedings of the International Oil Spill Conference, USA*. 2014–2023. <https://doi.org/10.7901/2169-3358-2014.1.2014>
- Harper, J. R., Sergy, G., & Britton, L. (2018). *uSCAT technical reference manual: Underwater seabed cleanup assessment technique for sunken oil*. [Technical Report]. Coastal & Ocean Resources. www.uscat.ca
- Hayter, E., McCulloch, R., Redder, T., Boufadel, M., Johnson, R., & Fitzpatrick, F. (2015). *Modeling the transport of oil particle aggregates and mixed sediment in surface waters*. [ERDC Technical Report]. U.S. Army Corp of Engineers.
- ICCOPR. (2015). *Oil pollution research and technology plan*. U.S. Interagency Coordinating Committee on Oil Pollution Research. <http://hdl.handle.net/2027/mdp.39015029854885>
- International Maritime Organization. (2014). *Operational guidelines on sunken and submerged oil assessment and removal techniques* (Annex of Report I) <http://www.imo.org/en/OurWork/Environment/PollutionResponse/Inventory%20of%20information/Pages/Oil-Spill-Response.aspx>
- Jacketti, M., Beegle-Krause, C. J., & Englehardt, J. D. (2020). A review on the sinking mechanisms for oil and successful response technologies. *Marine Pollution Bulletin*, 160, 111626. <https://doi.org/10.1016/j.marpolbul.2020.111626>
- Jacketti, M., Ji, C., Englehardt, J. D., & Beegle-Krause, C. (2019). Development of the SOSim model for inferential tracking of subsurface oil. *Proceedings of the Forty-Second AMOP Technical Seminar, CA*. 485–501.
- Khelifa, A., Stoffyn-Egli, P., Hill, P. S., & Lee, K. (2002). Characteristics of oil droplets stabilized by mineral particles: Effects of oil type and temperature. *Spill Science & Technology Bulletin*, 8(1), 19–30. [https://doi.org/10.1016/S1353-2561\(02\)00117-2](https://doi.org/10.1016/S1353-2561(02)00117-2)
- Kim, S.-C., Friedrichs, C. T., Maa, J. P.-Y., & Wright, L. D. (2000). Estimating bottom stress in tidal boundary layer from acoustic Doppler velocimeter data. *Journal of Hydraulic Engineering*, 126(6), 399–406. [https://doi.org/10.1061/\(ASCE\)0733-9429\(2000\)126:6\(399\)](https://doi.org/10.1061/(ASCE)0733-9429(2000)126:6(399))
- King, T. L., Robinson, B., Boufadel, M., & Lee, K. (2014). Flume tank studies to elucidate the fate and behavior of diluted bitumen spilled at sea. *Marine Pollution Bulletin*, 83(1), 32–37. <https://doi.org/10.1016/j.marpolbul.2014.04.042>
- Koca, K., Noss, C., Anlanger, C., Brand, A., & Lorke, A. (2017). Performance of the Vectrino Profiler at the sediment–water interface. *Journal of Hydraulic Research*, 55(4), 573–581. <https://doi.org/10.1080/00221686.2016.1275049>
- Le Roux, J. P. (2005). Grains in motion: A review. *Sedimentary Geology*, 178(3), 285–313. <https://doi.org/10.1016/j.sedgeo.2005.05.009>

- Lee, K. (2002). Oil–particle interactions in aquatic environments: Influence on the transport, fate, effect and remediation of oil spills. *Spill Science & Technology Bulletin*, 8(1), 3–8. [https://doi.org/10.1016/S1353-2561\(03\)00006-9](https://doi.org/10.1016/S1353-2561(03)00006-9)
- Lehr, W., Jones, R., Evans, M., Simecek-Beatty, D., & Overstreet, R. (2002). Revisions of the ADIOS oil spill model. *Environmental Modelling & Software*, 17(2), 189–197. [https://doi.org/10.1016/S1364-8152\(01\)00064-0](https://doi.org/10.1016/S1364-8152(01)00064-0)
- Leopold, L. B., & Wolman, m. G. (1957). *River channel patterns: Braided, meandering and straight* (Geological Survey Professional Paper No. 282-B). Department of the Interior. <https://pubs.usgs.gov/pp/0282b/report.pdf>
- Limerinos, J. T. (1970). *Determination of the manning coefficient from measured bed roughness in natural channels* (Geological Survey Water-Supply Paper No. 1898-B). United States Department of Interior, United States Geological Survey. <https://doi.org/10.3133/wsp1898B>
- Luo, P., & Gu, Y. (2007). Effects of asphaltene content on the heavy oil viscosity at different temperatures. *Fuel*, 86(7), 1069–1078. <https://doi.org/10.1016/j.fuel.2006.10.017>
- Madsen, O. S., & Grant, W. D. (1976). QUANTITATIVE DESCRIPTION OF SEDIMENT TRANSPORT BY WAVES. *Coastal Engineering Proceedings*, 15, 64–64. <https://doi.org/10.9753/icce.v15.64>
- Martin, J. D., Adams, J., Hollebone, B., King, T., Brown, R. S., & Hodson, P. V. (2014). Chronic toxicity of heavy fuel oils to fish embryos using multiple exposure scenarios. *Environmental Toxicology and Chemistry*, 33(3), 677–687. <https://doi.org/10.1002/etc.2486>
- Mehaute, B. L., & Hanes, D. M. (2005). *Ocean Engineering Science*. Harvard University Press.
- Michel, J., & Hansen, K. A. (2017). *Chapter 13: Sunken and submerged oil* (2nd ed.). Oil Spill Science and Technology. Elsevier.
- Michel, J. (2008). Spills of nonfloating oil: Evaluation of response technologies. *Proceedings of the International Oil Spill Conference, USA*. 261–267. <http://ioscproceedings.org/doi/abs/10.7901/2169-3358-2008-1-261>
- Michel, J., & Bambach, P. (2020). *A response guide for sunken oil mats (SOMs): Formation, behavior, detection and recovery*. Department of Commerce, National Oceanic and Atmospheric Administration, National Ocean Service, Office of Response and Restoration, Emergency Response Division.
- Michel, J., & Galt, J. A. (1995). Conditions under which floating slicks can sink in marine settings. *Proceedings of the International Oil Spill Conference, USA*.
- Millero, F., Chen, C., Bradshaw, A., & Schleicher, K. (1980). *A new high pressure equation of state for seawater*. 255–264.

- NASEM. (2016). *Spills of diluted bitumen from pipelines: A comparative study of environmental fate, effects, and response*. The National Academies of Sciences, Engineering and Medicine. <http://nap.edu/21834>
- Nelson, J. M., Shreve, R. L., McLean, S. R., & Drake, T. G. (1995). Role of near-bed turbulence structure in bed load transport and bed form mechanics. *Water Resources Research*, *31*(8), 2071–2086.
- Nikora, V., & Goring, D. (2000). Flow turbulence over fixed and weakly mobile gravel beds. *Journal of Hydraulic Engineering*, *126*(9), 679–690.
[https://doi.org/10.1061/\(ASCE\)0733-9429\(2000\)126:9\(679\)](https://doi.org/10.1061/(ASCE)0733-9429(2000)126:9(679))
- NOAA. (2015). *APEX 3508*. Incident News. <https://incidentnews.noaa.gov/incident/9169>
- NOAA. (2018). *Athos I oil spill infographic*.
https://response.restoration.noaa.gov/sites/default/files/athos-oil-spill-infographic_rev_noaa_819.jpg
- NOAA ORR. (2019). *High water and sunken oil on the great Mississippi*. Office of Response and Restoration, Oil and Chemical Spills - Significant Incidents.
<https://response.restoration.noaa.gov/oil-and-chemical-spills/significant-incidents/high-water-and-sunken-oil-great-mississippi.html>
- NOAA Scientific Support Team. (2012). *Fact sheet: No. 6 fuel oil (Bunker C) spills*. NOAA Hazardous Materials Response and Assessment Division.
- Nortek AS. (2017). *Nortek manuals: The comprehensive manual*.
https://www.nortekgroup.com/assets/documents/ComprehensiveManual_Oct2017_compressed.pdf
- Nortek Scientific. (2012). *Vectrino Profiler: Profiling Velocimeter* [User Guide].
- NRC, National Research Council (1999). *Spills of nonfloating oils: Risk and response*. National Academy Press. <https://doi.org/10.17226/9640>
- Örlü, R., Fransson, J. H. M., & Henrik Alfredsson, P. (2010). On near wall measurements of wall bounded flows—The necessity of an accurate determination of the wall position. *Progress in Aerospace Sciences*, *46*(8), 353–387.
<https://doi.org/10.1016/j.paerosci.2010.04.002>
- Passow, U. (2016). Formation of rapidly-sinking, oil-associated marine snow. *Deep Sea Research Part II: Topical Studies in Oceanography*, *129*, 232–240.
<https://doi.org/10.1016/j.dsr2.2014.10.001>
- Perkey, D. W., Smith, S. J., & Kirklin, T. (2014). *Cohesive sediment erosion field study: Kalamazoo River, Kalamazoo, Michigan*. [Letter Report]. U.S. Army Corps of Engineers Research and Development Center, Coastal and Hydraulics Laboratory.

- Petrae, L. G., ed. (1995). *Barge Morris J. Berman spill: NOAA's scientific response* (HAZMAT Report No. 95-10; p. 63). Hazardous Materials Response and Assessment Division, Office of Ocean Resources Conservation and Assessment, National Oceanic and Atmospheric Administration.
- Pope, N. D., Widdows, J., & Brinsley, M. D. (2006). Estimation of bed shear stress using the turbulent kinetic energy approach—A comparison of annular flume and field data. *Continental Shelf Research*, 26(8), 959–970. <https://doi.org/10.1016/j.csr.2006.02.010>
- Shields, Ing. A. (1936). *Application of similarity principles and turbulence research to bed-load movement*. (Publication No. 167). Hydrodynamics Laboratory - California Institute of Technology.
- Simecek-Beatty, D. (2007). A proposed method for computing re-suspension of submerged oil. *Proceedings of the Arctic and Marine Oil Spill Conference, CA*. 755–768.
- Soulsby, R. L. (1997). *Dynamics of marine sands*. Thomas Telford Services.
- Soulsby, R. L., & Whitehouse, R. (1997). *Threshold of sediment motion in coastal environments*. 1, 149-154.
- Stapleton, K. R., & Huntley, D. A. (1995). Seabed stress determinations using the inertial dissipation method and the turbulent kinetic energy method. *Earth Surface Processes and Landforms*, 20(9), 807–815. <https://doi.org/10.1002/esp.3290200906>
- Sternberg, R. W. (1973). Predicting initial motion and bedload transport of sediment particles in the shallow marine environment. In *Shelf sediment transport: Process and pattern*. 61–82.
- Stout, S., & Wang, Z. (2016). *Standard handbook oil spill environmental forensics* (Second edition.). Academic Press. [https://ebookcentral.proquest.com/lib/\[SITE_ID\]/detail.action?docID=4390319](https://ebookcentral.proquest.com/lib/[SITE_ID]/detail.action?docID=4390319)
- Strickler, A. (1923). *contributions to the question of a velocity formula and roughness data for streams, channels and closed pipelines*. 112.
- Thompson, C. E. L., Amos, C. L., Angelaki, M., Jones, T. E. R., & Binks, C. E. (2006). An evaluation of bed shear stress under turbid flows. *Journal of Geophysical Research: Oceans*, 111(C4). <https://doi.org/10.1029/2005JC003287>
- Thompson, C. E. L., Amos, C. L., Lecouturier, M., & Jones, T. E. R. (2004). Flow deceleration as a method of determining drag coefficient over roughened flat beds. *Journal of Geophysical Research: Oceans*, 109(C03001), 12. <https://doi.org/10.1029/2001JC001262>
- Thompson, C. E. L., Amos, C. L., Jones, T. E. R., & Chaplin, J. (2003). The manifestation of fluid-transmitted bed shear stress in a smooth annular flume—A comparison of methods. *Journal of Coastal Research*, 19(4), 1094–1103.

- U.S. Army Corp of Engineers. (1993). *Engineering and design: river hydraulics* (EM 1110-2-1416). Department of Army.
https://www.publications.usace.army.mil/Portals/76/Publications/EngineerManuals/EM_1110-2-1416.pdf?ver=2013-09-04-070758-670
- USEPA. (2016). *FOSC desk report for the Enbridge line 6b oil spill in Marshall, Michigan*. United States Environmental Protection Agency.
<https://www.epa.gov/sites/production/files/2016-04/documents/enbridge-fosc-report-20160407-241pp.pdf>
- van Rijn, L. C. (2007). Unified view of sediment transport by currents and waves: Initiation of motion, bed roughness, and bed-load transport. *Journal of Hydraulic Engineering*, 133(6), 649–667. [https://doi.org/10.1061/\(ASCE\)0733-9429\(2007\)133:6\(649\)](https://doi.org/10.1061/(ASCE)0733-9429(2007)133:6(649))
- Vanoni, V. A. (2006). *Sedimentation engineering: Classic edition*. American Society of Civil Engineers. <http://ebookcentral.proquest.com/lib/unh/detail.action?docID=3115252>
- Verfaillie, M., Gloekler, M., Kinner, N., Bernardy, C., Wilkins, Q., Balcom, E., Rosa, Z., & Ross, J. (2021). Snare performance for sunken and submerged oil detection and monitoring. *Proceedings of the International Oil Spill Conference, USA*.
- Waterman, D. M., Fytanidis, D., & Garcia, M. H. (2015). *Kalamazoo river in situ flume erosion study* (Report No 105; Hydraulic Engineering Series). University of Illinois.
<https://archive.epa.gov/region5/enbridgespill/data/web/pdf/enbridgespill-kalamazoo-river-in-situ-erosion-study-201508-88pp.pdf>
- Watkins, C. B. R. (2015). *Critical shear stress estimates of sunken Alberta bitumen* [Masters]. University of New Hampshire.
- Wengrove, M. E., & Foster, D. L. (2014). Field evidence of the viscous sublayer in a tidally forced developing boundary layer. *Geophysical Research Letters*, 41(14), 5084–5090.
<https://doi.org/10.1002/2014GL060709>
- Wengrove, M. E., Foster, D. L., Kalnejais, L. H., Percuoco, V., & Lippmann, T. C. (2015). Field and laboratory observations of bed stress and associated nutrient release in a tidal estuary. *Estuarine, Coastal and Shelf Science*, 161, 11–24.
<https://doi.org/10.1016/j.ecss.2015.04.005>
- White, F. M. (2003). *Fluid Mechanics* (5th ed.). McGraw-Hill.
- Whiting, P. J., & Dietrich, W. E. (1990). Boundary shear stress and roughness over mobile alluvial beds. *Journal of Hydraulic Engineering*, 116(12), 1495–1511.
[https://doi.org/10.1061/\(ASCE\)0733-9429\(1990\)116:12\(1495\)](https://doi.org/10.1061/(ASCE)0733-9429(1990)116:12(1495))
- Wilcock, P. R. (1996). Estimating local bed shear stress from velocity observations. *Water Resources Research*, 32(11), 3361–3366. <https://doi.org/10.1029/96WR02277>

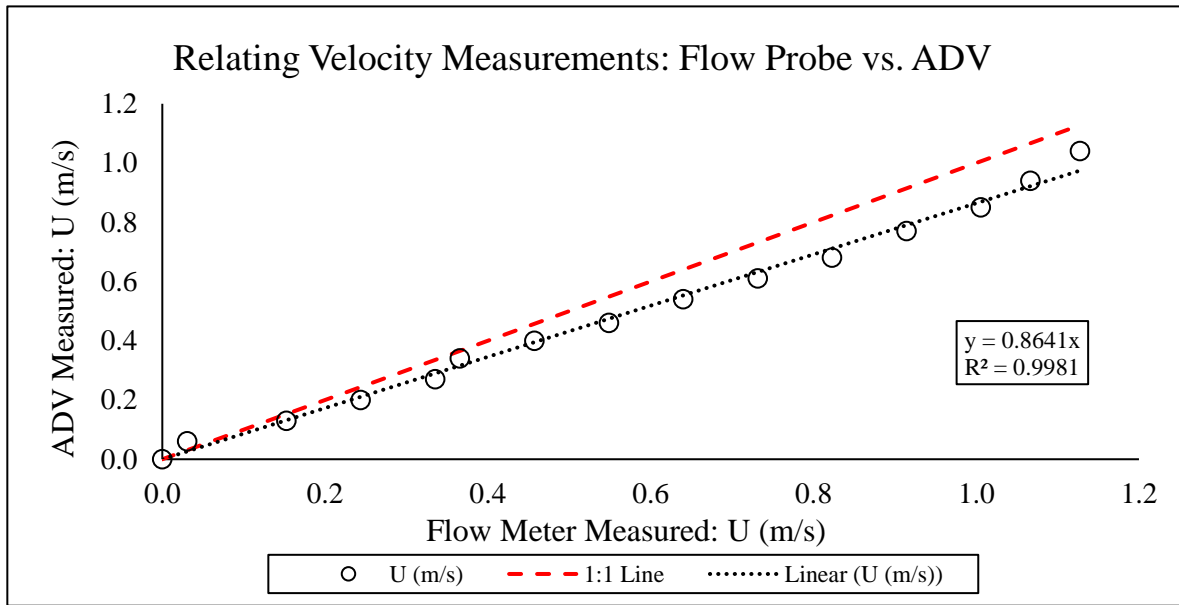
- Williams, S. J., Arsenault, M. A., Buczkowski, B. J., Reid, J. A., Flocks, J. G., Kulp, M. A., Penland, S., & Jenkins, C. J. (2006). *Surficial sediment character of the Louisiana offshore continental shelf region: A GSI compilation* [Open-File Report 2006-1195]. USGS. <https://pubs.usgs.gov/of/2006/1195/index.htm>
- Wren, D. G., Langendoen, E. J., & Kuhnle, R. A. (2011). Effects of sand addition on turbulent flow over an immobile gravel bed. *Journal of Geophysical Research: Earth Surface*, *116*(F1). <https://doi.org/10.1029/2010JF001859>
- Wren, D. G., Ursic, M. E., Kuhnle, R. A., & Langendoen, E. J. (2017). Examining the generality of τ_0 /TKE for gravel and cobble beds with sand fill. *Journal of Hydraulic Engineering*, *143*(4). [https://doi.org/10.1061/\(ASCE\)HY.1943-7900.0001265](https://doi.org/10.1061/(ASCE)HY.1943-7900.0001265)
- Yen, B. C. (2002). Open channel flow resistance. *Journal of Hydraulic Engineering*, *128*(1), 20-39.
- Zhao, L., Boufadel, M. C., Geng, X., Lee, K., King, T., Robinson, B., & Fitzpatrick, F. (2016). A-DROP: A predictive model for the formation of oil particle aggregates (OPAs). *Marine Pollution Bulletin*, *106*, 245–259.
- Zhao, L., Torlapati, J., Boufadel, M. C., King, T., Robinson, B., & Lee, K. (2014). VDROD: A comprehensive model for droplet formation of oils and gases in liquids - Incorporation of the interfacial tension and droplet viscosity. *Chemical Engineering Journal*, *253*, 93–106. <https://doi.org/10.1016/j.cej.2014.04.082>

APPENDICES

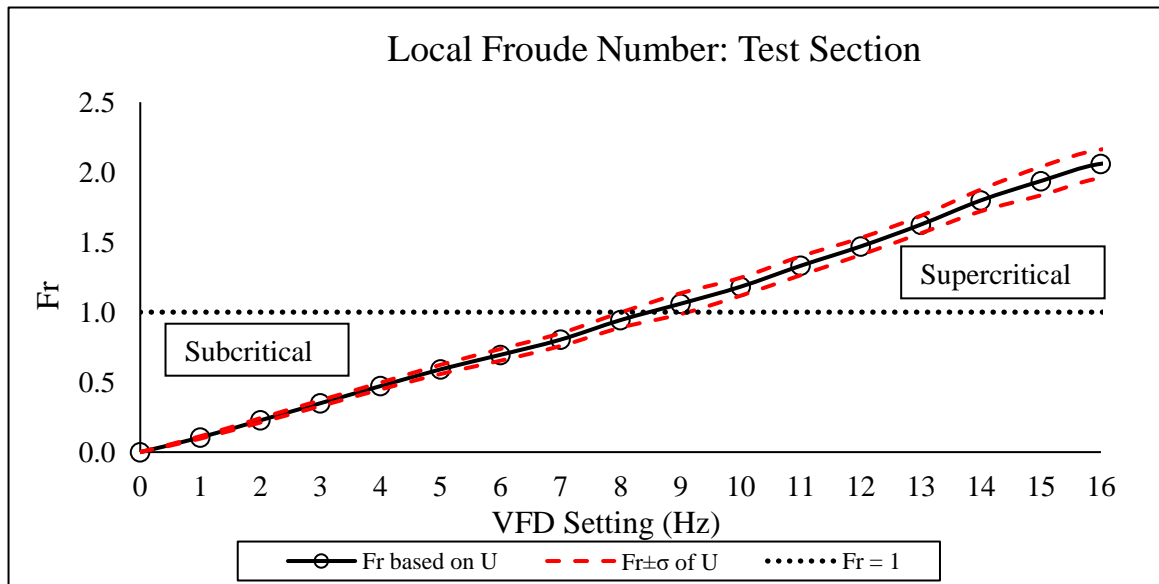
APPENDIX A: Chapter 2 Appendices

Appendix A.1: Hydraulic Analysis

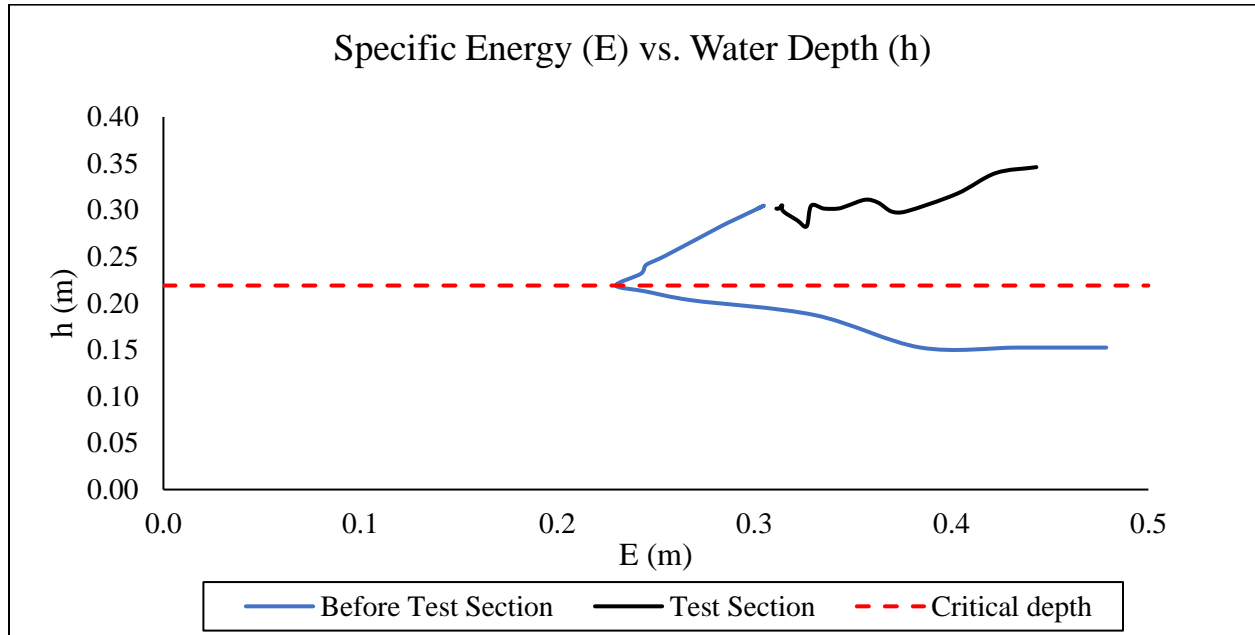
Flow Probe Correlation



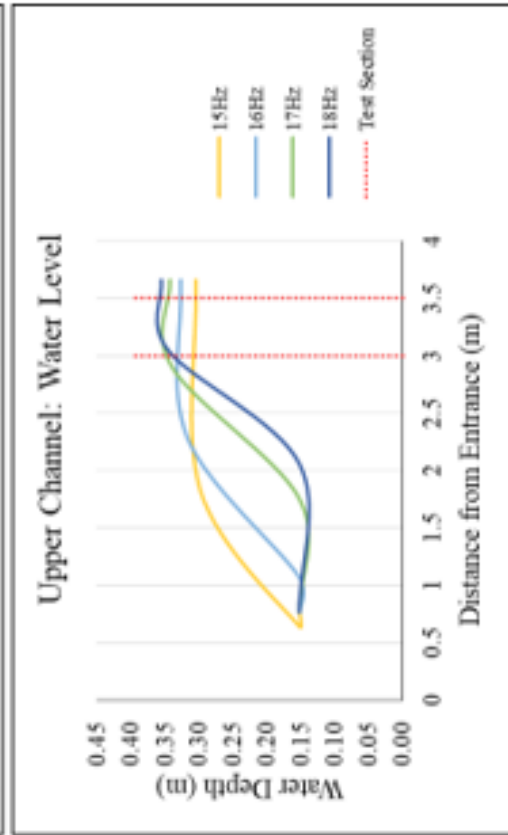
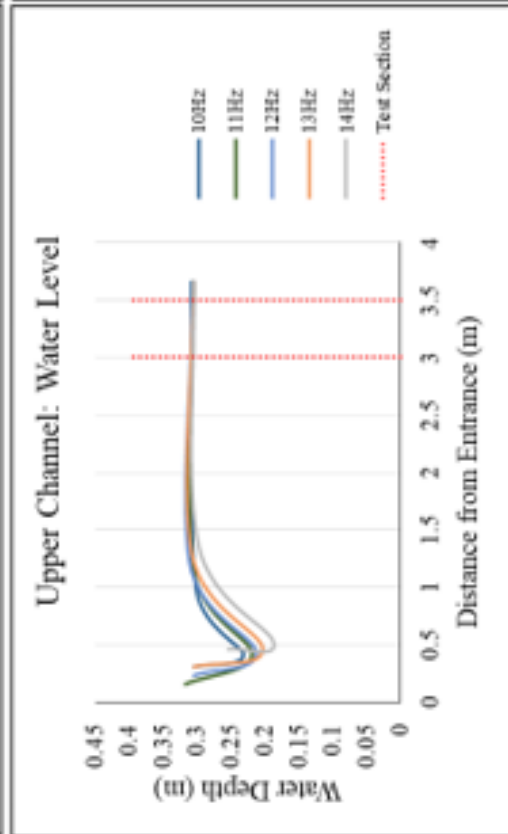
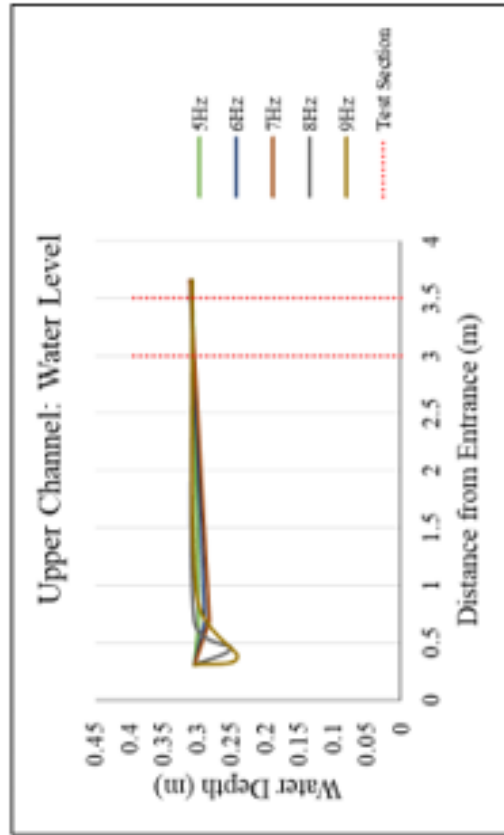
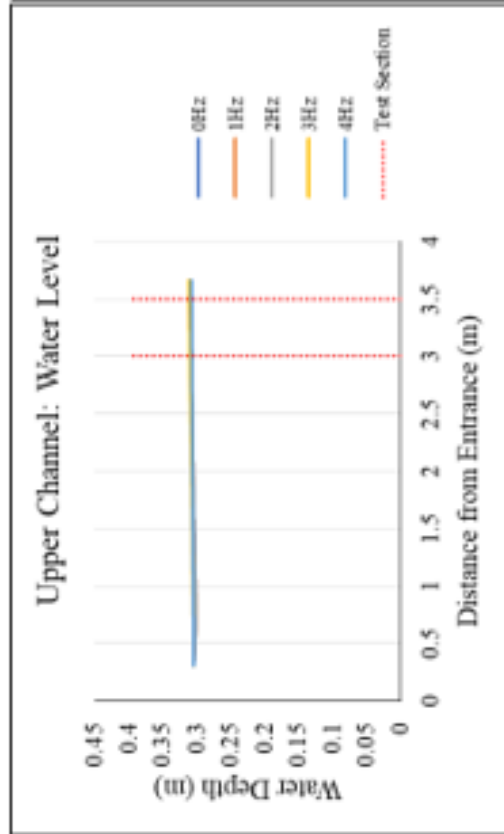
Froude Number



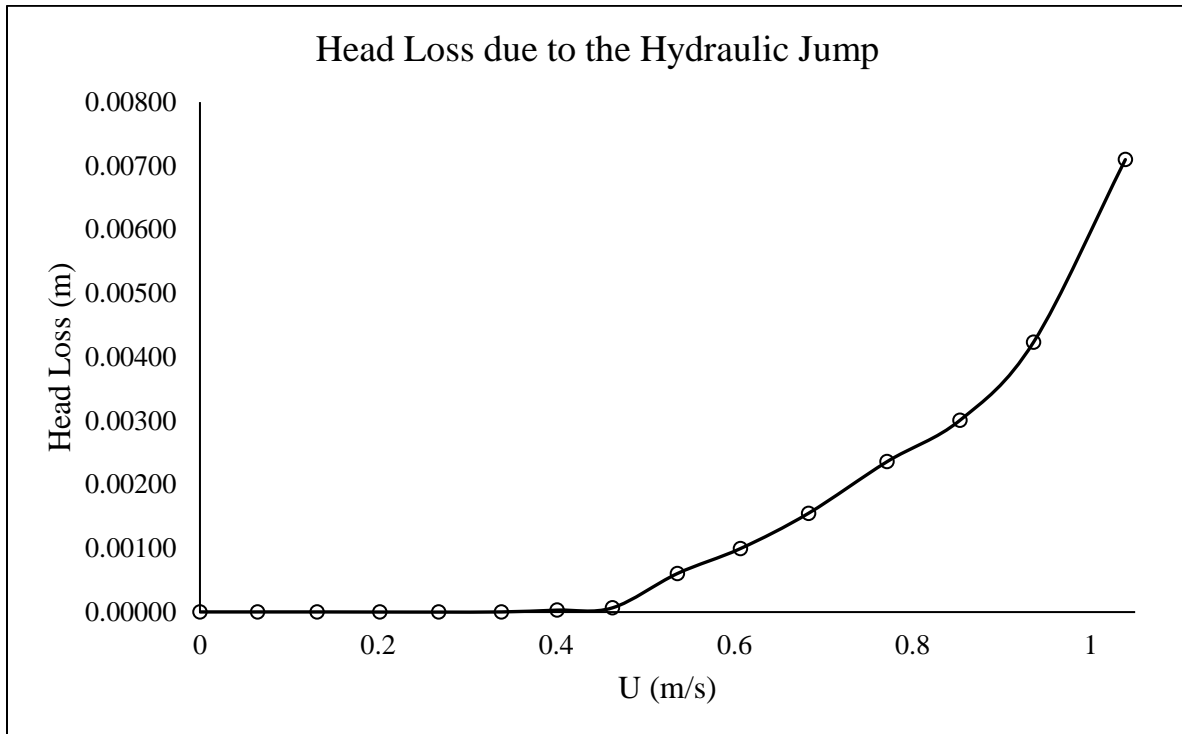
Specific Energy



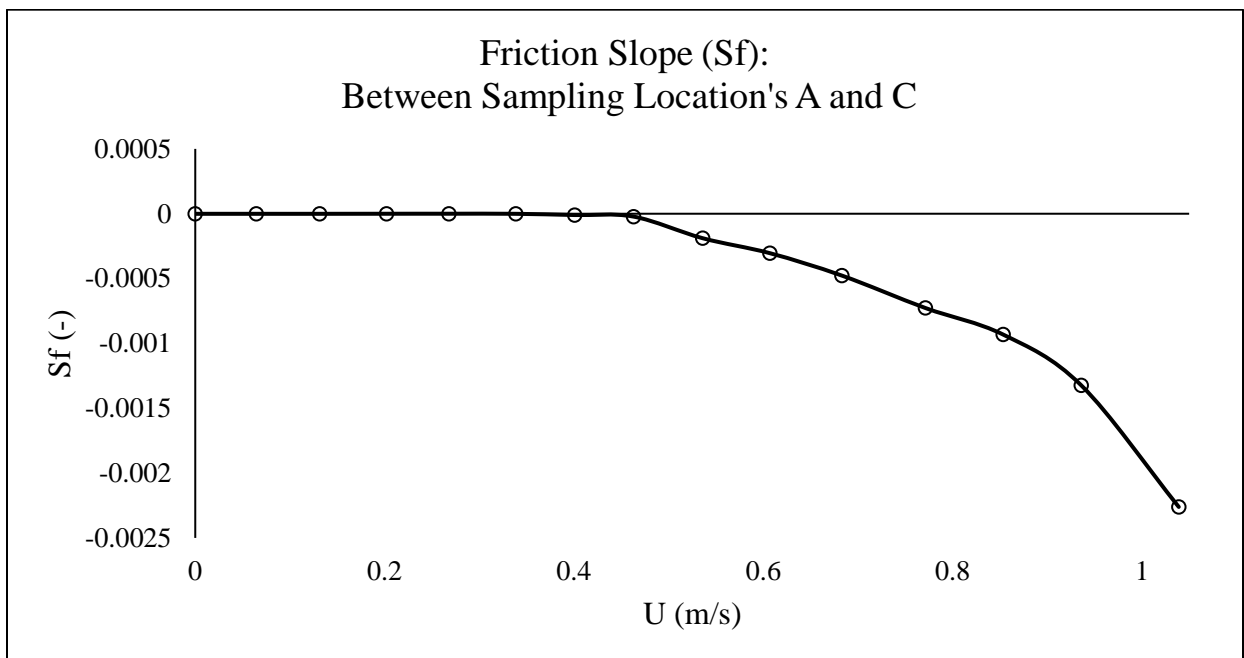
Water Level



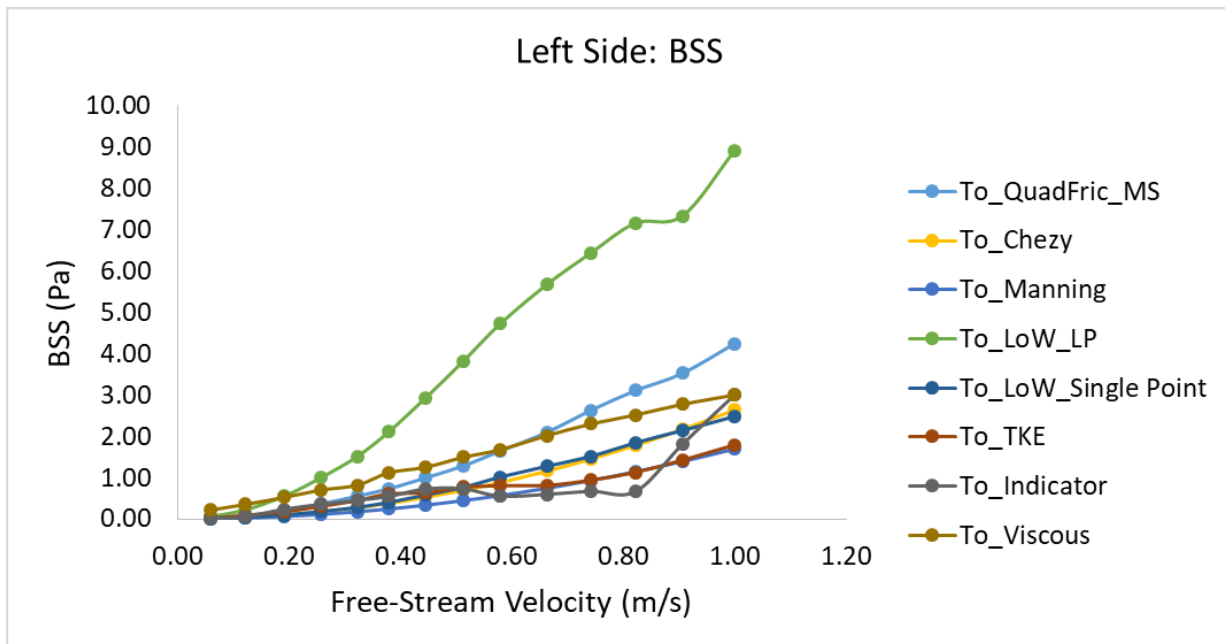
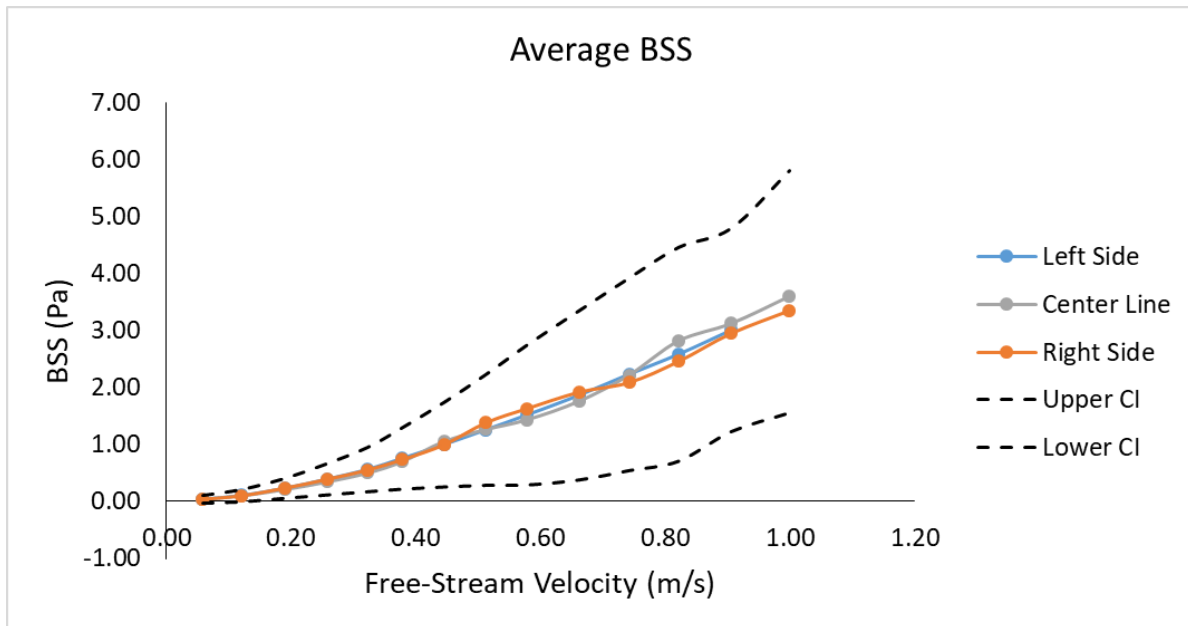
Head Loss Calculations

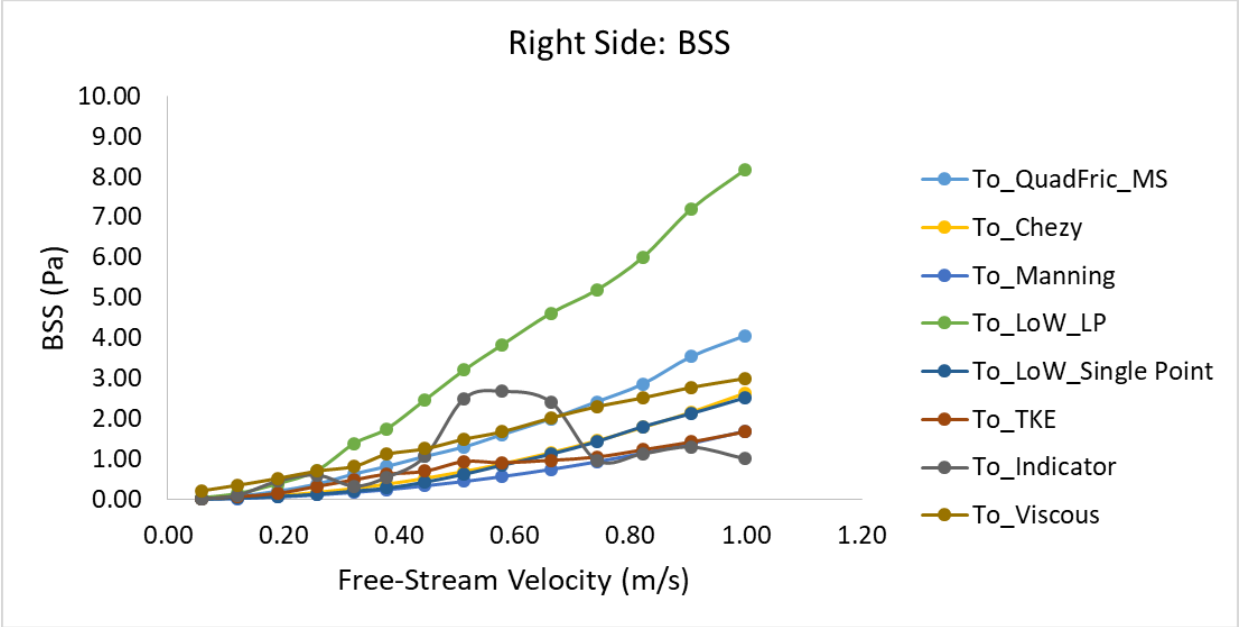


Friction Slope Calculations

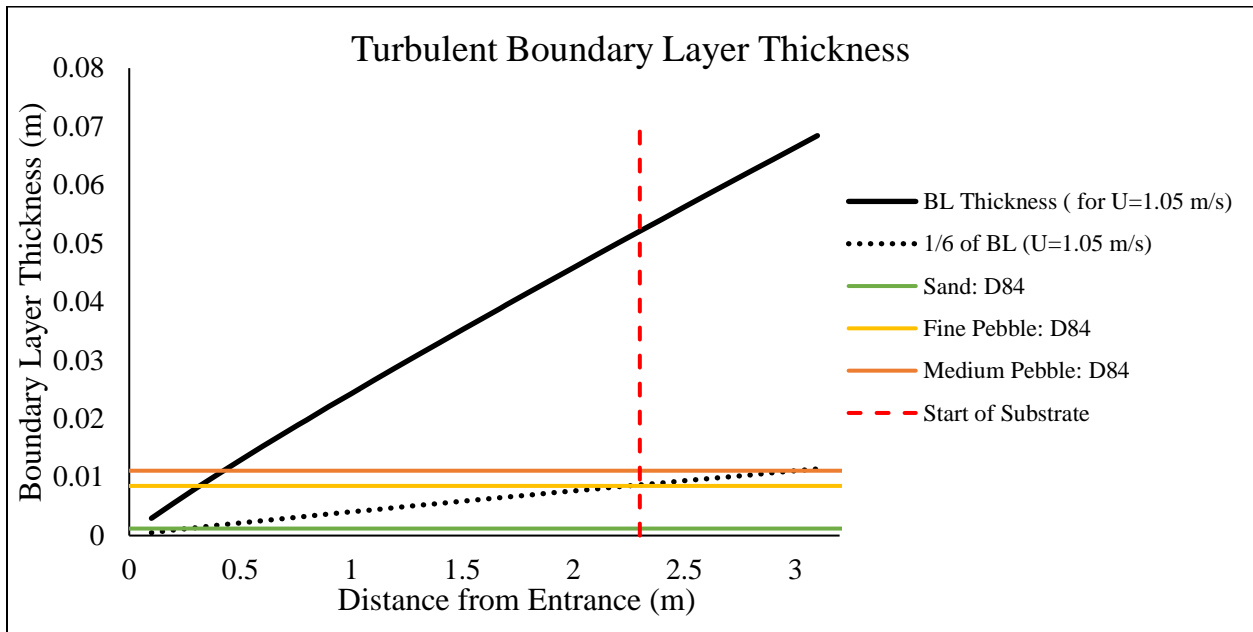


Appendix A.2: Cross-Sectional Hydraulic Analysis

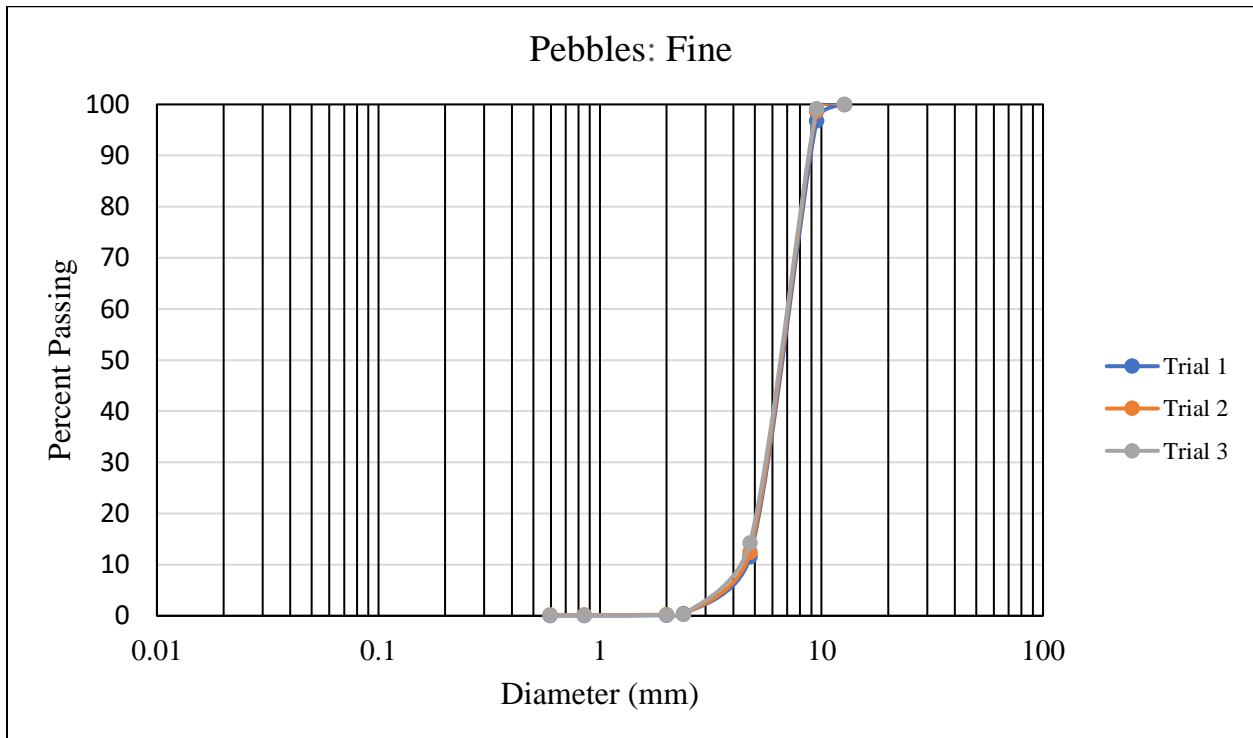
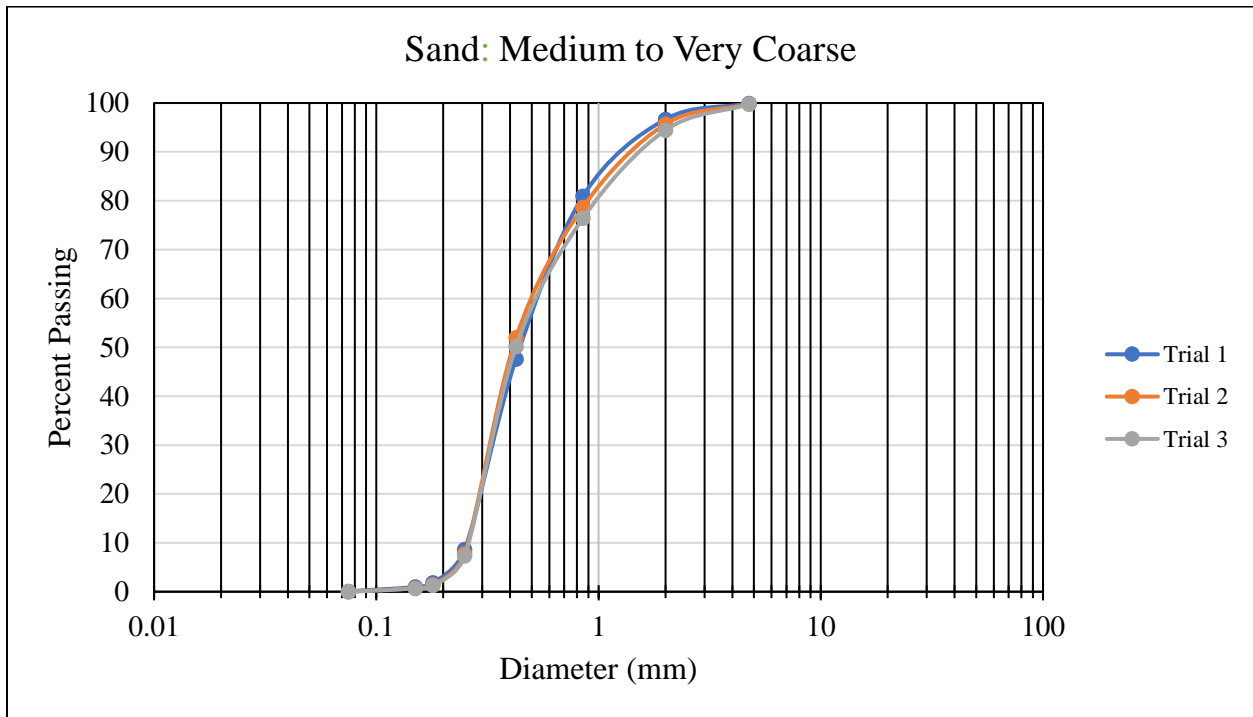


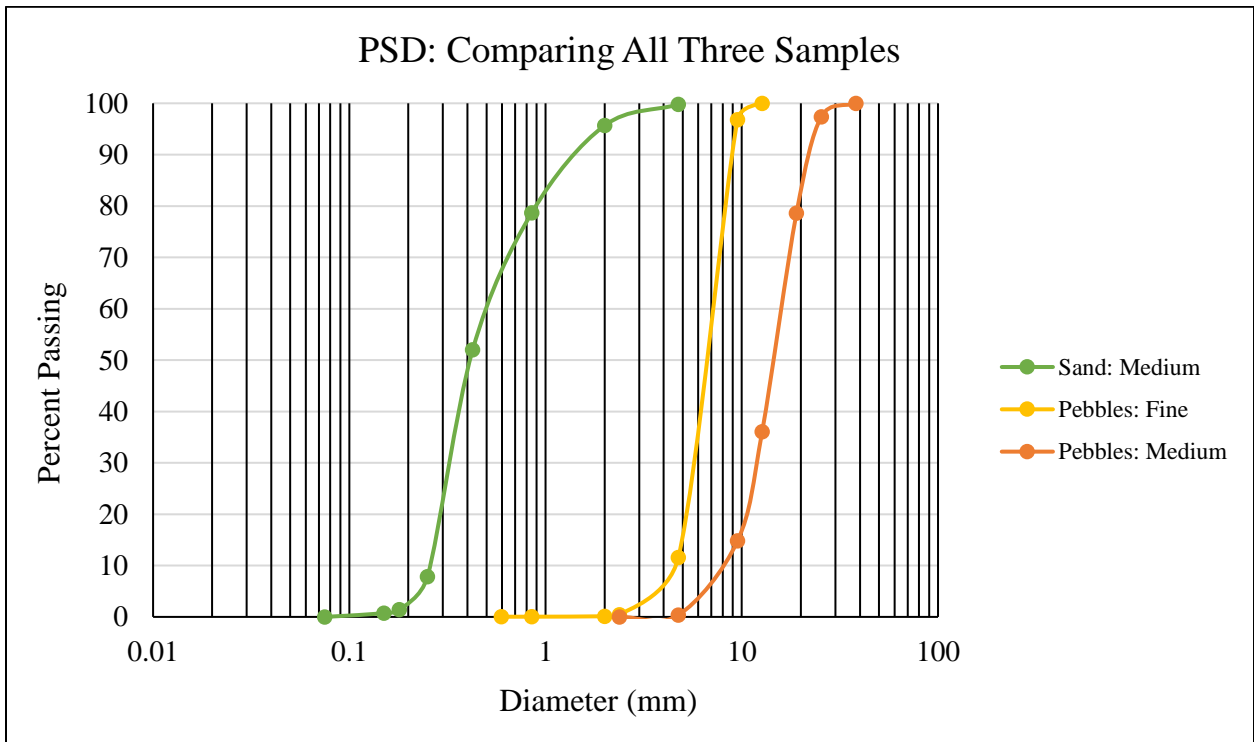
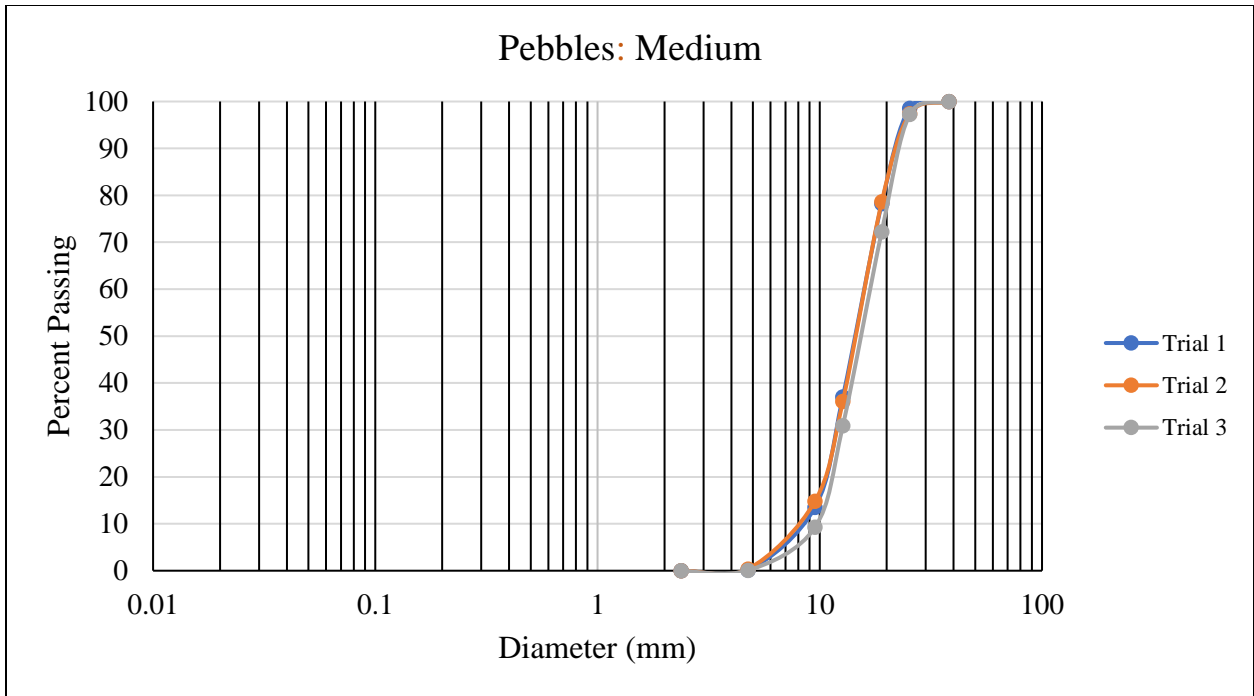


Appendix A.3: Boundary Layer Conditions



Appendix A.4: Particle Size Distribution





Wentworth Grade Scale:

Φ	PHI - mm CONVERSION Φ = log ₂ (d in mm) 1 μm = 0.001 mm		SIZE TERMS (after Wentworth, 1922)	SIEVE SIZES		Intermediate diameters of natural grains equivalent to sieve size	Number of grains per mg		Settling Velocity (Quartz, 20°C)		Threshold Velocity for traction cm/sec			
	mm	Fractional mm and Decimal inches		ASTM No. (U.S. Standard)	Tyler Mesh No.		Quartz spheres	Natural sand	Spheres (Cilbot, 1971) cm/sec	Crushed	(Herin, 1946)	(modified from Hjulstrom, 1939)		
-8	256	10.1"	BOULDERS (> -8φ) COBBLES											
-7	128	5.04"												
-6	64.0	2.52"	PEBBLES	very coarse	2 1/2"	2"						200	1 m above bottom	
-5	53.9				coarse	1 1/2"	1 1/2"						150	
-4	45.3	1.26"				1 1/4"	1.05"							
-3	33.1				medium	3/4"	.742"							
-2	32.0					1/2"	.525"							
-1	26.9	0.63"				7/16"	.371"							
0	22.6				fine	5/16"	.265"							
1	17.0	0.32"				4	4							
2	13.4	0.16"				5	5							
3	11.2				Granules	6	6							
4	8.00	0.08"			7	7								
5	6.73		SAND	very coarse	14	12	1.2	.72	.6	10	9	40	50	
6	5.66					16	14				8	7	40	
7	4.76	1 mm			coarse	20	20	.86	2.0	1.5	10	9	30	40
8	4.00	1/2				25	24				8	7	30	
9	3.36				medium	30	28	.59	5.6	4.5	7	6	30	
10	2.83	1/4				35	32				6	5	30	
11	2.38					40	35	.42	15	13	5	4	30	
12	2.00				fine	45	42				4	4	30	
13	1.70					50	48	.30	43	35	3	3	20	26
14	1.41	1/8				60	60				2	2	20	26
15	1.19			very fine	80	80	.215	120	91	1	1	20	26	
16	1.00	1/16			100	100	.155	350	240	0.5	0.5	20	26	
17	.840			very fine	120	115	.115	1000	580	0.1	0.1	20	26	
18	.707	1/32			140	150				0.05	0.05	20	26	
19	.545	1/64		coarse	170	170	.080	2900	1700	0.023	0.023	20	26	
20	.500		SILT		200	200				0.01	0.01	20	26	
21	.420	1/32			medium	230	250				0.0057	0.0057	20	26
22	.354	1/64				270	270				0.0014	0.0014	20	26
23	.297	1/128			fine	325	325				0.00036	0.00036	20	26
24	.250	1/256		very fine	400	400				0.0001	0.0001	20	26	
25	.210		CLAY											
26	.177	1/8												
27	.149													
28	.125	1/16												
29	.105													
30	.088	1/32												
31	.074	1/64												
32	.062													
33	.053	1/128												
34	.044	1/256												
35	.037													
36	.031	1/1024												
37	.025													
38	.020													
39	.016													
40	.012													
41	.009													
42	.007													
43	.005													
44	.004													
45	.003													
46	.002													
47	.001													

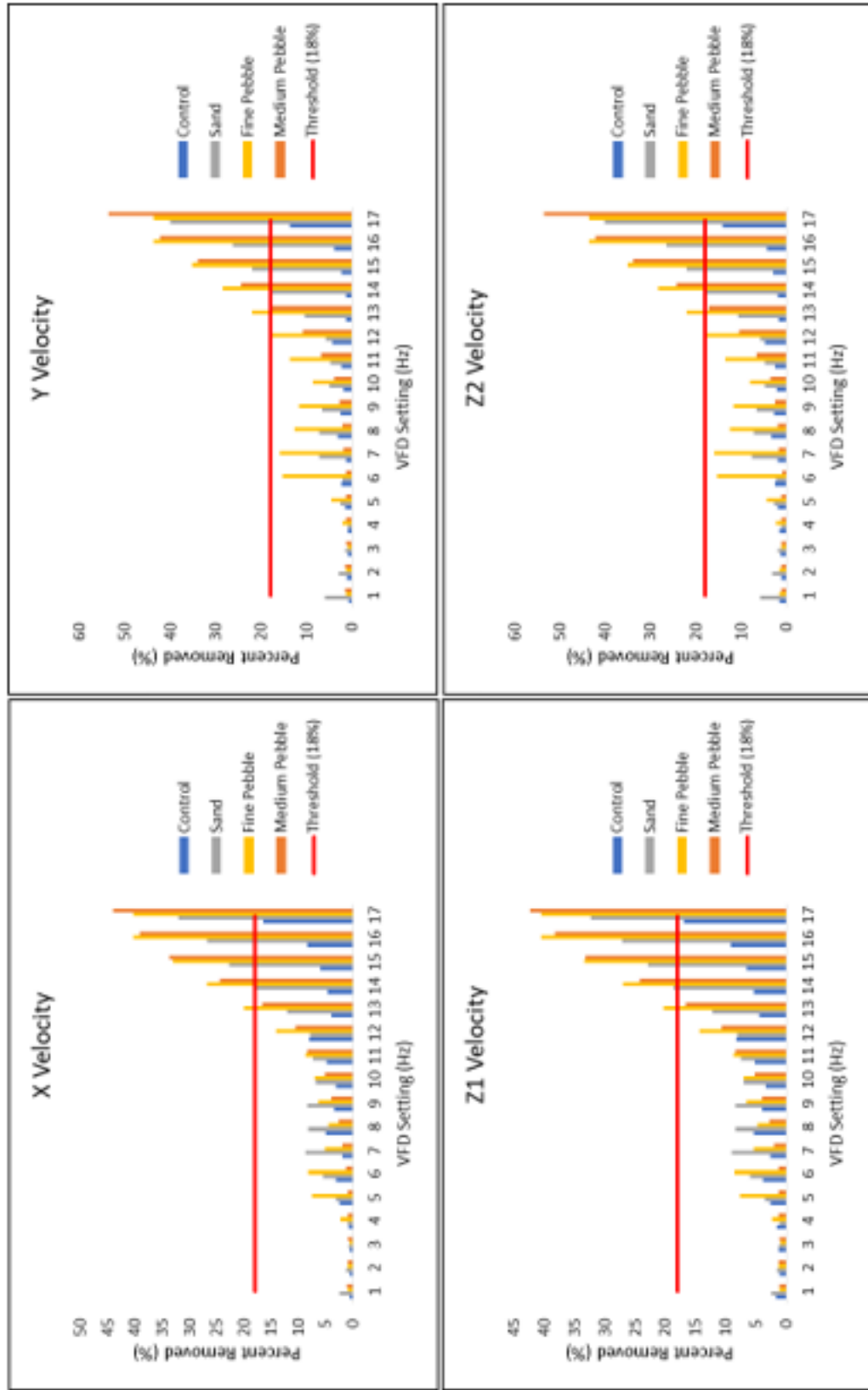
<https://pubs.usgs.gov/of/2006/1195/html/docs/nomenclature.htm>

Appendix A.5: Estimating Manning's n

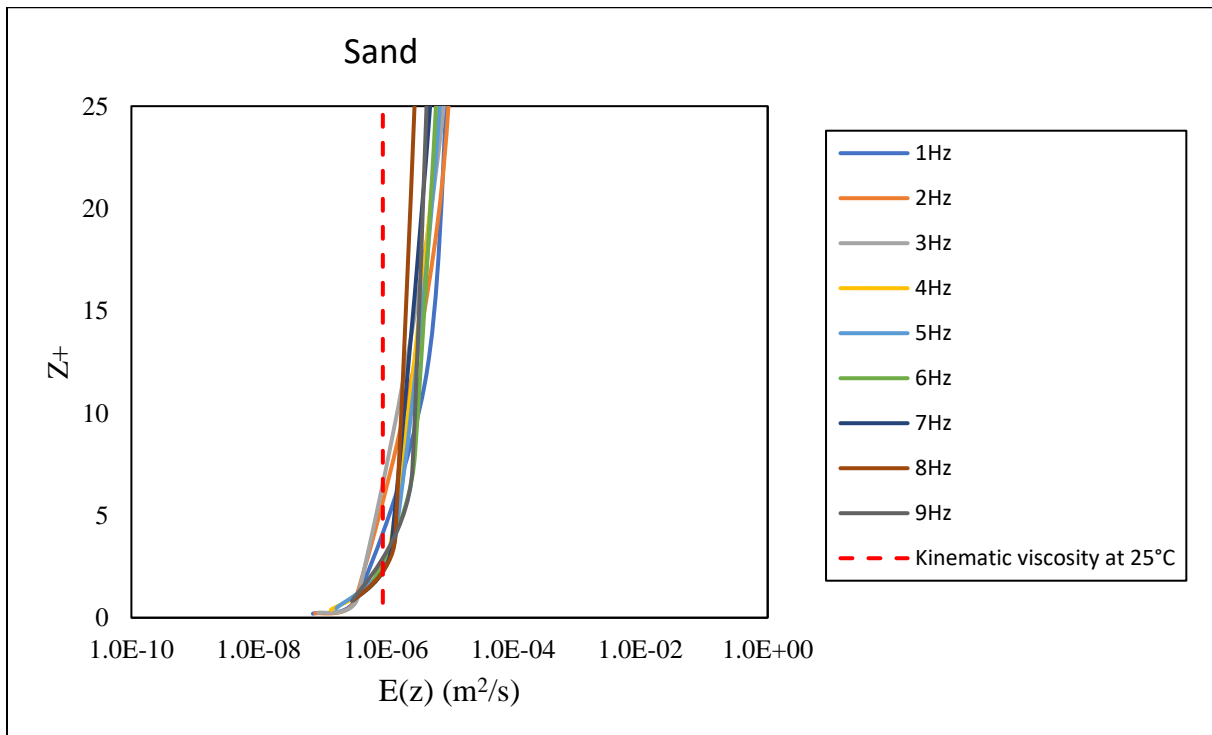
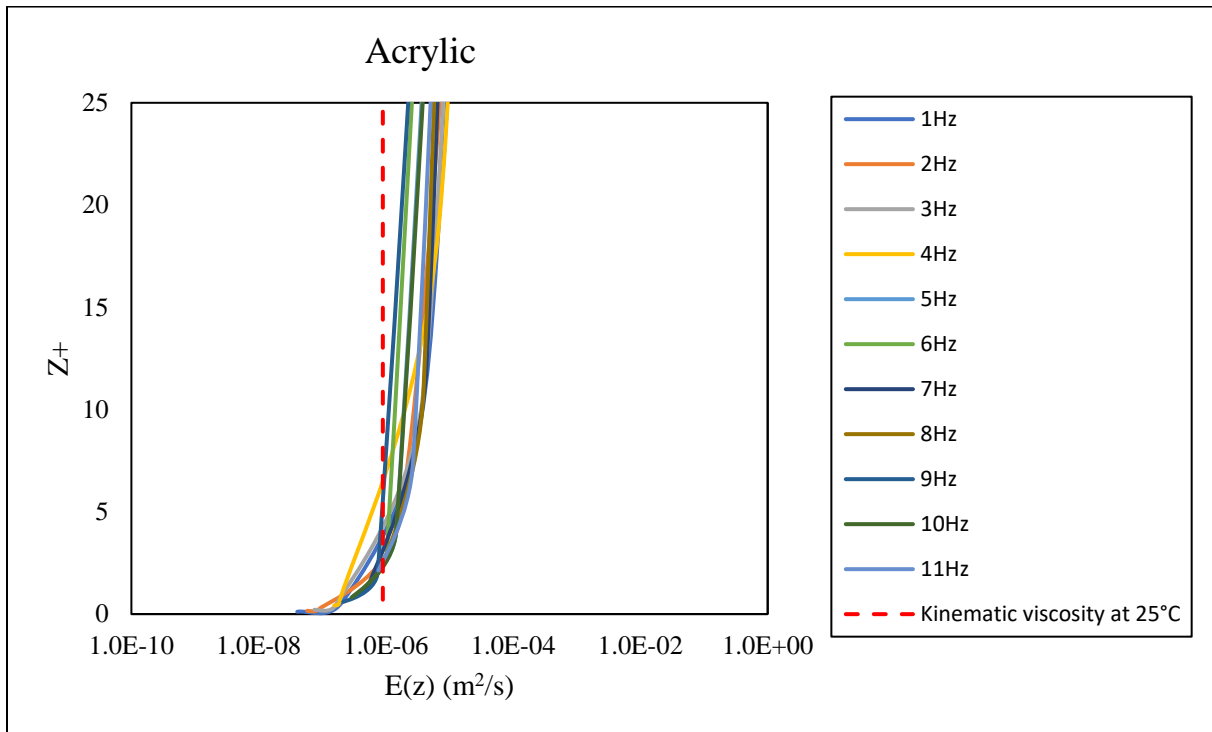
Reference	Equation	Variables	Values (meters)	Sand	Fine Pebble	Medium Pebble
VT Chow (1959)	$n = KuDx^{1/6}$	Ku	0.042	0.0114	0.0180	0.0195
		D50	see PSD			
Anderson et al. (1970)	$n = KuDx^{1/6}$	Ku	0.048	0.0132	0.0208	0.0226
		D50	see PSD			
US Army Corp of Eng (1991)	$n = KuDx^{1/6}$	Ku	0.046	0.0156	0.0210	0.0218
		D90	see PSD			
Strickler (1923)	$n = KuDx^{1/6}$	Ku	0.047	0.0130	0.0205	0.0222
		D50	see PSD			
Wong and Parker (2006)	$n = KuDx^{1/6}$	Ku	0.043	0.0146	0.0197	0.0204
		D90	see PSD			
Manning-Strickler	$u/u^* = \alpha(H/Dx)^{1/6}$ $\alpha = 8.1$ for mountain, gravel-bed streams	Rh	0.102	0.0202	0.0150	0.0145
		D90	see PSD			
		α	0.010			
Limerinos	$n = (Ku * Yo^{1/6}) / (1.16 + 2 \log(Yo/D84))$	Ku	0.113	0.0155	0.0217	0.0230
		Yo	0.305			
		D84	see PSD			
Use median Manning "n" in BSS calculations			Median n	0.0146	0.0205	0.0218

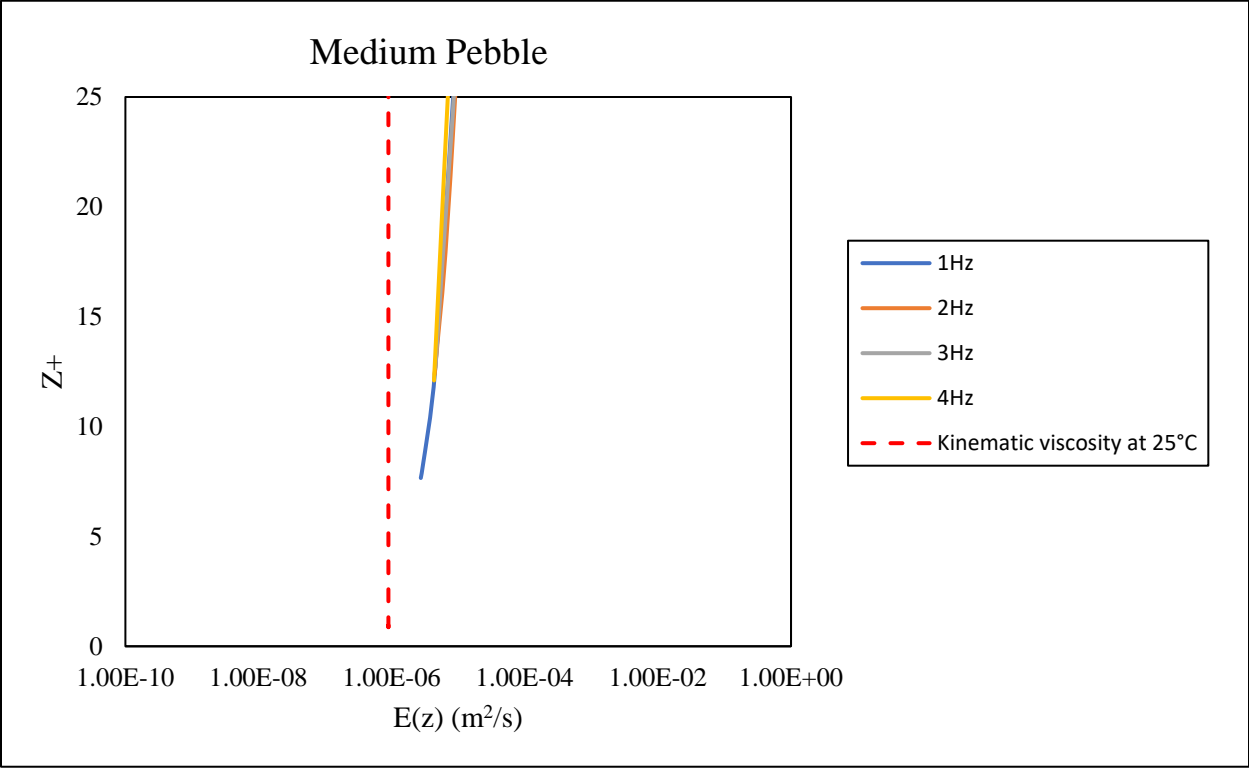
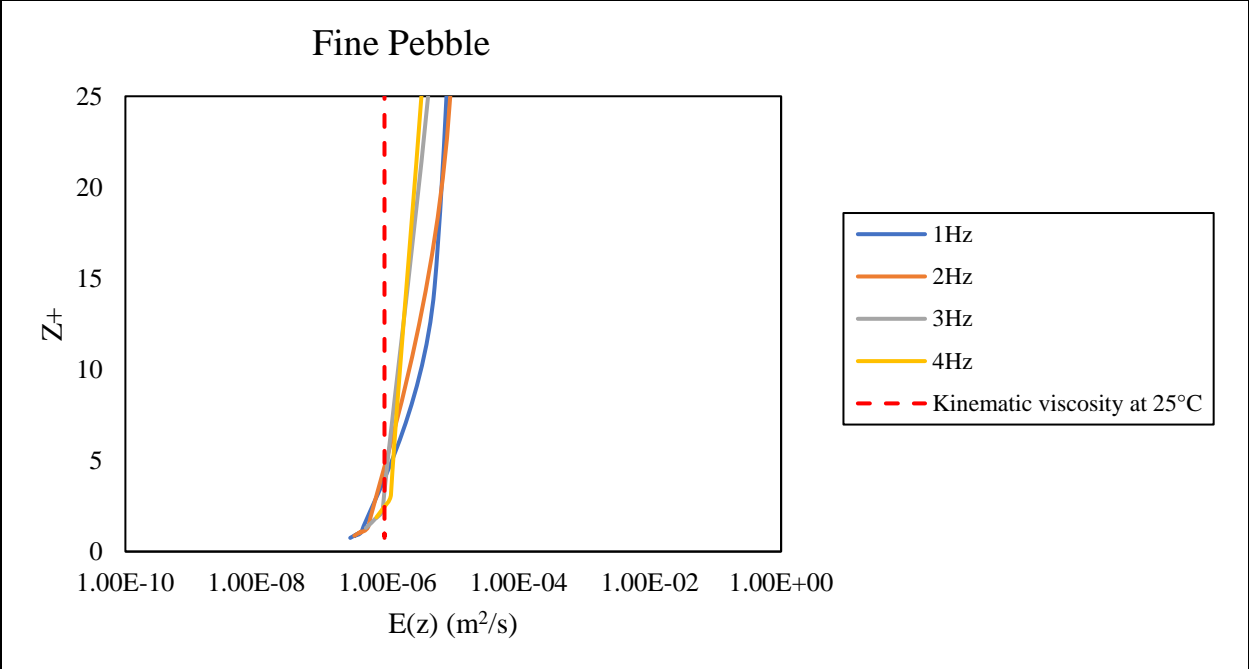
	Sediment Size (m)		
	Sand	Fine Pebble	Medium Pebble
D10	0.0003	0.0046	0.0090
D25	0.0003	0.0055	0.0103
D50	0.0004	0.0065	0.0106
D75	0.0009	0.0079	0.0108
D84	0.0012	0.0085	0.0111
D90	0.0015	0.0090	0.0112
LOG(Yo/D84)	2.40	1.55	1.44

Appendix A.6: Percent Removal of Velocity Data



Appendix A.7: Eddy Diffusivity ($E(z)$) vs. Dimensionless Height (Z^+)

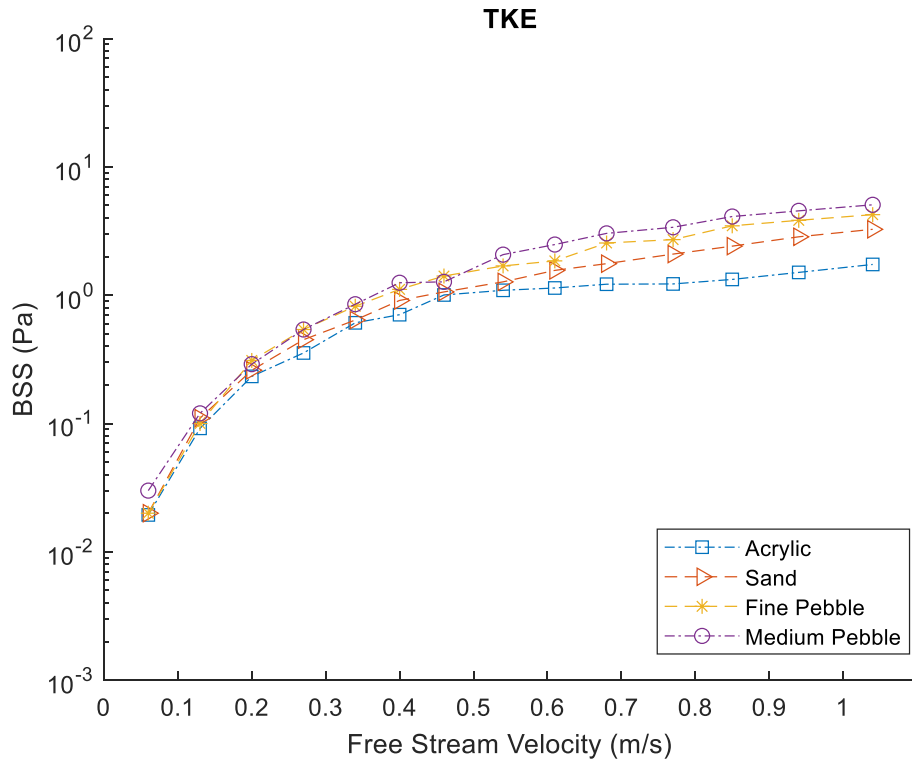
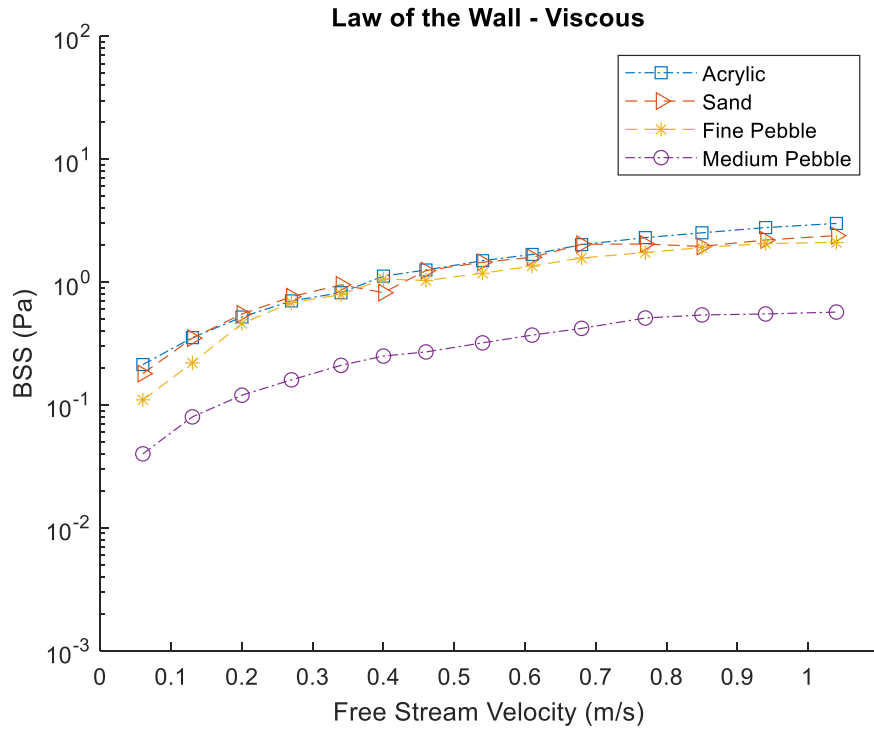


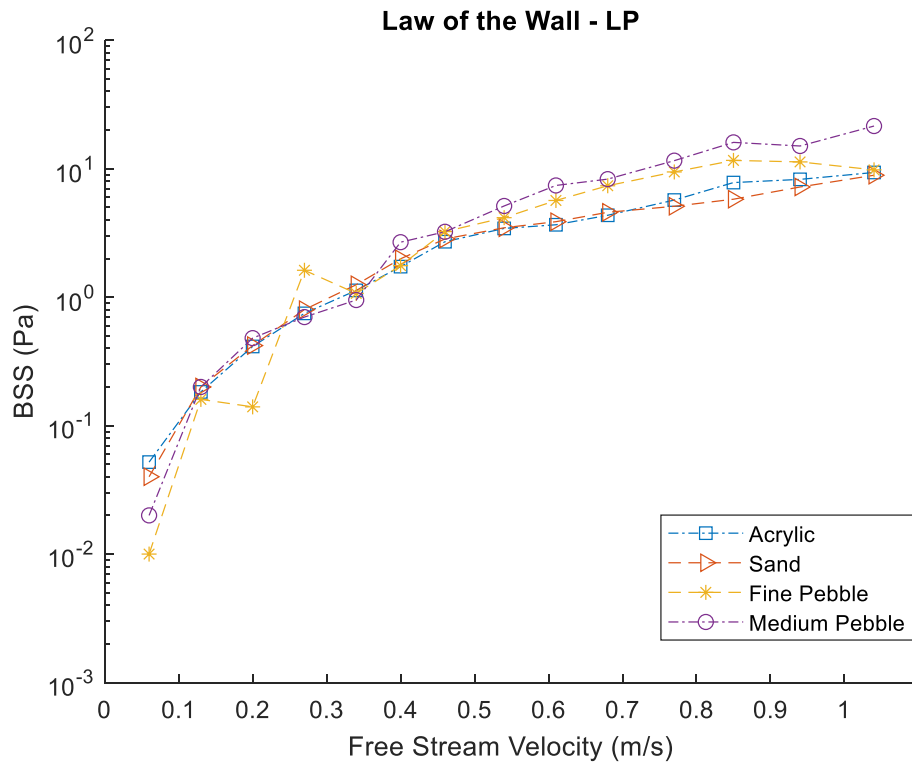
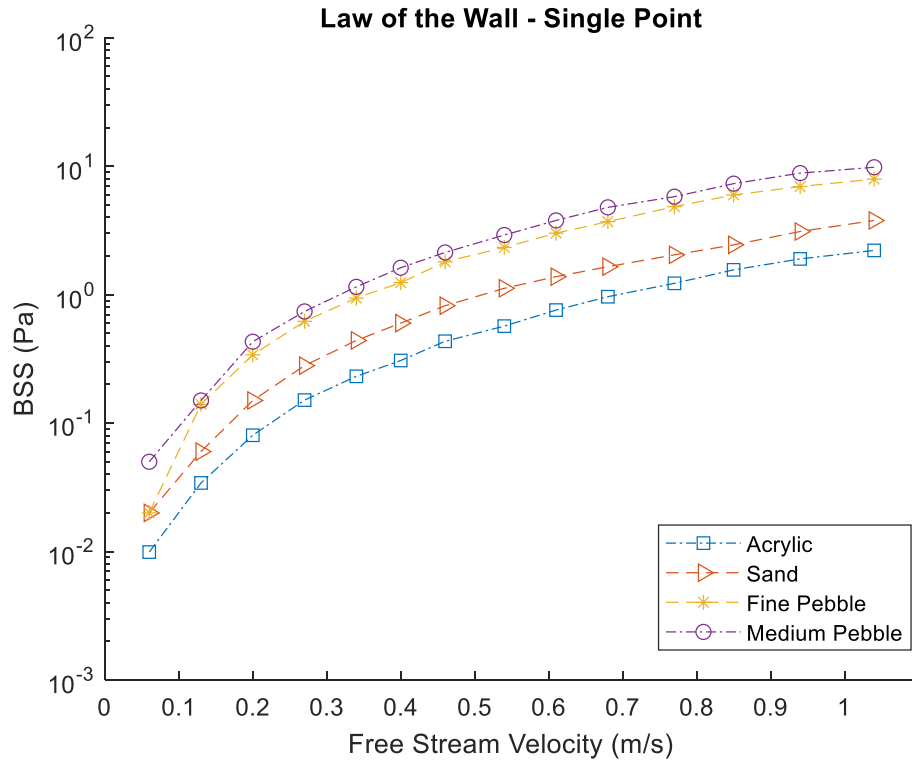


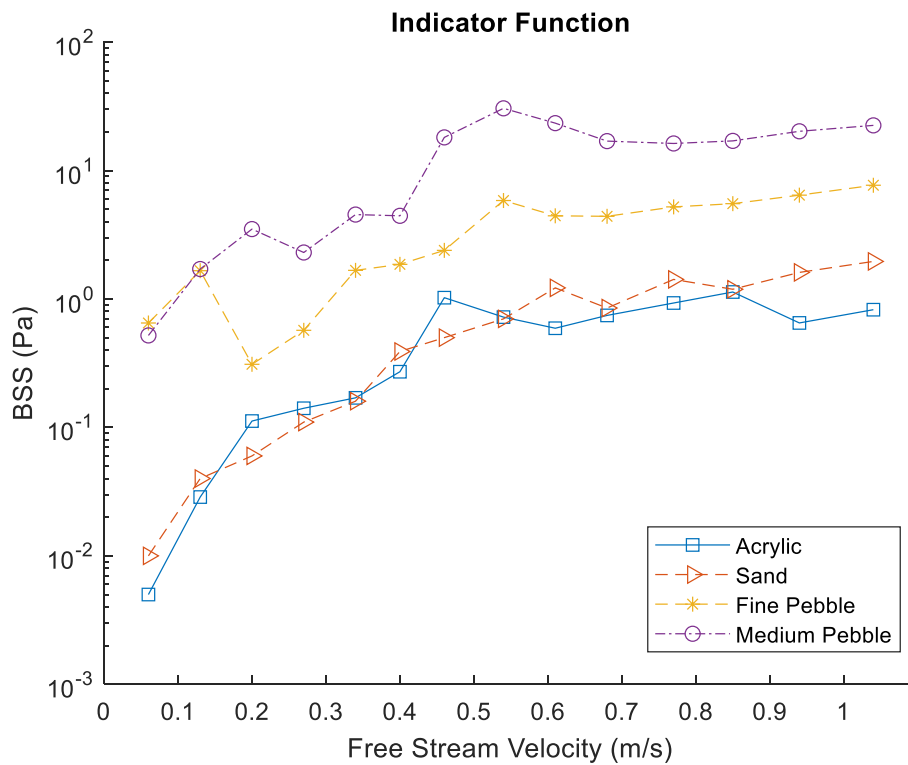
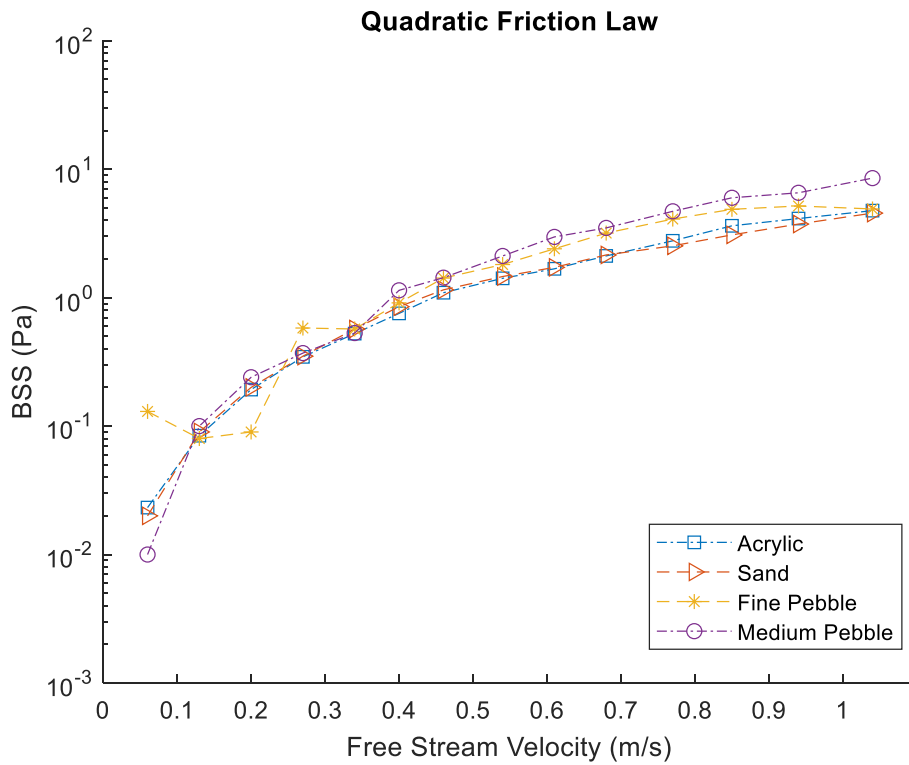
Appendix A.8: Velocity Measurement Location

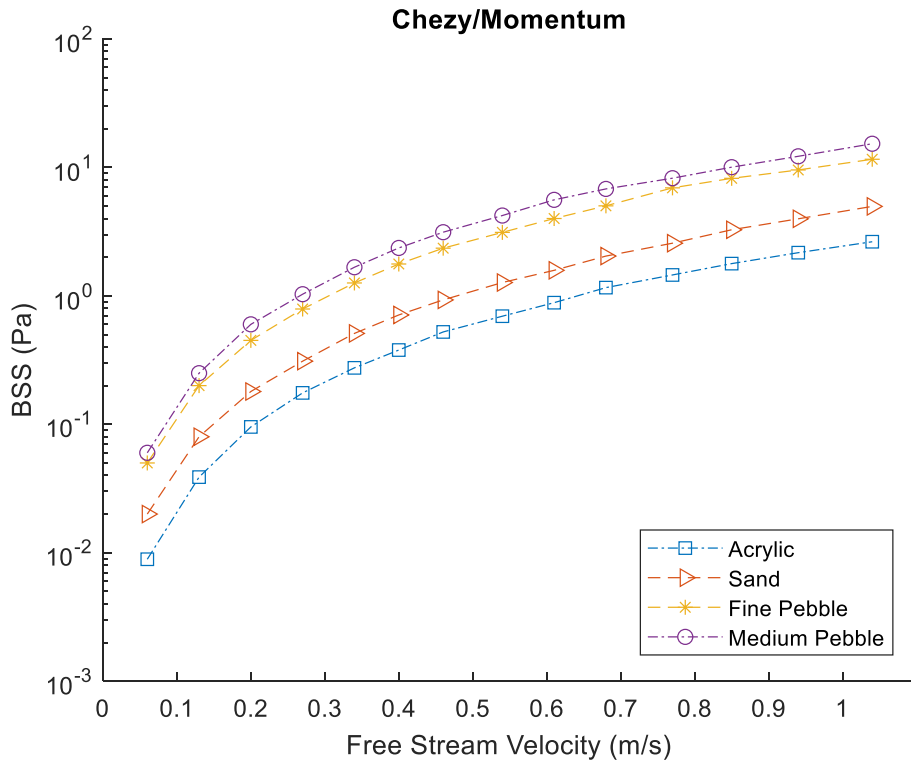
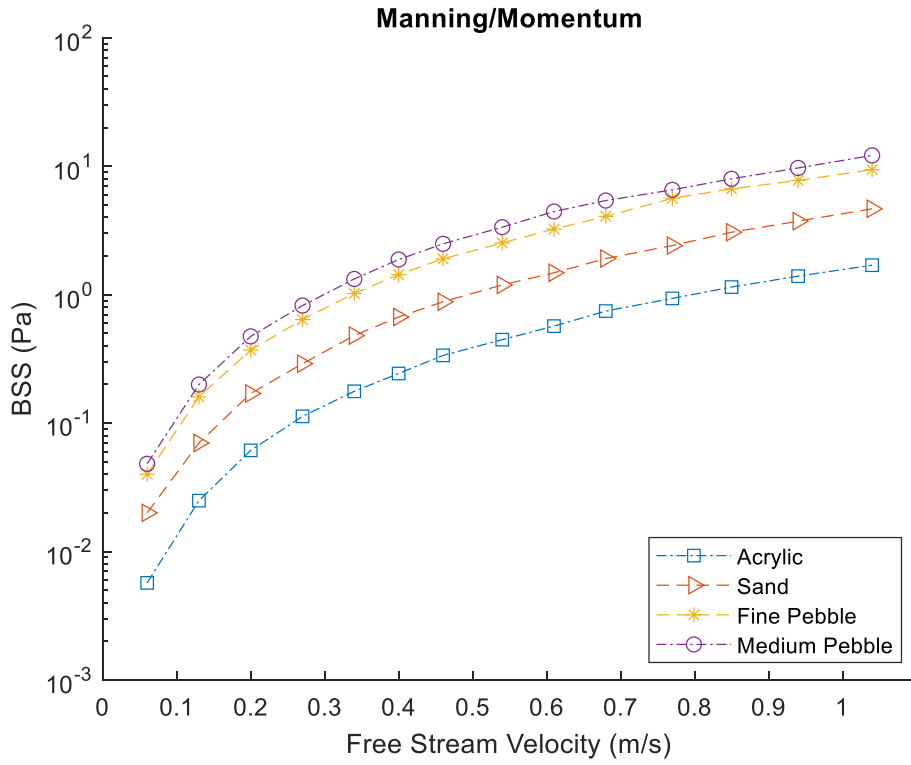
Method Name	Velocity measurement used in BSS calculations	Measurement Location: Distance from the Bottom, z, (cm)			
		Acrylic	Sand	Fine pebble	Medium pebble
Newton's Law of Viscosity	Derivative of velocity profile in viscous sublayer	0.13-0.54	0.20-0.51	0.51-0.81	n/a
TKE	Turbulent fluctuations (0.1h)	0.027	0.028	0.027	0.027
Law of Wall – LP	Time averaged profile	0.13-3.13	0.20-3.20	3.20-6.20	3.70-6.70
Law of Wall – Single Point	Time averaged between 2 cm and 2/10ths flow depth	2.20	2.30	5.20	5.80
Quadratic Friction Law	Depth and time averaged velocity (0 to 9 cm)	0.13-8.87	0.20-9.23	0.23-9.24	1.04-10.67
Indicator Function	Derivative of time averaged profile	0.13-2.82	0.20-2.88	0.19-2.46	1.04-4.00
Chézy/Momentum	Free-stream velocity	8.90	9.20	9.20	9.50
Manning/Momentum	Free-stream velocity	8.90	9.20	9.20	9.50

Appendix A.9: BSS Method for All Substrate Types

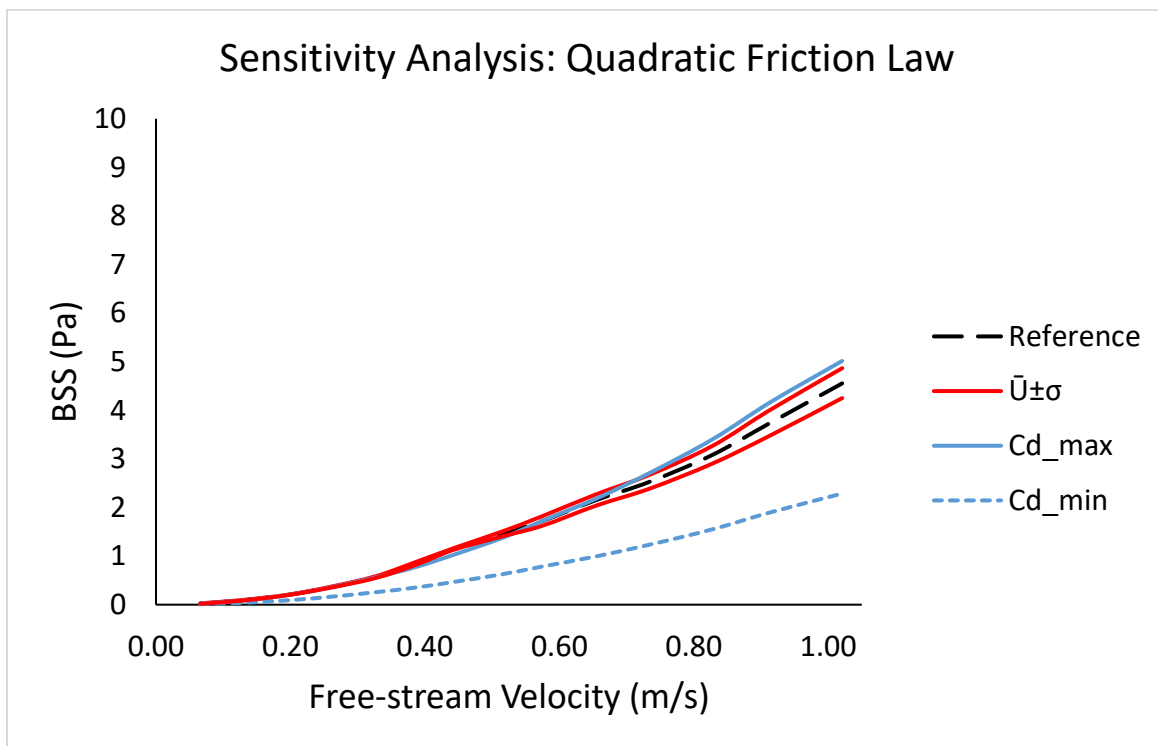
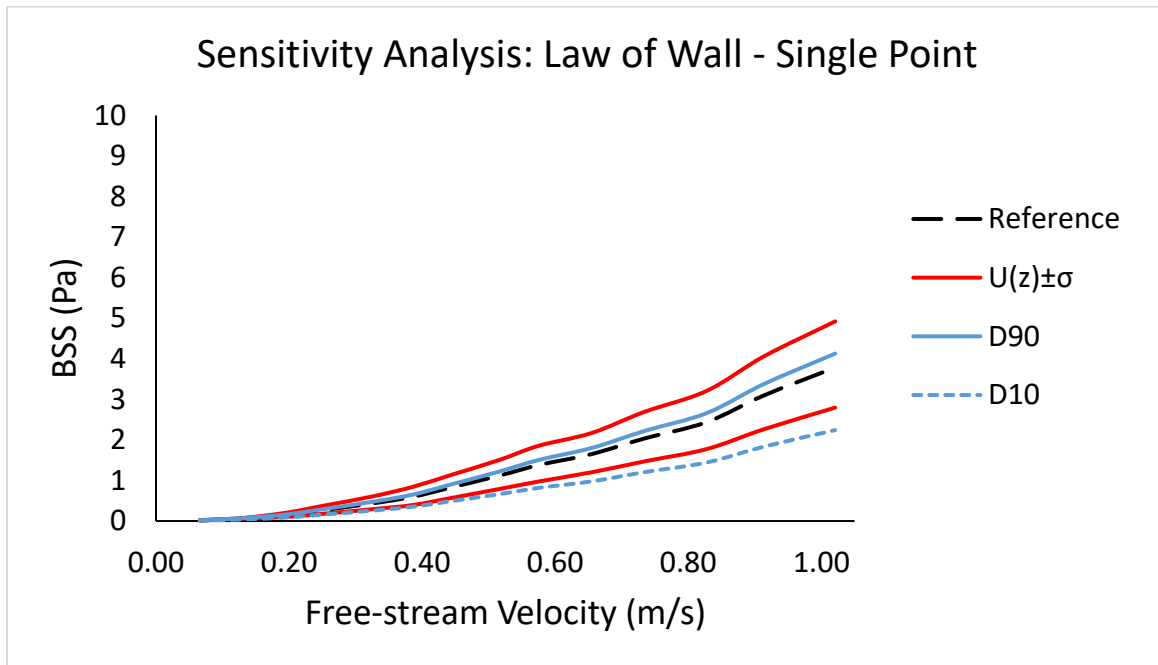


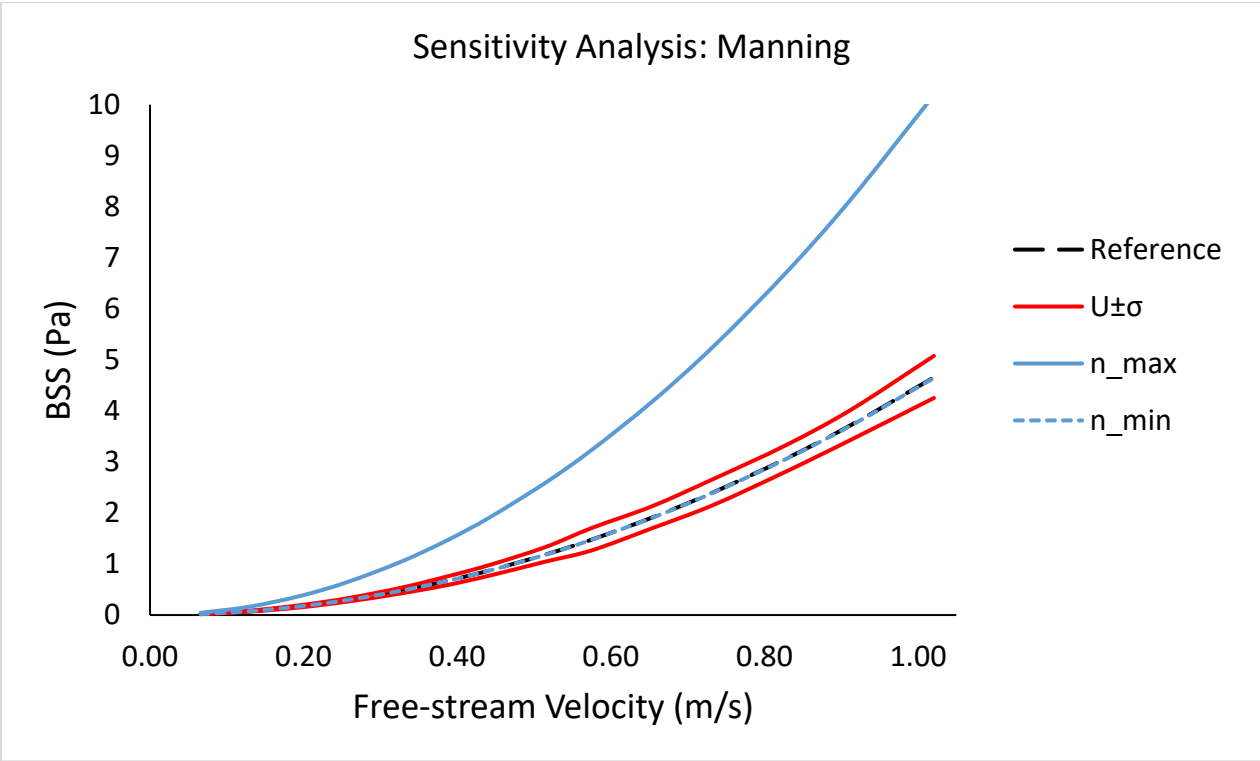
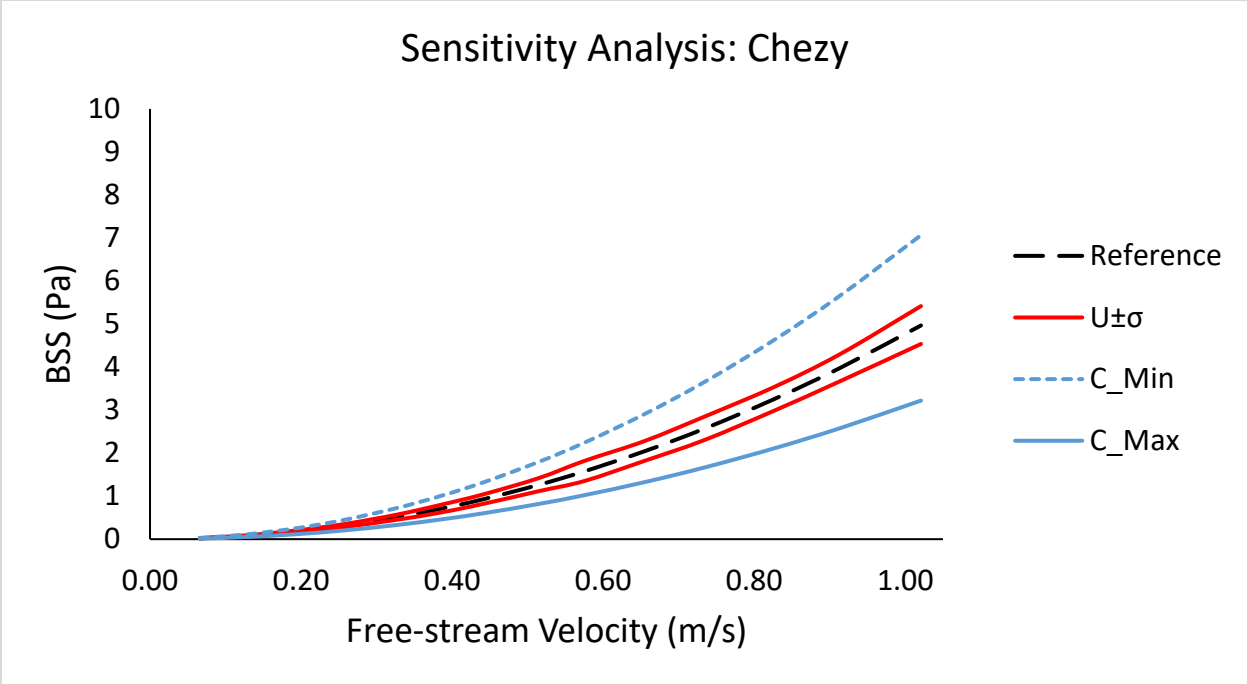






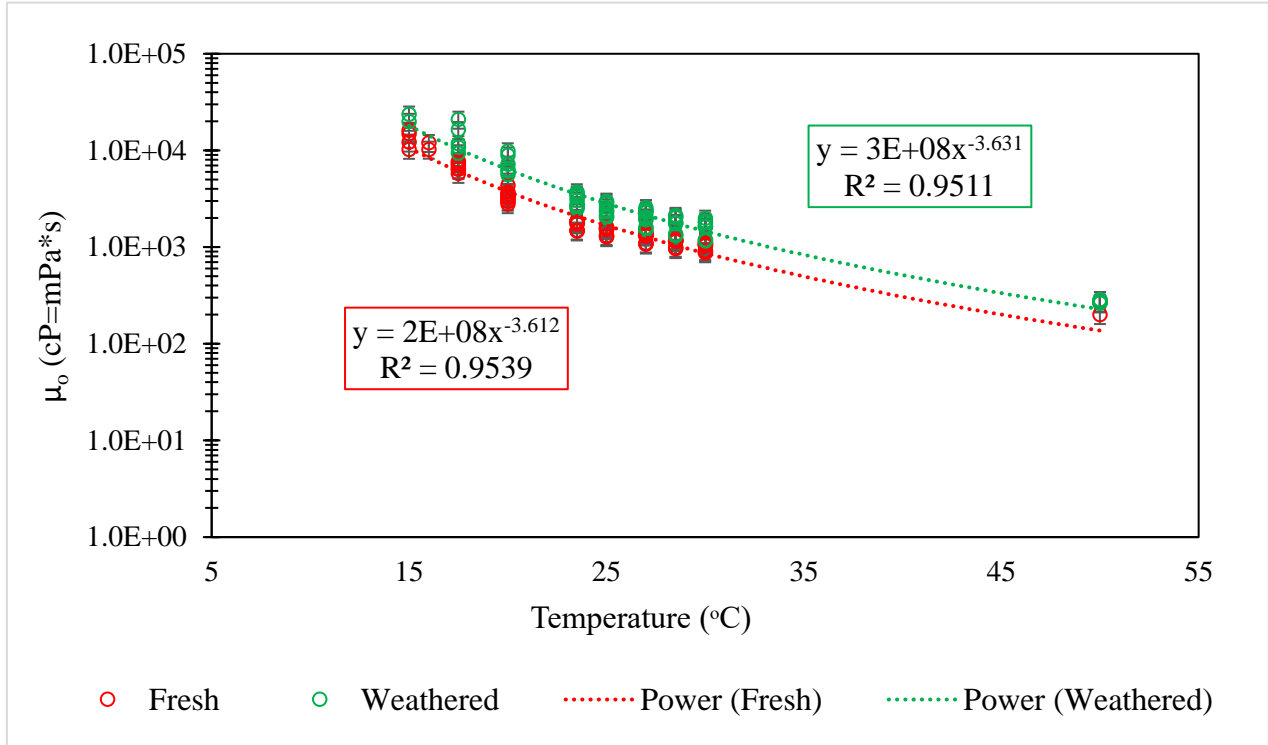
Appendix A.10: Sensitivity Analysis Plots



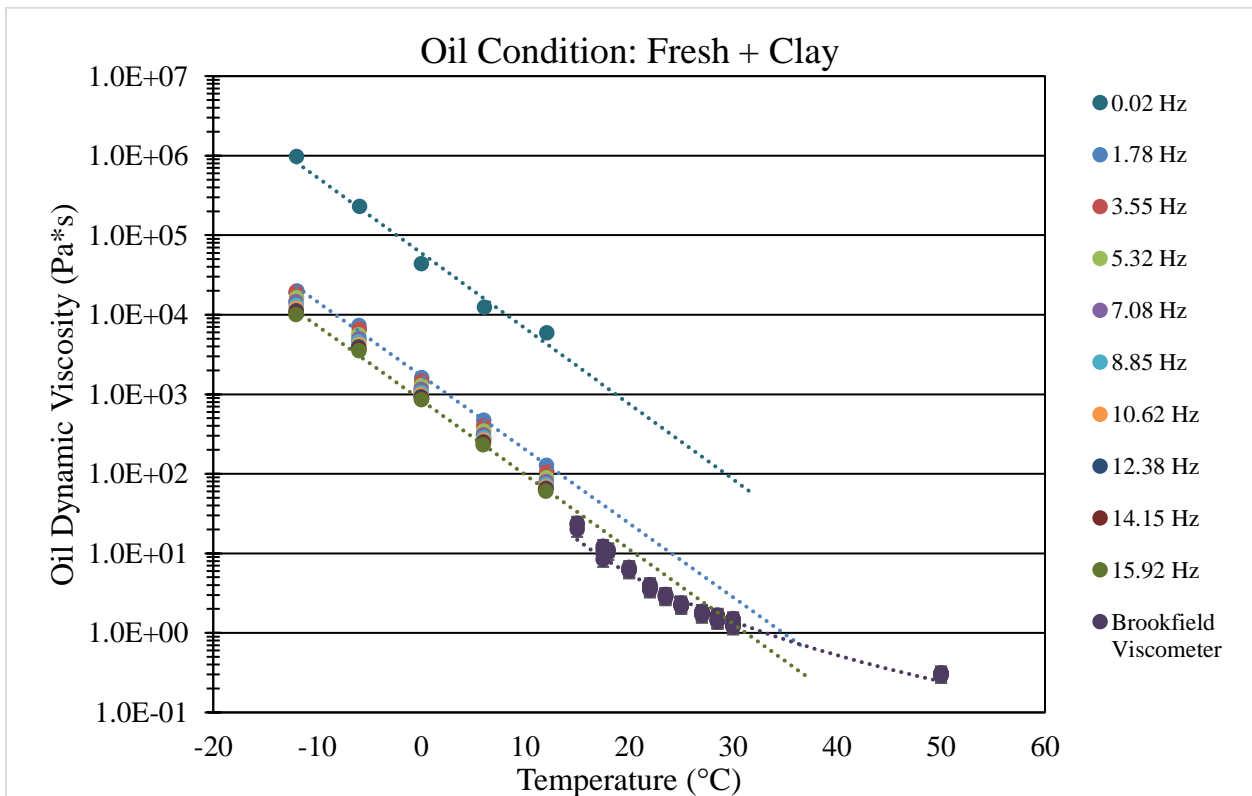
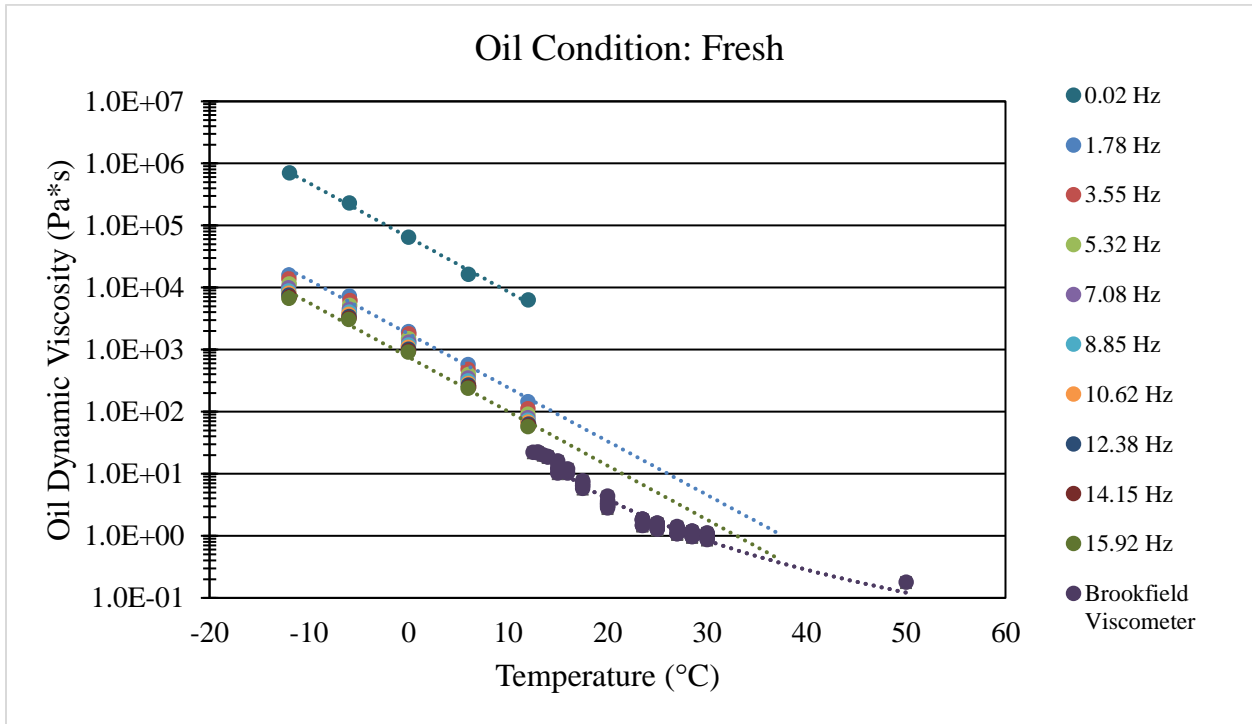


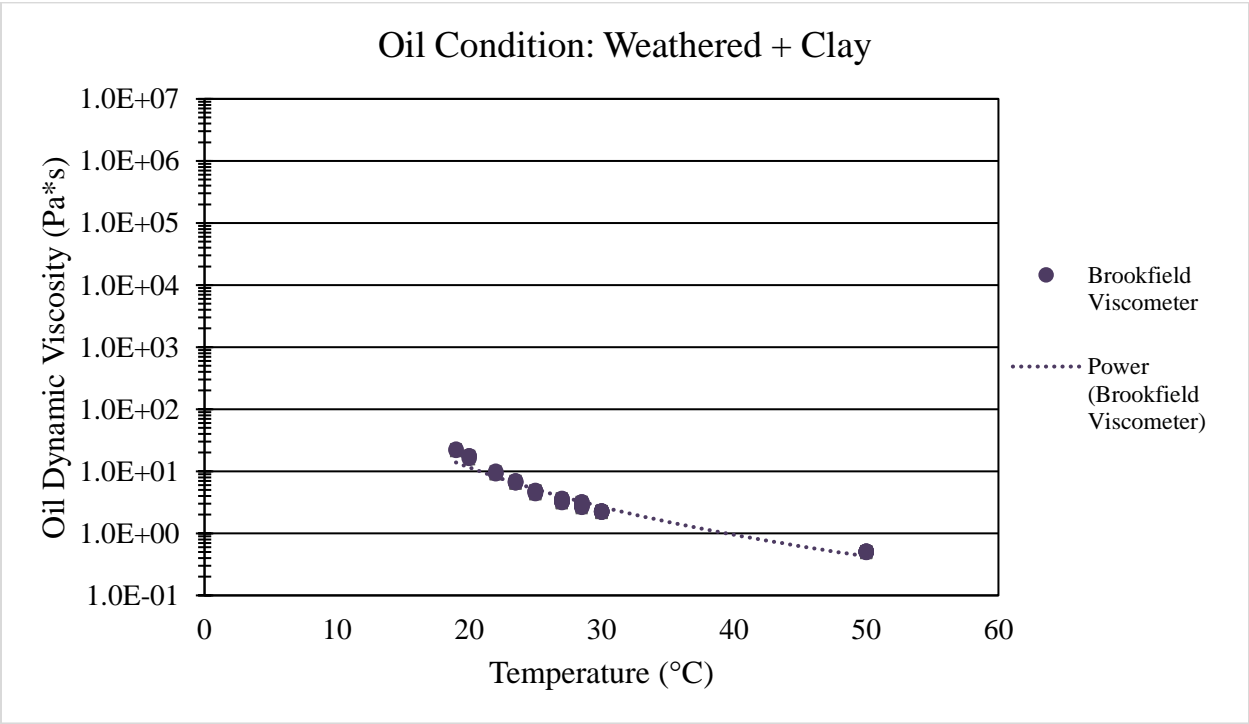
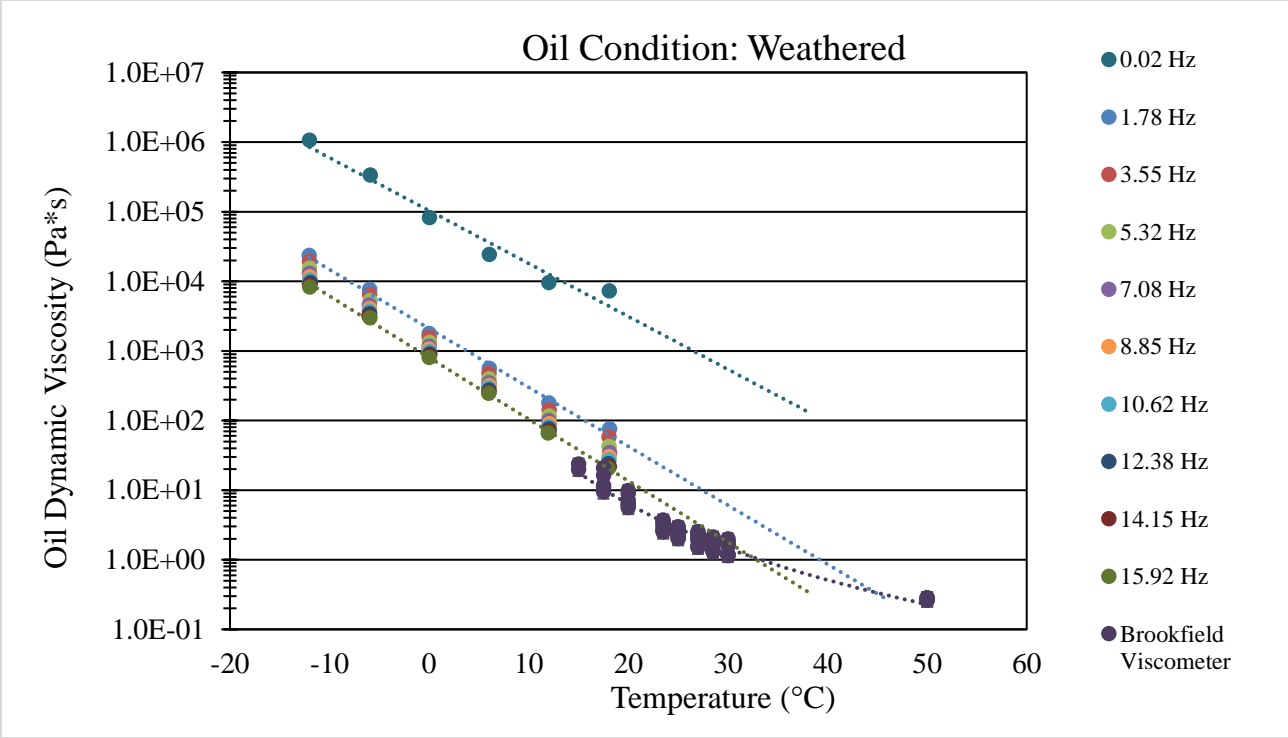
APPENDIX B: Chapter 3 Appendices

Appendix B.1: Fresh & Weathered Brookfield Viscosity



Appendix B.2: DHR and Brookfield Viscosity

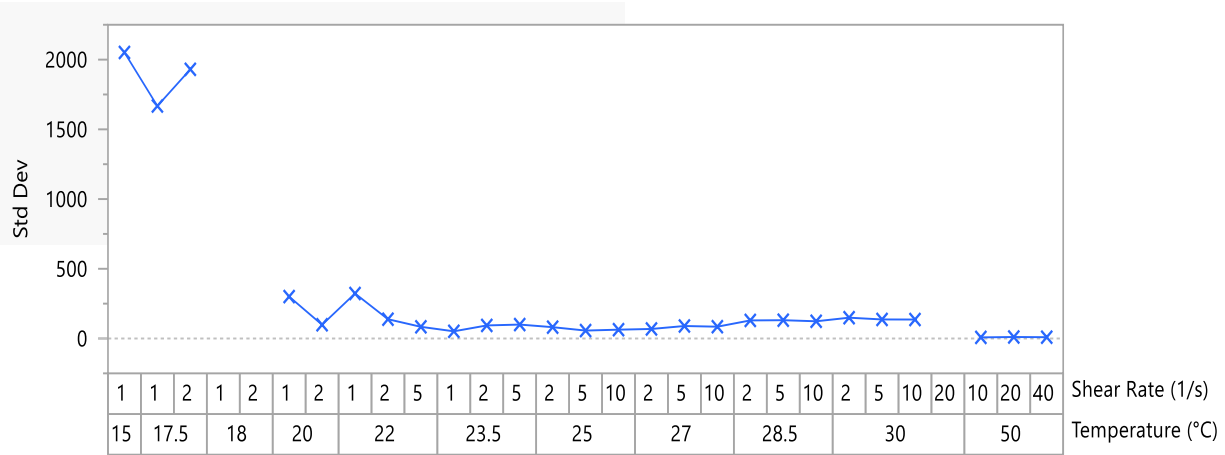
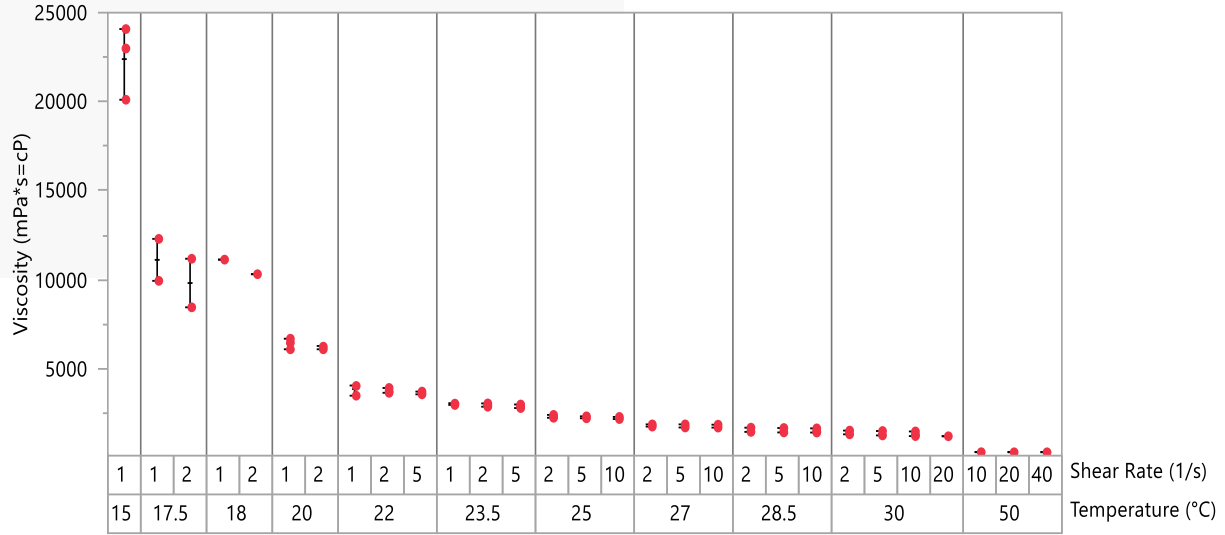




Appendix B.3: Wells-Brookfield Viscosity Variability

Fresh+Clay Sample

Variability Gauge Chart for Viscosity (mPa*s=cP)



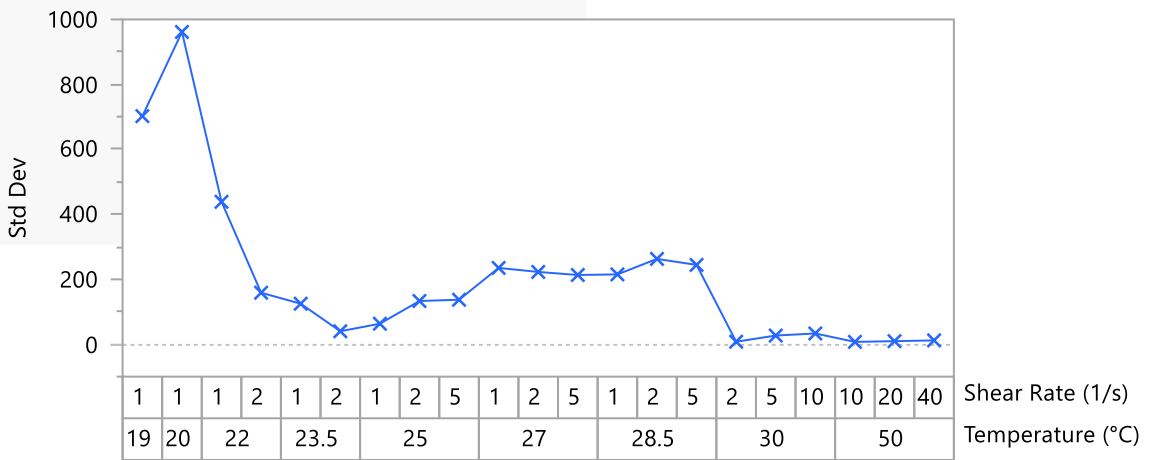
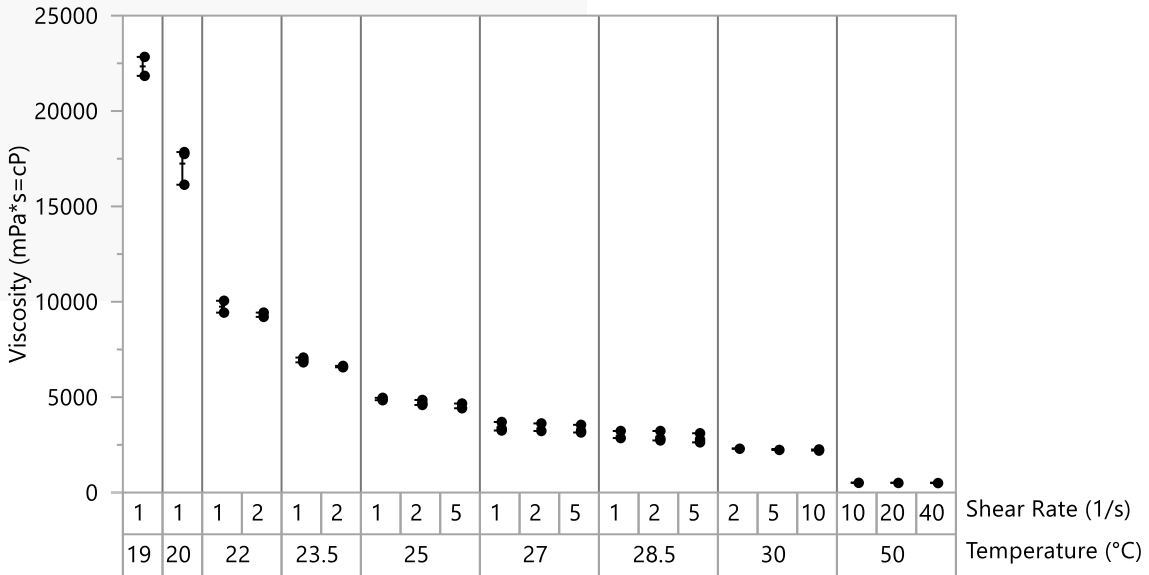
Variability Summary for Viscosity (mPa*s=cP)

Fresh+Clay	Mean	Std Dev	RSD	CV	Std Err Mean	Lower 95%	Upper 95%	Minimum	Maximum	Range	Median	Observations
Viscosity (mPa*s=cP)	3,754	4,618	123%	123	523	2713	4796	294	24078	23784	2219	78
Temperature (°C)[15]	22,390	2,051	9%	9	1,184	17294	27486	20107	24078	3971	22986	3
Temperature (°C)[17.5]	10,457	1,654	16%	16	827	7825	13088	8440	12287	3847	10549.5	4
Temperature (°C)[18]	10,712	579	5%	5	410	5508	15915	10302	11121	819	10711.5	2
Temperature (°C)[20]	6,299	231	4%	4	94	6057	6541	6082	6677	595	6249.5	6
Temperature (°C)[22]	3,739	209	6%	6	70	3578	3899	3475	4046	571	3704	9
Temperature (°C)[23.5]	2,943	94	3%	3	31	2870	3015	2780	3053	273	2954	9
Temperature (°C)[25]	2,256	73	3%	3	24	2200	2312	2162	2395	233	2234	9
Temperature (°C)[27]	1,765	72	4%	4	24	1710	1820	1681	1862	181	1738	9
Temperature (°C)[28.5]	1,512	112	7%	7	37	1426	1597	1403	1676	273	1460	9
Temperature (°C)[30]	1,327	126	9%	10	42	1230	1424	1195	1514	319	1268	9
Temperature (°C)[50]	306	8	3%	3	3	299	312	294	315	21	308	9
Temperature (°C)[15] Shear Rate (1/s)[1]	22,390	2,051	9%	9	1,184	17294	27486	20107	24078	3971	22986	3
Temperature (°C)[17.5] Shear Rate (1/s)[1]	11,108	1,667	15%	15	1,179	-3873	26089	9929	12287	2358	11108	2
Temperature (°C)[17.5] Shear Rate (1/s)[2]	9,805	1,930	20%	20	1,365	-7539	27149	8440	11170	2730	9805	2
Temperature (°C)[18] Shear Rate (1/s)[1]	11,121	#VALUE!	11121	11121	0	11121	1
Temperature (°C)[18] Shear Rate (1/s)[2]	10,302	#VALUE!	10302	10302	0	10302	1
Temperature (°C)[20] Shear Rate (1/s)[1]	6,404	301	5%	5	174	5658	7151	6082	6677	595	6454	3
Temperature (°C)[20] Shear Rate (1/s)[2]	6,194	98	2%	2	57	5949	6438	6082	6268	186	6231	3
Temperature (°C)[22] Shear Rate (1/s)[1]	3,847	323	8%	8	186	3046	4649	3475	4046	571	4021	3
Temperature (°C)[22] Shear Rate (1/s)[2]	3,761	138	4%	4	80	3418	4104	3637	3910	273	3736	3
Temperature (°C)[22] Shear Rate (1/s)[5]	3,608	84	2%	2	48	3400	3816	3550	3704	154	3570	3
Temperature (°C)[23.5] Shear Rate (1/s)[1]	3,012	51	2%	2	30	2884	3140	2954	3053	99	3028	3
Temperature (°C)[23.5] Shear Rate (1/s)[2]	2,942	94	3%	3	54	2709	3174	2855	3041	186	2929	3
Temperature (°C)[23.5] Shear Rate (1/s)[5]	2,875	100	3%	3	58	2627	3123	2780	2979	199	2865	3
Temperature (°C)[25] Shear Rate (1/s)[2]	2,308	81	4%	4	47	2107	2510	2234	2395	161	2296	3
Temperature (°C)[25] Shear Rate (1/s)[5]	2,251	57	3%	3	33	2109	2392	2204	2314	110	2234	3
Temperature (°C)[25] Shear Rate (1/s)[10]	2,209	63	3%	3	37	2052	2366	2162	2281	119	2184	3
Temperature (°C)[27] Shear Rate (1/s)[2]	1,783	68	4%	4	39	1613	1953	1738	1862	124	1750	3
Temperature (°C)[27] Shear Rate (1/s)[5]	1,763	90	5%	5	52	1540	1985	1688	1862	174	1738	3
Temperature (°C)[27] Shear Rate (1/s)[10]	1,749	85	5%	5	49	1539	1960	1681	1844	163	1723	3
Temperature (°C)[28.5] Shear Rate (1/s)[2]	1,527	130	9%	8	75	1205	1849	1440	1676	236	1465	3
Temperature (°C)[28.5] Shear Rate (1/s)[5]	1,509	131	9%	9	76	1184	1835	1410	1658	248	1460	3
Temperature (°C)[28.5] Shear Rate (1/s)[10]	1,499	123	8%	8	71	1192	1805	1403	1638	235	1455	3
Temperature (°C)[30] Shear Rate (1/s)[2]	1,409	149	11%	11	106	68	2749	1303	1514	211	1408.5	2
Temperature (°C)[30] Shear Rate (1/s)[5]	1,332	137	10%	10	79	993	1671	1241	1489	248	1266	3
Temperature (°C)[30] Shear Rate (1/s)[10]	1,312	136	10%	10	79	974	1650	1204	1465	261	1268	3
Temperature (°C)[30] Shear Rate (1/s)[20]	1,195	#VALUE!	1195	1195	0	1195	1
Temperature (°C)[50] Shear Rate (1/s)[10]	307	8	3%	3	5	287	327	298	313	15	310	3
Temperature (°C)[50] Shear Rate (1/s)[20]	306	11	4%	3	6	279	332	294	315	21	308	3
Temperature (°C)[50] Shear Rate (1/s)[40]	304	9	3%	3	5	281	327	294	312	18	307	3

Note: The viscosity variability was a function of shear rate (1/s = Hz) and temperature (°C). Non-Newtonian fluids, such as No. 6 HFO, do not have constant viscosities, at a constant temperature, with increasing or decreasing shear rates. For example, at 25°C and shear-rate of 2 Hz, viscosity = 2,308 mPa*s. At 25°C and shear-rate of 5 Hz, viscosity was 2,251 mPa*s. The decline in viscosity as shear-rate increases suggests that this fluid is a shear-thinning fluid.

Weathered+Clay Sample

Variability Gauge Chart for Viscosity (mPa*s=cP)

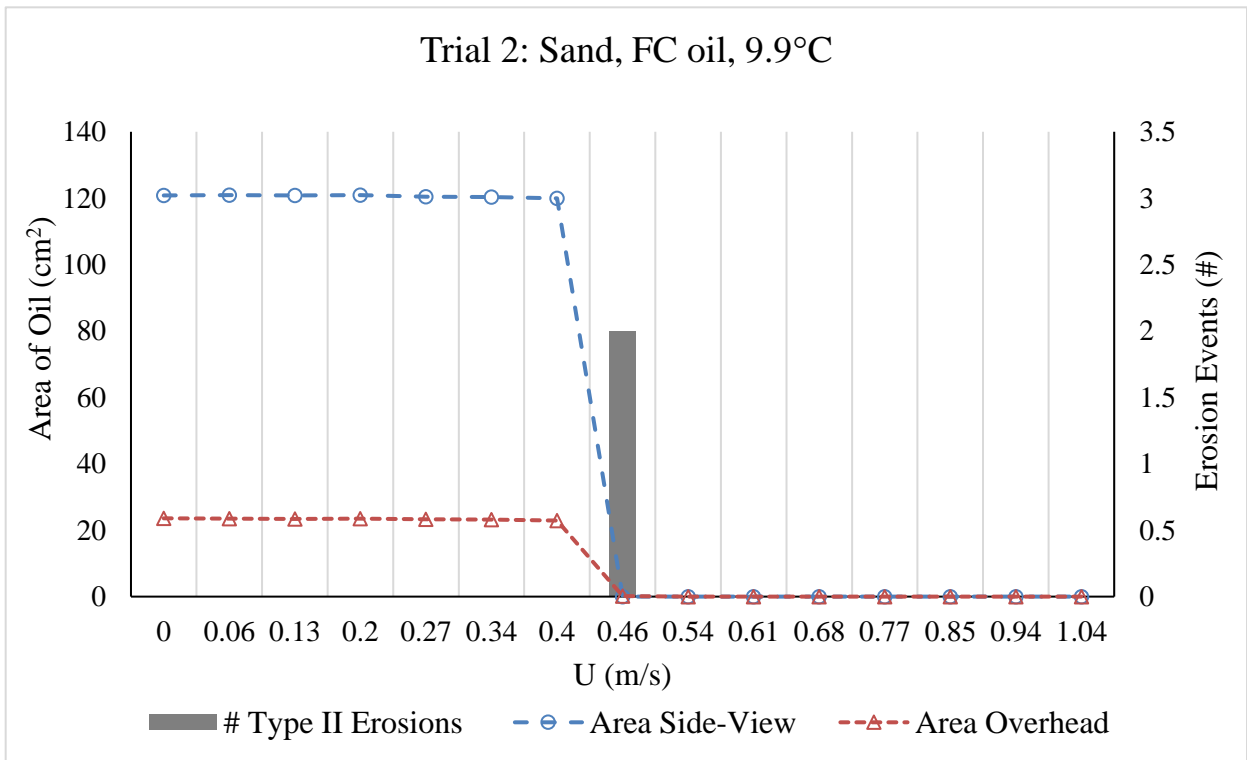
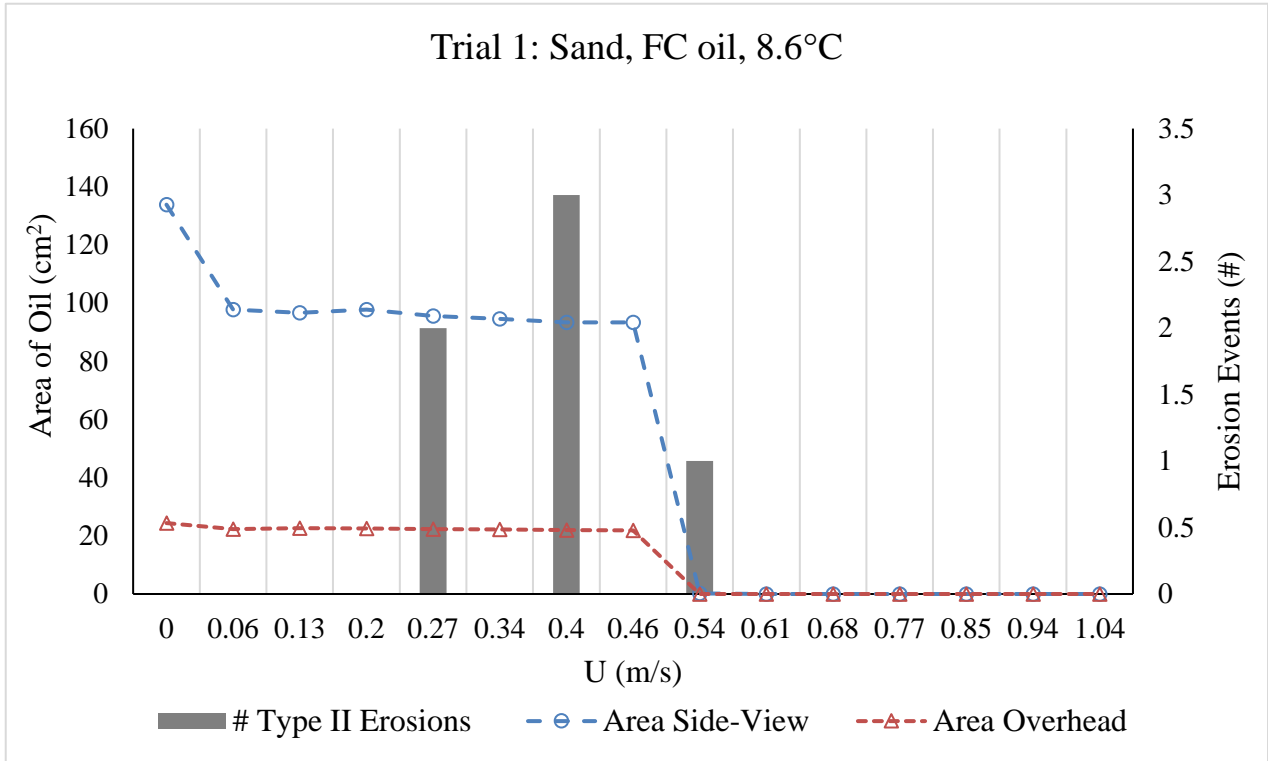


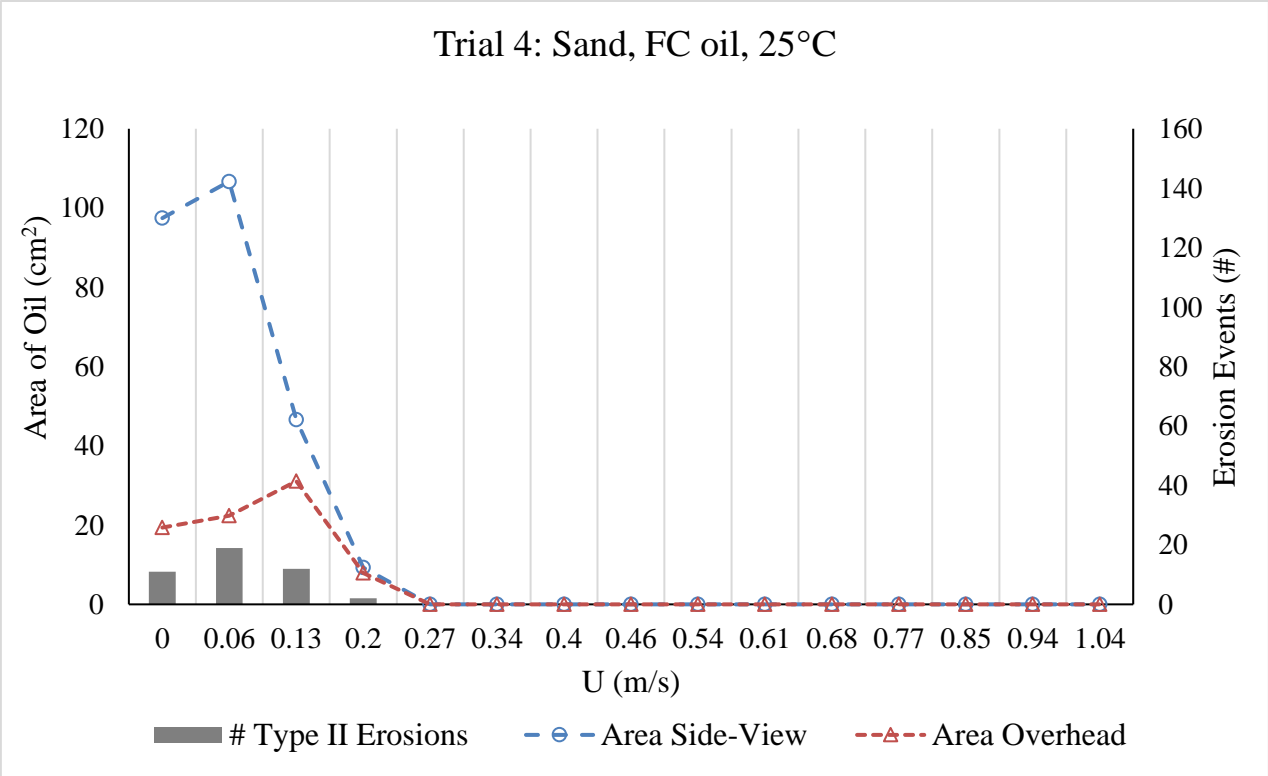
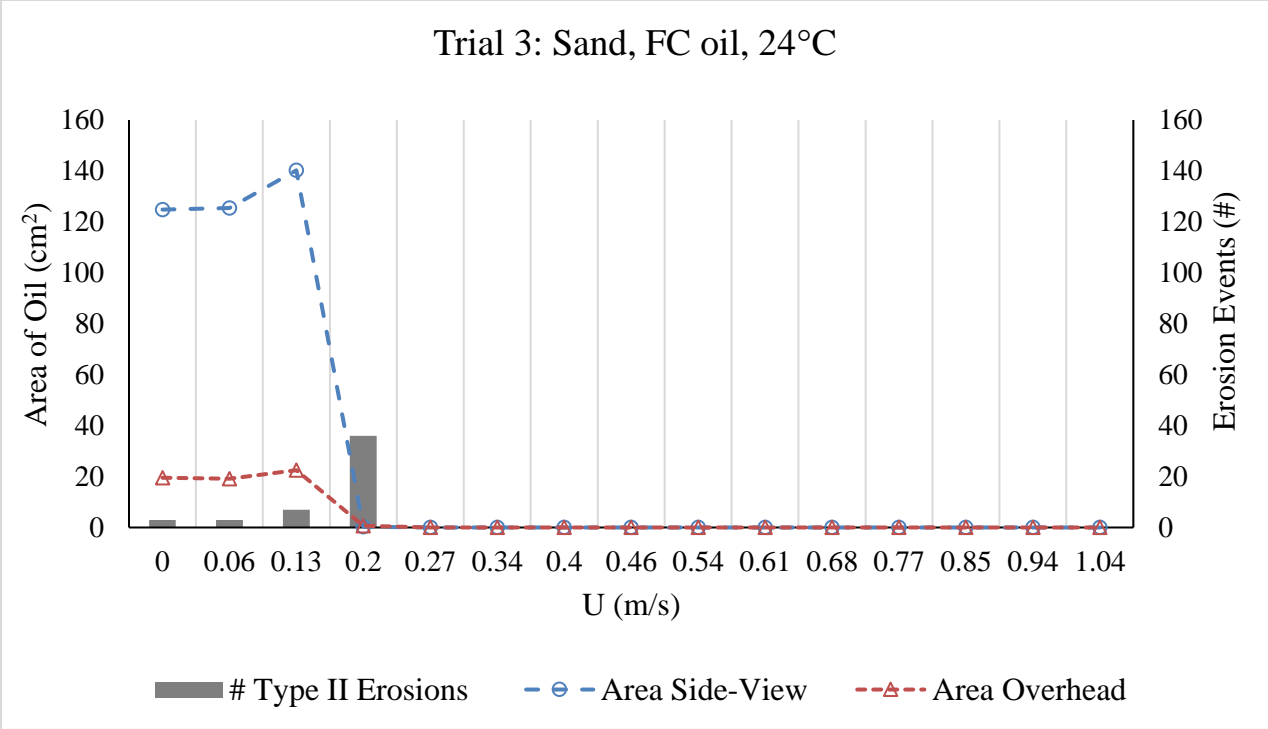
Variability Summary for Viscosity (mPa*s=cP)

Weathered+Clay	Mean	Std Dev	RSD	CV	Std Err Mean	Lower 95%	Upper 95%	Minimum	Maximum	Range	Median	Observations
Viscosity (mPa*s=cP)	4984	4990	100%	100	644	3695	6273	496	22837	22341	3240	60
Temperature (°C)[19]	22341	702	3%	3	497	16032	28649	21844	22837	993	22341	2
Temperature (°C)[20]	17244	961	6%	6	555	14855	19632	16135	17848	1713	17748	3
Temperature (°C)[22]	9532	363	4%	4	182	8954	10110	9209	10053	844	9433	4
Temperature (°C)[23.5]	6773	212	3%	3	86	6550	6995	6566	7075	509	6733	6
Temperature (°C)[25]	4705	196	4%	4	65	4555	4856	4419	4965	546	4679	9
Temperature (°C)[27]	3370	201	6%	6	67	3215	3525	3148	3699	551	3252	9
Temperature (°C)[28.5]	2916	218	7%	7	73	2749	3083	2631	3227	596	2855	9
Temperature (°C)[30]	2259	40	2%	2	13	2228	2290	2197	2309	112	2259	9
Temperature (°C)[50]	511	8	2%	2	3	504	517	496	521	25	509	9
Temperature (°C)[19] Shear Rate (1/s)[1]	22341	702	3%	3	497	16032	28649	21844	22837	993	22341	2
Temperature (°C)[20] Shear Rate (1/s)[1]	17244	961	6%	6	555	14855	19632	16135	17848	1713	17748	3
Temperature (°C)[22] Shear Rate (1/s)[1]	9743	438	4%	4	310	5804	13682	9433	10053	620	9743	2
Temperature (°C)[22] Shear Rate (1/s)[2]	9321	158	2%	2	112	7898	10744	9209	9433	224	9321	2
Temperature (°C)[23.5] Shear Rate (1/s)[1]	6950	125	2%	2	72	6641	7260	6826	7075	249	6950	3
Temperature (°C)[23.5] Shear Rate (1/s)[2]	6595	40	1%	1	23	6496	6693	6566	6640	74	6578	3
Temperature (°C)[25] Shear Rate (1/s)[1]	4898	63	1%	1	36	4742	5055	4840	4965	125	4890	3
Temperature (°C)[25] Shear Rate (1/s)[2]	4708	133	3%	3	77	4378	5038	4592	4853	261	4679	3
Temperature (°C)[25] Shear Rate (1/s)[5]	4510	137	3%	3	79	4170	4849	4419	4667	248	4443	3
Temperature (°C)[27] Shear Rate (1/s)[1]	3434	235	7%	7	136	2851	4017	3252	3699	447	3351	3
Temperature (°C)[27] Shear Rate (1/s)[2]	3368	222	7%	7	128	2815	3920	3227	3624	397	3252	3
Temperature (°C)[27] Shear Rate (1/s)[5]	3308	213	6%	6	123	2779	3837	3148	3550	402	3227	3
Temperature (°C)[28.5] Shear Rate (1/s)[1]	2979	215	7%	7	124	2445	3513	2855	3227	372	2855	3
Temperature (°C)[28.5] Shear Rate (1/s)[2]	2929	262	9%	9	152	2277	3581	2731	3227	496	2830	3
Temperature (°C)[28.5] Shear Rate (1/s)[5]	2840	244	9%	9	141	2233	3446	2631	3108	477	2780	3
Temperature (°C)[30] Shear Rate (1/s)[2]	2300	8	0%	0	4	2282	2319	2296	2309	13	2296	3
Temperature (°C)[30] Shear Rate (1/s)[5]	2254	26	1%	1	15	2188	2320	2234	2284	50	2244	3
Temperature (°C)[30] Shear Rate (1/s)[10]	2222	33	1%	1	19	2140	2303	2197	2259	62	2209	3
Temperature (°C)[50] Shear Rate (1/s)[10]	513	7	1%	1	4	496	530	509	521	12	509	3
Temperature (°C)[50] Shear Rate (1/s)[20]	511	9	2%	2	5	488	534	503	521	18	509	3
Temperature (°C)[50] Shear Rate (1/s)[40]	508	12	2%	2	7	479	537	496	519	23	509	3

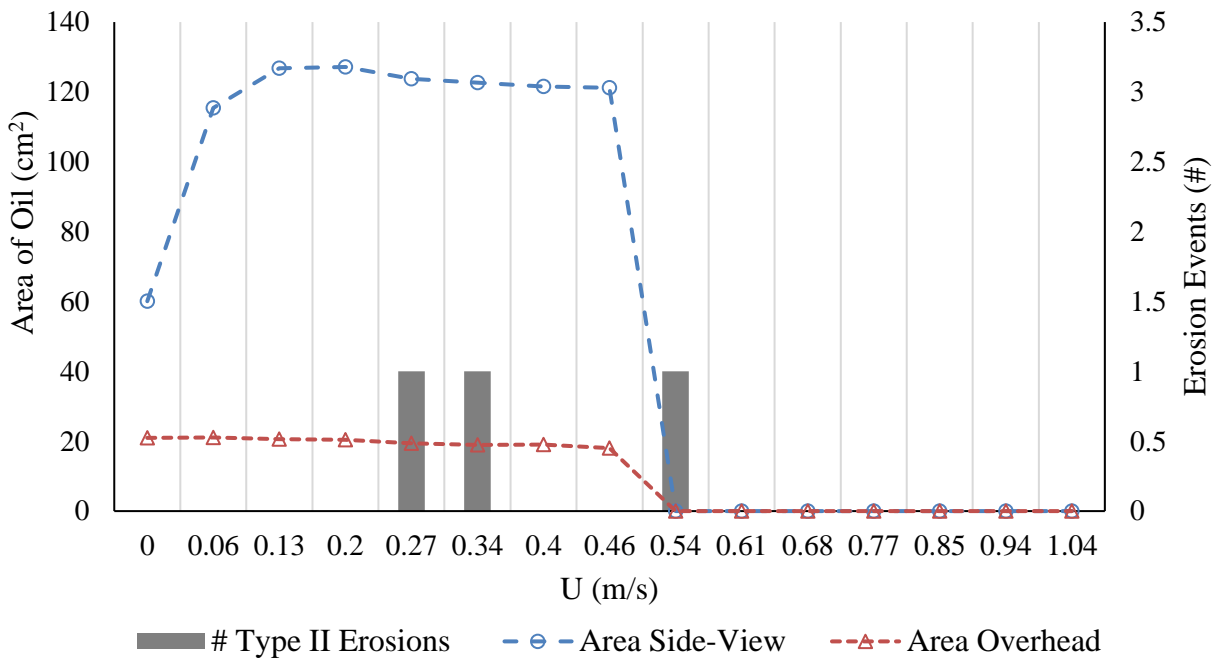
Note: The viscosity variability was a function of shear rate (1/s = Hz) and temperature (°C). Non-Newtonian fluids, such as No. 6 HFO, do not have constant viscosities, at a constant temperature, with increasing or decreasing shear rates. For example, at 25°C and shear-rate of 2 Hz, viscosity = 4708 mPa*s. At 25°C and shear-rate of 5 Hz, viscosity was 4510 mPa*s. The decline in viscosity as shear-rate increases suggests that this fluid is a shear-thinning fluid.

Appendix B.4: Plots of Measured Responses

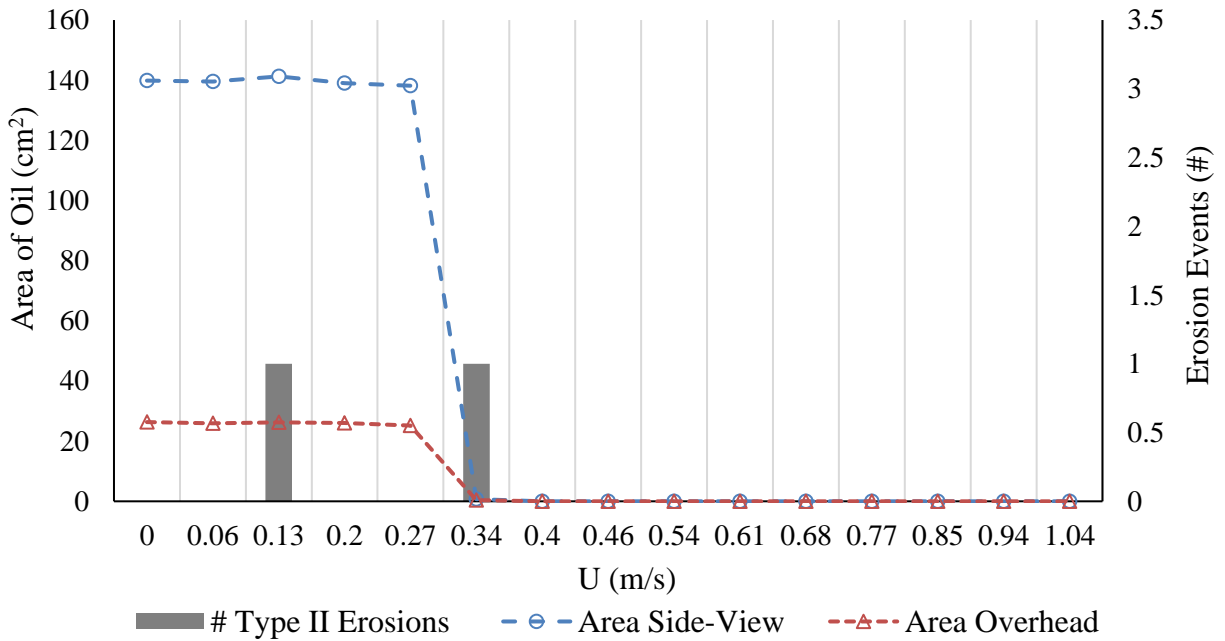


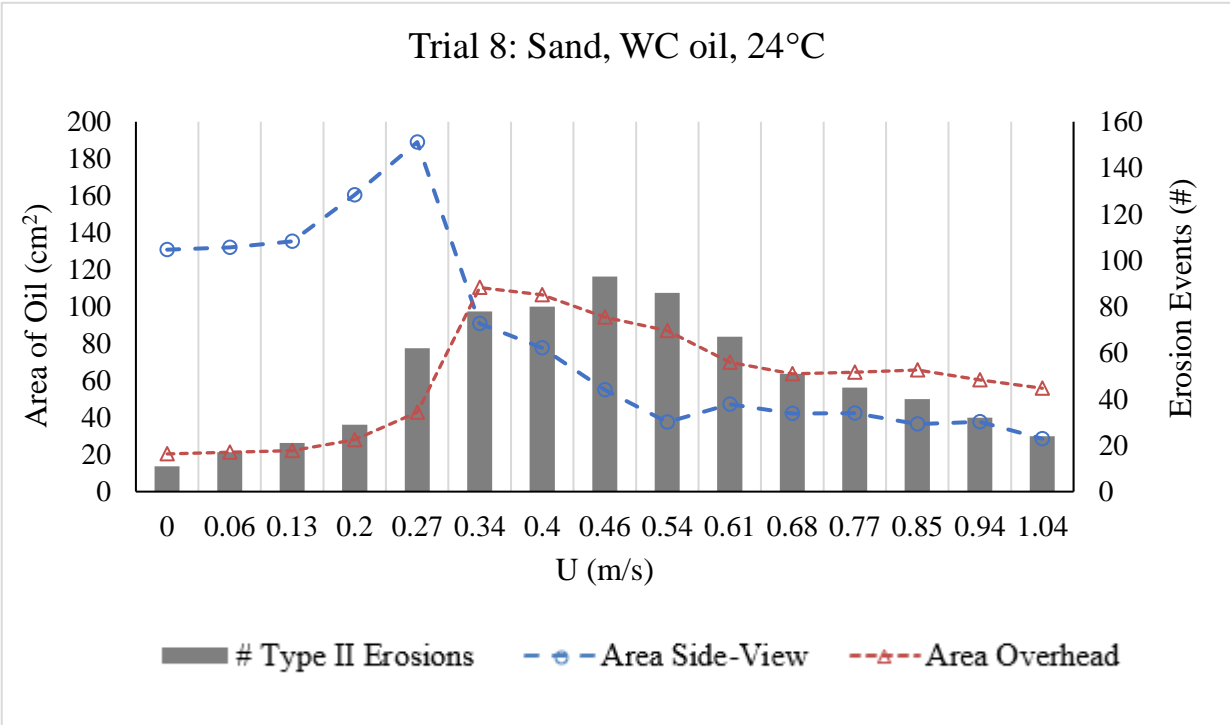
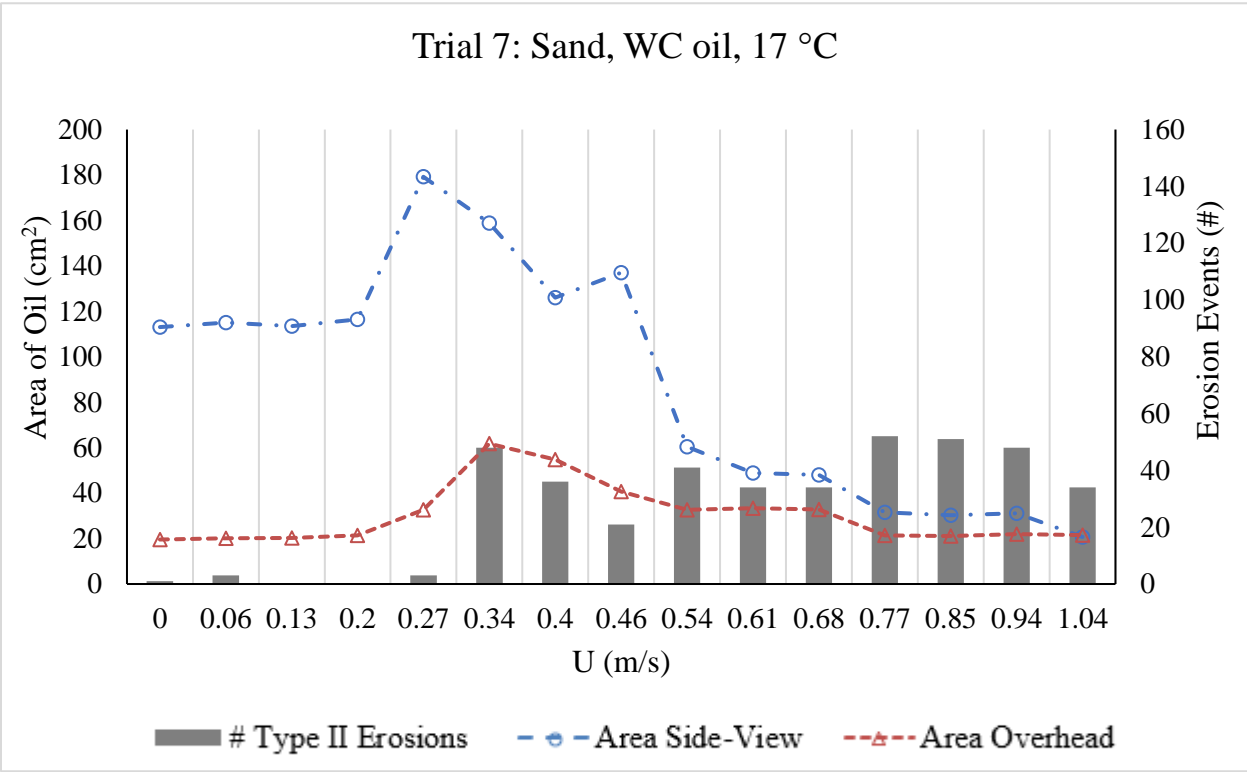


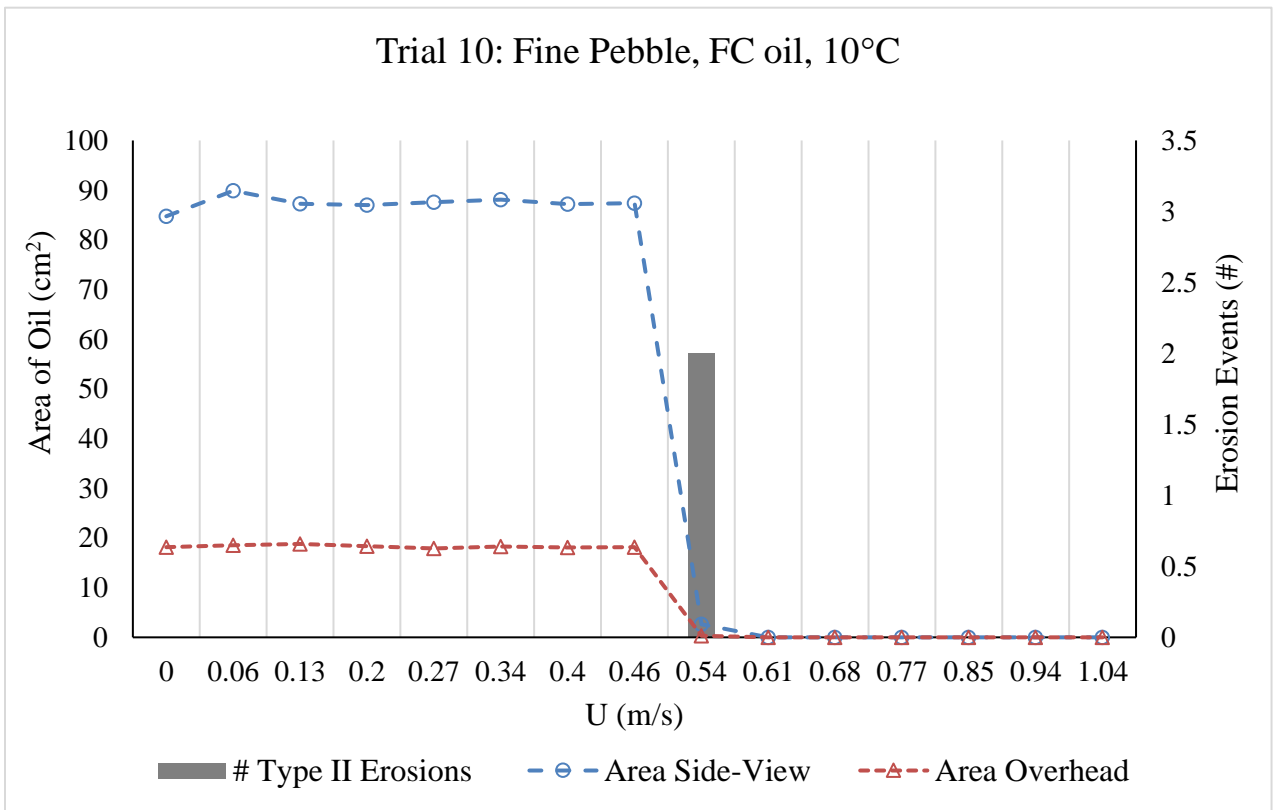
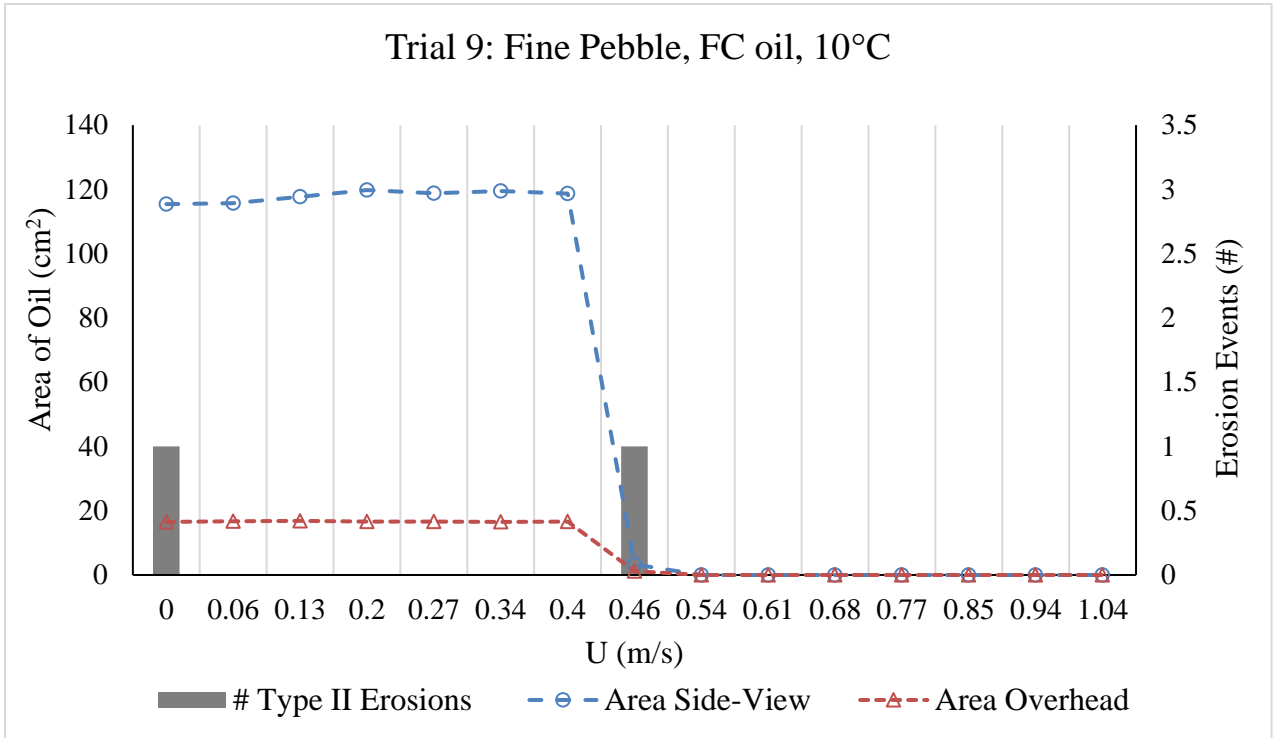
Trial 5: Sand, WC oil, 7.2°C

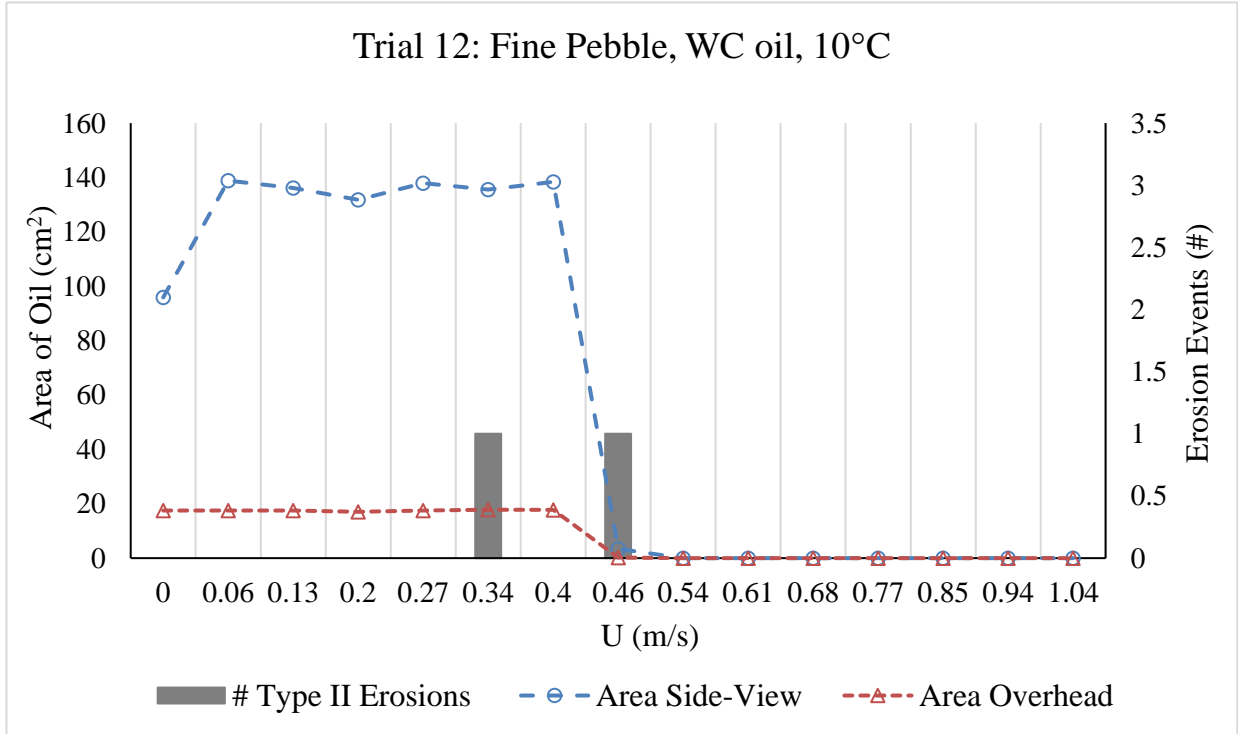
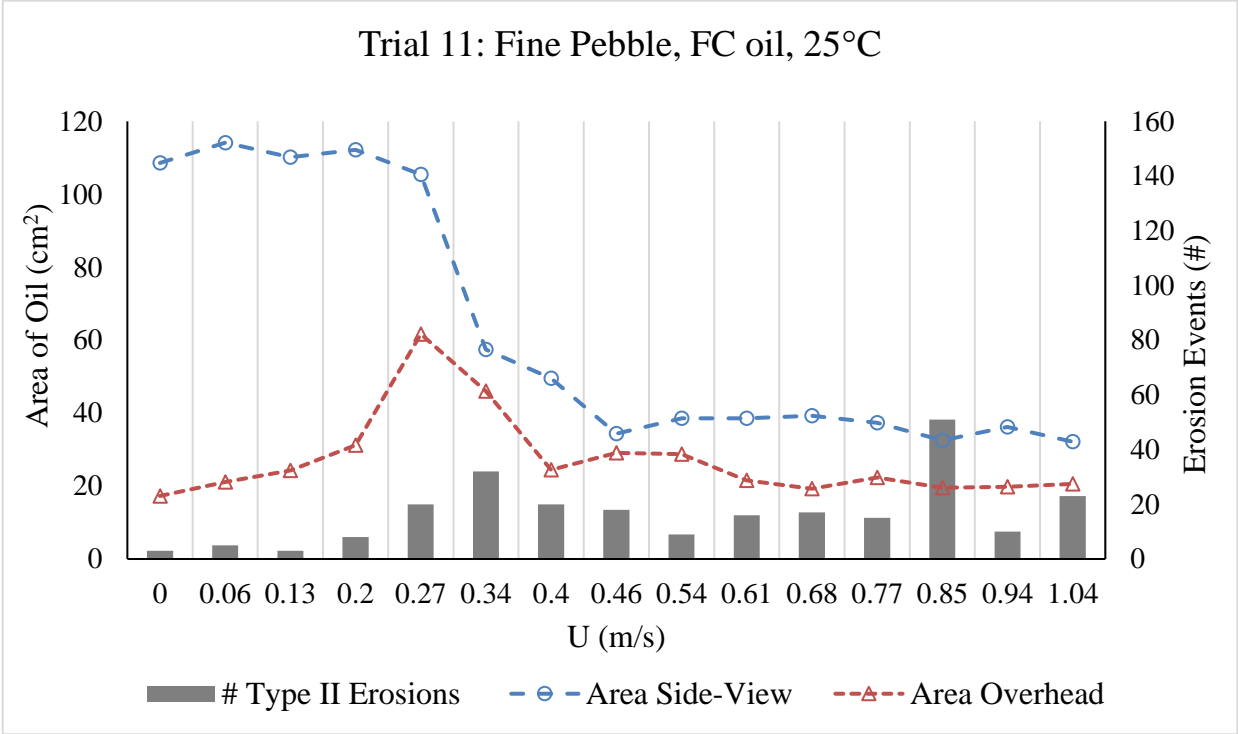


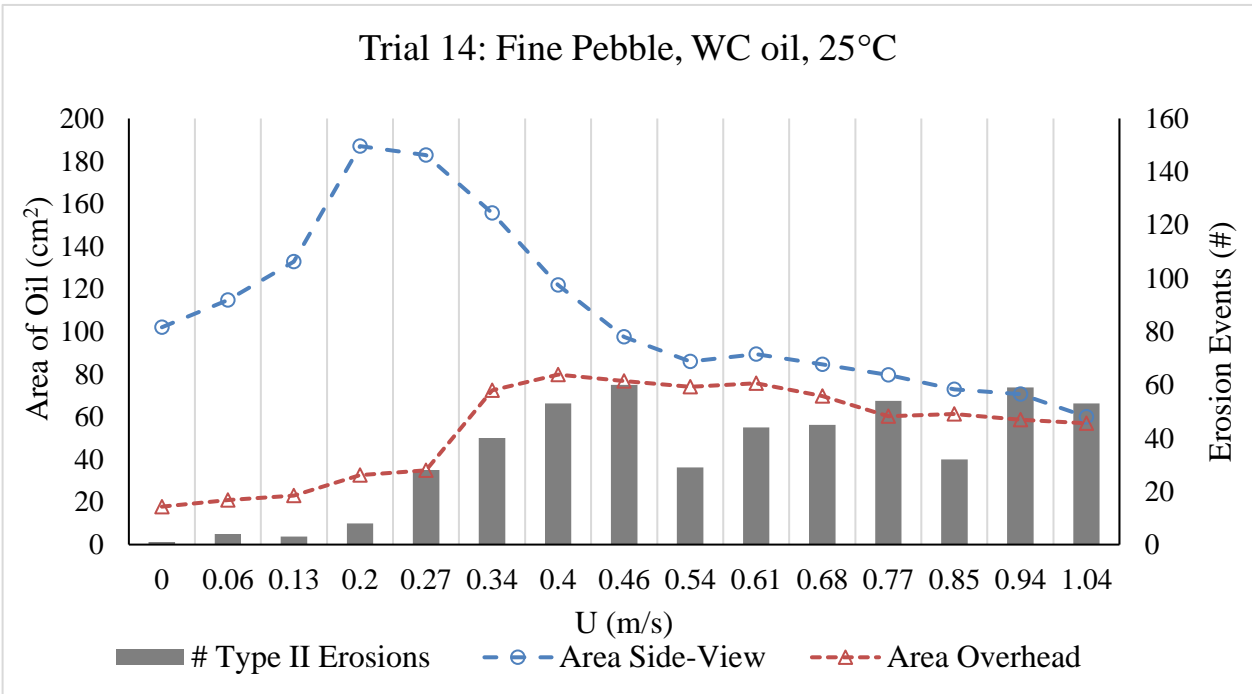
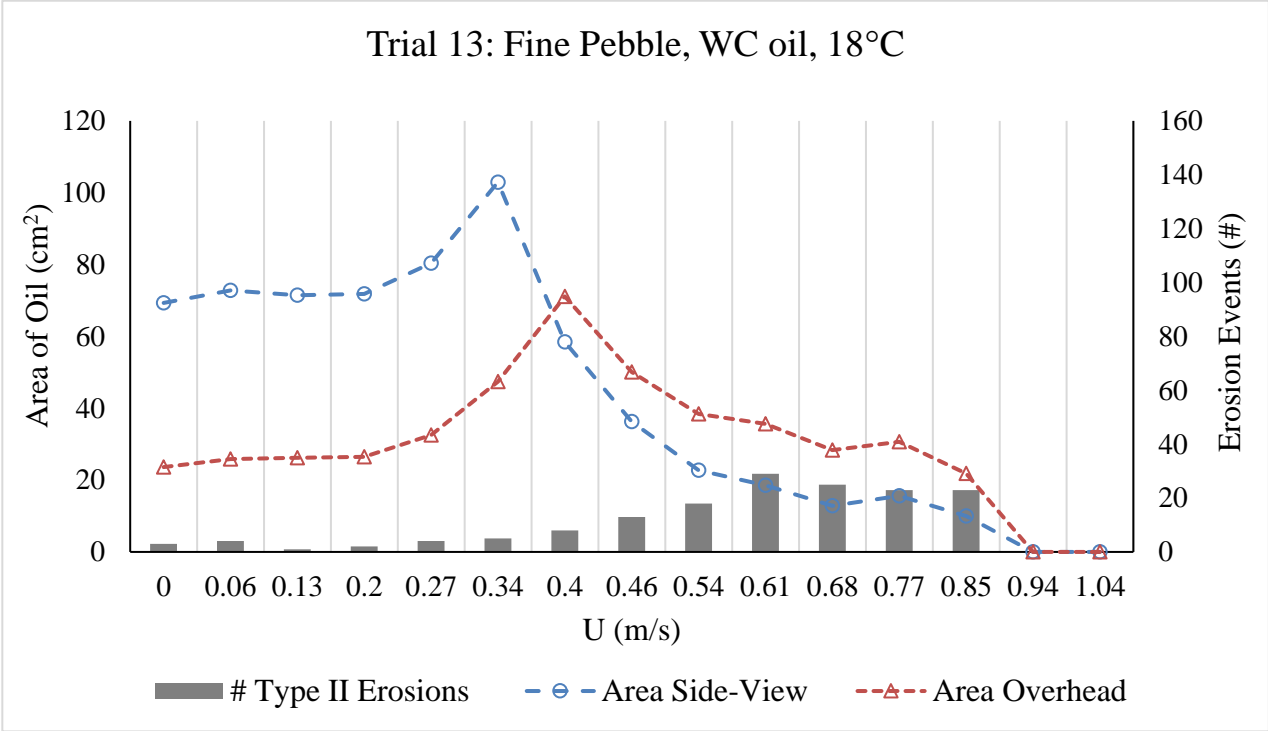
Trial 6: Sand, WC oil, 10°C



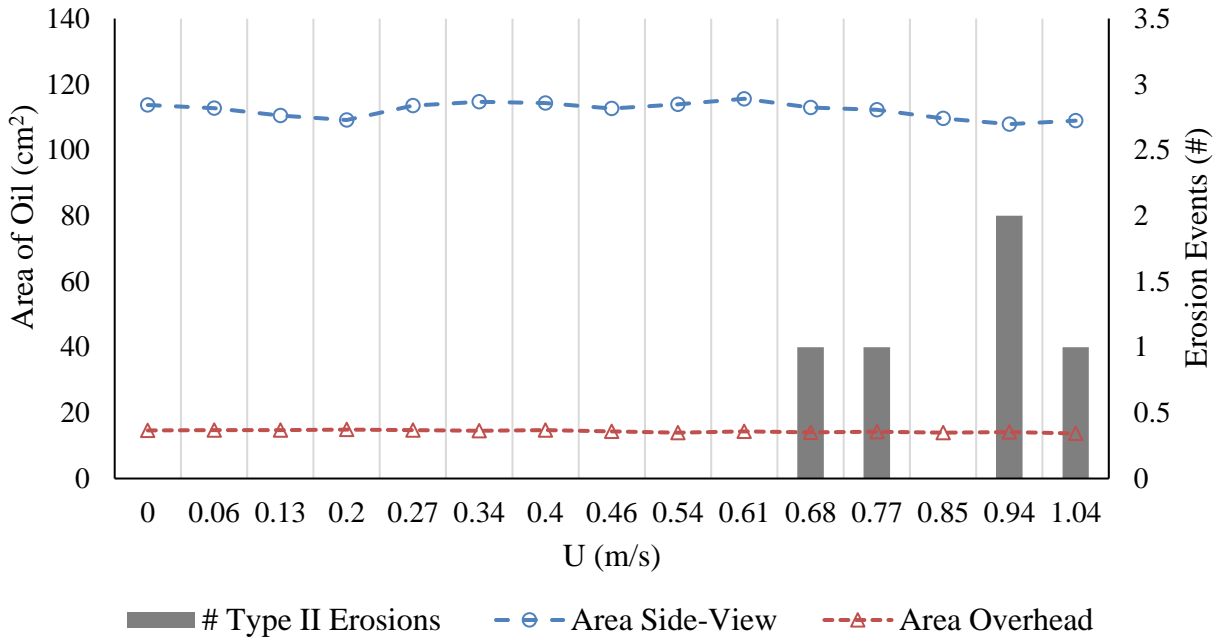




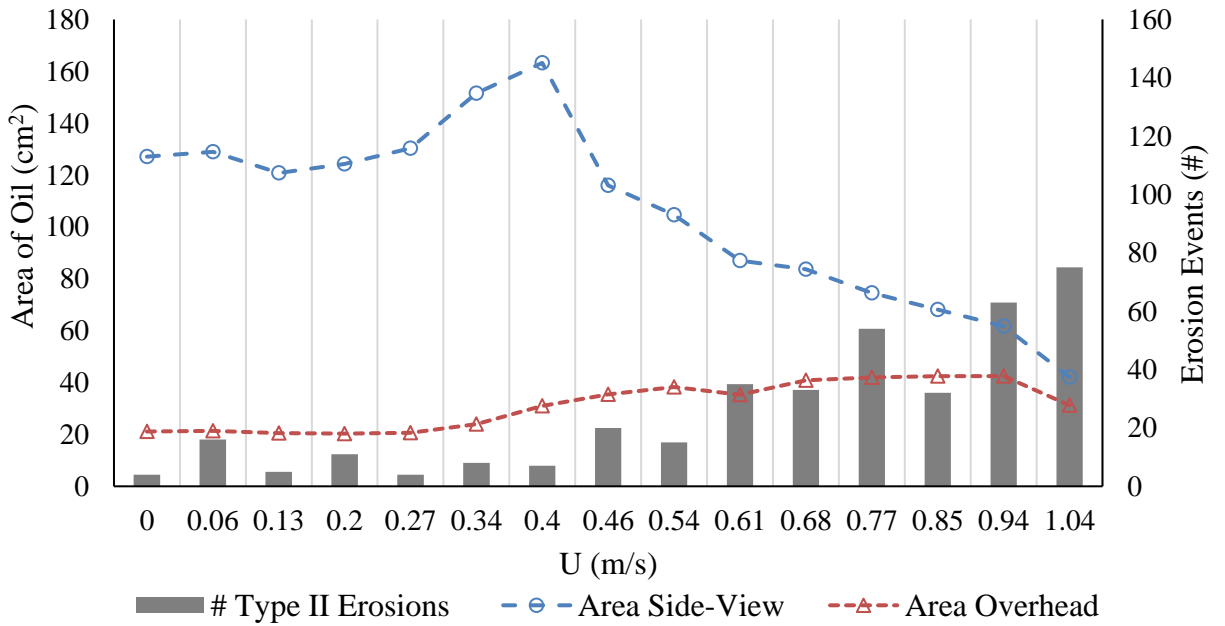




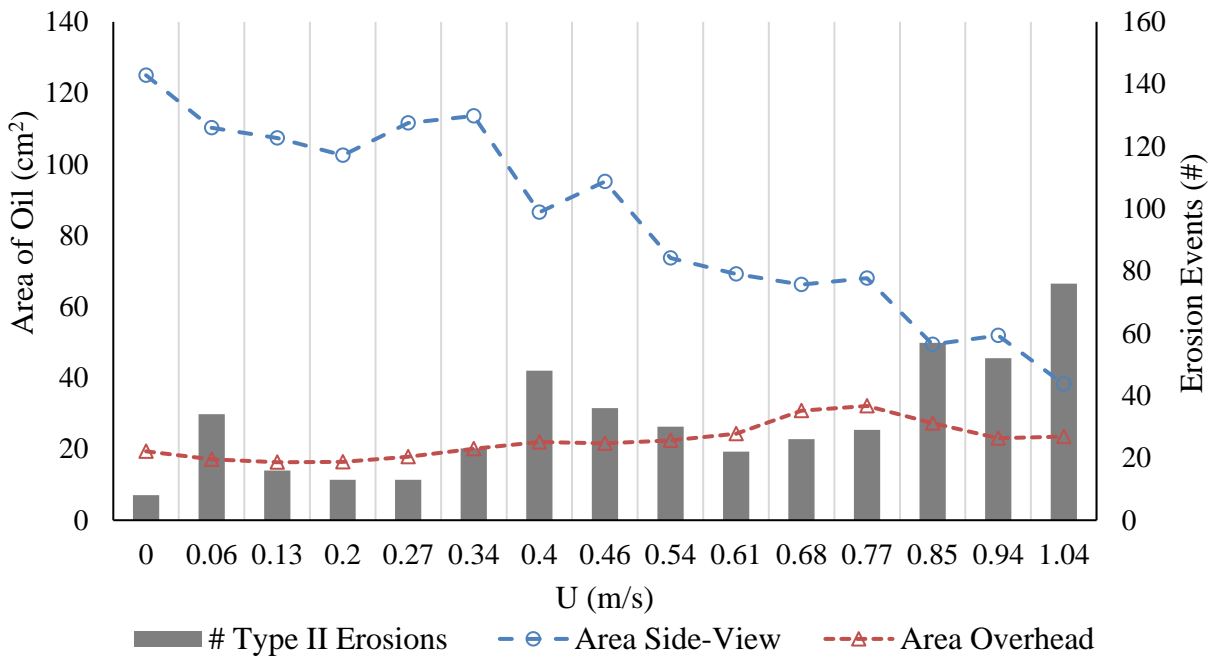
Trial 15: Medium Pebble, FC oil, 9.5°C



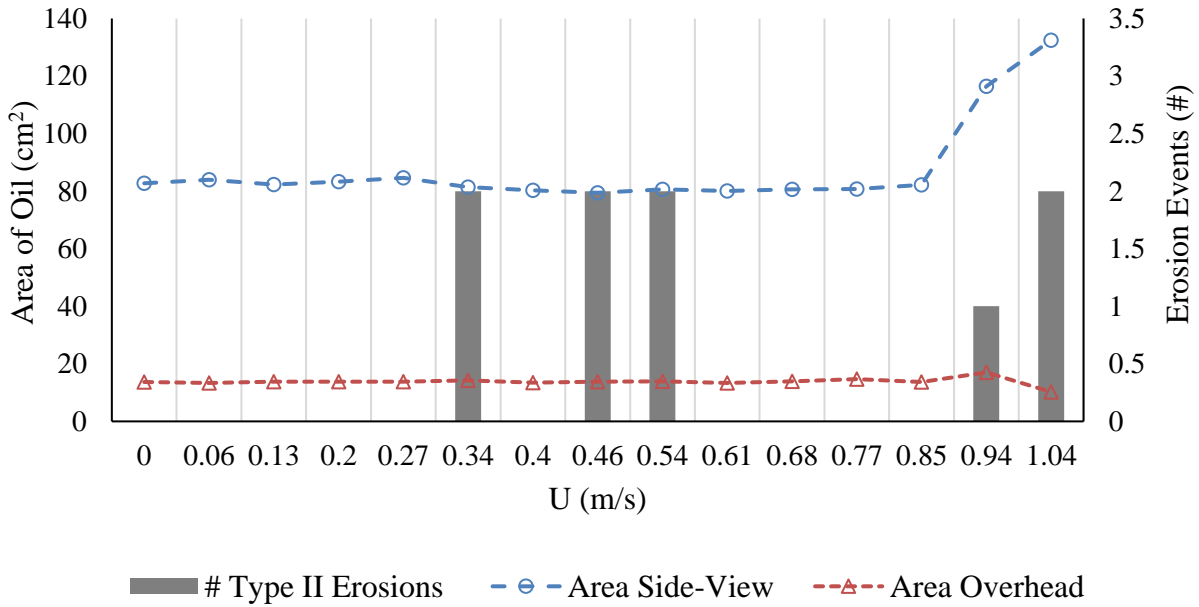
Trial 16: Medium Pebble, FC oil, 18°C



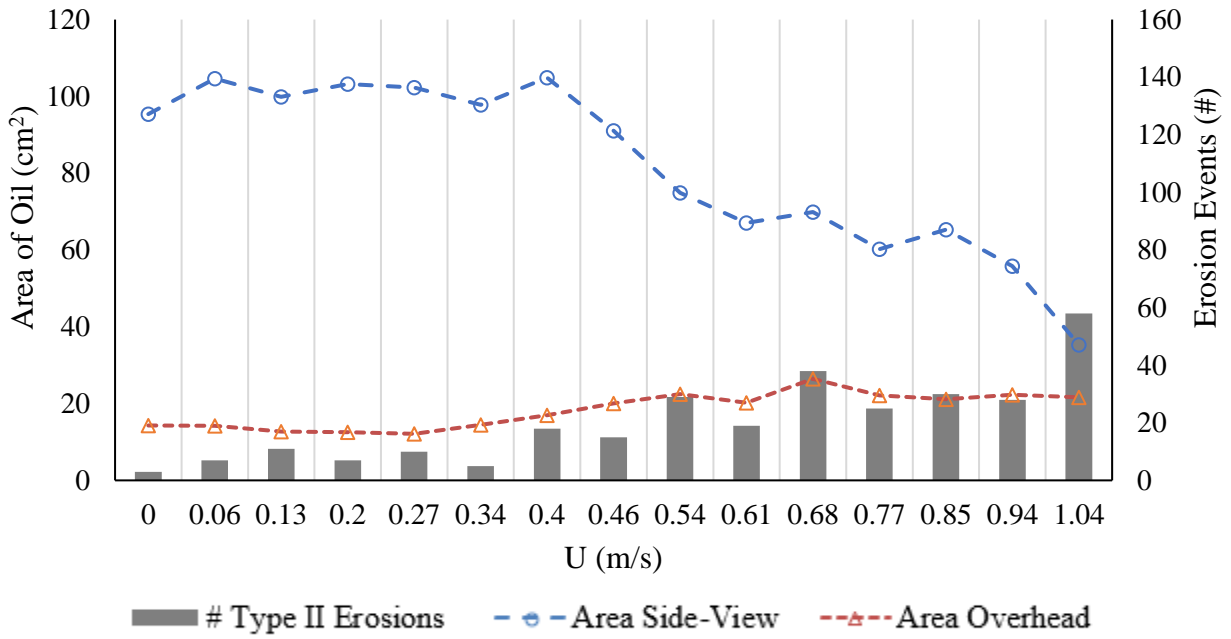
Trial 17: Medium Pebble, FC oil, 22°C



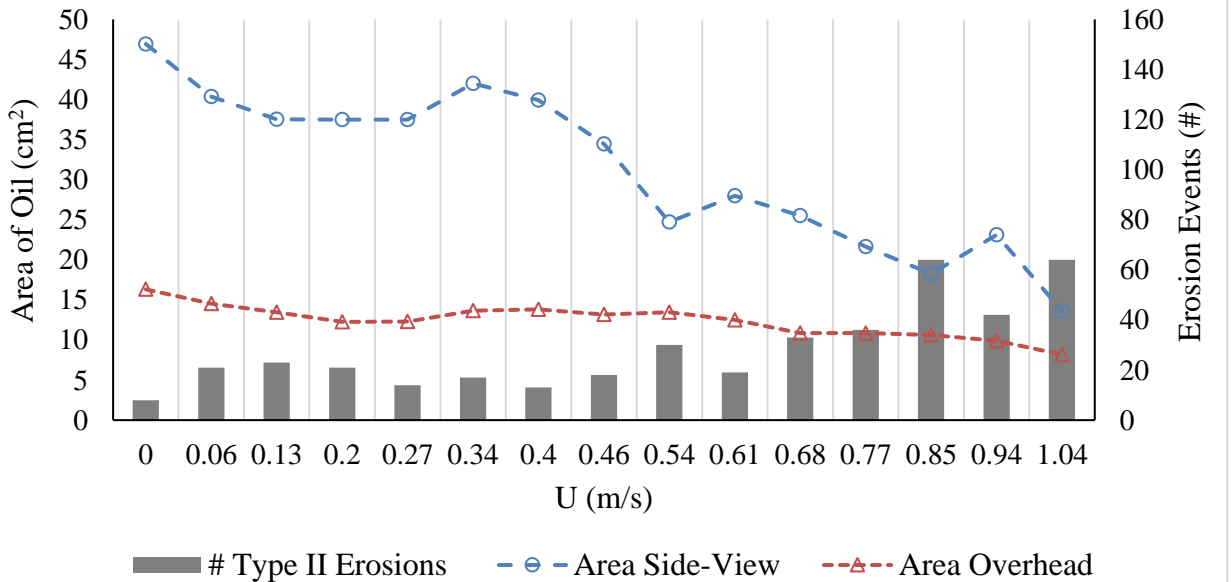
Trial 18: Medium Pebble, WC oil, 11°C



Trial 19: Medium Pebble, WC oil, 25°C



Trial 20: Medium Pebble, WC oil, 25°C



APPENDIX C: Chapter 4 Appendices

Appendix C.1: Catalogue of Sunken Oil Images

NOTE: Due to the size of the catalogue, it was saved as an external document (*Sunken Oil Catalogue.pdf*)

Table of Contents

Bookmark Name	Page #
High Viscosity Threshold Criteria Table.....	2
Type II Erosion Example.....	3
SOP Bedload Transport Example.....	4
Low Viscosity Threshold Criteria Table.....	8
Gravity Spreading Example.....	9
Rope Formation Example.....	11
Ripple Formation Example.....	12
Type II Erosion Example.....	13
SOP Break-Apart/Resuspension Example.....	14
Fresh/Clay, Sand, 8.6 °C.....	16
Fresh/Clay, Sand, 9.9 °C.....	26
Fresh/Clay, Sand, 24 °C.....	36
Fresh/Clay, Sand, 25 °C.....	41
Weathered/Clay, Sand, 7.2°C.....	46
Weathered/Clay, Sand, 10°C.....	57
Weathered/Clay, Sand, 17°C.....	65
Weathered/Clay, Sand, 24°C.....	81
Fresh/Clay, Fine Pebble, 10°C.....	97
Fresh/Clay, Fine Pebble, 10°C.....	107
Fresh/Clay, Fine Pebble, 25°C.....	118
Weathered/Clay, Fine Pebble, 10°C.....	134
Weathered/Clay, Fine Pebble, 18°C.....	144
Weathered/Clay, Fine Pebble, 25°C.....	158
Fresh/Clay, Medium Pebble, 9.5°C.....	174
Fresh/Clay, Medium Pebble, 18°C.....	190
Fresh/Clay, Medium Pebble, 22°C.....	206
Weathered/Clay, Medium Pebble, 11°C.....	222
Weathered/Clay, Medium Pebble, 25°C.....	238
Weathered/Clay, Medium Pebble, 25°C.....	254

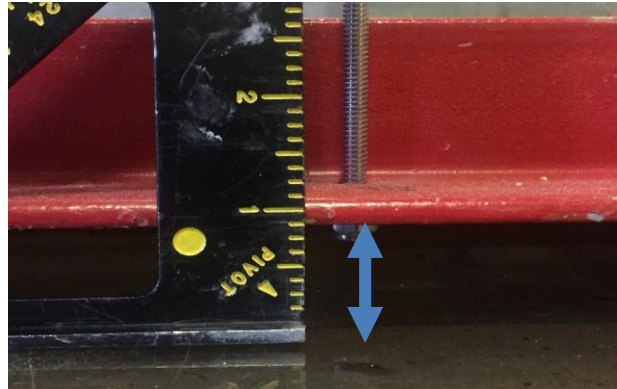
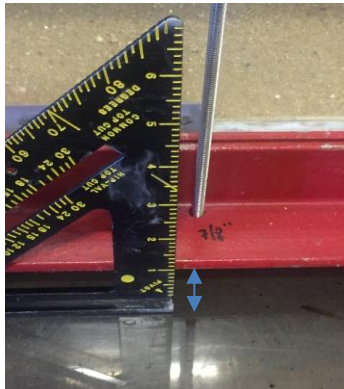
APPENDIX D: Protocols and Methods

Appendix D.1: MacFarlane Flume Protocol

Set-up and Start-up:

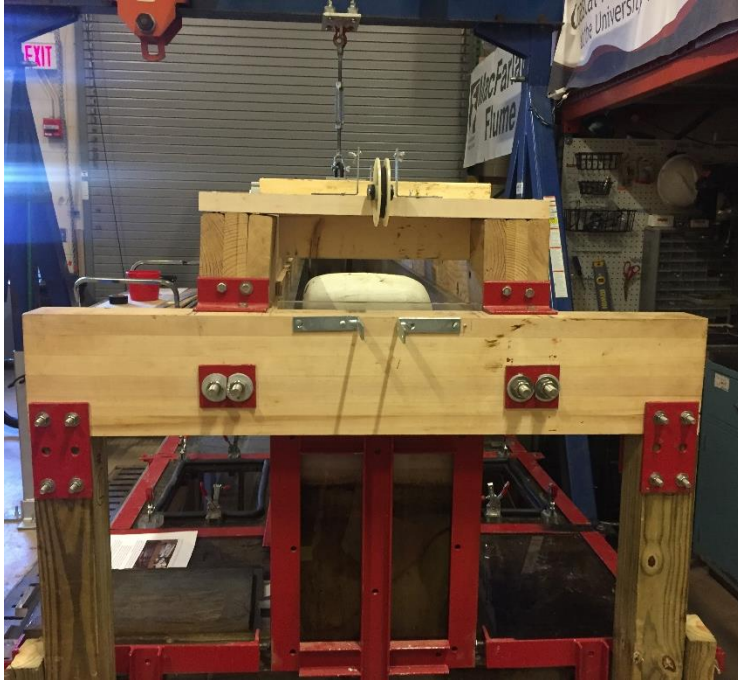


1. Check distance between the bottom of the cradle to top of plastic at each steel rod location using a speed square or a carpenter's square. The gap between the cradle and the plastic furthest from the center should be $\sim 5/8''$. Moving from outside rods towards the center, the gap should increase by $1/8''$ at each rod. The gap under the central rods should be $\sim 1''$. For example:
 - a. If the gap is less than the desired value, tighten the nuts at the top of the rods while holding the rod in place. Otherwise, rod will spin and nothing will tighten.



- b. After tightening, check the lower nut to make sure the bottom of the rod is flush with the bottom of the nut. If not, adjust upper nut while restraining the bottom one from spinning- this will draw the steel rod vertically and allow for the bottom to be flush.
2. Check the tension of each rod. Start by pulling up on each rod to make sure there is no space between the lower nut and the cradle. Once all are taught, tighten the top nut using a 7/16" wrench until you feel resistance. Check the tightness by trying to move the washer under the top nut, if you can move the washer, tighten the nut a 1/4 turn. Do so until the washer does not move.
 - a. If you tension the rods, go back to step 1, and make sure spacing between cradle and plastic is correct.
3. In locations where the upper/lower section come in contact (NE side, second and third steel rod from when facing the Flume signs), place gasket material under the nuts to minimize damage to the plastic when they come in contact. At higher velocities, the lower section bulges more.
4. Make sure blocking material is placed along the length of the flume; the blocking material ensures beams do not rotate towards the center when loaded with water
5. Check the hardware on the end-posts (1" wrench) and end-beam (#15 wrench) to make sure it is tight. If any bolts or nuts are loose, tighten them. Do not overtighten.





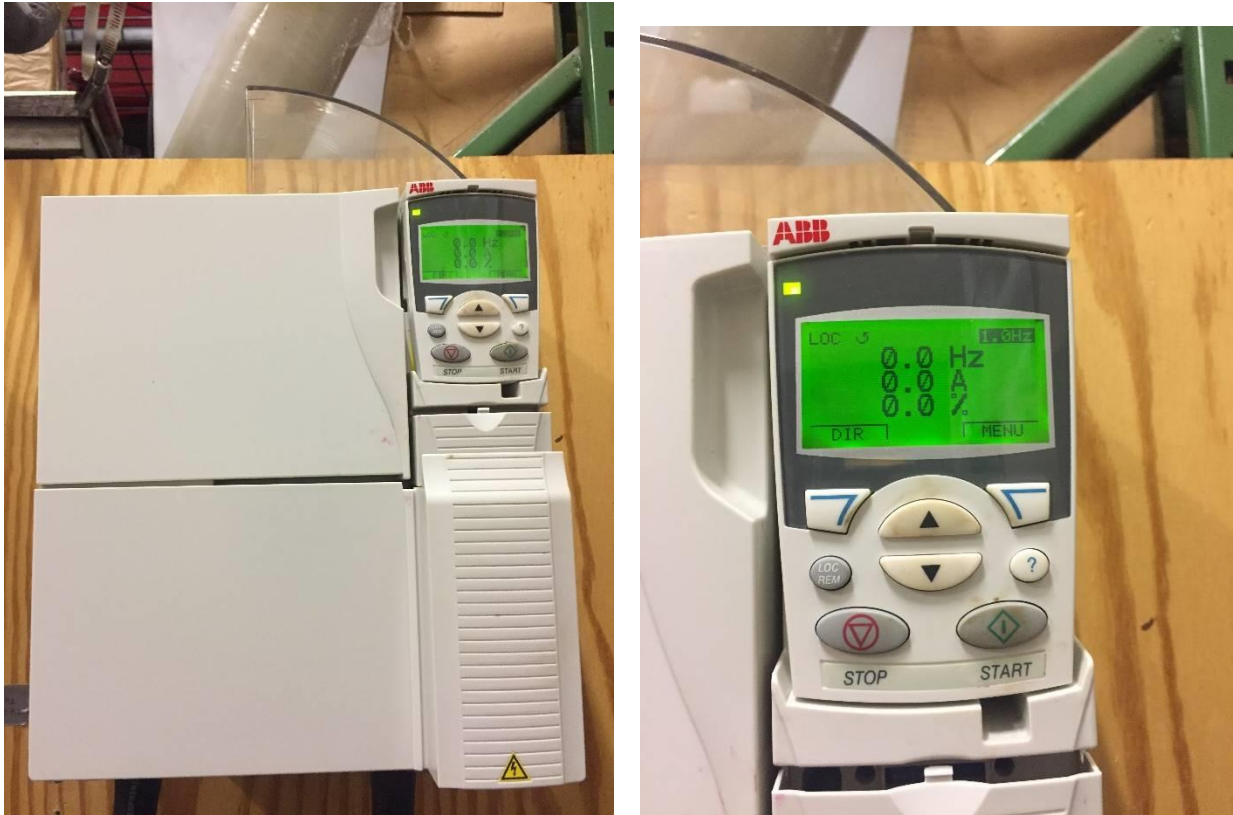
6. Put on all hatch covers. Make sure not to force the cover into place, all of them are labeled “L” (i.e., Left) and “R” (i.e., Right) side. Place the covers on-top of the hatch, each one fits into the cutout; move the left and ride side up and down until it moves freely in the hatch cutout. If you make contact with the plastic, work the cover around until it moves freely as you push up and down on the left and right sides.
 - a. Before securing the latch, check that each rubber knob is secured. If it is not, tighten the nuts. In order to secure the latches, sit on top of the hatch. As you’re sitting on the hatch, secure the front right corner first, followed by the back left corner, back right corner and front left corner.
 - b. The hatch above the propeller closest to the workbench, requires a plastic shim under the front right latch. Place the thickest part of the shim under the latch and then secure.
 - c. Put lead blocks on the three largest hatches (a good indicator to not step near them and minimize unwanted leaking).

- d. Sometimes the latches break off- in order to fix it, get a 1/4"- 20 tap and die set, a 3/16" drill bit with power drill, a vacuum, rubbing alcohol, paper towels/oil rags, a chisel, 1" stainless steel machine screws, and acrylic glue. Using the chisel, remove excess glue from the flume's plastic and plastic block to make sure fit is flush for future connection. Align the holes in the block with the holes in the flume top-sheet, secure in place with a clamp or machine screws; if using machine screws place in 2 opposing corners. Once secure, measure 1" on the 3/16" drill bit and mark with masking tape. Drill 1" through the holes and into the flume's plastic top (~0.25"). Remove as much excess material as possible. **DO NOT DRILL THROUGH THE FLUME TOP.** Vacuum out excess material from the holes, once clean, tap the holes. If you feel resistance while tapping, back it out and remove excess material. Do so to all 4 holes. Test the new 1" machine screws to make sure they fit and secure the block in place. Clean the faces being glued together using rubbing alcohol. Apply acrylic glue (make sure to wear a respirator), and secure in place by tightening screws down. Allow to dry for 24 hours before using latch.
7. For experiments using substrates, install at this point following *Protocol for Substrate Preparation and Installation*.
8. Fill the flume by placing the hose behind the white turning section near the garage door. If both hot and cold nozzles are fully open, the lower section takes approximately 45 minutes to fill. As the water reaches the upper section, you'll hear bubbling. This is normal as the central part of the flume in the lower section needs to fill with water.

9. Turn down the flow for hot and cold, to slowly fill the upper section with water. Fill the top section until the depth is 12” or less depending upon the experiment (critical flow depth~9”).
10. Filter water using the fine screen baskets; this eliminates unwanted particles from the water. May take 10-15 minutes – make sure to hold the baskets in place.
11. Install the Vectrino, see *Vectrino Protocol*.
12. Turn on motors using both VFDs; to turn on VFDs, move the emergency off switch from “off” to “on”. This provides power to the system. Allow the VFDs to warm up for 1 minute prior to using.



13. Set VFDs to 1 Hz prior to turning on using the “up” and “down” arrows on the control system.

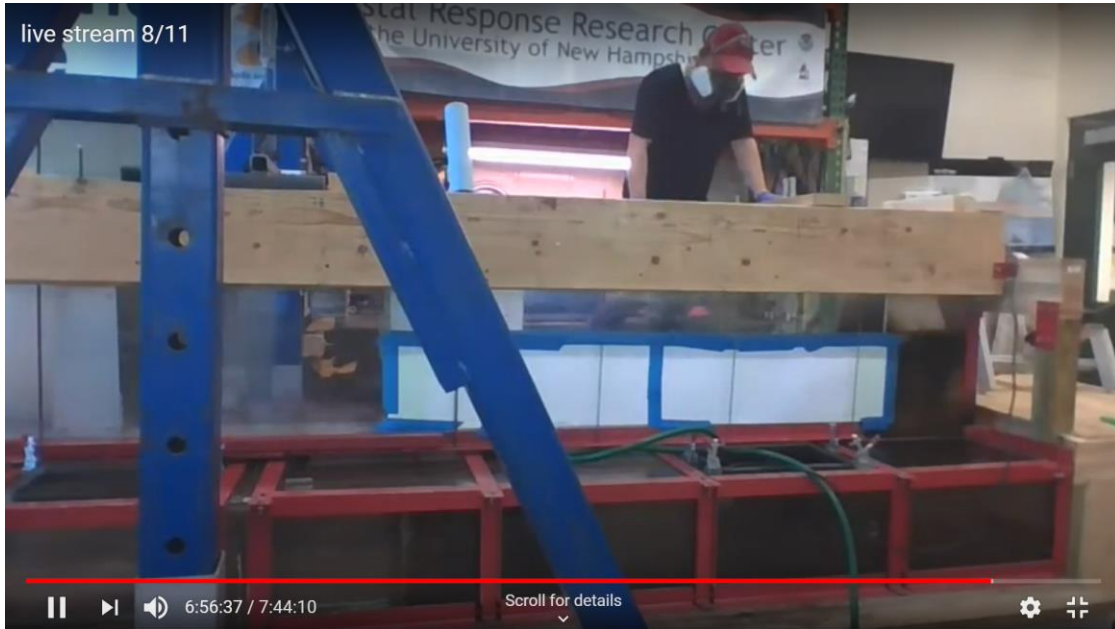


14. Warm up motors: turn on motors using VFD control system, by pressing “Start”. Allow to remain at 1 Hz for 1 minute, slowly increase the VFD setting to 5 Hz and leave at this setting for 1 minute. Increase VFD setting to 8 Hz, and leave at this setting for 1 minute (helps mix the seeding material prior to oil injection). Finally, lower the VFD setting from 8 to 1 Hz and then press stop using the VFD controller NOT the emergency shut off.

15. You are now ready to conduct experiments in the MacFarlane Flume.

Clean-up and Shut-Down:

1. Simultaneously, lower both VFD frequencies to 1 Hz using the up/down arrows. Turn off the VFDs by switching the emergency shut off from “on” to “off”.
2. Remove the hose used to fill the flume with water and coil it around the hose rack.
3. Place the sump-pump in the lower section of the flume by lowering it through the turning section closest to the motors so it rests on the bottom of the lower tank. Place the hose in the drain and then plug the sump pump into the outlet.
4. Once the top section is emptied, unplug the sump-pump, and allow the sump to drain the lower section using the established suction.
5. Unscrew and disconnect the cord from the Vectrino and remove it from the flume. Using Kim wipes and Citra-Solve gently wipe the prongs and shaft of the Vectrino by spraying the solvent onto the Kim wipe and then wiping the instrument. Once cleaned, place the Vectrino back into the blue “Vectrino” box and store the box in a safe location.
6. Remove the substrate from the bottom (it is easier while the tape is still wet); if the substrate is contaminated with oil, coil, and place in hazardous waste bin. Clean the test section (acrylic bottom and sides) using soap and water if no oil was in flume. If oil was used, clean bottom and sidewalls using Citra-Solve (make sure to wear a respirator, gloves, safety glasses, and lab coat).
 - a. Sweep water out of upper section using the clean broom (it won’t drain on its own)
 - b. Wipe out any additional water using the paper towel/oil towels
 - c. Using rubbing alcohol, wipe down acrylic where you’re attaching substrate or filming through.



7. Once the water level is below the hatch level, remove all hatches to ensure gaskets recover to their original shape. Wipe away oil using the oil rags and dispose contaminated rags in the hazardous waste bucket. Do not put hatches back into place until using the flume again.
8. When ~1" of water remains in the lower section of the flume remove the sump pump and vacuum out the rest of the water using the shop vac.
 - a. Remove the shop vac's filter.
 - b. Vacuum any water that pooled on the wood deck (allow the wood to dry out as much as possible).
 - c. Clean propellers, propeller shafts, and stands after every trial. The brass will corrode if in contact with oil.
9. Clean the lower section using Citra-solve and oil rags to remove oil from the acrylic sidewalls, top, and bottom.
 - a. Wash flume out with hot water.

- b. Start vacuuming the oil/water/citrasolve mixture at the garage door side of the flume. The water drains towards the end of the flume with the propellers.
- c. Vacuum acrylic until dry.
- d. Dispose any oiled rags in the hazardous waste bin.

Appendix D.2: Nortek Vectrino Profiler II Protocol

See Nortek Vectrino Manuals for further information/clarification

1. Hardware:

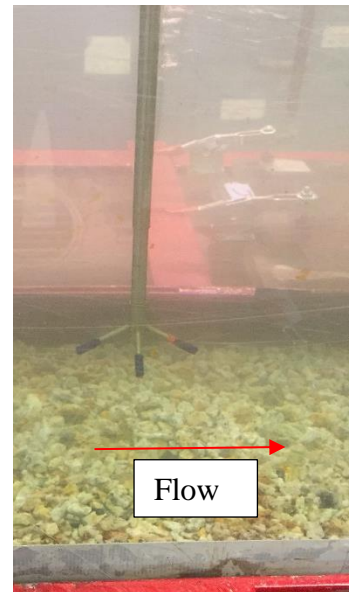
- a. Place and secure the Vectrino stand in the sampling location (~10.5ft from Entrance); tighten sides using Alan wrench. Make sure stand is level in all directions, otherwise the Vectrino is pitched for experiments (introducing excess noise).



- b. Remove Vectrino from the blue case, clean prongs, and central beam with Kim Wipes prior to installation.
- c. Secure Vectrino in the stand using hose clamps; hose clamps should align with grooves in Vectrino. The red-tabbed probe should face in the direction of flow. Beam 1 (i.e., X), moving clockwise, and Beam 2 (i.e., Y) measure horizontal velocity components, and Beam 3 (i.e., Z1) and Beam 4 (i.e., Z2) measure the vertical velocity components.

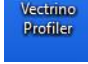


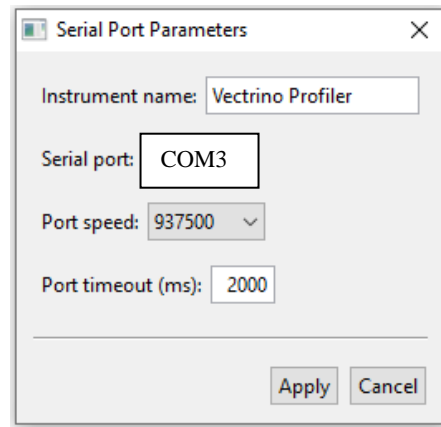
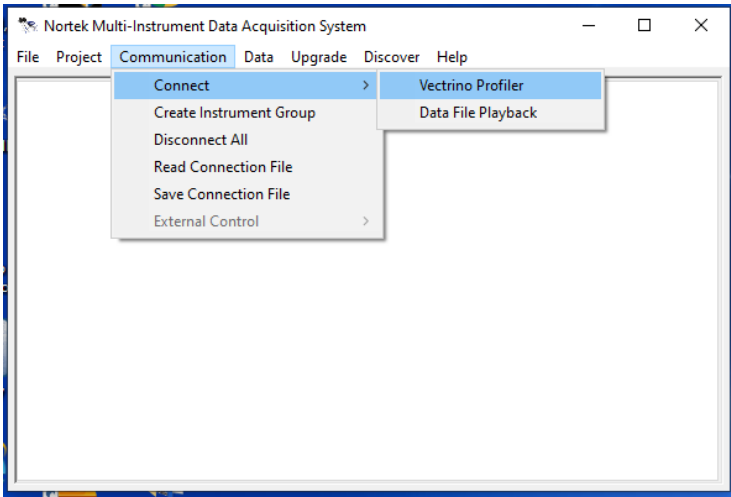
- d. Adjust the location of the Vectrino by sliding the 80-20 material horizontally and vertically, fasteners are tightened using an Alan wrench. If measuring velocity in the center, place Vectrino equal distance from both side-walls. Vertical adjustments depend upon sampling location in the water column. For example, if measuring the bottom 3 cm, the center probe should be roughly 7 cm from the bottom.
- e. Make sure the Vectrino prongs are equal distance from the bottom (i.e., no horizontal pitch in either direction). Prongs 1 and 3 should be parallel to flow direction, and Prongs 2 and 4 should be perpendicular to the flow direction.
- f. Plug the blue-USB into the computer (this connects the Vectrino to the computer)
- g. Plug the blue-corded cable into the top of the Vectrino (match up the prong pattern); the plug should sit flush on top of the Vectrino. Screw down the cap to protect from water damage.
- h. Final vertical adjustments of the Vectrino should be made using the Vectrino's "Bottom Check" function.



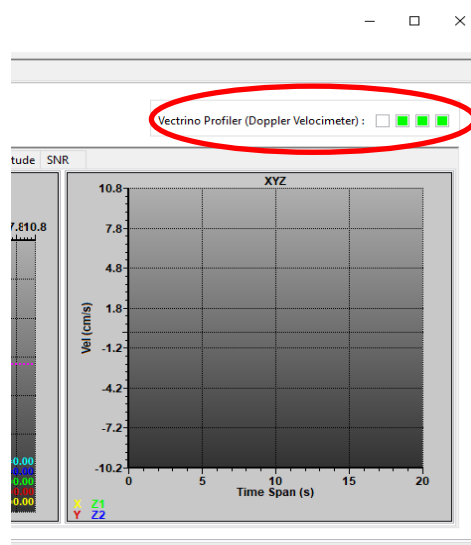
2. Software:

- a. Turn on the computer
- b. Plug in the computer power cord
- c. Computer Account password: bubba1234

- d. Open the “Vectrino Profiling”  Icon
- e. Select “Communication”  →”Connect “→”Vectrino Profiler”→”Serial Port” = COM3 → “Port Speed = 937500 → “Port Timeout”=2000



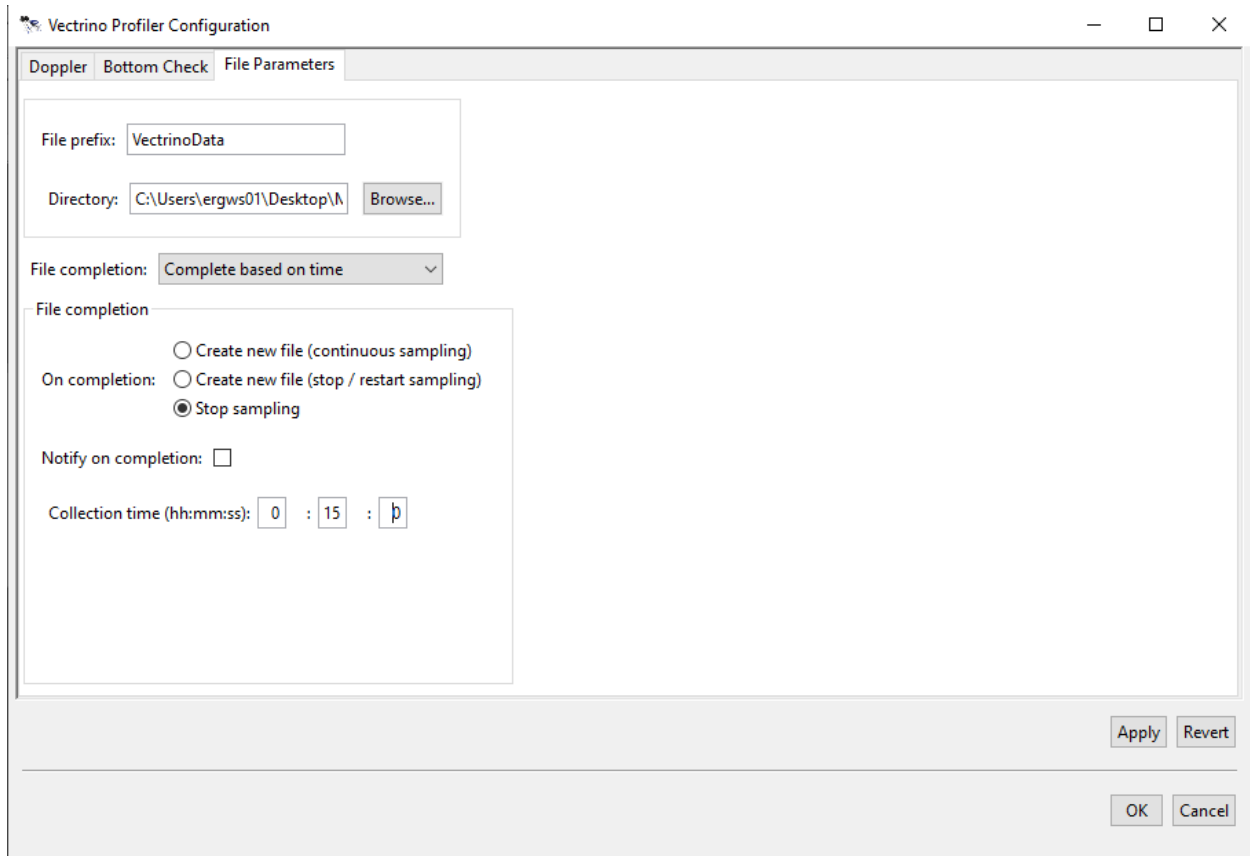
- f. A successful connection is indicated by the three green lights (shown in red circle), and successful data collection is shown by four green lights.



Icon Descriptions:



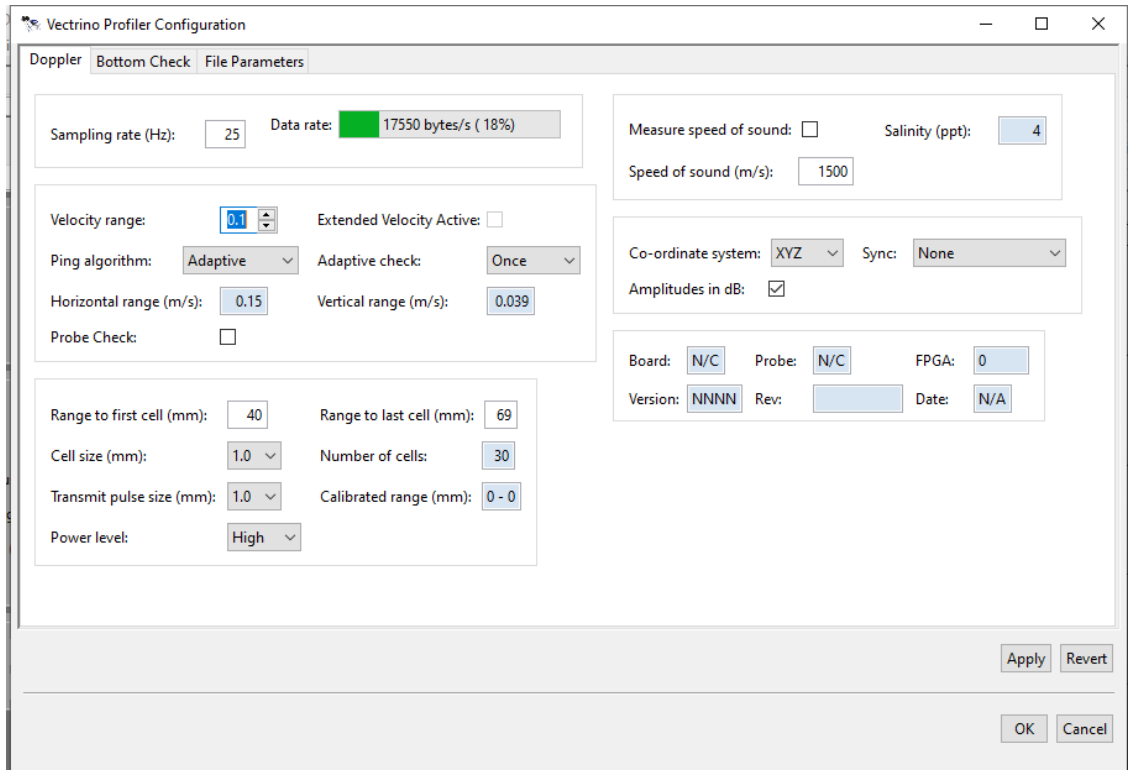
- A. Start and stop data collection (blue highlight = data collection started)
- B. Pause data collection
- C. Save data being collected (indicated by blue highlight)
- D. Configuration (Doppler, Bottom Check, File Parameters)
- E. Option to show different plots
- F. Time span and instantaneous
- G. Standard deviation shown in plots
- H. Selection of plots
 - g. Open Configuration Icon → File Parameters → Select locations for Vectrino Files to be saved in (generally easiest to make a single file on the desktop and direct files into that location).
 - i. File completion: complete based on time
 - ii. On completion: stop sampling
 - iii. Collection time (hh:mm:ss): e.g., 00:15:00 = 15 minute collection duration (or whatever the duration of the experiment is).



h. Adjust Doppler Settings:

- i. Click on the “instrument configuration” icon, and the Vectrino Profiler.

Configuration window should show, select the “Doppler” tab:



- ii. Adjust the Sampling rate (Hz) as needed, the higher the sampling rate the better the temporal resolution (however, if the sampling rate is too high then the computer drops sampling records and which disrupts the time series, rendering the record useless). A sampling rate of 25 Hz is recommended for data collection of about 15-17 minutes. A sampling rate of 10 Hz is recommended for data collection of 60 minutes.
- iii. Ping Algorithm: Adaptive
- iv. Adaptive check: once
- v. Velocity range adjusted depending upon *in-situ* flow conditions.
 1. Velocity Range: Function of Velocity, changes with VFD settings and bottom substrate type.
 - a. VFD Setting: 1 to 8 Hz → Velocity Range = 1.5
 - b. VFD Setting: 9 to 11Hz → Velocity Range = 2.0

c. VFD Setting 12 to 13 Hz → Velocity Range = 2.5

d. VFD Setting 14 to 17 Hz → Velocity Range = 3

vi. Range to first cell: 40

vii. Range to last cell: 69

viii. Click: Apply at the bottom right corner to save settings

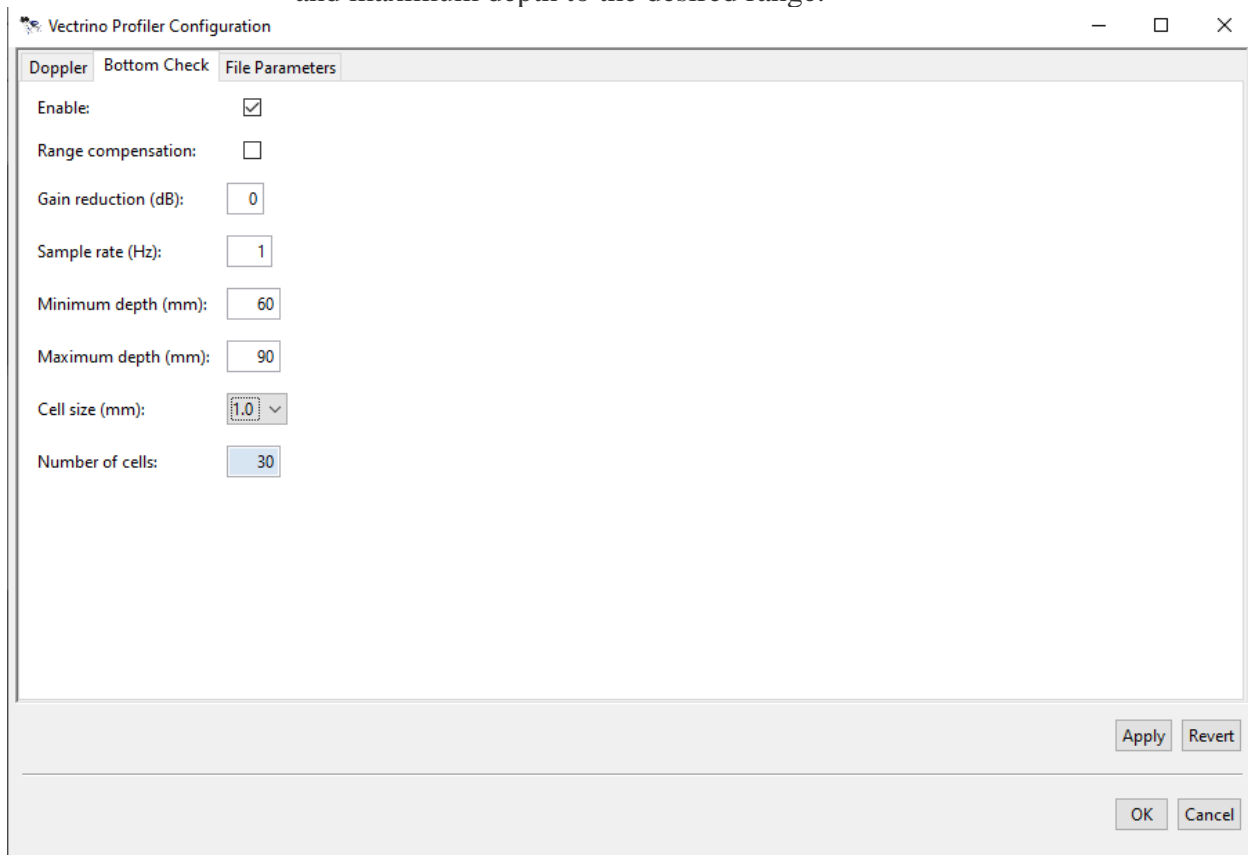
i. Bottom Check:

i. Open “Configuration” icon → Bottom Check

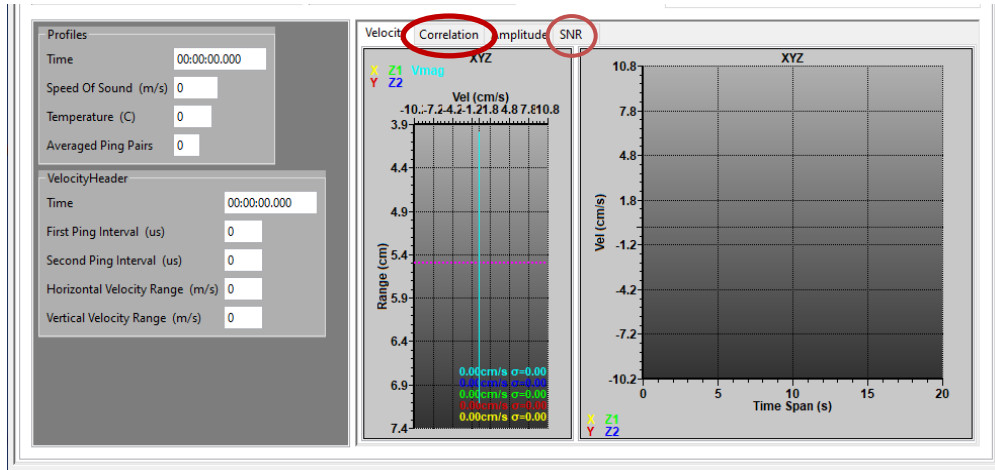
ii. Check the “Enable” box

iii. Set the range (mm) of where the bottom is expected to be, if Vectrino probe is placed 7 cm from bottom, then settings should be:

iv. If probe is placed higher in the water column, adjust the minimum depth and maximum depth to the desired range.



- j. Once the Vectrino is in position and settings are correct; start data collection.
- k. Start by not saving data while collecting data to adjust the Ping Algorithm and Velocity Range to optimize data quality. These adjustments move the weak spot and improve %Correlation and SNR (signal to noise ratio).
 - i. Note: the acrylic boundary will cause increased back scatter and poor data quality because the Vectrino cannot identify the bottom. Place multiple strips of black gorilla tape to improve the signal or a dark/thin alternative.
 - ii. Check data quality and weak spot location by clicking on the “Correlation” tab (red circle). Correlation should range be higher than 70%, but 100% is ideal.
 - iii. Check data quality using SNR (orange circle); this value should be greater than 10, but the higher the better.
- l. When %correlation and SNR show high values and minimal weak spots are detected; stop the data collection, restart to make sure settings are adequate. Allow data to collect for 5 seconds without saving; after 5 seconds, click the “save” icon. During that 5 second period, determine if the signal is strong or if interference is taking place. If the system is showing a lot of noise, stop and restart the collection process.



- m. After data collection has been stopped, name the file with descriptive title (e.g., WeatheredOil_10C). Note: do not use any "." in the file name or Matlab will not correctly import the file.
- n. After collecting data, export into Matlab files: select "Data" tab in toolbar → export as MatLab file → select the file and save to external hard drive.
- o. Unscrew/unplug the cord and remove the Vectrino from the flume. Using Kim wipes and Citra-Solve gently wipe the prongs and shaft of the Vectrino by spraying the solvent onto the Kim wipe and then wiping the instrument. Once cleaned, place the Vectrino back into the blue "Vectrino" box and store the box in a safe location.

Appendix D.3: Creation and Installation of Substrates Protocol

Materials:

- Respirator
- Lab Coat/Gloves/Closed-toed shoes/long pants
- 14"x50' roll of metal flashing
- Razor blade/box cutter
- Gorilla tape
- Small paint brush
- Metal-cutting shears/scissors (i.e., Tin snips)
- Yardstick
- Sharpie
- Aggregate (3/4 screen sand, 3/4" stone, 1/8" pea stone) Enough to cover an 11.5"x5' sheet of metal flashing
- Rubber contact cement
- Tape measure
- Rubbing alcohol
- Sandpaper
- Paper towels
- Large roll of paper wider than 14" (perform construction on paper, easier clean up)
- Cinder blocks (x2)

Creation of Substrate:

1. Put on gloves and safety glasses.
2. Unroll 6 ft of the metal flashing and place cinder blocks to hold down flashing. Measure 5 ft from the edge in two locations along the width of the metal flashing, mark with a sharpie and draw a line across the width at 5 ft using the yard stick.
3. Keeping the yard stick in the same spot, score the line using a razor blade/box cutter creating a preformation that runs the length of the yard stick.
4. Using the tin snips cut across the line. Once a small distance of the flashing has been cut, peel apart the flashing on either side of the score line to make a more precise cut resulting in a 14 inch by 5t ft sheet of flashing.

5. Using the yard stick measure 2.5” from one edge of the flashing width. Mark this 2.5” about 5-6 times down the length of the flashing and connect the markings to create one line.
6. Score the flashing down the line using the box cutter so there is a visible perforation. Make a small cut in the perforation using the tin snips and peel away the 2.5” of flashing. There should now be a piece of flashing 5’ in length and 11.5” in width
7. Using sand paper, sand one entire side of flashing and then wipe with paper towels and rubbing alcohol after to remove particles.
8. Mark the taping sections on the flashing. This is where the tape will be placed to hold the completed substrate in the flume. Mark $\frac{3}{4}$ ” from the edge of the width of the sheet on both sides. Use five or six markings that span the length of the flashing and connect these markings to make one straight line $\frac{3}{4}$ ” inside the width of the flashing. Repeat this for the other side of the flashing. There should be two straight lines, both $\frac{3}{4}$ ” from the edge of both sides of the flashing width. These lines should run the whole 5ft length of the flashing.
9. Using the same procedure as step 7 create 1” taping sections on the at both ends of the flashing. The marks should run the width of the flashing. Mark 1” from the edge of the top and bottom of the flashing, use multiple markings to draw a straight line across the width of the flashing. There should be two straight lines, both 1” from the edge on the top and bottom of the flashing.
10. Lay a paper sheet on the ground and tape down the marked and cut flashing on top of the paper sheet using gorilla tape (only a small piece on all four corners). This will allow for an easy clean up after applying the contact cement and aggregate.

11. Put on a respirator and a lab coat. Open the rubber contact cement and mix according to the directions on the can. Using the small paint brush, apply the cement to the flashing being careful not to get any in the marked taping sections. In general, the bigger the aggregate size the more glue will be needed to ensure the aggregate sticks to the flashing. It is best to pour the cement onto the flashing and spread it using the paintbrush.
12. Once the rubber contact has been applied, apply the aggregate. Always put on more aggregate than you presume you may need; ensure all spaces are filled with sediment. The excess will fall off once the contact cement dries. Be sure to fill in all areas within the taping section with aggregate, once finished wipe any glue or aggregate that may have moved onto the taping section off the flashing.
13. Glue in a scale or draw in using sharpie (cm x cm grid paper for the length of the substrate – do not cut laminated paper or it will bleed when wet)
14. Let the rubber cement dry for a minimum of 12 hours.
15. Turn the sheet over, allowing the excess aggregate to fall off the sheet. Collect this and use to make the next sheet.
16. The finished “substrate”, 11.5 inch wide by 5 ft long metal flashing with the adhered substrate, is now ready for installation into the flume.

Substrate Installation:

17. Use rubbing alcohol to clean the bottom of the flume and the lower 1 inch of the each of the side walls where the substrate is adhered. If the flume is dirty or wet the tape will not adhere to the acrylic and the substrate will lift up during trials.
18. Allow adequate time for rubbing alcohol to dry or wipe with paper towels.
19. Place sheet into the upper section of the flume. The end of the substrate should be adhered 3 inches from the exit.

20. Using the gorilla tape, tape one end of the substrate to the acrylic flume bottom. Ensure the substrate edges are parallel with the flume side walls. NOTE: For best results insert substrate 24 hours before experiment.
21. Tape does not need to span the entire sides of the sheet. Use 4 pieces of tape about 1' long and space them 6" apart from one another. Make sure to press the tape into the corner of the flume (tape should be ~1/2" up the sidewall). Ensure the edge of the tape is flush with the sharpie lines on the sheet to avoid bubbles in the tape (this is why no aggregate/rubber cement can be outside of the sharpie lines).
22. Finally, tape the other end of the substrate. Rub hand along the taped sections to ensure adequate contact.



Appendix D.4: Oil Open Pan Evaporative Protocol

Materials:

- Glass petri dish (139 mm)
- Ohaus Balance with high precision (0.0001 g)
- Sample oil (14.000 g)
- Thermometer
- Ruler
- Timer/clock
- PYREX 11”x17” glass pan
- 10 mL Syringe

Methodology:

1. Obtain 4, 139-mm glass Petri dishes
2. Wipe the inside and outside of each glass petri dish with a kim wipe and acetone.
3. Label the outside of the dishes: 1, 2, 3, 4.
4. Using the high precision scale (0.0001g), weigh the labeled glass petri dishes. (*Don't assume all are the same weight).
 - a. Note: check the scale's leveling bubble, it should be inside of the designated circle. If it is not, adjust the scale's feet to ensure bubble is inside the designated circle.
5. Record the weight in “g” and tare the petri dishes.
6. While on the scale, add 14 g of No.6 oil to the pan using 10 mL syringe
7. Keep thermometer in vicinity of sample to document air temperature at each weighing interval.



- a. Air temperature will be approximately 16 °C in the hood
8. Weigh sample weight every day; document the time and date.
9. Record the mass of the dish – repeat steps 6-7 until your desired %evaporation is reached.

- a. Example: No.6 experimental oil reached %Ev=5 in approximately 35 days

10. Place petri dish in the fume hood between sampling intervals.

11. If large batches of oil need to be evaporated, use a PYREX 11"x17" glass pan.

12. Add oil to the center of the pan, allow to spread until the minimum thickness is reached. Oil thickness should be ~1.5 mm thick.

13. Place PYREX pans into the fume hood, allow evaporation to occur until all 4 of the petri dish %Ev have reached the desired value.



Appendix D.5: Clay-Oil Mixtures and Testing Protocol

Materials:

- Respirator
- Lab coat
- Safety glasses
- Disposable gloves
- Distilled water
- Testing water (fresh water at testing temperature from sink)
- Squirt bottle
- Kiln-dried kaolinite clay (“clay”)
- No.6 fuel oil
- Box scale
- Hot plate and rubber holders
- Thermometer
- Hydrometer
- 125 mL Erlenmeyer flask (“flask”) with cap or stopper
- 100 mL beaker
- 500 mL beaker
- Plastic weigh boat
- Flat metal spatula (“spatula”)
- Container with lid for mixture (e.g., mason jar) (“container”)
- Mixing table
- Duct tape
- Soil Particle Density Data Sheet:
<https://www.globe.gov/documents/352961/6588fef2-7084-46a7-9531-2031f3cc193c>

Procedure:**Determine the Density of the Kaolinite Clay**

1. Place distilled water in a clean squirt bottle.
2. At the top of the *Soil Particle Density Data Sheet*, note the length of time since the clay was dried in a kiln, and how the clay has been stored (e.g. in plastic bag, air tight container, other).
3. Measure the mass of the empty flask without its cap. Record the mass on the *Soil Particle Density Data Sheet*.
4. Measure 25 g of clay in the flask.
5. Measure the mass of the flask containing the clay (without the stopper/cap). Record the mass on the *Soil Particle Density Data Sheet*.
6. Use the squirt bottle to wash any clay sticking to the neck of the flask down to the bottom of the flask. Add about 50 mL of distilled water to the clay in the flask.
7. Bring the clay/water mixture to a gentle boil by placing the flask on a hot plate. Gently swirl the flask (using the rubber holders) for 10 seconds once every minute to keep the clay/water mixture from foaming over. Boil for 10 minutes to remove air bubbles.
8. Remove the flask from the heat and allow the mixture to cool.
9. Once the flask has cooled, cap the flask, and let it sit for 24 hours.
10. After 24 hours, remove the cap and fill the flask with distilled water so that the bottom of the meniscus is at the 100 mL line.
11. Weigh the 100 mL-clay/water mixture in the flask (without the cap). Record the mass of the mixture on the *Soil Particle Density Data Sheet*.
12. Place the bulb of the thermometer in the flask for 2-3 minutes. When the temperature has stabilized, record the temperature of the mixture on the *Soil Particle Density Data Sheet*.

13. Follow the *Soil Particle Density Data Sheet* to compute calculations.

Determine the Mass Percentage of Clay and Oil for the Mixture

14. Determine specific gravity of the fresh water at the test temperature.

15. Using the 500 mL graduated cylinder, fill the graduated cylinder with 400 mL of water at your specified test temperature. Record the temperature.

16. Place the hydrometer into the 400 mL of water; once it has settled record the specific gravity and temperature. (To get the water at the testing temperature, use different temperatures from the sink and a thermometer to fully mix the water and read the temperature.)

17. Use the following equation to determine the specific gravity of oil and clay:

$$\text{Specific Gravity of Substance} = \frac{\text{Density of Substance}}{\text{Density of Water}}$$

18. The kaolinite clay's specific gravity is approximately 1.3

19. For sunken oil, specific gravity should be greater than that of water and for submerged oil, specific gravity should be the same as that of water. Therefore, set the following equation equal to the specific gravity of water to determine the minimum specific gravity required for the mixture to sink. Calculate x_1 . Since the minimum specific gravity of the mixture was determined, and a higher clay percentage would help the mixture sink.

$$\text{Specific Gravity of Mixture} = \frac{1}{\frac{x_1}{SG_{clay}} + \frac{x_2}{SG_{oil}}}$$

○ x_1 is the % weight of clay in the mixture (as a decimal)

○ x_2 is the % weight of oil in the mixture (as a decimal)

▪ $x_2 = 1 - x_1$

○ SG_{clay} = specific gravity of clay = 1.3 (determined in part A)

- SG_{oil} = specific gravity of oil (determined using ASTM D1298-12b (2017))

Example spreadsheet/calculation to determine starting clay:oil ratio given SG of oil and SG of clay:

Clay+Oil Mixture

SG Oil @15°C	0.962	P1	P2	SG Mixture		SG Oil @21°C	0.9593	P1	P2	SG Mixture		SG Oil @25	0.958576	P1	P2	SG Mixture	
SG Clay @15°C	1.3					SG Clay @21°C	1.3					SG Clay @25	1.3				
0	100	0.00962	0.962					0	100	0.009593	0.9593			0	100	0.009586	0.958576
1	99	0.009645	0.964508					5	95	0.00972	0.972037			5	95	0.009713	0.971331
2	98	0.00967	0.967029					6	94	0.009746	0.974626			6	94	0.009739	0.973923
3	97	0.009696	0.969563					7	93	0.009772	0.977228			7	93	0.009765	0.976529
4	96	0.009721	0.97211					8	92	0.009798	0.979844			8	92	0.009791	0.979148
5	95	0.009747	0.974671					9	91	0.009825	0.982474			9	91	0.009818	0.981752
6	94	0.009772	0.977245					10	90	0.009851	0.985118			10	90	0.009844	0.98443
7	93	0.009798	0.979833					15	85	0.009986	0.988555			11	89	0.009871	0.987093
8	92	0.009824	0.982435					16	84	0.010013	1.001286			12	88	0.009898	0.989769
9	91	0.009851	0.98505					20	80	0.010124	1.012363			13	87	0.009923	0.992461
10	90	0.009877	0.98768					25	75	0.010266	1.026559			14	86	0.009952	0.995167
15	85	0.01001	1.001041					30	70	0.010412	1.041159			15	85	0.009979	0.997888
20	80	0.010148	1.014768					35	65	0.010562	1.05618			17	83	0.010034	1.003374
25	75	0.010289	1.028877					40	60	0.010716	1.071641			19	81	0.010088	1.008921
30	70	0.010434	1.043384					45	55	0.010876	1.087561			20	80	0.010117	1.011718
35	65	0.010583	1.058306					50	50	0.01104	1.103961			25	75	0.010259	1.025937
40	60	0.010737	1.073661					55	45	0.011209	1.120864			30	70	0.010406	1.040562
45	55	0.010895	1.089488					60	40	0.011383	1.138292			35	65	0.010556	1.055609
50	50	0.011057	1.105747					65	35	0.011563	1.156271			40	60	0.010711	1.071099
55	45	0.011225	1.121252					70	30	0.011748	1.174826			45	55	0.01087	1.087049
60	40	0.011398	1.139811					75	25	0.01194	1.193987			50	50	0.011039	1.103482
65	35	0.011576	1.157641					80	20	0.012138	1.213784			55	45	0.011204	1.120419
70	30	0.01176	1.176039					85	15	0.012342	1.234248			60	40	0.011379	1.137884
75	25	0.01195	1.195031					90	10	0.012554	1.255413			65	35	0.011559	1.155902
80	20	0.012146	1.214646					95	5	0.012773	1.277318			70	30	0.011745	1.1745
85	15	0.012349	1.234917					100	0	0.013	1.3			75	25	0.011937	1.193707
90	10	0.012559	1.255875											80	20	0.012136	1.213552
95	5	0.012776	1.277536											85	15	0.012341	1.234068
100	0	0.013	1.3											90	10	0.012553	1.255289
														95	5	0.012773	1.277253
														100	0	0.013	1.3

**SG of mixture does not account for entrapped air in the mixture, ultimately requiring more clay to initially sink the mixture

Preparing the Oil: Clay Mixture

20. Calculate the amount of oil and clay to be used based on weight percentage and total weight of mixture that will be tested. For example, if 20% clay is required, and the total weight of the mixture will be 14 grams, then $14 \text{ g} * 0.20 = 2.8 \text{ g}$ of clay and $14 \text{ g} - 2.8 \text{ g} = 11.2 \text{ g}$ of oil.
21. Label containers with: Date, name of person preparing mixtures, oil type, clay:oil mixture ratio, mixture quantity (in grams).
22. If container does not max out scale: tare scale with container and measure out the exact amount of required oil into the container.

- a. If container does max out the scale: tare scale with 100mL beaker and spatula and measure out the required mass of oil, with an additional about 0.75g to account for oil stuck on the sides and spatula.
23. Record mass of oil in 100 mL beaker (measure with spatula in 100 mL beaker as well since it is accounted for in the tare and oil will be on spatula).
24. Transfer $\frac{1}{2}$ of the oil from the 100 mL beaker into the final storage container using the spatula. (Be sure to avoid contaminating anything other than the container, 100 mL beaker, and the spatula).
25. Tare scale with weigh boat and measure out the amount of required clay, with an additional about 0.0020 g.
26. Transfer clay into container with oil. It is OK to bend weigh boat; avoid using other materials to transfer the clay to minimize losses.
27. Measure the amount of clay remaining in the weigh boat. Subtract this value from the initial total amount of clay to determine the actual amount of clay transferred into the container.
28. Transfer the second, $\frac{1}{2}$ of oil remaining in the 100 mL beaker on top of the clay (layering the oil and clay helps minimize losses during mixing).

29. Measure the oil remaining in the 100 mL beaker and on the spatula.

Record values and subtract from the Initial total amount of oil measurement to determine the actual oil quantity (try to get this amount to the amount of additional oil added).

30. Cap/cover the oil/clay sample while setting up the over-head mixer.

31. Using the actual amounts of clay and oil added, calculate the actual weight percentage.

32. Using the same type of container, making sure it is empty, adjust the overhead mixer so that the blade falls within the center of the container. The blade should be 0.5 cm to 1 cm above the bottom of the container. Ensure the bottom of the container is resting flat.

33. Once the overhead mixer is properly adjusted, secure the actual oil/clay mixture in place using ring-stand clamps.

34. Slowly increase the overhead mixer motor; depending on the quantity of the mixture the rpm's necessary to adequately mix the sample varies.

35. When no more clay is visible, the overhead motor can be turned off.

Visually inspect all sides of the container to determine mixing is complete. If residual clay remains on the sides or bottom of the container, adjust the blade within the container to adequately mix that location.

36. To minimize oil loss, turn on overhead motor and hold blade inside of container. Allow blades to spin to remove excess oil.

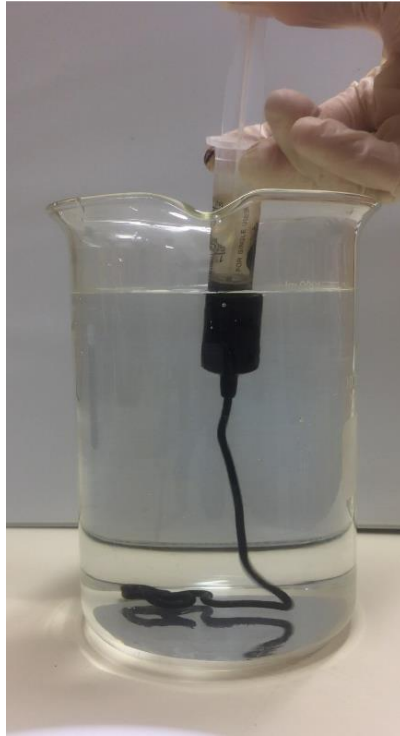
37. Store the mixture at room temperature in a dark location to minimize photo-oxidation; if the container is clear, wrap it in tinfoil (make sure the label is visible when storing).



38. MAKE SURE THERE IS NO HEADSPACE IN CONTAINER WHILE STORING!!

Testing the Oil:Clay Mixture

39. Using a 1000 mL beaker, fill the beaker ~800 mL with water. The temperature of water depends on the experimental goals and will vary from person to person. If using water with a temperature higher than that of the room, expect the water temperature to drop.
40. Record the temperature and the clay:oil mixture being tested.
41. If you wish to set up a GoPro or phone to record the experimental observations, do prior to coming in contact with the oil.
42. Using a 5 mL syringe, suck up the necessary quantity of oil. Make sure all air bubbles have been removed from the syringe by titling the syringe upside down and allowing the oil to move towards the back. Press the syringe so that some oil comes out of the opening, once only oil is coming out of the opening you are ready to inject it into the water.
43. Clean off the outside of the syringe.
44. Check the water temperature before injecting, if necessary, place the cap on the syringe opening and adjust the water temperature.
45. Depending upon your experimental objectives, either place the syringe above or below the water surface and inject the oil in one smooth, continuous motion.
46. Record the %clay:oil mixture, the temperature of the water and any observations (e.g., 100% of the oil sank to the bottom).



Appendix D.6: Density for Heavy Fuel Oil

Adjusted for No. 6 Fuel Oil, following: ASTM D1298 – 12b (reapproved 2017)

Materials:

- Respirator
- Lab Coat/Gloves/Closed toes shoes/safety glasses/long pants
- Hydrometer (Range 0.6 to 1.1)
- 500 mL Graduated Cylinder (Inner diameter of cylinder needs to be 25 mm greater than diameter of hydrometer)
- Thermometer
- Oil sample of 500 mL
- Temperature control room (15°C or 60°F)
- Syringe with steel tipped needle
- Funnel
- Tongue depressor

Methodology:

1. Set-up a ring stand, use a clamp to secure the 500 mL graduated cylinder; above the graduated cylinder tighten down another clamp. This will be used for holding the thermometer and hydrometer while they drip after sampling.
2. Using a funnel with a cut-off spout, add oil into the 500 mL graduated cylinder without fouling the sides. Add 500 mL of oil. Allow the funnel to drip, avoid fouling sides of the dish above the 500 mL line. If fouled, use a cleaning brush wrapped in an oil rag. Swirling the covered brush until oil residue is removed from the sides.



3. Place oil sample in temperature control room/in constant temperature bath [N.B. submerge graduated cylinder just above the 500 mL line] covering entire graduated cylinder column) for 24 hours; cover the top of the cylinder with aluminum foil.
4. After 24 hours, using the thermometer, mix the sample to ensure uniform temperature prior to testing.
5. Allow the oil to settle and pop any air bubbles on the oil's surface using a steel tipped needle.
6. Place hydrometer in the fluid, and slowly release in a twisting motion. Do not let the hydrometer hit the sides; use the clamp as guides for the top of the hydrometer. Allow hydrometer to settle until it reaches an equilibrium.
7. When hydrometer has come to rest floating freely away from the walls of the cylinder, read to nearest one-fifth or one-tenth of a full-scale division depending upon the number of subdivisions that is 5 or 10, respectively.
8. For opaque liquids record the hydrometer reading at the point on the hydrometer scale to which the sample rises above its main surface (Figure 2 in ASTM D1298-12b)
 - a. This reading requires a meniscus correction using the nominal values shown in table 1; record as meniscus correction.



9. Record specific gravity to the nearest measurement depending upon ASTM standards/ranges of hydrometer. Using the clamp, allow oil to drip for 2 minutes and then scrape the rest of oil of using a tongue depressor while slowly spinning the hydrometer. Remove as much oil as possible without fouling the sides of the graduated cylinder. Entirely remove hydrometer and wipe down using an oil rag.



10. Place the thermometer as far into the sample as possible without covering necessary temperature range. Record temperature to nearest 0.1 °C. If this temperature differs from previous measurement by 0.05°C, repeat the hydrometer observations and thermometer observations until temperature becomes stable.

11. Repeat experiment 3 times.

12. Perform Calculation; see attached sample calculation and ASTM D1298-12b Section 10 for specific calculation instructions. Use <https://my.hostmysite.com/ssl/30/thermotab.net/TAB/main.aspx> and *ASTM Standard Guide for Use of the Petroleum Measurement Tables* (D1250-08, 2013) to calculate Step 4b.

13. Clean all instruments, table tops and equipment using oil rags and Pro-Chem's Citra-Solv solvent.
14. Dispose of all oil and solvent contaminated rags or single use items (e.g., gloves, paint stirrers) in the labeled Hazardous Waste Bucket.
15. Put all equipment/glassware back where it was found.

Sample Calculation:

ISTM 21298-12b 2017	Sample Calc	SG Conversion	Glover M. 5/30/19
	<p>SG Readings: 1.162 @ 15°C for fresh No. 6 Crude oil 1.163 @ 70°F 1.099/liquid, correction to reading is taken from Table 1.</p> <p>B/C it is an opaque liquid, correction to reading is taken from Table 1.</p> <p>Sample: Refined, No. 6 Fuel oil Observed Temperature: 15°C = 59°F Observed Hydrometer Reading (R.D.) = 1.162 Observed Pressure: 0 PSIG Base Temperature: 60°F Correction: +0.0014 Corrected Hydrometer Reading: 1.1634</p> <p><u>Step 1:</u> Convert scale reading to density</p> $\text{Density (kg/m}^3\text{)} = \text{R.D.} \times 999.016$ $\rho_{\text{Density}} = 1.1634 \times 999.016 = 1162.3 \text{ kg/m}^3$ <p><u>Step 2:</u> HYC - thermal correction factor</p> <p>Base Temperature (T₀) of 60°F, where t = 59°F</p> $\text{HYC} = 1.0 - [0.0001278(t - 60)] - [0.000000062(t - 60)^2]$ $\text{HYC} = 1.00012774$ <p><u>Step 3:</u> HYC * Density = kg/m³_{HYC}</p> $= 1.00012774 \times 1162.3 \text{ kg/m}^3$ $\rho_{\text{HYC}} = 1162.31$ <p><u>Step 4a:</u> Calculate R.D</p> $\text{R.D.} = \frac{\rho_{\text{HYC}}}{999.016} = \frac{1162.31 \text{ kg/m}^3}{999.016 \text{ kg/m}^3} = 1.163$ <p><u>Step 4b:</u> Using ThermoTab.net ⇒ 1.163 @ 59 becomes 1.1626</p> <p><u>Step 4c:</u> API Gravity</p> $\text{API} = \left(\frac{141.5}{\text{RD}_{\text{WF}}} \right) - 131.5 = \left(\frac{141.5}{1.1626} \right) - 131.5$ $\text{API} = -9.832$		

Appendix D.7: Sunken Oil Critical Shear Stress Experimental Protocol

Preparation/Execution of Trial:

1. Install the substrate following the “Substrate Creation and Installation Protocol”.
2. Start filling the flume following the “*MacFarlane Flume Protocol*”.
3. The desired water temperature will determine how long the filling will take. Cold water in summer $\sim 21^{\circ}\text{C}$ and $\sim 8^{\circ}\text{C}$ in winter. Check the temperature with a thermometer while filling and adjust the temperature input as needed [N.B. do not rely on the Vectrino’s temperature read-out]. Stop the water when the top channel has $\sim 5''$ of water.
4. Charge GoPro batteries and clear SD cards.
5. Mix oil to ensure the clay is well distributed within the entire sample.
6. Add oil to the syringe:
 - a. Unscrew the plunger from the syringe.
 - b. Cap the syringe opening.



- c. Place the syringe, capped opening down, into the cylinder so that it stands vertically with the plunger opening at the top.
- d. Place a funnel in the plunger opening and scrape the oil sample into the syringe (e.g., 100g of oil).



- e. Add an extra 30 g more than the desired mass (i.e., 130 grams) because ~30 grams gets trapped in the syringe when it is injected.
- f. Be sure to scrape the excess oil from the funnel.
- g. Holding the syringe and capped opening, carefully put the plunger back into the opening and screw into place. While holding the cap, slowly release the cap to allow air to leave the syringe. Work the plunger so that it pushes the oil mass toward the syringe opening and all of the air has been worked out of the sample.
- h. Re-cap the syringe opening.
- i. Weigh the filled syringe (including the cap). Record the mass.



- j. Set-aside the syringe until injection.
7. Following the “*Vectrino Protocol*” to set-up the Vectrino stand; be sure to level and center the system before securing with clamps.

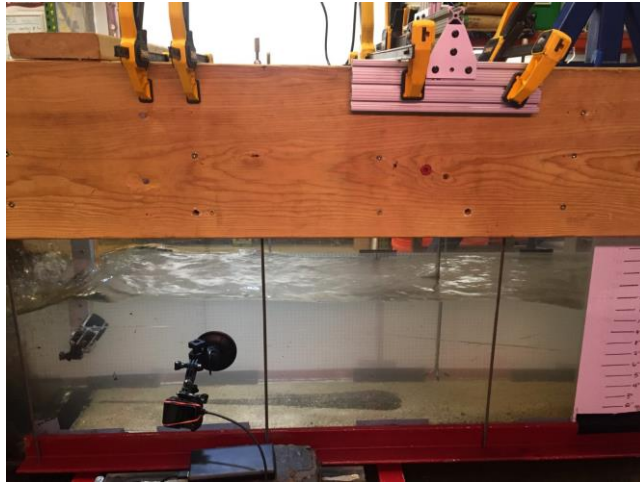


8. Conduct the Vectrino’s bottom check once prongs are submerged by water. Adjust the Vectrino so that it reads 7 cm from the bottom, the red-tabbed prong is pointing in the direction of flow, and there is no pitch/yaw/roll in the four prongs.

9. Check the placement of the overhead GoPro using the Wi-Fi connection. Using the Hero4 and an application on your phone, use the Wi-Fi connect to adjust the overhead camera's placement [N.B. the Wi-Fi connection is inhibited by water].
 - a. GoPro Usernames (Passwords):
 - i. Hero 4: SailorCam1 (Flume123)
 - ii. Hero 5: Flume Camera (Climb3889)
10. Finish filling the upper channel to 12" of water. If conducting cold water experiments, stop filling at 11" to leave room for ice addition.
11. If you need colder temperature water, use the 5th floor elevator key (found in Room 237) to access the 5th floor. There is an ice machine along the wall directly outside of the elevator. Using 2 five-gallon buckets, fill them with ice, and then bring them back down to the high bay. Return the key.
12. To mix the water, turn on the VFD's allowing them to warm up for 2 minutes. Then slowly increase the water velocity until you reach 10 Hz. Stay at 10 Hz for a minimum of 1 minute.
13. Adjust the Vectrino settings to optimize data quality based on substrate type and velocity. Increase the water velocity to the highest level expected in experimentation. Be sure the bottom is detected at this velocity.
14. If SNR is low, add 10 grams of clay to the upper channel and allow to mix.
15. Install Go Pros (overhead/sideview) and GoPro light. Attach the light using clamps, secure just downstream of oil mass.

- a. Side view camera sits outside of the water if you need more charge. Buy an external battery pack or run an extension cord. GoPro can still record while charging.

16. Turn on light and start GoPro recordings (red light will blink when recording).



17. Start a timer.

18. Inject oil, be sure to submerge opening before injection. To avoid oil drops, place oil rag under syringe while transferring it to the scale.



19. Put cap back-on syringe opening

20. Dry syringe using a rag
21. Weigh the empty syringe. Record the mass.



22. When timer reaches 2 minutes (or allotted time period). Switch the light to “flashing” mode, turn on motor to 1 Hz (or allotted velocity).
23. Start Vectrino, check that data collection is being saved.
24. Switch off “flashing” mode to the brightest continuous light.
25. Before increasing the velocity, switch light to flashing mode, increase the velocity on the VFD frequency, start Vectrino, and then turn light back to the brightest continuous light.
26. If bubbles start to collect on the Vectrino prongs, data quality is diminished. Using gloved fingers, gently remove bubbles.
27. Overhead GoPro battery will likely die around 2.5 hours, remove system from the water. Replace the pack. Put back into place. Note the time at which it occurs.
28. If water level lowers, adjust water level back to starting level using hose or by adding ice.

Break-down & Clean-up:

1. Simultaneously lower VFD frequencies to 1 Hz. Shut off VFD by turning emergency shut-off lever from “on” to “off”.
2. Drain the flume using the sump.
3. Stop GoPro recordings. Disassemble, dry-off, clean any oil from case.
4. Export videos from SD card to hard drive then erase from SD card.
5. Place GoPro batteries in charger
6. Rename Vectrino files, export to Matlab, save on hard drive
7. Remove the substrate
8. Once water level is below hatch level, remove, and clean hatches.
9. Vacuum remaining water from the lower tank using the Shop Vac
10. Clean oil from:
 - a. Vectrino
 - b. Upper channel and test section acrylic sidewalls and bottom
 - c. Propellers (including shafts and stands) and lower tank acrylic walls/bottom/top.
 - d. GoPro cases
 - e. Syringe (take apart and clean each individual section!)
 - f. Container that held oil sample
 - g. Tools/instruments used throughout experiment
11. Dispose oiled rags in the Hazardous Waste Bucket.